













THE UNIVERSITY OF ALBERTA

"A STUDY OF CHARGED PARTICLES AND  
SCATTERED PHOTONS IN MEGAVOLTAGE X-RAY BEAMS"

by



THOMAS ROCKWELL MACKIE


A THESIS

SUBMITTED TO THE FACULTY OF GRADUATE STUDIES AND RESEARCH  
IN PARTIAL FULFILMENT OF THE REQUIREMENTS FOR THE DEGREE  
OF DOCTOR OF PHILOSOPHY

DEPARTMENT OF PHYSICS

EDMONTON, ALBERTA

FALL 1984



Digitized by the Internet Archive  
in 2022 with funding from  
University of Alberta Library

<https://archive.org/details/Mackie1984>



This work is dedicated to:

My parents who brought me here,  
and Pamela who kept me here.





## ABSTRACT

The 6 MV and 15 MV photon beams produced by linear accelerators were studied for electron and scattered photon contamination. Tissue maximum ratios with and without accessories in the field indicate the presence of contamination. The surface dose was found to be attributable to contamination electrons and backscatter photons. The surface dose produced by accessories was reduced when electron filters made of materials with high atomic numbers were placed underneath the accessory. The surface dose for rectangular fields was measured and the equivalent squares for the surface dose were derived from these measurements. The 15 MV accelerator had a Gaussian lateral distribution, a linear dependence on field width for square fields and an inverse square dependence on distance from the bottom of the fixed head assembly. This geometrical dependence is consistent with the proposal that the field flattening filter is the main source of electron contamination at large field sizes when accessories are present. The electron contamination at 6 MV could not be localized to the same location. A permanent magnet was used to sweep electrons from the field. In general, electron contamination measured by a probe was produced by material close to the probe. A penetration curve for electron and scattered photon contamination was produced utilizing the linearity of dose with respect to field width. The derived contamination curve was similar to the measured build-up curve outside the field. The phantom generated tissue maximum ratio, obtained by subtracting the contamination contributions showed no dependence on





field size, source-to-probe distance or presence of accessories.

The phantom generated tissue maximum ratio was verified independently by Monte Carlo simulation. The clinical aspects of the study and the requirements for an electromagnet to sweep a large field completely free of contaminant electrons were discussed.

Volume 2 is introduced with a review of dose computation methods for radiotherapy. Several deficiencies were revealed, of which, the most important was a failure to account for the dose in situations of electronic disequilibrium. It was shown that the reduced central axis dose in a low-density heterogeneous region was due to electronic disequilibrium. It was also shown that electronic equilibrium never exists near the beam boundary and this gives rise to the beam penumbra for high energy linear accelerator beams.

A dose calculation method based on convolution was introduced which accounts for both the transport of charged particles and scattered photons. Arrays were generated using the Monte Carlo method representing the energy absorbed throughout water-like phantoms from charged particles and scattered radiation set in motion by primary x-ray interactions at one location. The resulting "dose spread arrays" were normalized to the collision fraction of the kinetic energy released by the primary x-rays. These arrays are convolved with the relative primary fluence interacting in a phantom to obtain 3-dimensional dose distributions. The method gives good agreement for the dose in electronic disequilibrium situations such as the build-up region, near beam boundaries and near low-density heterogeneities irradiated by beams with small field sizes.





## Preface

Volume 1 entitled, "Contamination of Megavoltage X-Ray Beams By Electrons And Scattered Photons", was originally written as a thesis for the partial fulfilment of a Master of Science degree. At the defense of the thesis in September of 1982, it was felt by the examining committee that Volume 1 should be used towards a Doctor of Philosophy degree.

Section 3, in Volume 1, addressed the problem of the transport of charged particles in the build-up region of a unit-density phantom. The committee felt that this Section provided a good foundation for a more complete study of the transport of charged particles generated by photon beams in an inhomogeneous medium. A decision was made to undertake this investigation to complete the thesis. Volume 2 contains the results of this study as well as a method to calculate the primary and scattered dose in heterogeneous media.

It was decided to break the thesis into two Volumes because Volume 1 is a self-contained study of photon beam contamination. The contents of Volume 2 are not referenced in Volume 1. For this reason, the Discussion, Conclusions and Appendices concerning contamination are left in Volume 1. However, in a number of instances, the reader of Volume 2 is referred to Volume 1, therefore, the pagination in Volume 2 is a continuation of Volume 1.



## ACKNOWLEDGEMENTS

Many parts of this study were suggested by my supervisor, Dr. John Scrimger. He has given me encouragement, sound advice and has freely shared his experiences in medical physics with me. I have also benefitted from the wisdom and knowledge of the physicists, Dr. Sid Usiskin, Dr. Jerry Battista and Rob Barnett. A special thanks must go to Rick Crilly, Adriano Zenari and David Perry who were always willing to talk through an idea.

Lee Santon and Colin Field eased me into the world of VAX. Linda Fleury patiently typed many early drafts of parts of the thesis. Lorentz Stenger, Frank Dolynchuk, John Issit and Finn Mortensen produced the specialized phantoms and devices used in the study. Sig Labahn instructed me in many aspects of the operation of the accelerators.

The Audio-Visual Department contributed a great deal to this thesis. Gene Brooks patiently drew all the graphs and many of the figures and Karl Liesner produced the excellent photographs.

I would also like to thank the Department of Radiotherapy for the use of their equipment.

This work was sponsored by the Alberta Heritage Foundation for Medical Research, the Provincial Cancer Hospitals Board (Alberta), the Alberta Division of the Canadian Cancer Society and the Physics Department of the University of Alberta.

This work has been dedicated to my wife, Pamela Kost, because without her it would not have been possible. Not only did she read, correct and immaculately type the manuscript, but she also gave me emotional support and guidance. She did not complain about my late laboratory evenings or my abstract absences when physically present.





# TABLE OF CONTENTS

| Chapter  | Page |
|--|------|
| 1. INTRODUCTION . . . . .  | 1    |
| 1.1 Rationale and Introduction to the Study . . . . .  | 2    |
| 1.2 Production and Interaction of X-Rays with Matter. . . . .  | 4    |
| 1.3 Interaction of Electrons with Matter. . . . .  | 15   |
| 1.4 Medical Electron Linear Accelerators. . . . .  | 18   |
| 1.5 Ionization Dosimetry . . . . .   | 31   |
| 1.6 Review of Previous Work on Contamination of<br>Photon Beams. . . . .   | 40   |
| 2. EXPERIMENTAL TECHNIQUES AND RESULTS. . . . .  | 49   |
| 2.1 Open Field Build-Up Curves. . . . .  | 50   |
| 2.2 Accessory Build-Up Curves . . . . .  | 55   |
| 2.3 Filtering the Electron Contamination. . . . .  | 64   |
| 2.4 Distance Distribution of the Surface Dose . . . . .  | 68   |
| 2.4.1 SPD Dependence of the Surface Dose . . . . .   | 68   |
| 2.4.2 Determination of the Apparent Source<br>of Contamination Electrons . . . . .   | 68   |
| 2.5 Lateral Distribution of the Surface Dose. . . . .  | 74   |
| 2.6 Surface Dose Measurements for Rectangular<br>Fields. . . . .   | 78   |
| 2.7 Penetration Curves Outside the Field. . . . .  | 81   |
| 2.7.1 Transmission Through the Collimators . . . . .   | 81   |
| 2.7.2 Determination of the Penetration Curves<br>Outside the Field. . . . .  | 81   |
| 2.8 Increase of Dose with Increasing Field Width. . . . .  | 87   |
| 2.8.1 Measurement of the Stem Effect . . . . .   | 87   |
| 2.8.2 Increase of Dose with Increasing Field<br>Width. . . . .   | 87   |
| 2.9 Determination of the Amount of Photon Backscatter<br>from the Phantom. . . . .   | 97   |
| 2.10 Sweeping Electrons from the Field Using a<br>Permanent Magnet. . . . .  | 101  |
| 2.10.1 Determination of the Field Distribution<br>of the Magnet. . . . .   | 101  |
| 2.10.2 Verifying Electrons are Swept by the<br>Magnet . . . . .  | 101  |
| 2.10.3 The Surface Dose with and without the<br>Magnet in Place. . . . .   | 108  |
| 2.10.4 Determination of the Penetration Curves of<br>Electron Contamination Produced Between<br>the Target and Magnet. . . . . | 127  |





# TABLE OF CONTENTS (CONT'D)

| Chapter  | Page |
|--|------|
| 2.11 A Method for Separating Contamination from<br>Phantom Generated Penetration Curves . . . . .    | .133 |
| 2.11.1 Determination of the Contamination<br>Penetration Curves . . . . .                            | .133 |
| 2.11.2 Determination of the Phantom<br>Generated Build-Up Curves. . . . .                            | .135 |
| 2.12 Blocking the Primary Beam. . . . .  | .156 |
| 2.13 Penetration Curve Outside a Magnetically<br>Swept Field. . . . .                                | .160 |
| 3. DISCUSSION . . . . .  | .162 |
| 3.1 Independent Modelling of the Phantom Generated<br>Build-Up Curves. . . . .                       | .163 |
| 3.1.1 Introduction . . . . .   | .163 |
| 3.1.2 Data Preparation Programs. . . . .   | .163 |
| 3.1.3 Generation of Charged Particles Set<br>in Motion. . . . .                                      | .164 |
| 3.1.4 The Monte Carlo Program. . . . .   | .178 |
| 3.1.5 Scattering Angle Transformation. . . . .   | .186 |
| 3.1.6 Assigning Dose . . . . .   | .190 |
| 3.1.7 Results. . . . .   | .192 |
| 3.2 The Source and Nature of Contamination . . . . .   | .200 |
| 3.3 Clinical Use of the Results. . . . .   | .217 |
| 4. CONCLUSIONS. . . . .  | .221 |
| 4.1 Conclusions. . . . .   | .222 |
| REFERENCES . . . . .   | .227 |
| APPENDICES . . . . .   | .231 |
| 1. Numerical Values of Constants. . . . .  | .232 |
| 2. Total and Compton Attenuation Coefficients . . . . .  | .233 |
| 3. Total Stopping Power of Electrons in Water . . . . .  | .234 |
| 4. Mean Square Mass Angular Scattering Power<br>of Electrons in Water and Lead . . . . .             | .235 |
| 5. Listing and Documentation for 'Seprimary.For'. . . . .  | .236 |
| 6. Listing and Documentation for 'Buildup3.For' . . . . .  | .237 |
| 7. Listing and Documentation for 'Normdist.For' . . . . .  | .248 |
| 8. Listing and Documentation for 'Addose.For' . . . . .  | .249 |
| 9. Reprint of "Contamination of a 15-MV Photon<br>Beam by Electrons and Scattered Photons" . . . . . | .250 |



# TABLE OF CONTENTS FOR VOLUME 2

| Chapter  | Page |
|--|------|
| 5. INTRODUCTION TO RADIOTHERAPY DOSE COMPUTATION ...   | 257  |
| 5.1 Statement of Purpose .....   | 258  |
| 5.2 Electronic Equilibrium .....   | 262  |
| 5.3 Contour Corrections .....  | 273  |
| 5.4 Corrections For Tissue Heterogeneity .....   | 281  |
| 6. MODELLING DOSE USING THE EGS MONTE CARLO CODE ...   | 295  |
| 7. A CONVOLUTION METHOD OF CALCULATING DOSE .....  | 308  |
| 7.1 Introduction .....   | 309  |
| 7.2 Primary Dose Spread Arrays .....   | 311  |
| 7.2.1 Definition of a Primary Dose Spread<br>Array.....  | 311  |
| 7.2.2 The Generation of Dose Spread Arrays<br>Using the MOCA Monte Carlo Code .....  | 311  |
| 7.2.3 Results .....  | 321  |
| 7.3 Scatter Dose Spread Arrays .....   | 332  |
| 7.4 Convolution Dose Calculation in a<br>Homogeneous Phantom .....   | 337  |
| 7.5 Extension to Heterogeneous Media .....   | 360  |
| 7.6 The Spatial Invariance of the Dose Spread<br>Arrays .....  | 380  |
| 7.7 Comparison with Other Methods and<br>Potential Improvements .....  | 384  |
| 7.8 Dose in a Non-Water-Like Heterogeneous<br>Phantom .....  | 394  |
| 8. DISCUSSION AND CONCLUSIONS CONCERNING THE<br>CONVOLUTION METHOD .....   | 397  |
| 8.1 Discussion .....   | 398  |
| 8.2 Conclusions .....  | 403  |
| REFERENCES .....   | 406  |
| APPENDICES .....   | 411  |
| 10. Listing of the MOCA Monte Carlo Code ...   | 412  |
| 11. Listing of the program Volve.for .....   | 429  |
| 12. Comparison of Heterogeneous Dose<br>Spread Arrays Calculated by the<br>Convolution Method and by the Monte<br>Carlo Method ..... | 441  |
| VITA .....   | 460  |





# LIST OF TABLES

| Table   | Page |
|---|------|
| 1. Conclusions of a Number of Authors on the Nature and Source of Contamination . . . . .   | 48   |
| 2. Surface Normalized Dose and Equivalent Squares for Rectangular Fields at 15 MV . . . . .   | 79   |
| 3. Contamination Dose Normalized to the Maximum Contamination Dose at 15 MV . . . . .   | 136  |
| 4. Normalized Dose, Tissue Maximum Ratio and Associated Errors for a 15 MV Beam at an SPD of 100 cm for Field Sizes of 3 cm x 3 cm and 4 cm x 4 cm in an Open Field. . . . .  | 141  |
| 5. Normalized Dose, Tissue Maximum Ratio and Associated Errors for a 15 MV Beam at an SPD of 100 cm for Field Sizes of 5 cm x 5 cm and 8 cm x 8 cm in an Open Field . . . . .   | 142  |
| 6. Normalized Dose, Tissue Maximum Ratio and Associated Errors for a 15 MV Beam at an SPD of 100 cm for Field Sizes of 10 cm x 10 cm and 12 cm x 12 cm in an Open Field . . . . .   | 143  |
| 7. Normalized Dose, Tissue Maximum Ratio and Associated Errors for a 15 MV Beam at an SPD of 100 cm for Field Sizes of 15 cm x 15 cm and 20 cm x 20 cm in an Open Field . . . . .   | 144  |
| 8. Normalized Dose, Tissue Maximum Ratio and Associated Errors for a 15 MV Beam at an SPD of 100 cm for a Field Size of 25 cm x 25 cm in an Open Field . . . . .  | 145  |
| 9. Normalized Dose, Tissue Maximum Ratio and Associated Errors for a 15 MV Beam at an SPD of 75 cm for a Field Size of 10 cm x 10 cm in an Open Field and with a 0.64 cm Lucite Accessory . . . . .                       | 146  |
| 10. Normalized Dose, Tissue Maximum Ratio and Associated Errors for a 15 MV Beam at an SPD of 75 cm for a Field Size of 30 cm x 30 cm in an Open Field and with a 0.64 cm Lucite Accessory . . . . .                      | 147  |
| 11. Normalized Dose, Tissue Maximum Ratio and Associated Errors for a 15 MV Beam at an SPD of 100 cm with a 3.18 cm Lucite Accessory and at an SPD of 140 cm with an Open Field Both at a Field Size of 30 cm x 30 cm . . | 148  |





# LIST OF TABLES (CONT'D)

| Table   | Page |
|---|------|
| 12. Normalized Dose, Tissue Maximum Ratio and Associated Errors for a 6 MV Beam at an SPD of 100 cm for Field Sizes of 5 cm x 5 cm and 10 cm x 10 cm in an Open Field . . . . .                             | 149  |
| 13. Normalized Dose, Tissue Maximum Ratio and Associated Errors for a 6 MV Beam at an SPD of 100 cm for Field Sizes of 20 cm x 20 cm and 30 cm x 30 cm. . . . .   | 150  |
| 14. Normalized Dose, Tissue Maximum Ratio and Associated Errors for a 6 MV Beam at an SPD of 75 cm for a Field Size of 30 cm x 30 cm in an Open Field and with a 0.64 cm Lucite Accessory. . . . .          | 151  |
| 15. Normalized Dose, Tissue Maximum Ratio and Associated Errors for a 6 MV Beam with a 3.18 Lucite Accessory in a 30 cm x 30 cm Field at 75 cm SPD and a 10 cm x 10 cm Field at 100 cm SPD . . . . .        | 152  |
| 16. Surface Normalized Dose with and without a Cerrobond Primary Beam Block Present on the Accessory Tray and the Surface Normalized Dose with the Accessory Tray in Place for a 4 cm x 4 cm Field. . . . . | 157  |
| 17. Difference Between the Primary Beam Blocked and Not Blocked with the Contamination Dose Removed . . . . .   | 159  |
| 18. Determination of the 6 MV Differential Spectrum from Measured Spectra . . . . .   | 167  |
| 19. Tissue Maximum Ratios in the Build-Up Region as Predicted by Equation 1.5.16. . . . .   | 208  |



## LIST OF TABLES FOR VOLUME 2

| Table  | Page |
|--|------|
| 20. Parameters for determining the effective<br>attenuation coefficient for 15 MV x-rays ..... | 339  |





## LIST OF FIGURES

| Figure |   | Page |
|--------|---|------|
| 1.     | Diagram of the Compton Effect. . . . .  | 7    |
| 2.     | Narrow and Broad Beam Geometries . . . . .  | 12   |
| 3.     | One Oscillation of an Electromagnetic Cavity . . . . .                                  | 19   |
| 4.     | An Electron Buncher. . . . .  | 20   |
| 5.     | Travelling Wave Accelerating Section . . . . .  | 22   |
| 6.     | Side-Coupled Standing Wave Accelerating Section. . . . .                                | 24   |
| 7.     | A 270 <sup>0</sup> Achromatic Beam-Bending Magnet. . . . .                              | 25   |
| 8.     | Treatment Head of a Mevatron -20 Medical Linear<br>Accelerator. . . . .                 | 27   |
| 9.     | The Field Defining System. . . . .  | 28   |
| 10.    | A Parallel-Plate Ionization Chamber. . . . .  | 32   |
| 11.    | The Arrangements for Measuring Percent Depth-Dose and<br>Tissue Maximum Ratios. . . . . | 37   |
| 12.    | Central Axis Open Field Build-Up Curve at 100 cm SPD<br>for a 15 MV Beam . . . . .      | 51   |
| 13.    | Central Axis Open Field Build-Up Curves at 100 cm SPD<br>for a 6 MV Beam. . . . .       | 52   |
| 14.    | Comparison Between 6 MV and 15 MV Central Axis Open<br>Field Build-Up Curves. . . . .   | 54   |
| 15.    | Accessory Build-Up Curves at 140 cm SPD for a 15 MV<br>Beam . . . . .                   | 56   |
| 16.    | Accessory Build-Up Curves at 100 cm SPD for a 15 MV<br>Beam . . . . .                   | 57   |
| 17.    | Accessory Build-Up Curves at 75 cm SPD for a 15 MV<br>Beam . . . . .                    | 58   |
| 18.    | Accessory Build-Up Curves at 75 cm SPD for a 6 MV<br>Beam . . . . .                     | 59   |
| 19.    | Accessory Build-Up Curves at 100 cm SPD for a 6 MV<br>Beam . . . . .                    | 60   |



# LIST OF FIGURES (CONT'D)

| Figure   | Page |
|--|------|
| 20. Comparison Between 6 MV and 15 MV Accessory Build-Up Curves at 75 cm SPD. . . . .  | 62   |
| 21. Comparison Between 6 MV and 15 MV Accessory Build-Up Curves at 100 cm SPD . . . . .  | 63   |
| 22. Surface Dose with Electron Filters at 15 MV. . . . .   | 65   |
| 23. Surface Dose with Electron Filters at 6 MV . . . . .   | 67   |
| 24. Distribution of the Surface Dose as a Function of SPD at 15 MV . . . . .   | 69   |
| 25. Graph Illustrating the Inverse Square Dependence of the Surface Dose on the Distance to the Source of Contamination at 15 MV . . . . . | 72   |
| 26. Graph Illustrating the Failure at 6 MV of the Inverse Square Dependence to a Localized Source of Contamination . . .                   | 73   |
| 27. Gaussian Distribution of the Surface Dose at 15 MV . . . . .   | 75   |
| 28. Comparison Between 6 MV and 15 MV of the Lateral Distribution of the Surface Dose at 100 cm SPD . . . . .                              | 76   |
| 29. Transmission Measurements Through the Collimators at 15 MV . . . . .   | 82   |
| 30. The Experimental Arrangement to Determine the Penetration Curve Outside the Field. . . . .   | 84   |
| 31. Penetration Curve at 15 MV Obtained 3 cm Outside of a 30 cm x 30 cm Field . . . . .  | 85   |
| 32. Penetration Curve at 6 MV Obtained 3 cm Outside of a 30 cm x 30 cm Field . . . . .   | 86   |
| 33. Linearity of the Surface Dose with Respect to Field Width Under a Variety of Conditions at 15 MV . . . . .                             | 90   |
| 34. Experimental Arrangement to Measure the Increase in Contamination with Increasing Field Width. . . . .                                 | 91   |
| 35. The Increase in ND Versus Field Width for Various Depths in an Open Field at 100 cm SPD for the 15 MV Beam . . . . .                   | 93   |
| 36. The Increase in ND Versus Field Width for Various Depths in an Open Field at 75 cm SPD for the 15 MV Beam . . . . .                    | 94   |





# LIST OF FIGURES (CONT'D)

| Figure   | Page |
|--|------|
| 37. The Increase in ND Versus Field Width for Various Depths with a 3.18 cm Lucite Accessory at 100 cm SPD for the 15 MV Beam. . . . .           | 95   |
| 38. The Increase in ND Versus Field Width for Various Depths in an Open Field at 100 cm SPD for the 6 MV Beam. . . . .                           | 96   |
| 39. The Normalized Dose Due to Backscatter Photons at 6 MV. . . . .  | 98   |
| 40. The Normalized Dose Due to Backscatter Photons at 15 MV . . . . .  | 99   |
| 41. The Magnetic Field Distribution of the Permanent Magnet. . . . .   | 102  |
| 42. The Angle of Deflection of an Electron in a Uniform Magnetic Field and the Measured Deflection of 18 MeV Electrons . . . . .                 | 103  |
| 43. The Set-Up to Verify that Contamination Electrons were Being Swept from the Field of the 15 MV Beam . . . . .                                | 106  |
| 44. Image of the Swept Electron Contamination . . . . .  | 107  |
| 45. The Magnet Attached to its Holder . . . . .  | 109  |
| 46. The Magnet Mounted from the Accessory Holder Position . . . . .  | 110  |
| 47. The Surface Normalized Dose with the Magnet in for Various Conditions at 100 cm SPD for the 15 MV Beam . . . . .                             | 111  |
| 48. Normalized Dose Due to Contamination Produced in Air as a Function of Field Width for an Open Field at 15 MV . . . . .                       | 113  |
| 49. Normalized Dose Due to Contamination Produced in Air as a Function of Field Width for an Open Field at 6 MV. . . . .                         | 114  |
| 50. Normalized Dose Due to Contamination Produced Between the Target and Magnet as a Function of Field Width for an Open Field at 15 MV. . . . . | 116  |
| 51. Normalized Dose Due to Contamination Produced Between the Target and Magnet as a Function of Field Width for an Open Field at 6 MV . . . . . | 117  |



# LIST OF FIGURES (CONT'D)

| Figure  | Page |
|---|------|
| 52. Normalized Dose Due to Contamination Produced in Air as a Function of SPD for an Open Field at 15 MV . . . . .  | 119  |
| 53. Normalized Dose Due to Contamination Produced Between the Target and Magnet as a Function of SPD for an Open Field at 15 MV. . . . .  | 120  |
| 54. Normalized Dose Due to Contamination Produced in Air as a Function of SPD for an Open Field at 6 MV. . . . .  | 121  |
| 55. Normalized Dose Due to Contamination Produced Between the Target and Magnet as a Function of SPD for an Open Field at 6 MV . . . . .  | 122  |
| 56. Dependence of the Dose Produced Between the Target and Magnet on the Inverse Square of the Distance from the Apparent Source with the Cross-Hair Tray in Place at 15 MV . . . . .     | 123  |
| 57. Dependence of the Dose Produced Between the Target and Magnet on the Inverse Square of the Distance from the Apparent Source with the Cross-Hair Tray in Place at 6 MV. . . . .       | 124  |
| 58. Dependence of the Dose Produced Between the Target and Magnet on the Inverse Square of the Distance from the Apparent Source with the Cross-Hair Tray Not in Place at 15 MV . . . . . | 125  |
| 59. Central Axis Penetration Curve for Electron Contamination Produced Between the Target and Magnet by the 15 MV Beam. . . . .   | 128  |
| 60. Penetration Curve for Electron Contamination Produced Between the Target and Magnet Measured Outside the Field of a 15 MV Beam . . . . .  | 129  |
| 61. Central Axis Penetration Curve for Electron Contamination Produced Between the Target and Magnet by the 6 MV Beam . . . . .   | 130  |
| 62. Comparison Between the 15 MV and 6 MV Contamination Produced Between the Target and Magnet. . . . .   | 131  |
| 63. Contamination Penetration Curve Determined by the Increase in Dose in a Limited Phantom as a Function of Field Width for a 15 MV Beam . . . . .                                       | 137  |





# LIST OF FIGURES (CONT'D)

| Figure   | Page |
|--|------|
| 64. Contamination Penetration Curve Determined by the Increase in Dose in a Limited Phantom as a Function of Field Width for a 6 MV Beam . . . . . | .138 |
| 65. The Phantom Generated Output Factor Compared to the Total Output Factor at 6 MV. . . . .   | .154 |
| 66. The Phantom Generated Output Factor Compared to the Total Output Factor at 15 MV . . . . .   | .155 |
| 67. The Scattered Photon Contamination Build-Up Curve Obtained Outside a Magnetically Swept 15 MV Field. . . . .                                   | .161 |
| 68. The Determination of the Zenith Scattering Angle . . . . .   | .165 |
| 69. The Smoothed and Unsmoothed Unnormalized Primary Photon Number Spectrum at 6 MV . . . . .  | .169 |
| 70. The Smoothed and Unsmoothed Unnormalized Primary Photon Number Spectrum at 15 MV. . . . .  | .170 |
| 71. The Flow Chart for Subroutine Impulse. . . . .   | .172 |
| 72. The Angular Distribution of Charged Particles Set in Motion by a 15 MV Photon Beam. . . . .  | .179 |
| 73. The Flow Chart for the Monte Carlo Section of the Main Program Buildup3.For. . . . .   | .182 |
| 74. Comparison Between the Monte Carlo Program and Spencer's Analytic Technique . . . . .  | .187 |
| 75. Relationship between Scattering Angles in the Particle and Phantom Coordinate Systems . . . . .  | .189 |
| 76. Distribution of Dose in a Semi-Infinite Water Phantom due to Electrons Set in Motion in the Top 0.1 cm Slab by a 6 MV Photon Beam . . . . .    | .193 |
| 77. Distribution of Dose in a Semi-Infinite Water Phantom due to Electrons Set in Motion in the Top 0.1 cm Slab by a 15 MV Photon Beam. . . . .    | .194 |
| 78. Comparison between Experiment and Computer Modelling of the Phantom Generated TMR Curve at 6 MV . . . . .                                      | .198 |
| 79. Comparison between Experiment and Computer Modelling of the Phantom Generated TMR Curve at 15 MV. . . . .                                      | .199 |
| 80. Comparison between Various Penetration Curves at 15 MV . . . . .   | .210 |
| 81. Comparison between Various Penetration Curves at 6 MV. . . . .   | .212 |



# LIST OF FIGURES FOR VOLUME 2

| Figure   | Page |
|--|------|
| 82. The state of longitudinal equilibrium in a heterogeneous phantom .....   | 263  |
| 83. Lateral electronic equilibrium in a homogeneous phantom .....  | 266  |
| 84. Lateral electronic equilibrium in a heterogeneous phantom .....  | 268  |
| 85. The experimental set-up to measure the inhomogeneity correction factor .....   | 270  |
| 86. The correction factor, for the experimental set-up illustrated in Figure 85 .....  | 271  |
| 87. Geometry to take into account contour corrections ..   | 274  |
| 88. The definition of the zero-area TAR and the scatter-air-ratio .....  | 278  |
| 89. The geometrical parameters required for the Batho or power-law method .....  | 283  |
| 90. An illustration of O'Connor's theorem .....  | 284  |
| 91. In the equivalent TAR method, the 3-dimensional electron density information is "coalesced" into one cross-sectional slice ..... | 288  |
| 92. The measurement of the perturbation of dose by a polystyrene annulus placed in a water tank .....                                | 292  |
| 93. The dose at point P gets a dose contribution from an annulus by "revolving" a pencil dose distribution about point P .....       | 298  |
| 94. The measured TMR is compared to the EGS calculation of the TMR .....   | 299  |
| 95. A comparison between pencil beam isodose curves in homogeneous and heterogeneous phantoms .....                                  | 302  |
| 96. A comparison of measured inhomogeneity correction factors and ones calculated using the EGS Monte Carlo code .....               | 304  |
| 97. A comparison between the calculated profiles of KERMA and dose for a heterogeneous and a homogeneous phantom .....               | 305  |



# LIST OF FIGURES FOR VOLUME 2 (CONT'D)

| Figure   | Page |
|--|------|
| 98. A comparison between dose and KERMA correction factors for the 15 MV spectrum and its spectral components .....                    | 307  |
| 99. Primary photons interact in the interaction voxel and the charged particles set in motion are followed through the phantom .....   | 312  |
| 100. Flow chart for photon transport part of MOCA .....  | 314  |
| 101. Flow chart for the part of MOCA dealing with the type of photon interaction .....   | 315  |
| 102. Flow chart for the charged particle transport part of MOCA .....  | 316  |
| 103. The Compton differential cross-section as function of kinetic energy .....  | 318  |
| 104. The choice of the kinetic energy for a Compton recoil electron .....  | 319  |
| 105. The choice of the kinetic energy for a pair production charged particle set in motion .....                                       | 320  |
| 106. A comparison of components of the percent dose predicted by MOCA and EGS for Cobalt-60 photons ....                               | 322  |
| 107. A comparison of components of the percent dose predicted by MOCA and EGS for 5 MeV photons .....                                  | 323  |
| 108. Primary dose spread arrays for 15 MV photons for gravimetric densities of 1.0, 0.8, and 0.6 when the voxel dimension is 1cm ..... | 324  |
| 109. Primary dose spread arrays for 15 MV photons for gravimetric densities of 0.4 and 0.2 when the voxel dimension is 1cm .....       | 325  |
| 110. Primary dose spread arrays for 6 MV and Co-60 photons .....   | 328  |
| 111. Primary dose spread array for 15 MV photons for a gravimetric density of 0.2 when the voxel dimension is 5cm .....                | 330  |
| 112. Truncated first scatter (TFS) dose spread array for 15 MV photons .....   | 334  |





# LIST OF FIGURES FOR VOLUME 2 (CONT'D)

| Figure  | Page |
|---|------|
| 113. Residual first and multiple scatter (RFMS) dose spread array for 15 MV photons .....   | 335  |
| 114. Illustration of the dose contribution from the interaction point of view .....   | 338  |
| 115. The variation of the effective attenuation coefficient as a function of depth .....  | 341  |
| 116. The variation of the measured effective attenuation coefficients as a function of nominal beam energy ..   | 342  |
| 117. Illustration of the dose contribution from the the dose deposition point of view .....   | 346  |
| 118. Measured and calculated TMR's for a 15 MV beam as a function of depth along the central axis .....   | 349  |
| 119. Measured and calculated percent depth-dose data for a 6 MV beam as a function of depth along the central axis .....                                  | 350  |
| 120. Measured and calculated dose profiles at dmax for a 15 MV beam .....   | 351  |
| 121. Dose profiles at dmax in homogeneous phantoms with various densities .....   | 352  |
| 122. The relative primary fluence profile for 15 MV beam wedges and the fluence profile used to obtain the calculated isodose curve in Figure 123 ..      | 354  |
| 123. The calculated isodose curve for the fluence profile shown in Figure 122 and the measured isodose curve for a 60 degree wedge for a 15 MV beam ..... | 355  |
| 124. The measured dose profile at a depth of 5 cm when a shield is placed in the 15 MV beam .....   | 357  |
| 125. The bar shield represented by three fields .....   | 359  |
| 126. Components of the percent depth dose in a homogeneous water phantom predicted by MOCA for a 6 MV beam .....  | 361  |
| 127. Components of the percent depth dose in a heterogeneous phantom predicted by MOCA for a 6 MV beam .....  | 362  |



# LIST OF FIGURES FOR VOLUME 2 (CONT'D)

| Figure  | Page |
|---|------|
| 128. Determination of the average density between the interaction and dose deposition voxels .....  | 364  |
| 129. Ray tracing is performed by sampling the density between the interaction and dose deposition voxels .....  | 366  |
| 130. Schematic representation of the slab phantoms tested to verify the approximations used in determining the dose in heterogeneous phantoms .....                                     | 370  |
| 131. The experimental and measured TMR correction factor for a 15 MV 5cm x 5cm beam .....   | 373  |
| 132. The experimental and measured TMR correction factor for a 15 MV 10cm x 10cm beam .....   | 374  |
| 133. The calculated homogeneous and heterogeneous TMR profile for a 15 MV .....   | 376  |
| 134. A comparison of separating the task of determining the wedge dose distribution and calculating an inhomogeneity correction factor and performing the calculation in one step ..... | 378  |
| 135. The dose spread array should be tilted to simulate the dose deposition from a divergent primary pencil beam interacting at i,j,k .....   | 382  |
| 136. A comparison of the convolution method with existing dose calculating methods .....  | 386  |
| 137. A flow chart of the host computer calculations required if an array processor is used to perform part of the convolution calculations .....  | 390  |
| 138. A flow chart of the array processor calculations ...   | 391  |
| 139. The part of an average density array calculated for one beam, that intersects with the average density array of another beam, may be reused by the second beam .....               | 392  |
| 140. The flow chart of the determination of the dose spread array and primary attenuation coefficient based on the transmission spectrum of a linear accelerator .....                  | 401  |



VOLUME 1

CONTAMINATION OF MEGAVOLTAGE X-RAY BEAMS  
BY ELECTRONS AND SCATTERED PHOTONS





## 1. INTRODUCTION

The errors of definitions  
multiply themselves accordingly  
as the reckoning proceeds;  
and lead men into absurdities,  
which at last they cannot avoid,  
without reckoning anew  
from the beginning.

Thomas Hobbs



## 1.1 Rationale and Introduction to the Study

Megavoltage photon beams are the radiation modality most often used in the treatment of cancer by radiotherapy. Photons produced by medical linear accelerators have become the most important method of delivery of these beams.\*

Megavoltage photon beams become contaminated with relativistic electrons and scattered photons. An understanding of the role of electron and scattered photon contamination is required to characterize dosimetry in the build-up region. Clinically, high energy x-ray build-up produces a skin-sparing effect and contamination tends to reduce this effect.

The Cross Cancer Institute in Edmonton, Alberta employs three Siemens linear accelerators, two of which operate at 6 MV photons and one which delivers a 15 MV photon beam. These accelerators have a very similar design so an opportunity existed to compare and contrast the contamination at two different nominal energies.

The dependence of position inside and outside the photon beam, distance from the source of primary photons and cross-sectional dimensions (field size) of the beam on the nature and amount of contamination was investigated. Accessories were placed in the path of the beam to determine their effect on contamination.

The photon beam was passed through the poles of a permanent magnet to sweep the contamination electrons out of the beam. The depth of penetration of the contamination electrons was determined by comparing dose measurements at depth in a phantom with and without the magnet in place.

\* Cobalt-60 isotope sources and betatrons can deliver megavoltage photon beams as well.



The depth of penetration for the electron and scattered photon components was determined utilizing the increase in dose with respect to the field size of the beam. The tissue maximum ratio (TMR) in the build-up region of the phantom generated component was obtained by subtraction of the contaminant contribution.

A knowledge of the nature of the primary photon component of the beam is important to the clinical use of such a photon beam because most treatment planning systems isolate the primary from the scattered photon component of dose. The validity of the phantom generated build-up curve, as obtained by subtraction of the contamination fraction, was verified by computer modelling the primary photon contribution.

The nature and sources of electron and scattered photon contamination, based on the experimental and calculated results, is discussed in detail.

The role in clinical radiotherapy of electromagnets to sweep electron contamination from the field, and electron "filters" to scatter electron contamination, is discussed briefly.





## 1.2 Production and Interaction of X-Rays with Matter

Megavoltage photons are packets of energy exceeding 1 million electron volts (MeV) each.\* Although photons have dual wave and particle properties, photons (as their name implies) in radiation physics, are treated as if they were particles.

X-rays are photons produced by the interaction of charged particles with matter. In commercial x-ray equipment each photon is produced by the interaction of a relativistic electron with an atomic electron or nucleus of a target material. This process is called bremsstrahlung. The differential cross-section with respect to the photon energy,  $h\nu$ , for bremsstrahlung production,  $\frac{d\sigma_{\text{brem}}}{d(h\nu)}$ , from a charged particle inter-

acting with an atomic nucleus is given by:

$$\frac{d\sigma_{\text{brem}}}{d(h\nu)} = \frac{e^2}{\hbar c} \left\{ \frac{e^2}{m_0 c^2} \right\}^2 Z^2 \frac{T + m_0 c^2}{T h\nu} B \quad (1.2.1)$$

where  $e$  is the electric quantum of charge

$\hbar$  is Plank's constant  $\hbar = (h/2\pi)$

$m_0$  is the charged particle mass

$c$  is the speed of light

$Z$  is the atomic number of the target nucleus

$T$  is the charged particle kinetic energy

$h\nu$  is photon energy

$B = B(Z, h\nu/T)$  is a dimensionless quantity from quantum electrodynamic theory and is of the order of unity (1)

(Appendix 1 lists numerical values of physical constants).

\* 1 MeV =  $1.602 \times 10^{-13}$  J



The effect of interactions with atomic electrons can approximately be taken into account by replacing the factor  $Z^2$  in Eqn. 1.2.1 by  $Z(Z+1)$ . The second order dependence of the cross-section on  $Z$  means that high atomic number materials are the most efficient targets for the production of bremsstrahlung. The inverse square dependence on charged particle mass explains why electron beams are always the accelerated charged particles used in commercial x-ray devices.

The number of photons produced by bremsstrahlung per photon energy intervals at a given electron energy is proportional to Eqn. 1.2.1 and so is proportional to  $1/h\nu$ . Therefore, the value of the photon number spectrum for bremsstrahlung produced by monoenergetic electrons is greater for lower energies. In the practical situation the electron beam interacting with the target is not monoenergetic. The initial energy of electrons has a small spread. More importantly, as the electrons interact with a target of finite thickness they lose energy as they traverse it. This results in fewer high energy photons and more lower energy photons than predicted using a "thin-target" bremsstrahlung approximation so the spectrum is strongly peaked at low photon energy. Consequently, the nominal megavoltage designation of photon sources produced by bremsstrahlung refers to the maximum photon energy of the beam.

With minor exceptions the interaction of photons with matter occurs via the photoelectric effect, Compton effect and pair production.

In the photoelectric process a photon is completely absorbed by an atom which becomes ionized by ejecting an electron. The photon energy is almost completely shared between the kinetic energy of the electron and the binding energy of the electron. Very little kinetic



energy is given to the ionized atom but most of the photon momentum is transferred to the atom. The probability of interaction is highest when the photon energy is near to but greater than an electron binding energy. For this reason, the photoelectric absorption probability for an element is discontinuous at the atomic shell binding energies. The interaction of the K-shell electrons contribute about 80% to the atomic cross-section. To a first approximation, the dependence of the atomic cross-section,  $a^T$ , on  $Z$  and incident photon energy has the form (1):

$$a^T \propto \frac{Z^n}{(h\nu)^3} \quad (1.2.2)$$

where  $n$  is found empirically to vary between 4.0 and 4.6 depending on the photon energy. The photoelectric effect is the dominant mode of interaction at low x-ray energies in high atomic number materials.

At intermediate photon energies the Compton effect dominates\*. In the Compton effect an incoming photon interacts with an electron. The photon is absorbed and another photon with a lower energy is created. The electron recoils with an energy representing almost all of the difference between the incoming and outgoing photon. The outgoing photon, usually termed the scattered photon, and recoil electron directions are in the same plane as the incoming photon direction. The directions of the scattered photon,  $\phi$ , and recoil electron,  $\theta$ , shown in Figure 1, are given by (2):

\* The Compton effect is the most important process from 30 KeV to 20 MeV in water and from 600 KeV to 4 MeV in lead (9).





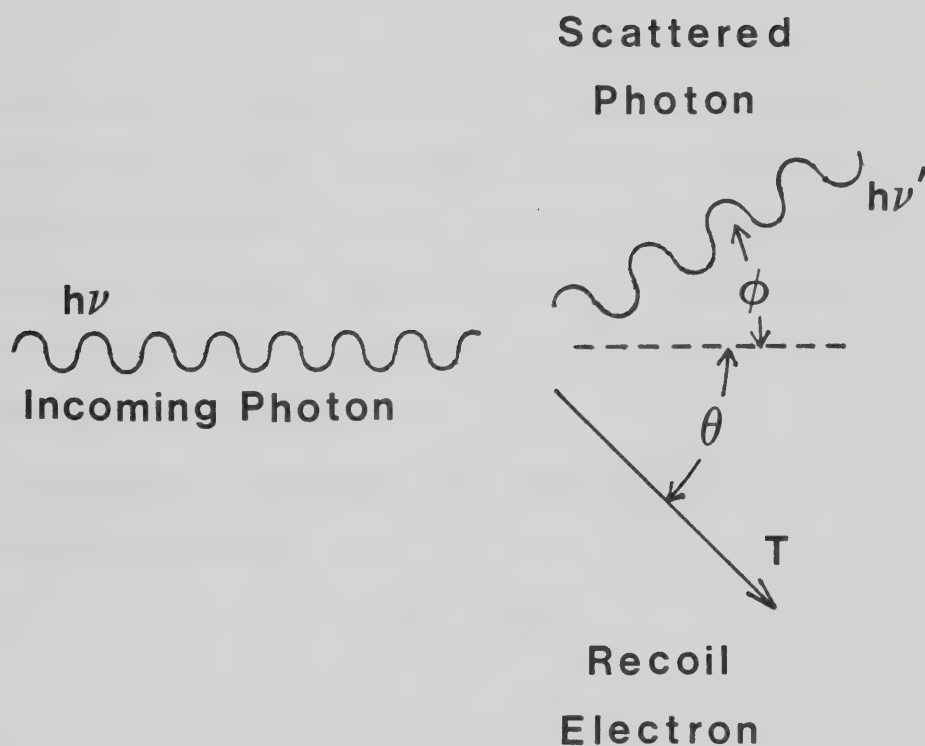


Figure 1. The Compton effect is an interaction of a photon with energy,  $h\nu$ , with an electron at rest. A scattered photon with energy,  $h\nu'$ , and a recoil electron with kinetic energy,  $T$ , result from the interaction.



$$\cos \phi = 1 - \frac{T}{\alpha_o(h\nu - T)} \quad (1.2.3)$$

$$\tan \theta = \frac{1}{(1 + \alpha_o) \tan(\phi/2)} \quad (1.2.4)$$

$$\text{where } \alpha_o = \frac{h\nu}{m_o c^2}$$

Equations 1.2.3 and 1.2.4 were derived from considerations of conservation of energy and momentum. Equations 1.2.3 and 1.2.4 suggest that the scattered photon and recoil electron directions are forward peaked at high incident photon energy. Scattered photons, each possessing a direction different from the incident primary photon direction, degrade the collimation of the primary photon beam.

The differential cross-section with respect to recoil electron energy for the Compton interaction,  $d\sigma/dT$ , is given by (3):

$$\frac{d\sigma}{dT} = \pi r_o^2 m_o c^2 C(h\nu, T) \quad (1.2.5)$$

$$C(h\nu, T) = \frac{1}{(h\nu - T)^2} \left\{ \left[ \frac{m_o c^2 T}{(h\nu)^2} \right]^2 + 2 \left[ \frac{h\nu - T}{h\nu} \right]^2 + \frac{h\nu - T}{(h\nu)^3} \left[ (T - m_o c^2)^2 - (m_o c^2)^2 \right] \right\} \quad (1.2.6)$$

$$\text{where } r_o = \frac{e^2}{m_o c^2}$$

Klein and Nishina in deriving the above equations assumed that the electron is originally at rest and the binding energy of the electron to the atom is negligible compared to the energies of the primary and scattered photon and recoil electron. Both of these assumptions are equivalent to assuming a free electron at rest in the laboratory frame. These assumptions result in the total Compton atomic cross-



section,  $\sigma_t$ , being proportional to the number of electrons in the atom, i.e., proportional to  $Z$ .

The interaction of a photon with the Coulomb field of a charged particle sometimes causes the photon to disappear with the creation of an electron and positron. Consequently, the energy threshold for this interaction is equal to the rest mass of the pair of 1.022 MeV. The remaining photon energy released is transformed into kinetic energy of the charged particles. When the Coulomb field is due to a nucleus, the process is called pair production. Triplet production is when an atomic electron, rather than a nucleus, is involved in the interaction. In this case, the atomic electron recoils with a considerable fraction of the available kinetic energy; consequently, the threshold for triplet production is higher than that of pair production.

The differential cross-section for the pair production interaction with respect to charged particle (electron or positron) energy,  $d\pi/dT$ , is given by (4):

$$\frac{d\pi}{dT} = 4\alpha_o r_o^2 \frac{Z}{h\nu} P(h\nu, T) \quad (1.2.7)$$

$P(h\nu, T)$  is the kinetic energy dependent part of the differential cross-section which can be expressed in a compact form if an energy parameter,  $v$ , is defined (4):

$$v = \frac{T + m_o c^2}{h\nu} \quad (1.2.8)$$

Therefore,  $v$  is the ratio of total charged particle energy compared to the photon energy.

$$P(h\nu, v) = \left[ v^2 + (1-v)^2 + \frac{2v(1-v)}{3} \right] \left[ \ln \left( \frac{2E}{m_o c^2} v(1-v) \right) - \frac{1}{2} - c(\gamma) \right] \quad (1.2.9)$$





where  $c(\gamma)$  is a dimensionless quantity usually much less than 1 which decreases rapidly with increasing  $\gamma$ .  $\gamma$  is the dimensionless screening parameter in the Fermi-Thomas model of the atom and is given by (4):

$$\gamma = 100 \frac{m_0 c^2}{h\nu} \frac{v}{1-v} Z^{-1/3} \quad (1.2.10)$$

In low  $Z$  materials and for megavoltage energies less than 20 MeV, the parameter,  $c(\gamma)$ , may be assumed to be zero. Triplet production may be included by replacing  $Z$  in Equation 1.2.7 with  $Z+1$ .

The root mean angle between the direction of a secondary charged particle and the primary photon is given by (4):

$$\left(\overline{\theta^2}\right)^{1/2} = q(T, h\nu, Z) \frac{\ln \alpha_0}{\alpha_0} \quad (1.2.11)$$

where  $q(T, h\nu, Z)$  is of the order unity and is given in Appendix 1.

The total atomic pair production cross-section,  $a_\pi$ , is proportional to  $Z^2$  so high atomic number materials have a large cross-section.

When a positron and electron get close enough they annihilate liberating their energy. This usually occurs when the positron and electron have little kinetic energy. The rest energy is converted to two 511 KeV photons which are emitted in opposite directions.

Other less important interactions of photons with matter occur such as photodisintegration, Cerenkov radiation, Auger electron production and fluorescence. Of these, fluorescence is the most important, especially in crystal structures. Atoms can be excited due to the passage of x-rays. When the atom returns to its ground state fluorescence radiation is emitted. When the process is delayed long after the initial excitation, the radiation emitted is called phosphorescence.

The total cross-section for a beam of photons interacting in matter depends on the beam geometry. In narrow beam geometry both absorption



and scattering of photons are effective in reducing the intensity at the detector. Figure 2 illustrates a narrow beam of photons interacting in a thin layer of matter,  $dx$ , between the incident beam and a small detector. The number of photons that arrive at the detector is given by:

$$N(x) = N(x=0)e^{-\mu_t x} \quad (1.2.12)$$

$\mu_t$  is the total linear attenuation coefficient and is given by:

$$\mu_t = \frac{N_O}{A} \rho (a^T + a^\sigma + a^\pi) \quad (1.2.13)$$

where  $N_O$  = Avagadaro's number

$A$  = molar weight

$\rho$  = physical density

$a^T$ ,  $a^\sigma$  and  $a^\pi$  are the photoelectric, Compton and pair production atomic cross-sections, respectively.

Broad-beam geometry assumes that the cross-section of the primary photon beam is wide. Only complete absorption of photons contributes to the attenuation. Scattering of photons away from the detector are compensated by scattering of photons toward the detector. The number of photons arriving at the detector from a broad beam is given by:

$$\mu_a = \frac{N_O \rho}{A} (a^T + a^\sigma_a + a^\pi) \quad (1.2.15)$$

where  $a^\sigma_a$  is the Compton atomic absorption coefficient.

$a^\sigma_a$  represents the average fraction of the primary energy absorbed by the electron multiplied by the total Compton attenuation coefficient.

$$a^\sigma_a = \frac{(hv - hv')}{hv} a^\sigma_t \quad (1.2.16)$$

where  $hv'$  is the energy of the scattered photon. The Compton

atomic scattering coefficient,  $a^\sigma_s$ , is a complementary quantity to  $a^\sigma_a$ :



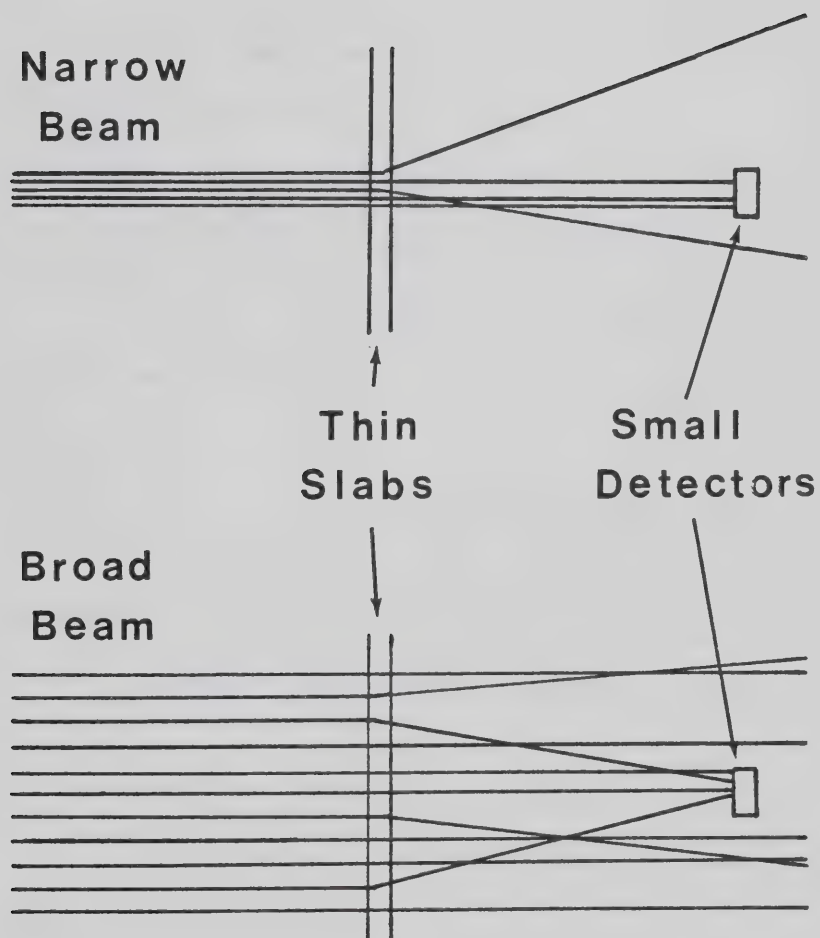


Figure 2. Narrow beam geometry assumes that all scattered photons are not detected. Broad beam geometry assumes that as many photons are scattered toward as away from the detector.





$$a^{\sigma}_s = \frac{h\nu'}{h\nu} a^{\sigma}_t = a^{\sigma}_t - a^{\sigma}_s \quad (1.2.17)$$

At low energies  $a^{\sigma}_s$  approaches  $a^{\sigma}_t$  and at high energies  $a^{\sigma}_a$  contributes most of the attenuation. A listing of total attenuation coefficients,  $\mu_t$ , and total Compton attenuation coefficients,  $a^{\sigma}_{\frac{N_O}{A}}$ , for water at selected energies appears in Appendix 2.

The linear coefficients,  $\mu_a$  and  $\mu_t$  are often normalized to the physical density,  $\rho$ , and then the term "mass" replaces "linear". The mass attenuation coefficient,  $\mu_t/\rho$ , for ice and water, are the same even though their linear attenuation coefficients are different.

Other linear absorption coefficients are often used. The mass energy transfer coefficient,  $\mu_k/\rho$ , and the mass energy absorption coefficient,  $\mu_{en}/\rho$ , are defined analogously to the mass absorption coefficient,  $\mu_a/\rho$ .  $\mu_a/\rho$  takes into account the escape of Compton scattered photons.  $\mu_k/\rho$  takes into account the escape of Compton scattered photons, fluorescence and annihilation photons.  $\mu_{en}/\rho$  takes into consideration all the escape photons that  $\mu_k/\rho$  does and includes bremsstrahlung photons. The general formulae for all these coefficients are (9):

$$\mu_x/\rho = \frac{N_O}{A} (a^T f_x^T + a^{\sigma} f_x^{\sigma} + a^{\pi} f_x^{\pi}) \quad (1.2.18)$$

where x can be "k", "a" or "en"

$f_x^{'s}$  are conversion factors which weight the average fraction of photon energy that is converted to charged particle kinetic energy taking into account the amount and form of energy that escapes the region of primary interaction.

For example, we have seen earlier that  $f_a^T = f_a^{\pi} = 1$   $f_a^{\sigma} = \frac{h\nu - h\nu'}{h\nu}$

(see Equation 1.2.16)



Sometimes it is convenient to compare the linear attenuation or absorption properties of two types of matter. The equivalent thickness of one substance compared to another is defined to be:

$$(t_{eq})'_t = \frac{\mu_t^t}{\mu_t} \quad (1.2.19)$$

The primed and unprimed coefficients refer to two different materials.

Since the linear attenuation coefficient depends on energy, the photon spectrum is going to be modified as it passes through matter. This especially affects low energy (below megavoltage energies) spectra because the photoelectric effect is strongly energy dependent. Low energy photons will be depleted faster than high energy photons so the mean energy of the beam will increase. This is known as hardening of the beam.

Hardening is not as important in megavoltage beams because few of the interactions (in low Z materials) occur via the photoelectric effect. Most of the interactions occur via the Compton effect.\* Forward scattered photons tend to replenish the low energy part of the spectrum. In addition, the linear attenuation coefficient, over the energy range of megavoltage spectra, does not decrease rapidly with energy (in low Z materials). The photon spectrum of a beam of x-rays is often called the "quality" of the beam.

\* If very high energies are employed, pair production could become important. The pair production cross-section increases with increasing energy so the spectrum would be depleted in high energy photons. "Softening" could be said to occur.



### 1.3 Interaction of Electrons with Matter

For the purpose of medical physics, a free electron can be thought of as a point particle with a rest energy of 511 KeV (rest mass =  $9.11 \times 10^{-31}$  kg) and an electric charge of  $1.602 \times 10^{-19}$  Coulombs.\* Free electrons are produced through ionization of atoms. The source of electrons in a linear accelerator is from thermionic emission from a heated filament or indirectly heated cathode. The photoelectric, Compton and pair production interactions also produce free electrons with a considerable kinetic energy.

When an electron traverses through matter the Coulomb interaction between it and atomic electrons produce ionization of the atomic electrons and excitation of the ionized atom. This results in the kinetic energy of the electron,  $t$ , being deposited along its path which results in the electron slowing down. The energy lost in any given collision may be as low as a few electron volts or as high as one half of the electron energy. The energy lost per unit mass of matter is defined to be the radiation dose absorbed by the matter. The collision or ionization stopping power is defined to be the average amount of energy lost per unit path length traversed,  $[dT/dx]_{\text{ion}}$ , and is given by:

$$\left[ \frac{dT}{dx} \right]_{\text{ion}} = \frac{2\pi e^4}{m_o c^2} \frac{N_o Z_p}{A} \left\{ \frac{(T+m_o c)^2}{T(T+2m_o c)^2} \ln \left[ \left( \frac{T+2m_o c^2}{m_o c^2} \right) \frac{T^2}{I^2} \right] - 1 \right\} \quad (1.3.1)$$

\* Since electron beams encountered in medical physics are not polarized, spin effects of free electron can be neglected.



where  $I$  is the average ionization potential of the atoms through which the electron is traversing.

The factor  $(N_0 Z \rho / A)$  has the dimensions of  $\text{cm}^{-3}$  and represents the number of electrons per  $\text{cm}^3$  of a material and is called the electron density.

When  $T$  is large ( $T \gg m_0 c^2$ ) the collisional stopping power increases slowly because the factor in front of the logarithm approaches unity and taking the logarithm modifies the approximate  $T^3$  dependence of its argument. At low energies ( $T \ll m_0 c^2$ ) the stopping power increases approximately inversely with decreasing electron kinetic energy.

As was discussed in Section 1.2, bremsstrahlung is produced by fast electrons interacting in matter. The stopping power due to bremsstrahlung, often called the radiative stopping power, can be found from the differential bremsstrahlung cross-section (Equation 1.2.1):

$$\left[ \frac{dT}{dx} \right]_{\text{brems}} = \frac{N_0 \rho}{A} \int_0^T h\nu d\sigma_{\text{brems}} \quad (1.3.2)$$

The collisional stopping power is much greater than the radiative stopping power except at high electron energy or high atomic number materials. The total stopping power is just the sum of the collisional and radiative stopping powers. Appendix 3 lists the total stopping powers of electrons in water as a function of electron energy.

The average path length, P.L., traversed by the electron is given by:

$$\text{P.L.} = \int_{T_{\min}}^{T_0} \frac{1}{\left[ \frac{dT}{dx} \right]_{\text{tot}}} dT + \text{P.L.}_{\text{residual}} \quad (1.3.3)$$

where  $T_0$  is the initial energy





$T_{\min}$  is the kinetic energy when the electron can be considered to be almost stopped

P.L.<sub>residual</sub> is the residual path length after the electron has reached an energy,  $T_{\min}$ .

All electrons do not have the same path length because of the considerable fluctuation of collisional energy loss.

The range of an electron in matter can be defined to be the distance between the point of entry of the electron in matter and the position where it stops. The mean range is always less than the mean path length. The electron having a small mass is easily scattered by the Coulomb field of the atomic nucleus. These interactions are usually elastic so only the electron direction is changed. The multiple scattering of electrons after passing through a path,  $\ell$ , is often assumed to have a Gaussian angular distribution. The mean square mass angular scattering power  $\overline{\theta^2}/\rho \cdot \ell$  of a material is a measure of the angular spread of an electron beam.  $\overline{\theta^2}/\rho \cdot \ell$  is directly proportional to  $Z^2/T^2$  so the scattering increases rapidly with high atomic number materials and decreasing electron kinetic energy. Appendix 4 lists  $\overline{\theta^2}/\rho \cdot \ell$  as a function of kinetic energy for electrons in water and lead.

If an electron source is located at a point and directed in a direction,  $\vec{z}$ , then the electron fluence,  $\Phi$ , at a distance,  $r$ , from the point compared to the initial electron fluence,  $\Phi_0$ , after it has traversed a distance,  $z$ , into a material is (5):

$$\Phi = \frac{\Phi_0 e^{-\theta^2/2\overline{\theta^2}}}{1+\tan^2\theta} \quad (1.3.4)$$

where  $\theta$  is the angle between the  $\vec{z}$  and  $\vec{r}$  directions

$$1+\tan^2\theta = r^2/z^2$$



## 1.4 Medical Electron Linear Accelerators

The x-ray tube common to all diagnostic x-ray units is the simplest type of electron accelerating device. Potentials larger than 1 MVp across a space of a few centimeters cannot be maintained because dielectric breakdown occurs. In order to produce high kinetic energies, a linear accelerator requires an accelerating electric field travelling in the same direction and velocity as the electrons. In a linear accelerator, an electron can gain several MeV/m, yet the potential difference between any two points at any time can be less than several hundred kVp.

The basic accelerating unit is the microwave resonance cavity. A cavity is merely a microwave waveguide that has been enclosed at the electric field minima points. Figure 3 illustrates the relation between the magnetic and electric fields in a microwave cavity for one complete oscillation. The cavity oscillation can be set up by connecting the cavity to a source of microwave radiation such as a klystron or magnetron.

A klystron comprises two coupled microwave cavities (6) - one called the buncher and the other called the catcher (see Figure 4). The oscillating electric field from a low amplitude, high stability microwave source alternately retards and accelerates a continuous stream of low energy electrons produced by a hot filament. This modulates the velocities of the electrons leaving the buncher. The buncher and collector tubes are joined by a drift tube which allows higher velocity electrons to catch up to lower velocity electrons. When the electrons enter the catcher cavity they generate strong retarding electric fields by inducing charges on the ends of the cavity.



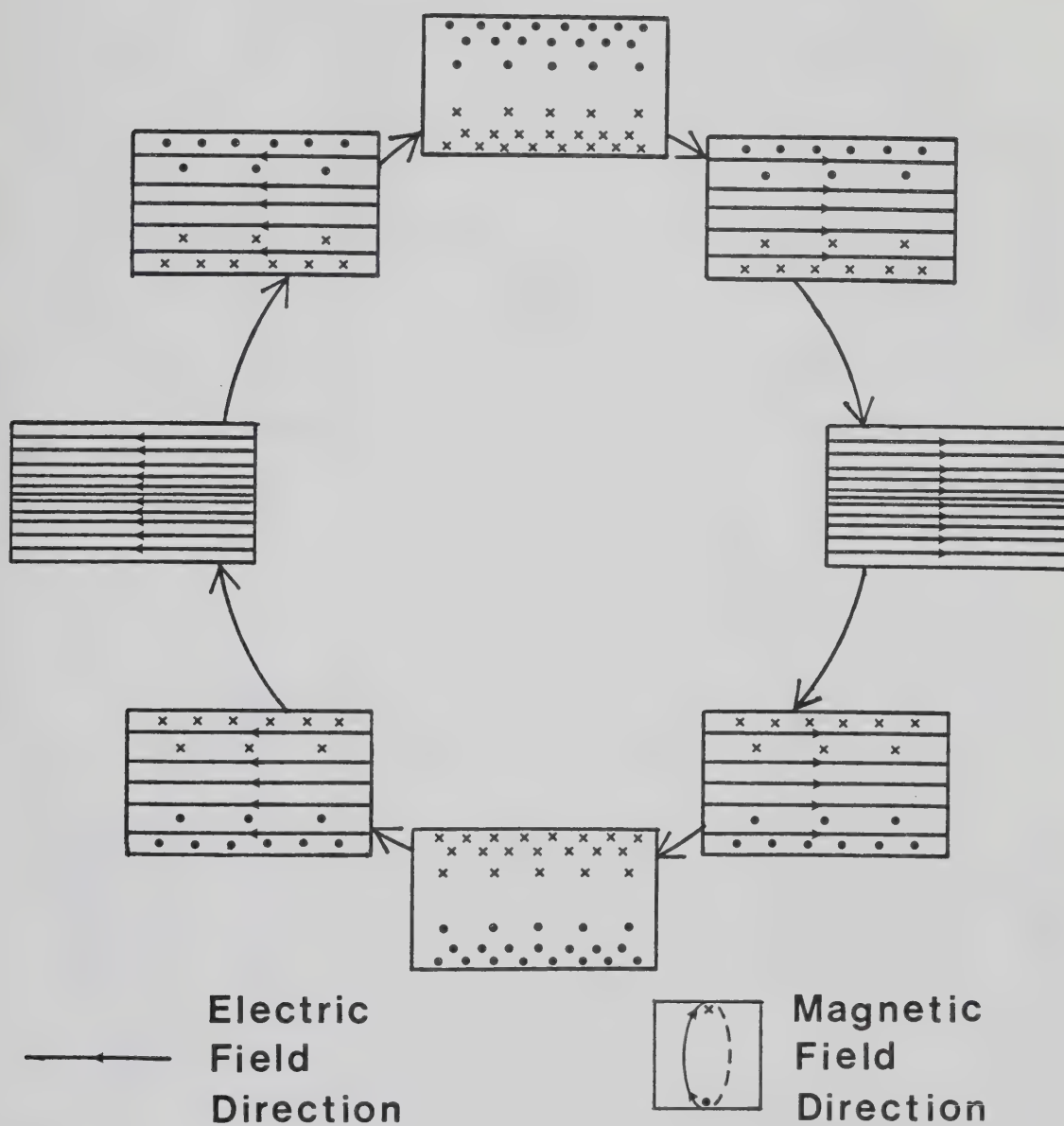


Figure 3. One oscillation of an electromagnetic cavity. The electric field is a result of charges at either end of the cavity. The magnetic field is due to charges moving along the cavity in response to the electric field. Microwaves can induce or be produced by such oscillations.





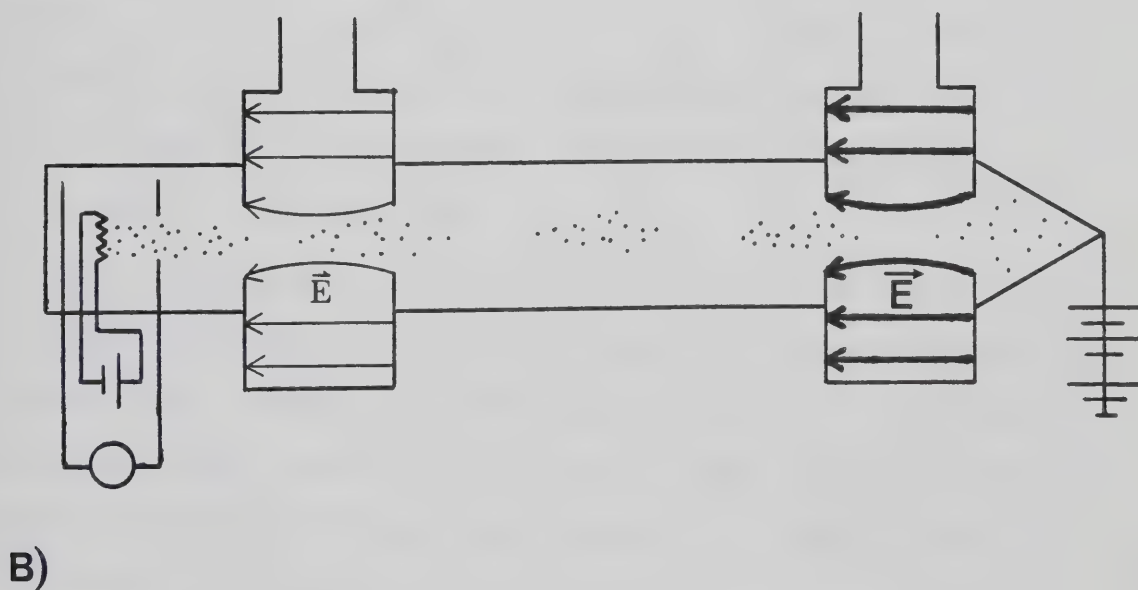
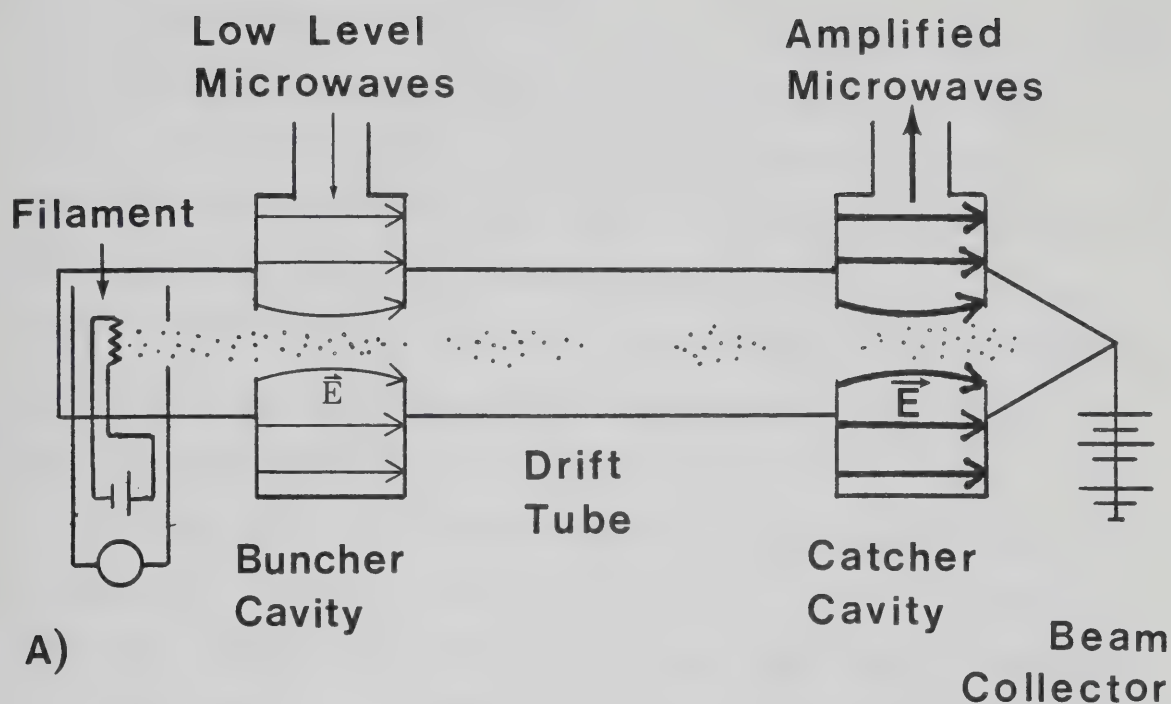


Figure 4. A) Retarding and B) accelerating phases of the operation of a buncher. A weak microwave cavity modulates an electron beam. The kinetic energy of the beam is transformed into an amplified microwave signal.



This reduces the electron velocity. The modulated beam current arriving at the catcher induces high amplitude microwaves utilizing most of the kinetic energy of the electrons. The electron beam collector is a dump for removing the electrons. The kinetic energy not converted to microwaves heats the collector which must be water cooled. Some low energy bremsstrahlung is produced in the collector which must, therefore, be shielded. The microwave power is produced by a klystron in the Mevatron -20 accelerator.

In the Mevatron -6 accelerator the microwave power is produced by a magnetron. A magnetron has a flat cylindrical geometry. A central cylindrical cathode is surrounded by an outer anode which is separated by a drift space. A D.C. magnet field is applied perpendicularly to the plane of the cylinder. A pulsed electric field is applied radially inward. Electrons spiralling from the cathode to anode induce an alternating charge distribution on the anode which produces, and has the same frequency as, the microwaves. Most of the electron kinetic energy is converted to microwave energy.

The two types of accelerator structures in use are the travelling wave and standing wave side-coupled designs. Both accelerators used in the study were standing wave side-coupled designs so the travelling wave design will be mentioned only briefly. Both types of accelerators accelerate electrons that have been produced and grouped in much the same fashion as a buncher cavity of a klystron.

In a travelling wave accelerator, radiofrequency power enters the first cavity (see Figure 5). The electric field travels down the waveguide which is a series of resonant cavities at the same group velocity as the accelerating electrons. Since the electron



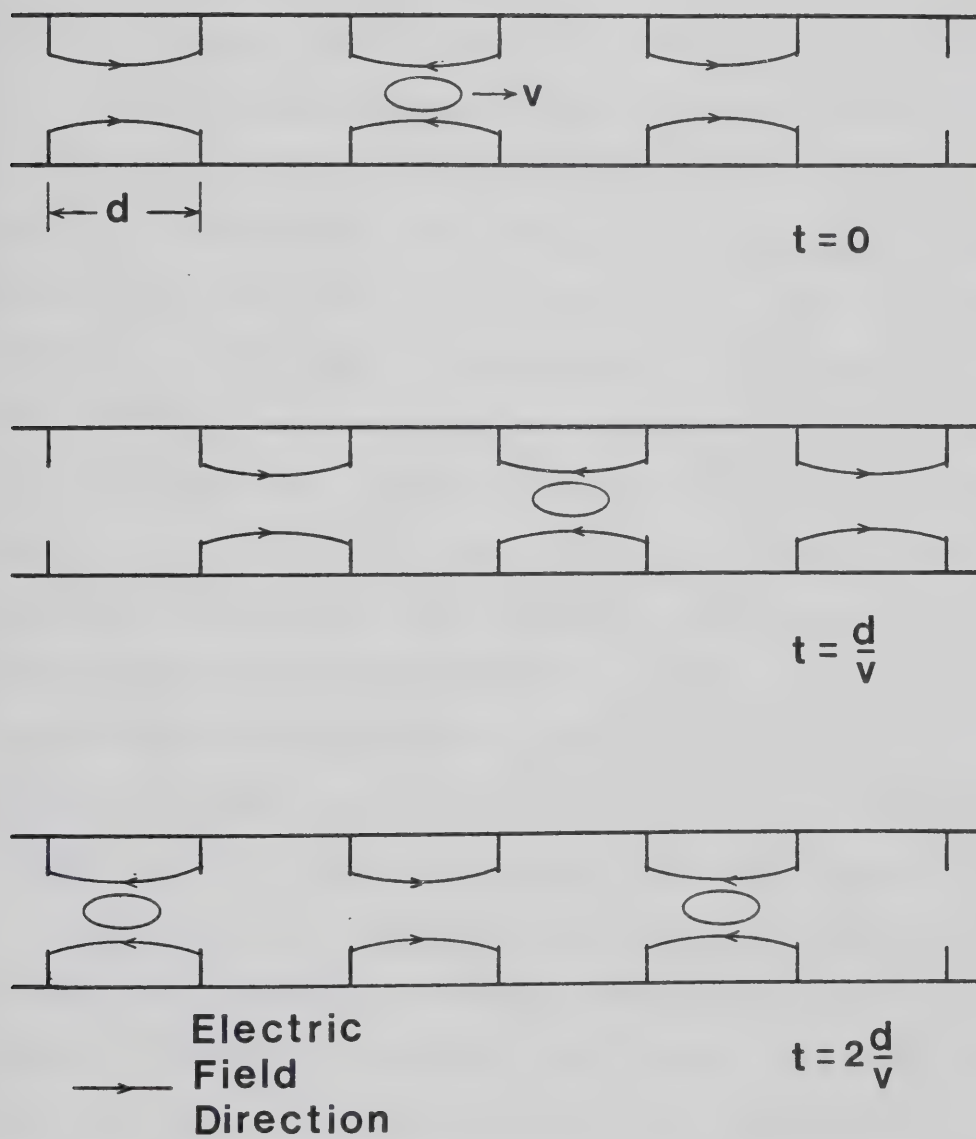


Figure 5. Schematic diagram of a travelling wave accelerator accelerating section.



velocity increases, the spacing between the cavities are increased in length toward the distal end of the waveguide. Upon reaching the distal end of the waveguide, the radiofrequency power is dissipated in a resistive load.

In a standing wave accelerator the microwaves are not dissipated with a concomitant saving of energy, but are allowed to reflect such that a standing wave is set up throughout the waveguide (see Figure 6). Since half of the cavities have a zero or small electric field at all times and so play a small role in acceleration, these cavities may be moved off axis. A waveguide with such a configuration is said to be side-coupled. The separation of the roles of the coupling and accelerating cavities allows optimization of the size and shape of each cavity type. This increases the amount of energy that can be gained per unit length which reduces the waveguide length. Figure 6 illustrates hypothetical longitudinal and cross-sections of a standing wave side-coupled accelerator waveguide. The phase velocity of the standing waves are matched to the electron velocity such that a group of electrons experiences the same direction and magnitude of electric field throughout its passage along the accelerator structure.

To be effective in treating patients from all directions, the accelerator must be able to be rotated about an axis. Since the accelerator structure is more than a meter long it has proven convenient to place the accelerating waveguide parallel or nearly parallel to the axis of rotation. In order to direct the beam perpendicular to the axis, a magnet must be employed to bend the beam. To accomplish this the beam could be bent through a right angle, but a  $270^{\circ}$  achromatic bending magnet is usually employed (see Figure 7).





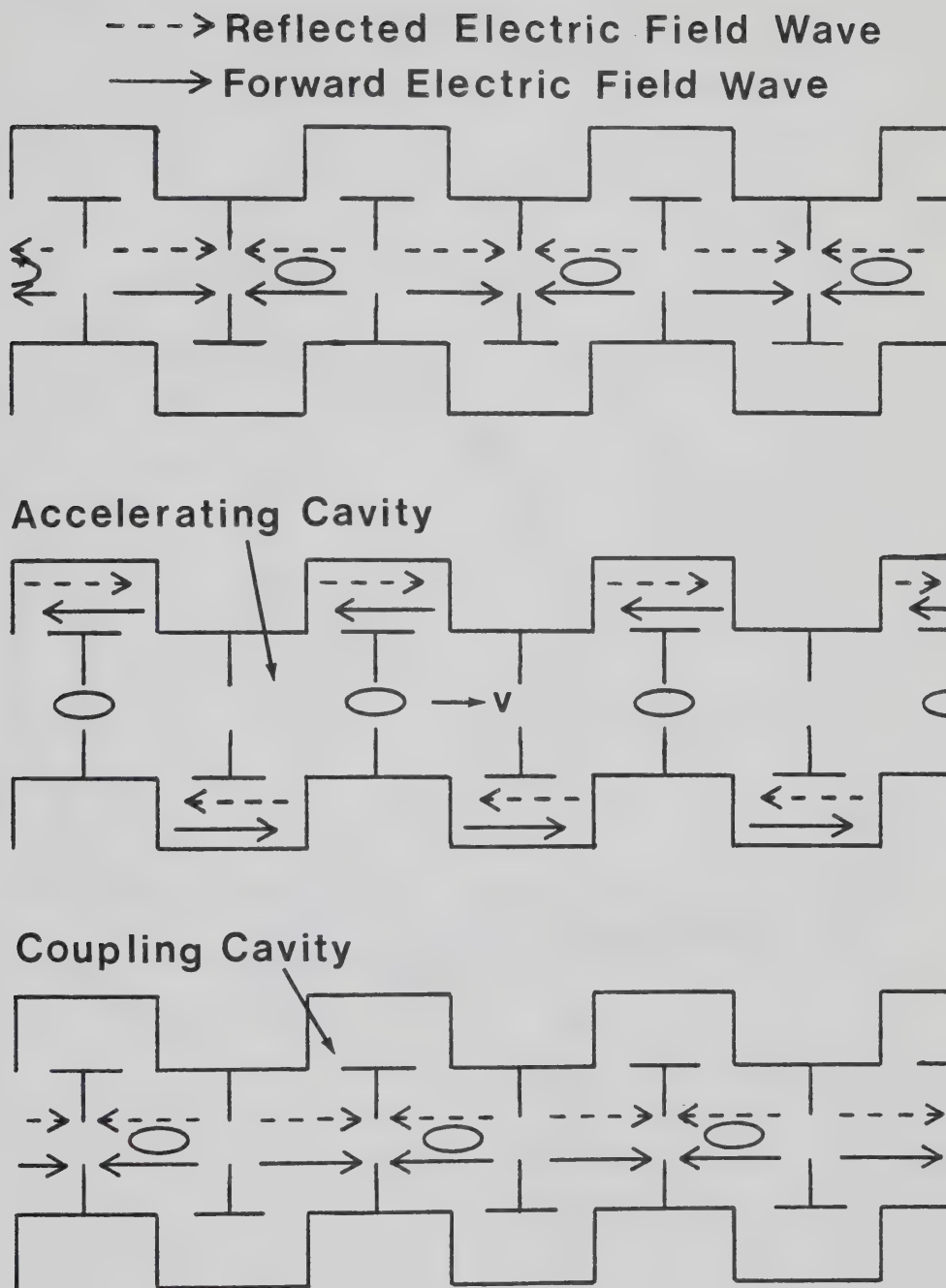


Figure 6. Schematic diagram of a side-coupled standing wave accelerator accelerating section. The forward wave travels from left to right and the reflected from right to left. The waves travel between accelerating cavities via coupling cavities.



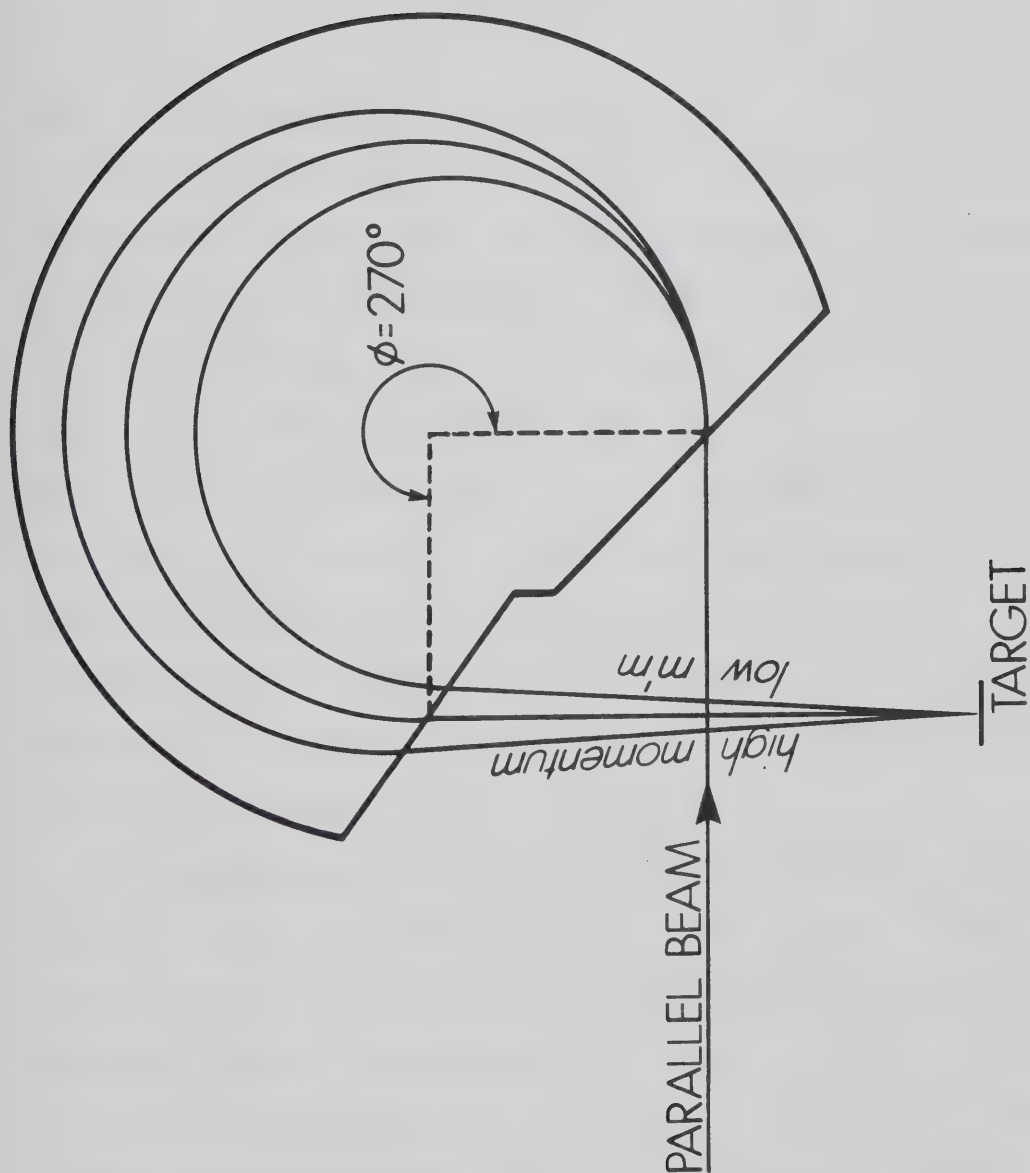


Figure 7. A 270<sup>0</sup> achromatic beam-bending magnet.



The relationship between the kinetic energy, magnetic field strength and the radius of curvature of a particle in a magnetic field is given by:

$$r = \frac{m_0 c}{eB} \left[ \left( \frac{T + m_0 c^2}{m_0 c^2} \right)^2 - 1 \right]^{1/2} \quad (1.4.1)$$

where B is the magnitude of the magnetic field.

An achromatic bending magnet has a greater magnetic field near the outside of the magnet. Electrons with higher than average kinetic energy will travel to outer radial parts of the field where they will be bent more. Slower electrons experience an opposite effect. The net result is that all electrons, regardless of small deviations in their kinetic energy, arrive at the same point. This is desirable because if a target (see Figure 8) is placed at this point the bremsstrahlung produced will emerge from a limited area. Photons from a small source when collimated will produce sharply defined edges, i.e. a small penumbra (see Figure 9). Additionally, an achromatic magnet results in a more stable delivery of electrons to the target.

The treatment head can be divided into the fixed head assembly and the movable collimator. The fixed head assembly consists of the target, electron absorbers, primary collimator, field flattening filter, monitor ion chamber and field light mirror (see Figures 8 and 9).

The electron absorber is a low Z material placed in the beam after the target to stop low energy electrons. The primary collimator limits the beams angular width to  $22^\circ$ .

The bremsstrahlung produced by the target is forward peaked in intensity so there are more photons directed along the central axis than at points off axis. The field flattening filter is machined in a conical



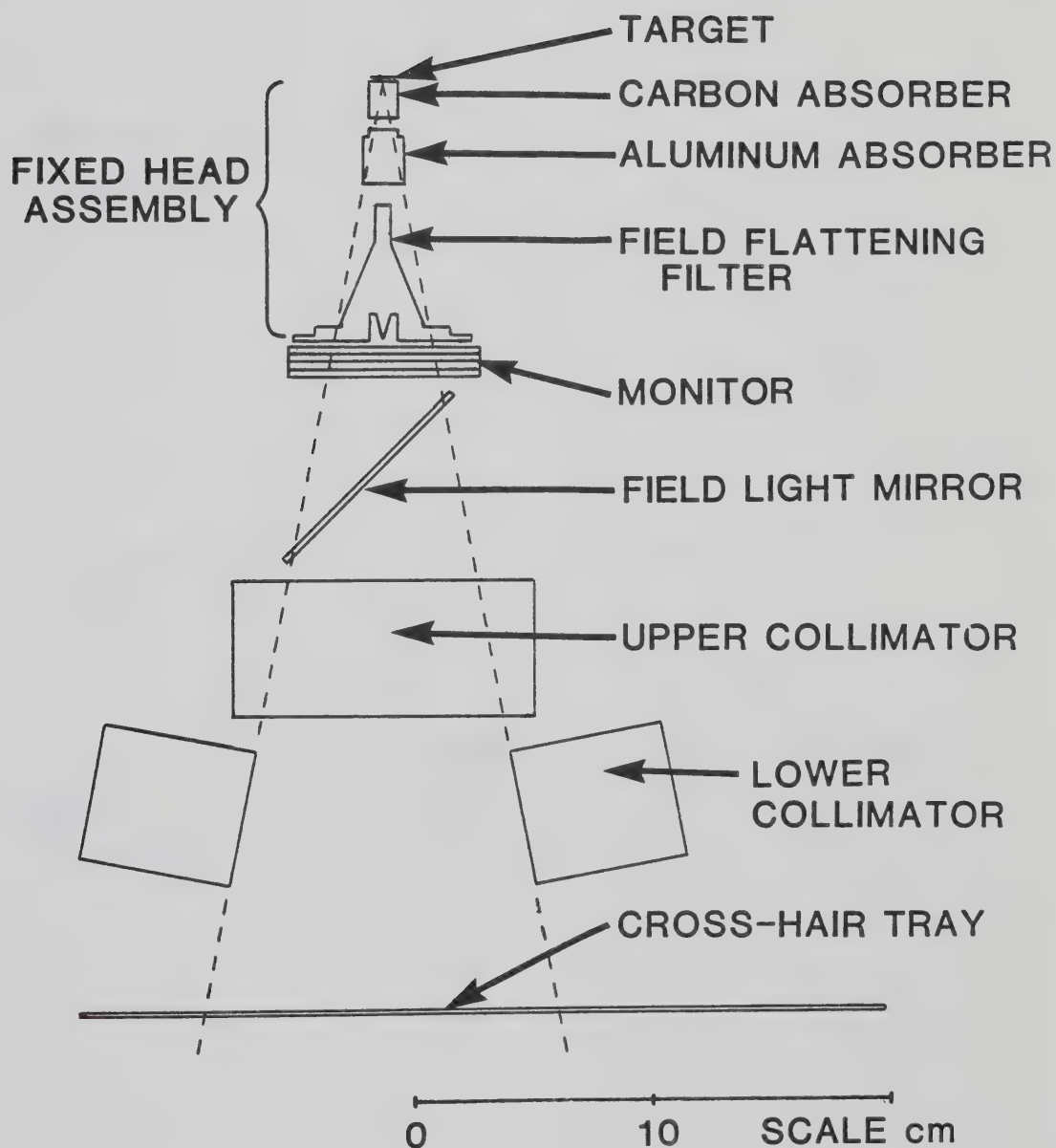


Figure 8. Scale drawing of the treatment head of a Mevatron -20 medical linear accelerator.





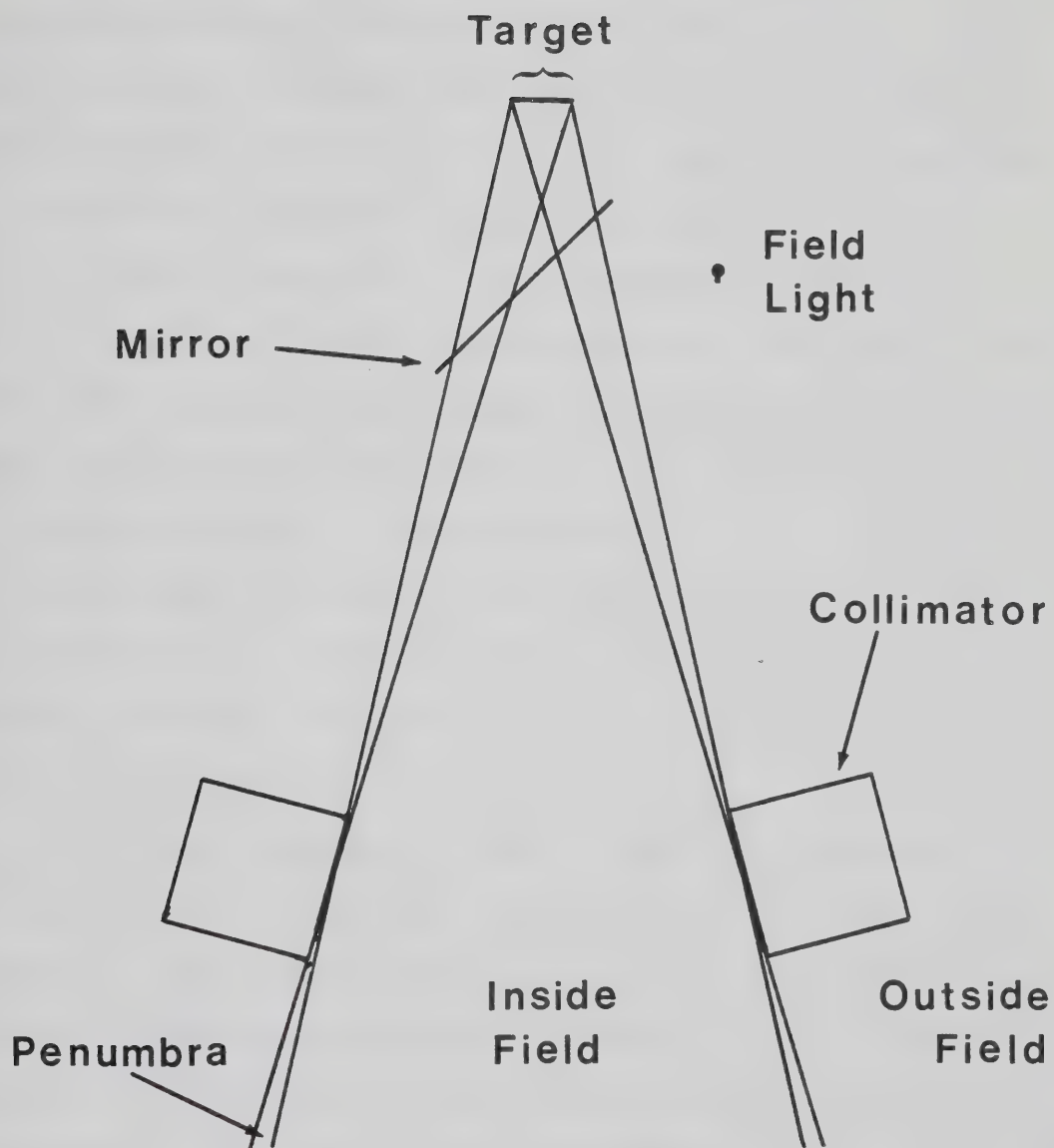


Figure 9. Diagram of the field defining system.



shape to attenuate the photon beam preferentially along rays near the central axis. The result is a photon fluence distribution which is relatively uniform over the entire cross-sectional area of the beam. Since introducing attenuation into a photon beam tends to harden the beam, the lateral distribution of the photon spectrum is not uniform. This can produce a nonuniform distribution of dose.

A multiplate ion chamber is usually placed in the fixed head assembly to measure dose rate, integral dose and field symmetry. This allows monitoring of the dose received by patients (timer systems are always used as back-ups) and is used as part of the verification of the safe operational status of the accelerator.

A field light, the source of which appears to be at the same position as the x-ray source, illuminates the field. This illusion is obtained by placing a thin mirror in the field and placing the light source off axis (see Figure 9).

The collimator system can consist of steel, lead, tungsten alloy or depleted uranium blocks thick enough to reduce the primary photon fluence to a fraction of a percent of the fluence in the field without producing photoactivation neutrons. A penumbra at the field edge occurs because of the finite width of the electron beam and target thickness (see Figure 9). The field boundary is defined to be where the dose falls to 50% of the dose at the central axis. The amount of the collimator jaws covering the field are continuously adjustable to produce square or rectangular fields with dimensions up to 30 cm x 30 cm.

A removable thin lucite tray with cross-hairs inscribed on it can be placed directly beneath the collimator jaws (see Figure 8). The shadow of the cross-hairs in the illuminated field define the position



of the central axis.

The beam axis of rotation for most accelerators is 100 cm from the photon source. Accessories such as beam wedges or blocking filters are often placed between the collimators and the patient at a distance of 60 cm from the source in the Mevatron accelerators on a Lucite accessory or "shadow" tray. When there are no accessories or beam modifying devices in place the field is said to be open.

A phantom consists of tissue equivalent material such as polystyrene or water, in the case of soft tissue, in which a radiation measuring device has been placed. The distance from the source to the phantom is specified by the source to (phantom) surface distance, SSD, and the source to probe distance, SPD. The phantom material used for all the experiments to be reported is polystyrene (electron density =  $3.50 \times 10^{23}$  e<sup>-</sup>/cm<sup>3</sup>, physical density = 1.08 g/cm<sup>3</sup>) and the probe was usually a thin-window parallel-plate ion chamber.



### 1.5 Ionization Dosimetry

The absorbed dose, or simply, dose, is the amount of kinetic energy deposited in a small mass of material or:

$$\text{Dose} = \frac{\Delta T}{\Delta m} \quad (1.5.1)$$

Dose is not a differential quantity. The dimension of the energy absorbing mass,  $\Delta m$ , must be much larger than the average distance between ionization-excitation events given by:

$$\text{Average Distance Between Ionization Events} = \frac{\bar{W}}{dT/dx} \quad (1.5.2)$$

where  $\bar{W}$  is the average energy lost in an ionization-excitation event.

Typically, the average distance between events produced by fast electrons is less than a micron so the dose can be defined for very small masses.

Dose is defined in terms of an amount of kinetic energy absorbed. The amount of rest energy deposited is not included so dose cannot be defined in terms of  $\Delta E$  where  $E = T + m_0 c^2$ .

The Gray (1 Gray = 1J/kg) is the SI unit of dose, However, for historical reasons the rad = 1 centiGray is often unofficially used.

An ion chamber measures the amount of charge accumulated due to ionization of air. One of the simplest ion chambers in design and the type used in most of the experiments conducted is the parallel-plate ionization chamber (see Figure 10). In essence, it is a single element parallel-plate capacitor separated by air. A potential is maintained between the plates. The potential is sufficient such that all ion pairs produced in the air are accelerated to the plates but not large enough for the accelerated ions to produce more ionization of the air. There is some recombination of ion pairs as they traverse the chamber,





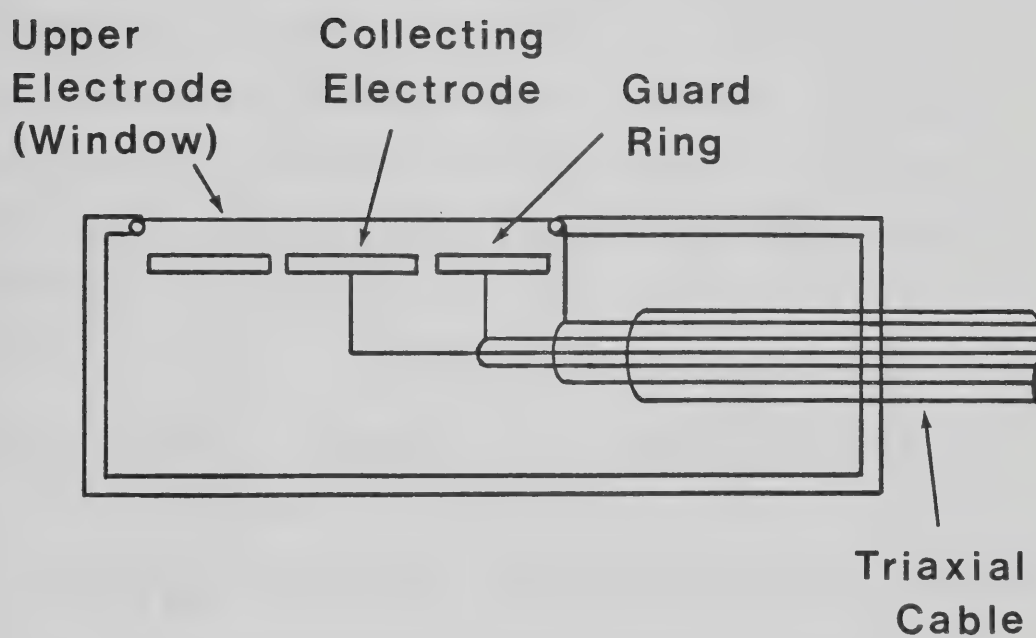


Figure 10. Schematic drawing of a parallel-plate ionization chamber.



but if the ionization current density is low the amount of recombination will be negligible. The amount of charge required is determined using an electrometer by measuring the amount of charge placed on the parallel-plates required to maintain a constant potential.

Although an ion chamber reading does not yield an absolute measure of dose, it is possible to theoretically relate the ionization in the ion chamber probe with the dose received in matter in the absence of the probe (7). In practice, the conversion relating the amount of ionization in a given probe to dose is established by a standards laboratory. The amount of dose is given by (8):

$$\text{Dose} = C C_A K_1 K_2 P R \quad (1.5.3)$$

where R is reading of charge accumulated per unit mass of air

C is the calibration factor

$C_A$  is the energy dependent conversion factor between charge/mass and dose

$K_1$  is a temperature and pressure correction factor

$K_2$  is a factor that corrects for difference such as the quality of the radiation beam

P is a factor that takes into account the perturbation the probe makes in the fluence of the medium

Dose deposition due to photons is a two-stage process. First, charge particles are set in motion, then the charged particles slow down depositing their kinetic energy as dose. The concept of KERMA, kinetic energy released in the medium, describes the first step.

KERMA is given by:

$$\text{KERMA} = h\nu \frac{\mu_k}{\rho} \Phi_\gamma \quad (1.5.4)$$

where  $\mu_k/\rho$  is the mass energy transfer coefficient

$\Phi_\gamma$  is the photon fluence in particles per unit area



Since the photon fluence is decreasing as a function of depth in the phantom, the KERMA decreases as well. The charge particles set in motion are mostly forward directed so their fluence as a function of depth initially builds up. Once set in motion these charged particles slow down and are stopped so their fluence reaches a maximum intensity at some depth. At this position, maximum fluence will produce maximum ionization in a probe placed there. This point is called  $d_{\max}$ . After  $d_{\max}$  the charged particle fluence decrease follows the KERMA decrease. The following differential equation has been used to describe the region where the dose builds up:\*

$$\frac{d\psi_{e^{\pm}}(x)}{dx} = \frac{\bar{\mu}_{\gamma}}{\rho} \psi_{\gamma}(x) - \frac{\mu_{e^{\pm}}}{\rho} \psi_{e^{\pm}}(x) \quad (1.5.6)$$

and the solution is

$$\psi_{\gamma}(x) = (\psi_{\gamma})_0 e^{-(\mu_{\gamma}/\rho)x} \quad (1.5.7)$$

$$\psi_{e^{\pm}}(x) = \frac{\mu_{\gamma}(\psi_{\gamma})_0}{\mu_{e^{\pm}} - \mu_{\gamma}} \left( e^{-(\mu_{\gamma}/\rho)x} - e^{-(\mu_{e^{\pm}}/\rho)x} \right) \quad (1.5.8)$$

where  $\psi_{\gamma}(x)$  is the total amount of energy fluence due to a full spectrum of photons and is given by:

$$\psi_{\gamma}(x) = \int_{\text{spectrum}} \Phi_{\gamma}(h\nu, x) d h\nu \quad (1.5.9)$$

where  $(\psi_{\gamma})_0$  is the initial photon energy fluence

$\psi_{e^{\pm}}(x)$  is the energy fluence of charged particles and is defined analogously to Equation 1.5.7

\* Equations 1.5.6, 1.5.7 and 1.5.8 have been modified from similar ones by Cassen, Corrigan and Hayden (10).



$x$  is the thickness of phantom (in units of mass/area)

$\mu_{\gamma}$  is the energy weighted mean linear energy absorption coefficient and is given by:

$$\mu_{\gamma}(x) = \frac{\int_{\text{spectrum}} \mu_k(h\nu) \Phi_{\gamma}(h\nu, x) d(h\nu)}{\int_{\text{spectrum}} \Phi_{\gamma}(h\nu, x) d(h\nu)} \quad (1.5.10)$$

$\mu_{e^{\pm}}$  is the mean "energy absorption coefficient" of charged particles set in motion at a point (in units of mass/area)

The above expression is analogous to the decay of a parent-daughter isotope if the daughter isotope initially has zero concentration. The effective energy transfer coefficient and the mean energy absorption of charged particles is depth dependent due to hardening of the beam, and the production of scattered photons. However, to a good approximation they can be considered to be a constant in the build-up region. The energy absorption coefficient can be used instead of the energy transfer coefficient at low energies in low  $Z$  materials. It has been assumed that once produced the energy fluence of electrons set in motion at a given point in the phantom decays exponentially with depth. The first term on the right hand side of Equation 1.5.6 represents the total KERMA of the beam.

The depth of the maximum dose,  $d_{\text{max}}$ , occurs at the point of the maximum charged particle energy fluence and is given by:

$$d_{\text{max}} = \frac{1}{\mu_{e^{\pm}} - \mu_{\gamma}} \ln \frac{\mu_{e^{\pm}}}{\mu_{\gamma}} \quad (1.5.11)$$

The output factor is defined to be the reading at  $d_{\text{max}}$  for a given field size and SPD divided by the reading at a field size of





10 cm x 10 cm at the same field size. The output factor has a small dependence on SPD.

The dose at a given depth is often normalized to the dose which occurs at a reference depth. There are two common procedures for doing this. They are the percentage depth dose,  $P(x, x_0, W_s, SSD, (h\nu)_{\max})$  and the tissue maximum ratio,  $TMR(x, W, (h\nu)_{\max})$ .

The percentage depth dose depends on the depth (measured from the surface) in the phantom,  $x$ , the depth to the reference point,  $x_0$ , the field dimension measured at the surface,  $W_s$ , the source-to-surface distance, SSD, and the nominal photon beam energy  $(h\nu)_{\max}$ . The percentage depth dose is defined to be (8):

$$P(x, x_0, W_s, SSD, (h\nu)_{\max}) = \left( \frac{\text{Dose at } x}{\text{Dose at } x_0} \right) 100\% \quad (1.5.12)$$

The position of the dose measured at points  $x$  and  $x_0$  are shown in Figure 11. The percentage dose is obtained by keeping the SSD constant and determining the dose at each depth by moving the measuring probe.

The tissue maximum ratio is a ratio between the dose as measured at a depth,  $x$ , in a phantom compared to the dose as measured at  $d_{\max}$ . The measurements are made by keeping the source-to-probe distance, SPD, constant and the depth from the surface is varied by changing the thickness of overlying material. The field dimension is measured at the source-to-probe distance. The tissue maximum ratio is defined to be (8):

$$TMR(x, W, (h\nu)_{\max}) = \frac{\text{Dose at } x}{\text{Dose at } d_{\max}} \quad (1.5.13)$$



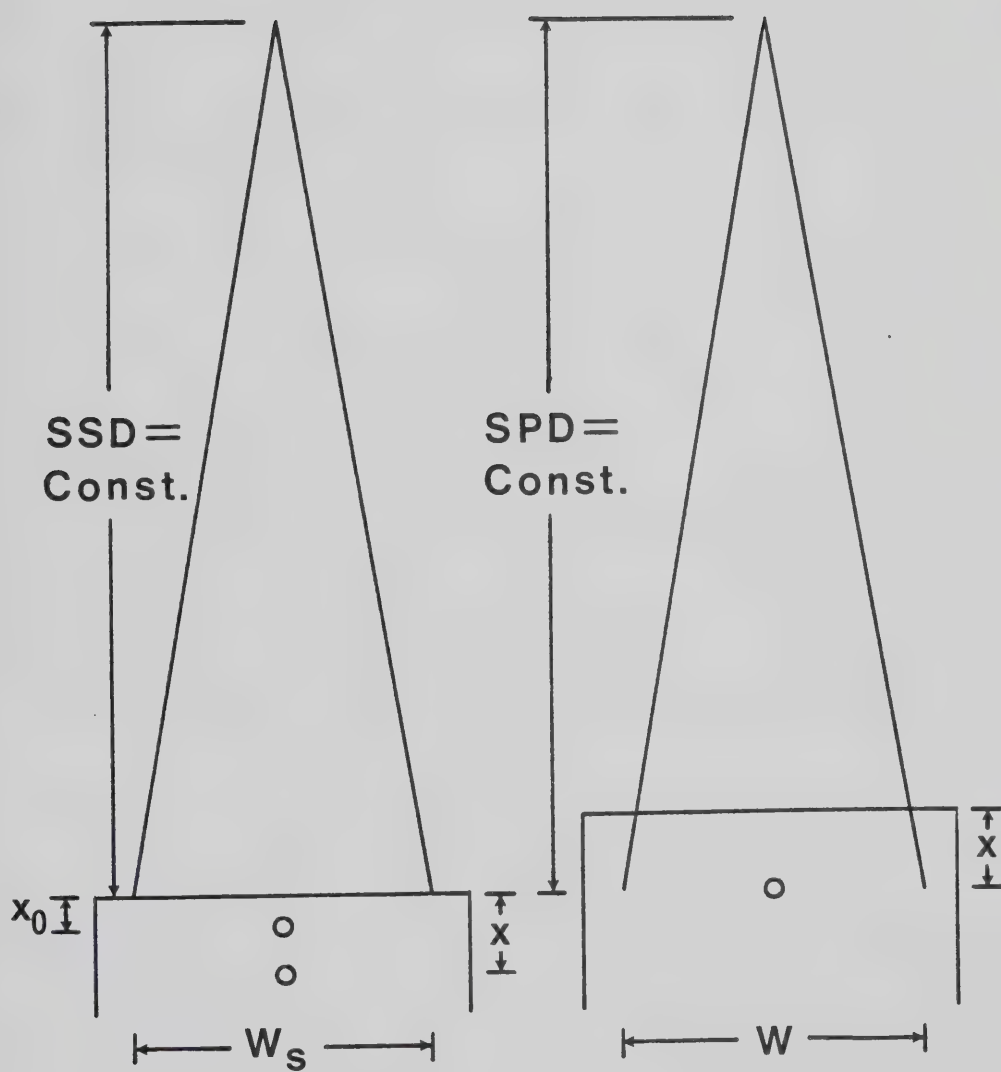


Figure 11. The arrangements for measuring percent depth dose is shown on the left and tissue maximum ratios on the right. The position of maximum dose in the TMR measurement,  $d_{\text{max}}$ , is not shown.



The dose at point  $x$  is shown in Figure 11. The percentage depth dose can be obtained from tissue maximum ratios by the expression (8):

$$P(x, x_0, W, SSD, (hv)_{\max}) = \frac{TMR(x, W, (hv)_{\max})}{TMR(x_0, W, (hv)_{\max})} \left( \frac{SSD+x_0}{SSD+x} \right)^2 \times 100\% \quad (1.5.14)$$

where  $\frac{SSD+x_0}{SSD+x}$  takes into account a  $1/r^2$  fall-off in the primary fluence between points  $x_0$  and  $x$ .

Using Equation 1.5.3, the tissue maximum ratio can be found:

$$TMR = \frac{C_\lambda(x) k_2(x) R(x)}{C_\lambda(d_{\max}) k_2(d_{\max}) R(d_{\max})} \quad (1.5.15)$$

In the build-up region the quality of radiation does not change appreciably so the ratio  $k_2(x)/k_2(d_{\max})$  can be taken as unity. The ratio  $C_\lambda(x)/C_\lambda(d_{\max})$  is approximately unity as well.\* Therefore, the tissue maximum ratio is just the ratio of readings taken at a depth,  $x$ , and at  $d_{\max}$ .

Using Equation 1.5.8, the tissue maximum ratio is predicted to be:

$$TMR = \frac{e^{-(\mu_\gamma/\rho)x} - e^{-(\mu_e/\rho)x}}{e^{-(\mu_\gamma/\rho)d_{\max}} - e^{-(\mu_e/\rho)d_{\max}}} \quad (1.5.16)$$

Equations 1.5.8 and 1.5.16 predict that the dose at the proximal surface of the phantom (i.e.  $x=0$ ) is zero. The reason is that no charged particles have been set in motion. The low surface dose can have important clinical effects. For example, the skin is a fairly radiosensitive tissue and often is not affected by deeper seated cancerous tissue. When this

\*  $C_\lambda(x)/C_\lambda(d_{\max})$  is approximately equal to  $\bar{S}_{\text{air}}^{\text{water}}(x)/\bar{S}_{\text{air}}^{\text{water}}(d_{\max})$  (7) where  $\bar{S}_{\text{air}}^{\text{water}}(x)$  is the stopping power ratio of water to air averaged over the electron fluence at a depth,  $x$ , in the phantom. Nahon (53) has shown that  $\bar{S}_{\text{air}}^{\text{water}}(x=0)$  is within 2% of  $\bar{S}_{\text{air}}^{\text{water}}(d_{\max})$  in the energy range between 6 MV and 15 MV.



is the case, the dose to the skin should be as low as possible.

In practice, the surface dose is non-zero. In part this is due to backscattered radiation. The backscatter dose can be divided into two components. Some dose is due to forward directed primary photons which produce charged particles set in motion near the surface of the phantom which scatter backwards. The rest is due to photons scattering backwards and producing charged particles set in motion which are then mainly back directed.

The rest of the surface dose is due to contamination. The contamination component of the beam is defined as charged particles and scattered photons produced by interactions of the primary beam with material outside the phantom. Since the dose is directly due to the slowing down of charged particles, the surface contamination dose is due to charged particles produced outside the phantom.

The primary photon beam is defined to be photons emerging through the collimators which appear to have been produced by bremsstrahlung in the target.\*

\* Other photons which are indistinguishable from bremsstrahlung produced photons are also considered primary. These include bremsstrahlung photons that have been forward scattered by beam modifying components such as the field flattening filter or annihilation photons directed parallel to the primary photon beam.





## 1.6 Review of Previous Work on Contamination of Megavoltage Photon Beams

The University of Illinois (Urbana, Illinois) betatron was the first device used in radiotherapy to produce a megavoltage photon beam. This betatron could produce bremsstrahlung photons from electrons with kinetic energies of 5 MeV to 20 MeV. The presence of electron contamination was evident in the beam. Quoting from a 1942 paper by Koch, Kerst and Morrison (11):

"Experience in taking these [depth-dose] data has shown that the surface dose can be greatly affected by stray electrons striking the phantom. These electrons arise from two sources; some are original beam electrons which escape in large numbers from the acceleration chamber and others are Compton electrons scattered from objects near the x-ray beam. To obtain consistent results the primary beam was stopped by absorbers placed close to the target and the secondaries [contamination electrons] were avoided by keeping scattering objects from the vicinity of the beam. The magnetic field of the betatron undoubtedly removes a great number of secondary electrons."

The surface dose, when compared to the maximum dose produced by the Illinois betatron, decreased as a function of increasing nominal beam energy.

A 1941 paper by Johns, Darby, Haslam, Katz and Harrington (13) described the depth-dose and isodose distributions from a 22 MeV betatron. There is no mention of the production of contamination. They claim depth-dose curves are independent of field size or source to surface distance (retrospectively, there was some small dependence on these factors). The measuring equipment employed did not allow measurements to be made less than 0.5 cm from the surface and the largest field was a 10 cm diameter circle measured at 70 cm SPD. These conditions are not conducive to observing contamination.



The absence of a build-up dose dependence on field size found on the Saskatchewan betatron was contradicted by Laughlin, Beattie, Lindsay and Harvey who found a dependence on field size when the Illinois betatron was operating at 25 MV (12).

The introduction of the  $\text{Co}^{60}$  isotope therapy devices clearly indicated that megavoltage primary photon beams were contaminated. Johns, Epp, Cormack and Fedoruk (14) determined that the beam was being contaminated mainly by electrons. They found that the surface dose, as measured with a thin window parallel-plate chamber, increased as a function of field width and decreased with greater source to surface distance. The contamination resulted in a shift in  $d_{\text{max}}$  towards the surface and produced an elevated value of the maximum dose. They recommended a distance of 20 cm between the diaphragm (secondary collimator) and the patient's surface. An aluminum absorber placed in the beam following the primary collimator reduced the amount of contamination.

The results of the measurements of Johns et al have been confirmed for  $\text{Co}^{60}$  beams by many other investigators. The dose in the build-up region increases as a function of increasing field size (15-21). The dose at depths below  $d_{\text{max}}$  increases with decreasing distance to the source (15, 17, 20, 22). Contamination of  $\text{Co}^{60}$  beams produces a dramatic shift in the position of the maximum dose (15, 20, 21).

Following the theoretical calculations of Wilson and Perry (23) in 1951 which showed that medium Z materials could be used to reduce electron contamination, many authors experimentally confirmed their findings. The best electron filter materials were claimed to be cadmium,  $Z=48$ , (15); tin,  $Z=50$ , (22); and copper,  $Z=29$  (26, 27). Other



authors used low or high Z materials as electron filters, for example, lead,  $Z=82$ , (17); leaded glass (25) and perspex (21).

In contrast to the findings that materials placed in the beam reduced the amount of contamination, it was found by authors that accessories placed in a  $\text{Co}^{60}$  field increased the amount of contamination (26).

In linear accelerators a great deal of contamination is produced by the introduction of accessories into the beam. Rao, Pillai and Gregg (28) measured contamination at many beam energies produced by accessories. They found that the amount of contamination increased with accessory tray thickness up to a certain thickness (about 8 mm for a lucite accessory 29 cm above the phantom when the field size was 25 cm x 25 cm in a 6 MV beam) and was constant with increasing thickness for greater thicknesses. The amount of accessory tray contamination increases with larger fields and smaller source to surface distances. Other authors have confirmed these results for linear accelerators (19, 25).

Rao, Pillai and Gregg (28) found that a lead sheet placed under the accessory tray reduced the dose at all depths below  $d_{\text{max}}$ . Gray (25), based on the success of  $\text{Co}^{60}$  contaminant filtering, suggested using a leaded glass accessory tray in linear accelerators and Wu (29) recommended placing a tin sheet beneath the accessory tray in 10 MV photon beams.

Scrimger and Kolitsi (30) studied the effect outside the beam when scattering layers were placed inside the field. An 8 MV linear accelerator was used. The relative dose outside the field fell off rapidly with depth suggesting that the scattered radiation is mostly electrons. The amount of scattered radiation outside the field increased



with field area and decreased with increasing distance to the scatterer.

A field flattening filter is designed so that the lateral distribution at  $d_{\max}$  for megavoltage photon beams is as flat as possible. However, it has been found that the surface dose is generally higher near the central axis compared to the dose near and beyond the beam edges (19, 21, 25, 30, 36).

As was observed for  $\text{Co}^{60}$  beams, megavoltage photon beams from linear accelerators have an increased dose due to contamination when the field size is large or the source to probe distance is small (25, 28, 29, 31, 32, 33, 34, 35).

Contaminated accelerator beams produce a shift in  $d_{\max}$  through the entire range of energies currently employed in radiotherapy; for example, at 2 MV (24), 4 MV (18, 25), 10 MV (38), 25 MV (18, 37, 39), 34 MV (34) and 45 MV (40).

Penetration characteristics of the contamination component have been measured in an number of different ways. Dawson (34) produced what he called "difference curves". The difference in dose between neighboring field sizes at a fixed depth and source to surface represents the effect of an increase in field size. At shallow depths the difference curves decrease rapidly. Attenuation of the dose due to contamination electrons is cited as the cause. These measurements were done in a phantom greater in extent than the field so some of the difference between the dose at neighboring field sizes is due to photons scattered in the phantom arriving at the measuring point. This is evident in Dawson's data because the difference curves increase with depth when measurements are made at a depth beyond  $d_{\max}$ .

Marbach and Almond (37) placed a lead pyramid-shaped block on the





accessory tray to shield a detector from the primary beam. Contamination was then claimed to be the only component of the beam arriving at the phantom. They measured depth-dose curves for the contamination component. Unfortunately, the shallowest depth-dose measurement obtained was 2 cm from the surface. A key to the validity of such an approach is to confirm that the lead block does not shield or produce a significant amount of contamination. Surface dose measurements taken before and after the placement of the lead blocks would have determined if there was any change in contamination.

Marbach and Almond subtracted the contamination curves from the total curves to yield the primary depth-dose curves. The primary depth-dose curves did not have a shift in  $d_{\max}$  and when normalized to their own maxima were independent of field size.

Marbach and Almond went on to hypothesize that electrons were not the cause of the  $d_{\max}$  shift. They placed a 1/4 inch aluminum plate in the field below the collimators in the anticipation that this would remove all of the electron contamination. Since there was little change in the depth dose curve, they concluded there were no contamination electrons in the beam. Their interpretation was not necessarily valid. As many electrons may have been produced as were stopped and scattered. Indeed, even though their contamination depth-dose did not include shallow depths, a rapid increase in dose with decreasing depth is evidence for an electron contamination component.

Biggs and Ling (41) repeated the method of primary beam blocking developed by Marbach and Almond (37). They produced contamination attenuation curves that included the dose at the surface and at other depths below  $d_{\max}$ . These curves exhibit a rapid fall off at shallow



depths and tend to be an asymptotic constant at deeper depths. They did not subtract the contaminant component to obtain the primary build-up curves.

Clifton Ling and colleagues (41, 43, 44, 45) have employed electromagnets with maximum central magnetic fields between 1.8 kG and 3.9 kG to sweep electrons from the field. Padikal and Deye (42) used a permanent magnet with variable gap pole pieces. The smallest central field strength still capable of sweeping all of the 10 MV contamination electrons produced between the target and the magnet was 0.5 kG.

Biggs and Ling (41) showed that the build-up curve for a 25 MV photon beam was field size independent when the magnet was sweeping contamination electrons from the field.

Padikal and Deye (42) defined a parameter,  $\alpha$ , to be the difference between the reading of the ionization chamber without the magnet and the ionization reading with the magnet normalized to the reading at  $d_{\max}$ . Since the only difference between the readings was an absence of electrons produced between the target and magnet,  $\alpha$  represents the component of the TMR curve attributable to those contaminant electrons. The electron contaminant TMR curve had a peak between 1 and 2 mm and rapidly decreased to zero at about 2.5 cm. Despite evidence to the contrary, they claimed that the shift in  $d_{\max}$  with field size is due to a relative enhancement in the soft x-ray component as the collimator jaws are opened.

Ling (43) has shown that a magnet in a 4 MV photon beam produced no shift in  $d_{\max}$ . There is a slight field size dependence of the surface dose and the build-up curves at shallow depths. This is interpreted as due to electrons originating from the air volume between



the magnet and the phantom. Ling, Schell and Rustgi (45) repeated the measurements at 10 MV and found similar results. They measured the build-up curves with the magnet in place at two different source to surface distances to see if the contamination that was previously attributed to air was SSD dependent as theory would predict (37). Their results were inconclusive so they have stated that they will repeat the measurements with a helium-filled bag to replace the air volume.

Ling, Rustgi and Gromadzki (44) have measured the production of secondary radiation by 10 MV photons from scatterers placed in the beam. The measurements were done outside the primary beam field when a magnet was off and on. The depth of ionization curves for scattered photons and electrons were obtained separately. They investigated the amount of electron production as a function of the atomic number of the scatterer. For a target thickness of  $1.7 \text{ gm/cm}^2$  and a scattering angle of  $10^\circ$  high Z materials such as lead produced less ionization.

Recently, Nilsson and Brahme (46) have done calculations predicting the nature and amount of contamination due to scattered photons using the Monte Carlo method. The scattered photon spectrum for both 6 MV and 21 MV does not change appreciably between the central axis and the field edge for a 20 cm circular field. The maximum energy of the scattered photons is about 85% of the maximum energy of the primary spectrum. The peak in the scattered and primary spectrum occur at the same energy although the relative number of photons in the peak are greater in the scattered photon spectrum. The absorbed dose at  $d_{\text{max}}$  due to scattered photon contamination for both 6 MV and 21 MV photons was found to be about 2.5 - 3.0% at the central axis for a 20 cm circular



field. The main source of scattered photons was the collimator for a 6 MV photon beam and the field flattening filter for a 21 MV photon beam.

The main disagreement in the literature concerns the type and origin of contamination. Some authors say electrons and others say scattered photons are the main cause. Every component between the source of primary radiation and the phantom has been suggested as the main source of contamination. Table 1 summarizes the conclusions of a number of authors on the nature and source of the contamination.





Table 1      Conclusions Of A Number Of Authors  
On The Nature And Source Of Contamination

| Author                           | Date | Type                | Source                              |            |     |
|----------------------------------|------|---------------------|-------------------------------------|------------|-----|
|                                  |      |                     | Field<br>Flat-<br>tenning<br>Filter | Collimator | Air |
| Johns, Epp,<br>Cormack, Fedoruk  | 1952 | Electron            |                                     | X          | X   |
| Richardson,<br>Kerman, Brucer    | 1954 | Electron            |                                     | X          | X   |
| Ibbott, Hendee                   | 1970 | Electron            |                                     | X          |     |
| Jackson                          | 1971 | Electron            |                                     |            | X   |
| Gray                             | 1973 | Electron            | X                                   | X          |     |
| Bagne                            | 1974 | Photon              |                                     | X          |     |
| Velkley, Manson<br>Purdy, Oliver | 1975 | Electron            |                                     | X          |     |
| Dawson                           | 1976 | Electron            |                                     | X          |     |
| Smith,<br>Sutherland             | 1976 | Electron            |                                     | X          |     |
| Marbach, Almond                  | 1977 | Photon              | X                                   |            |     |
| Padikal, Deye                    | 1978 | Electron,<br>Photon |                                     | X          |     |
| Nilsson, Brahme                  | 1979 | Electron            |                                     |            | X   |
| Bagne                            | 1980 | Electron            | X                                   | X          | X   |
| Wu                               | 1980 | Electron            |                                     | X          |     |



## 2. EXPERIMENTAL TECHNIQUES AND RESULTS

The documentation  
of experimentation  
often has too much elaboration  
and not enough elocution.



## 2.1 Open Field Build-Up Curves

Tissue maximum ratio curves were measured for 15 MV and 6 MV photon beams from Siemens Mevatron -20 and Mevatron -6 linear accelerators. A schematic diagram of the beam defining head of the Mevatron -20 is shown in Figure 8. The Mevatron -6 has a similar design. All determinations were made at constant source-to-probe distances (SPD) using 0.16 cm (1/16") thick and 0.64 cm (1/4") thick square polystyrene slabs. The phantom slabs used in the determination of the open field build-up curves each had cross-sectional dimensions of 25 cm x 25 cm.

The detector used in this section and others was a Capintec 192A electrometer with a PS-033 thin window parallel-plate ionization chamber which has an effective volume of 0.5 ml. The entrance window was aluminized polyester film  $0.5 \text{ mg/cm}^2$  thick.

The field size is referred to as the lateral field dimensions defined at 100 cm. Only square fields were used.

The central axis build-up curves at SPD = 100 cm for a 15 MV beam for various field sizes are illustrated in Figure 12. These build-up curves demonstrate a field size dependence. There is little backscatter expected at 15 MV so the dose at the surface should be very small and only weakly dependent on field size. Therefore, most of the field size dependence and the elevated surface dose can be attributed to contamination.

The open field build-up curve at SPD = 100 cm for a 6 MV beam are shown in Figure 13. The build-up curves were measured at the central axis for various field sizes. Greater field sizes result in larger tissue maximum ratios (TMR) for the same depth. Since a very similar effect was observed at 15 MV, the open field build-up curves at the two



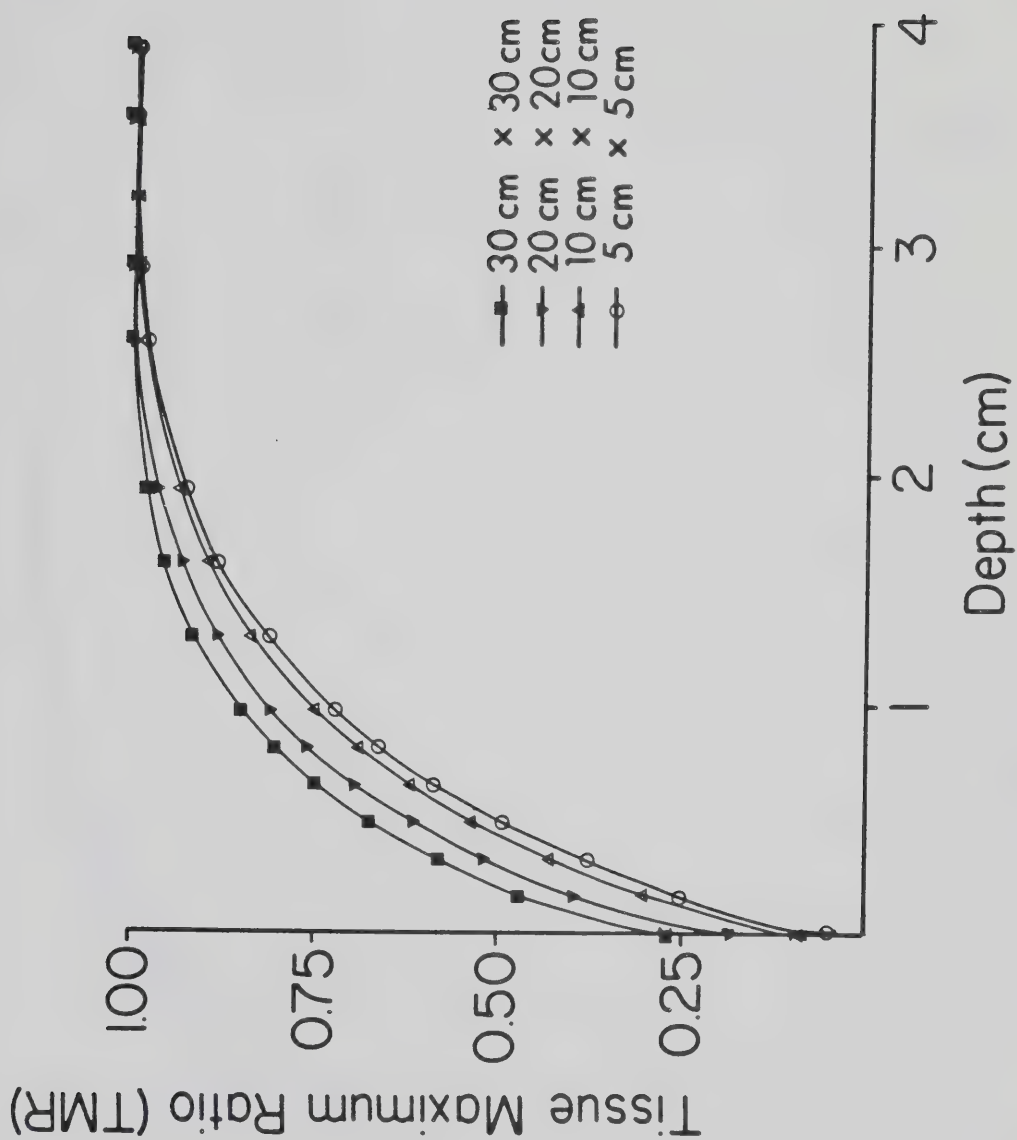


Figure 12. Central axis open field build-up curve at 100 cm SPD for a 15 MV beam.





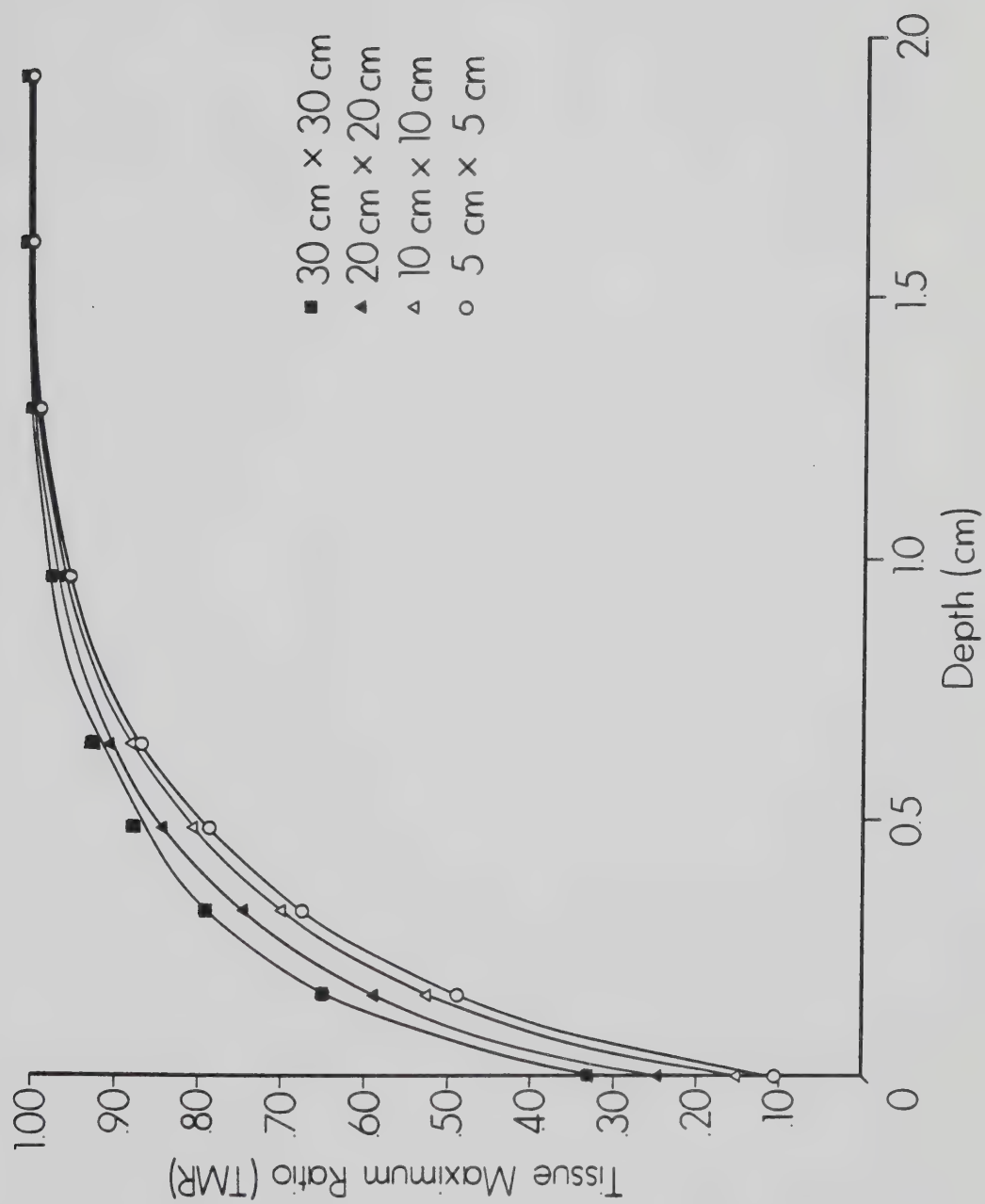


Figure 13. Central axis open field build-up curve at 100 cm SPD for a 6 MV beam.



energies have been compared by normalizing the depth with respect to  $d_{\max}$  of each curve. The result is illustrated in Figure 14. At field sizes of 10 cm x 10 cm and 30 cm x 30 cm, the TMR curves for the 6 MV photon beam have a similar form to those for the 15 MV beam at depths less than  $d_{\max}$ . However, at any normalized depth the TMR values for 6 MV slightly exceed those for 15 MV. The 6 MV surface dose exceeds that of the 15 MV beam for the same field size.



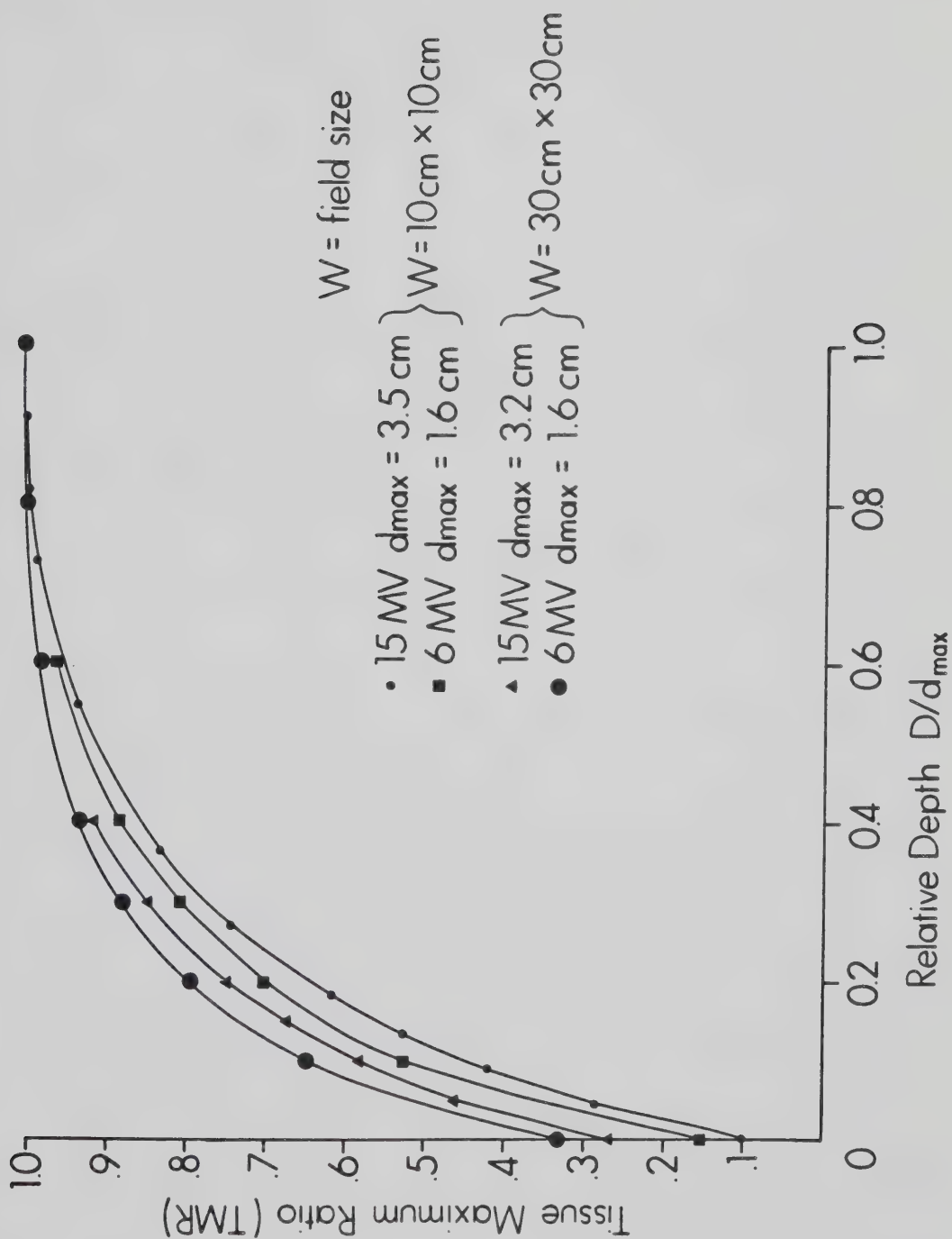


Figure 14. Comparison between 6 MV and 15 MV central axis open field build-up curves.



## 2.2 Accessory Build-Up Curves

Various thicknesses of Lucite (density =  $1.18 \text{ g/cm}^3$ ) alone or Lucite and lead (density =  $11.4 \text{ g/cm}^3$ ) slabs were placed in the beam to determine their effect on the build-up curves. The distal surface of the slabs was placed at the accessory tray holder position 56 cm from the source. In all cases, a Lucite surface was facing the probe.

Figures 15, 16 and 17 show the build-up at an SPD of 140, 100 and 75 cm, respectively. The field size in all cases is 30 cm x 30 cm. When accessories are placed in the field at the tray holder position, a larger TMR for all depths less than  $d_{\text{max}}$  is observed. There is also a shift in the point of  $d_{\text{max}}$  to shallower depths. This is more pronounced at SPD = 75 cm (Figure 17). There is virtually no difference in the build-up curves between a 3.2 cm (1-1/4") Lucite accessory and a 0.30 cm lead slab on top of a 0.64 cm (1/4") Lucite tray.

At smaller source-to-probe distances there is a greater difference between the tissue maximum ratio with and without accessories present. Therefore, as the distance to the source of contamination decreases, the dose increases. The tissue maximum ratio for SPD = 75 cm (Figure 17) is greater than the tissue maximum ratios for SPD = 100 cm and SPD = 120 cm (Figures 15 and 16) at all depths. The difference between the tissue maximum ratios as a function of source-to-probe distance is most pronounced at the surface.

The accessory build-up curves were measured on the Mevatron -6 for SPD = 75 cm and SPD = 100 cm. They show very similar features when compared to the 15 MV curves (see Figures 18 and 19). Accessories placed in the field increase the TMR at all depths below  $d_{\text{max}}$ . There





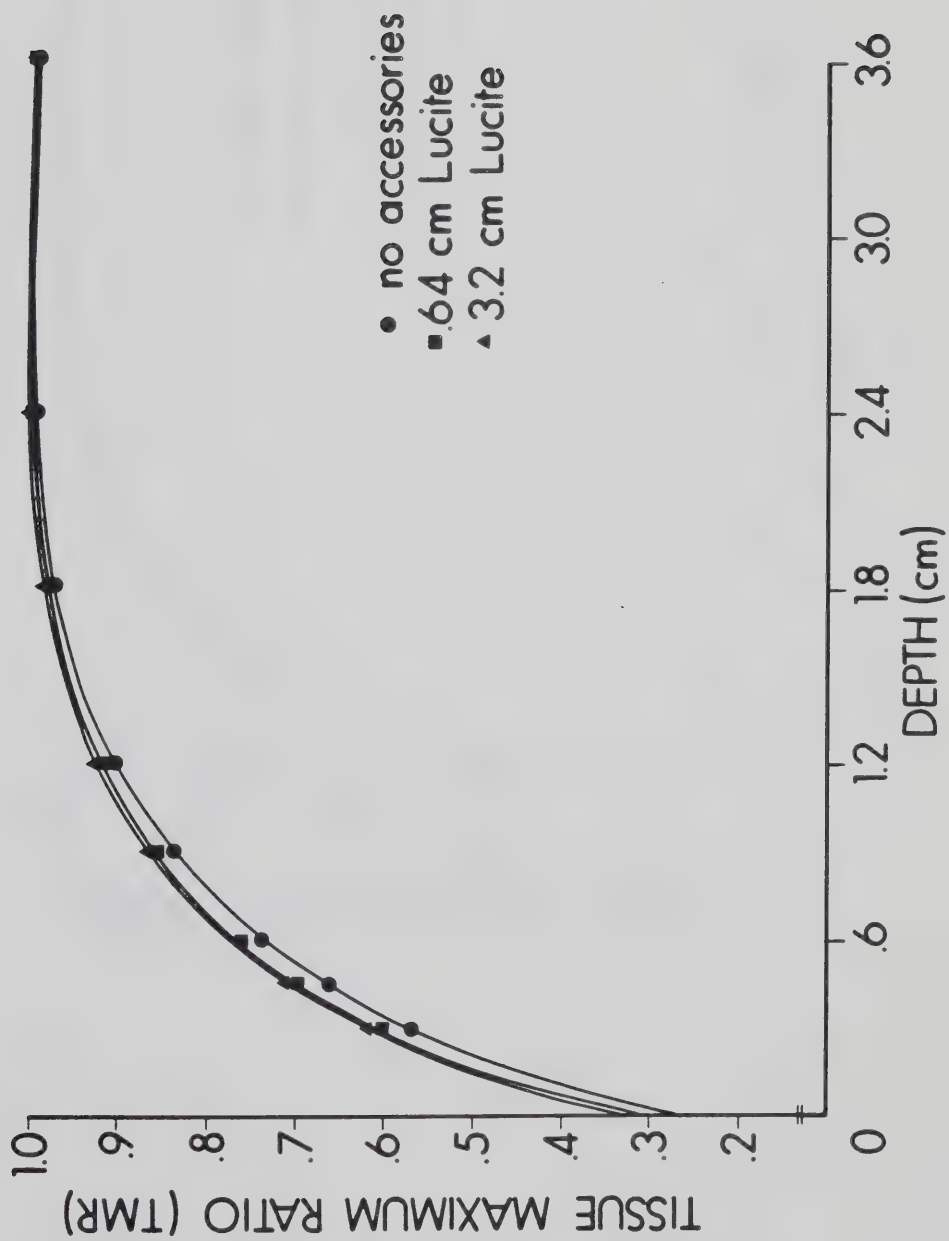


Figure 15. Accessory build-up curves at 140 cm SPD for a 15 MV beam.



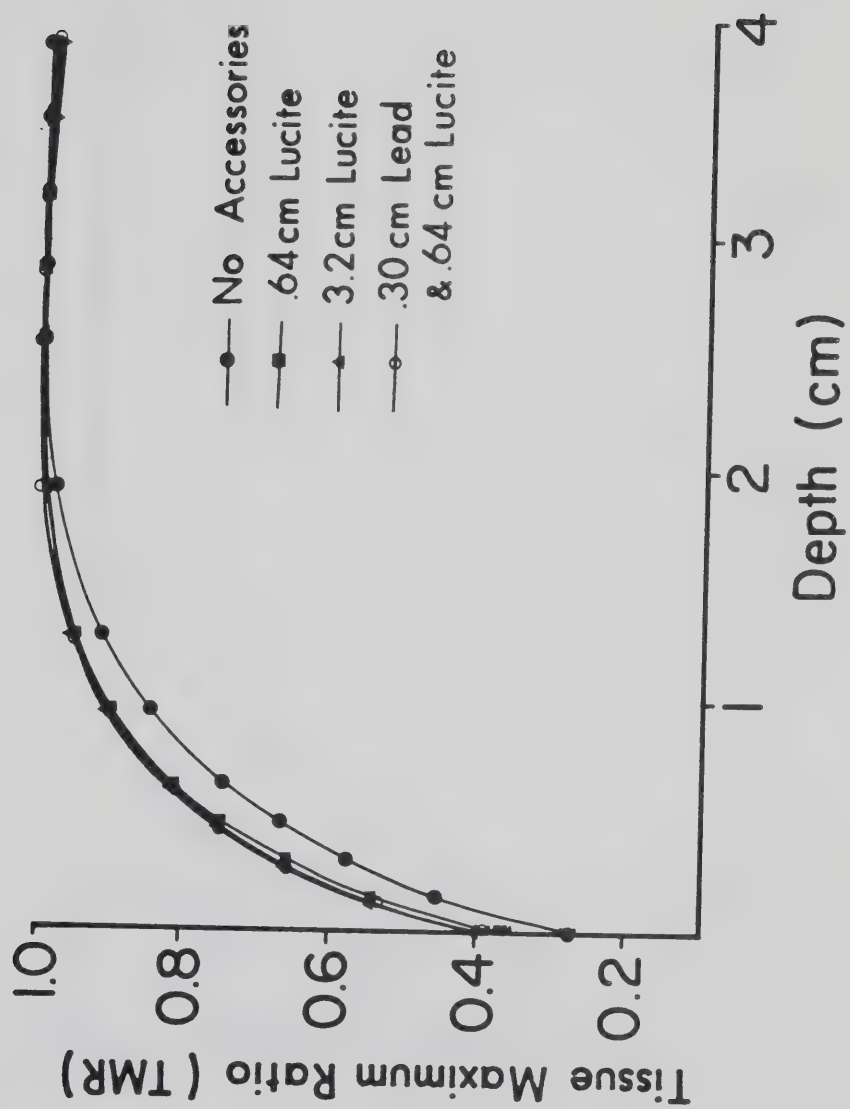


Figure 16. Accessory build-up curves at 100 cm SPD for a 15 MV beam.



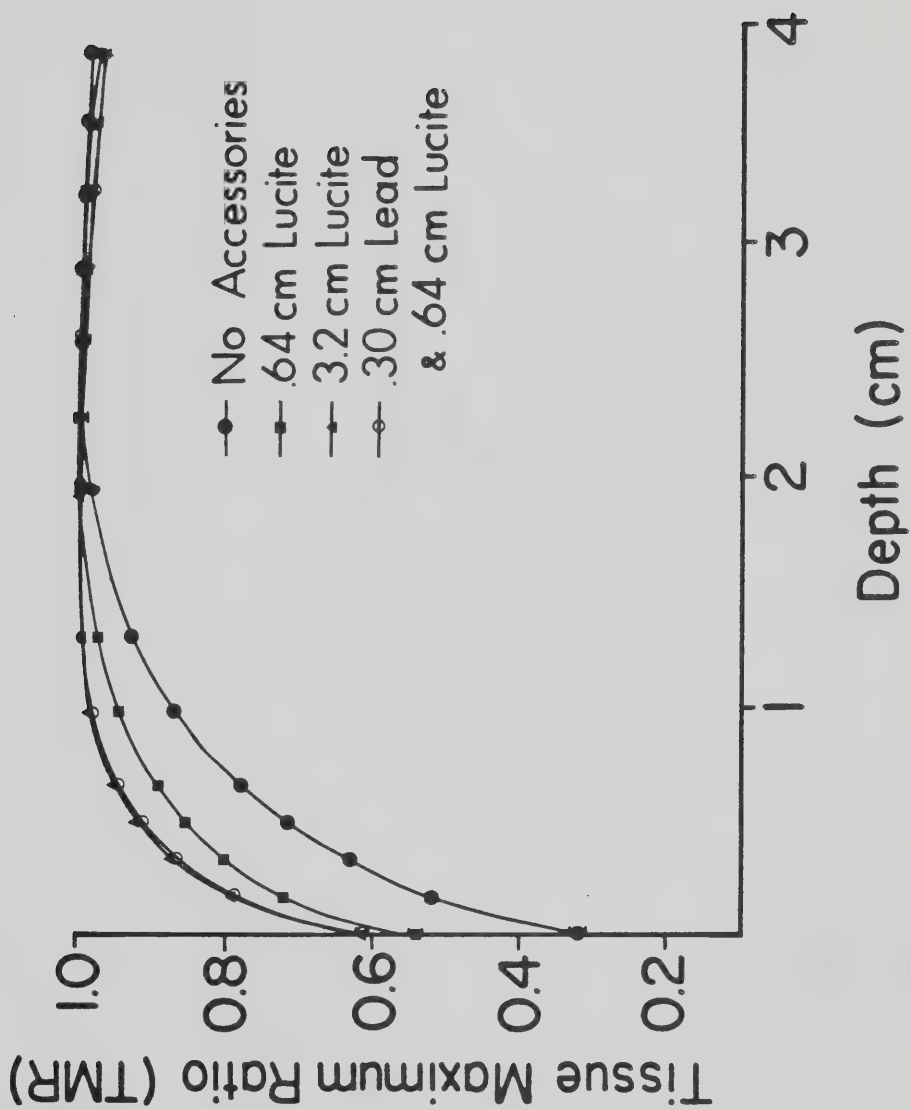


Figure 17. Accessory build-up curves at 75 cm SPD for a 15 MV beam.



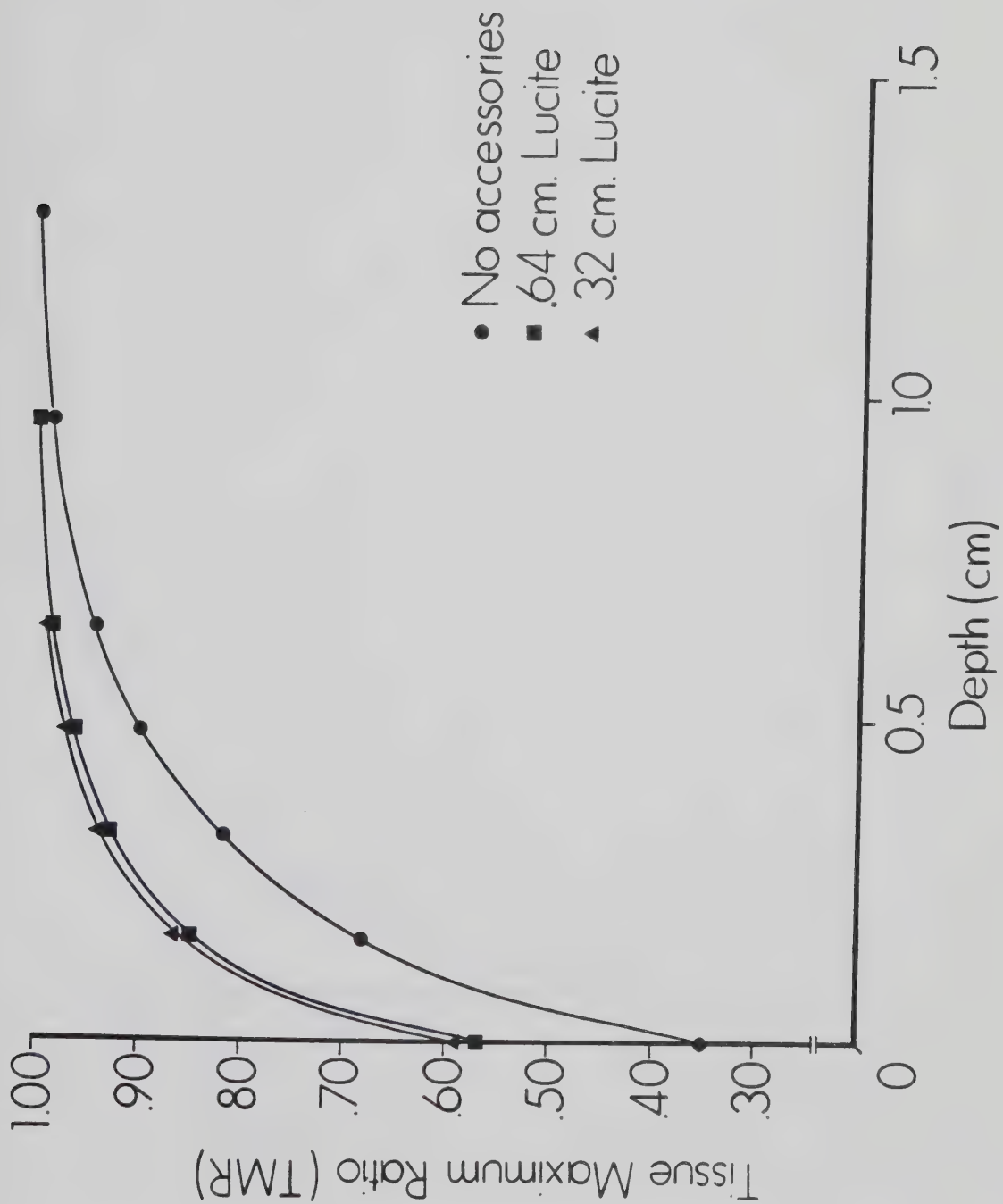


Figure 18. Accessory build-up curves at 75 cm SPD for a 6 MV beam.





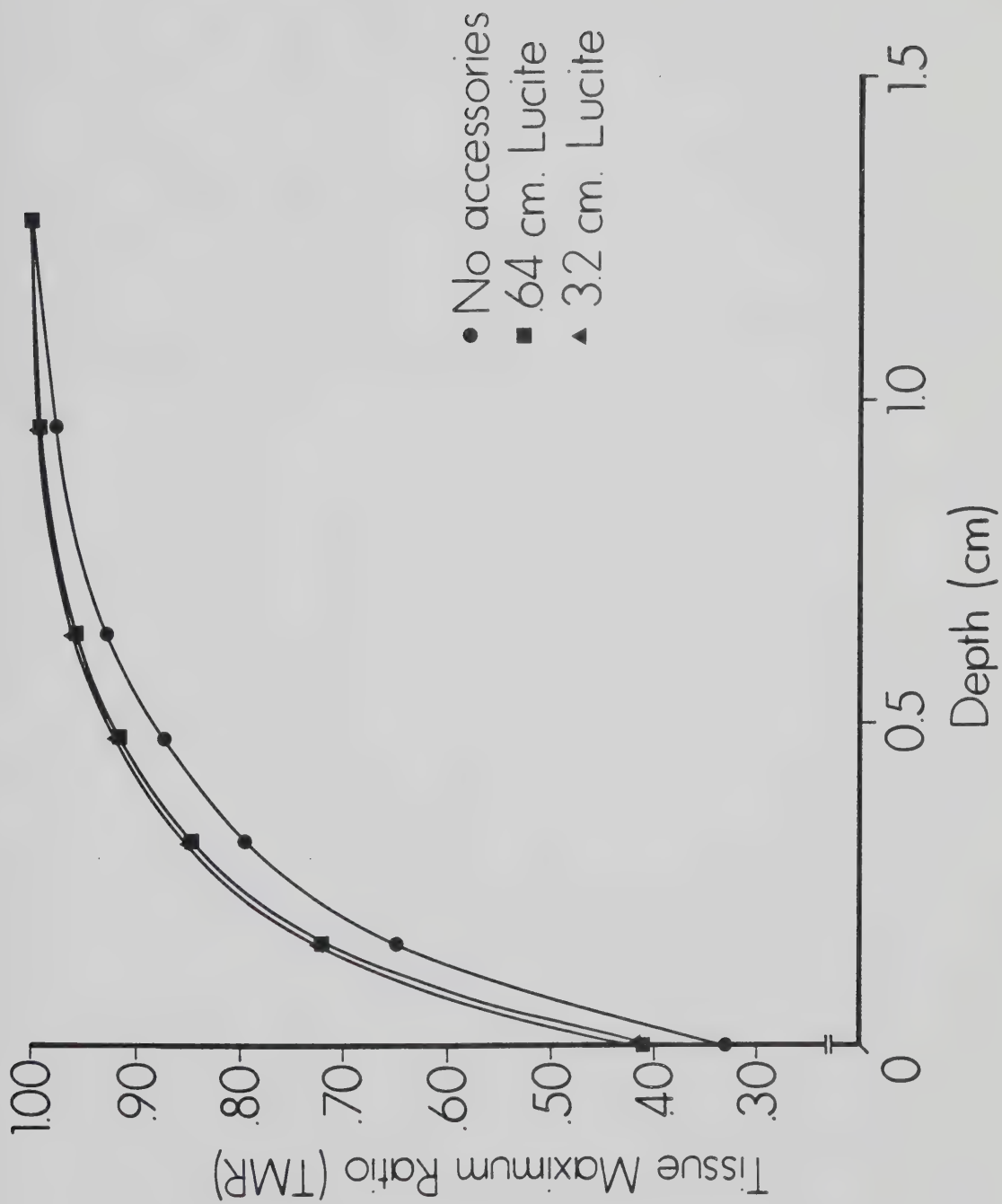


Figure 19. Accessory build-up curves at 100 cm SPD for a 6 MV beam.



is no difference between a 3.2 cm and a .64 cm thick Lucite accessory at an SPD of 100 cm. However, a small difference is observed in TMR between the same two thicknesses of Lucite when introduced at SPD = 75 cm. The depth at which  $d_{\text{max}}$  occurs is shifted from 1.6 cm to 1.3 cm with the introduction of the Lucite accessories at both SPD = 75 cm and 100 cm. A comparison between 6 MV and 15 MV was made by normalizing the depth to  $d_{\text{max}}$ . The comparison is illustrated in Figures 20 and 21. As observed for the open field build-up curves, the accessory build-up curves at 6 MV exceed those at 15 MV at the same relative depth. This applies for both source-to-probe distances of 75 cm and 100 cm.



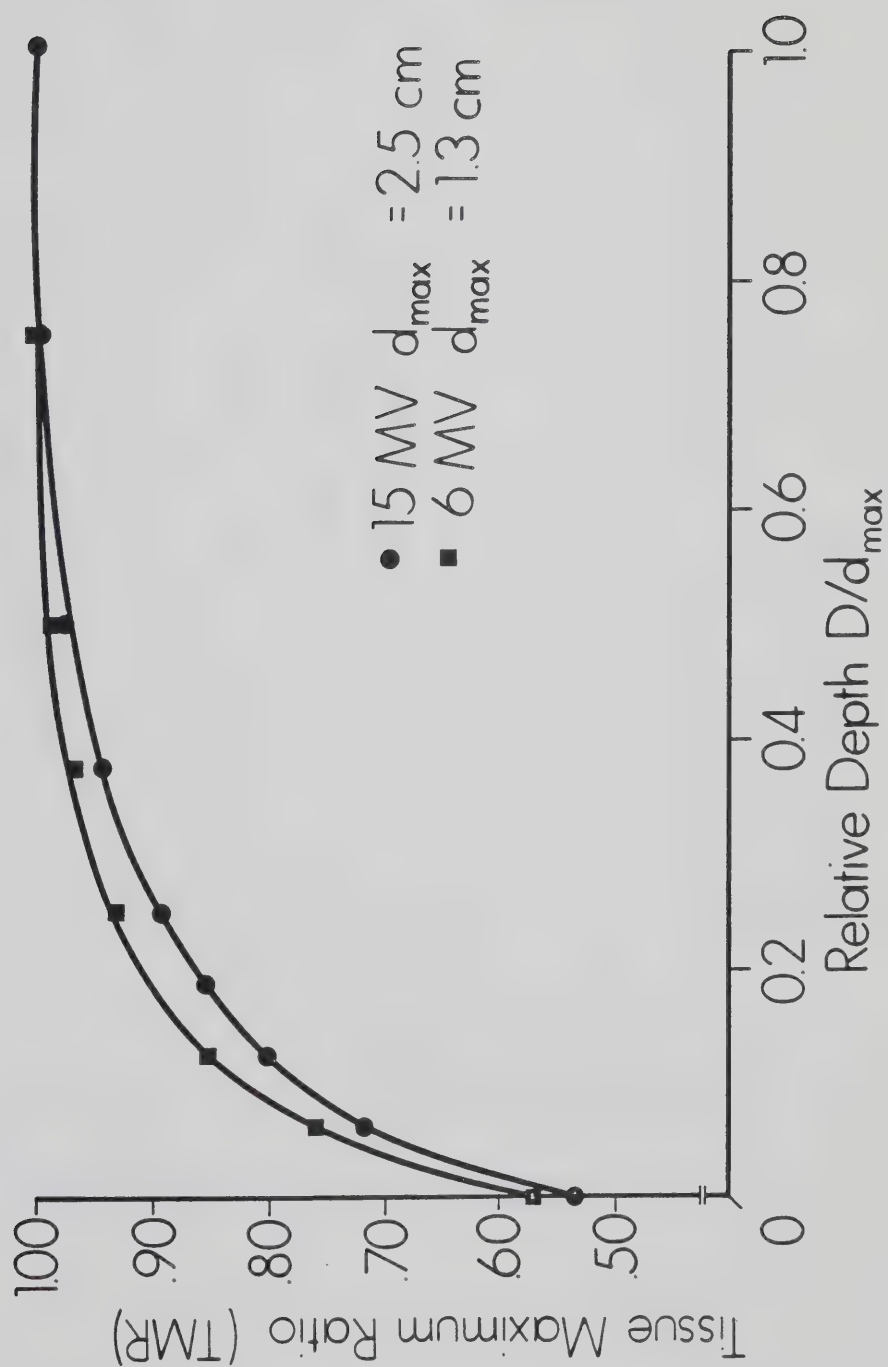


Figure 20. Comparison between 6 MV and 15 MV accessory build-up curves at 75 cm SPD.



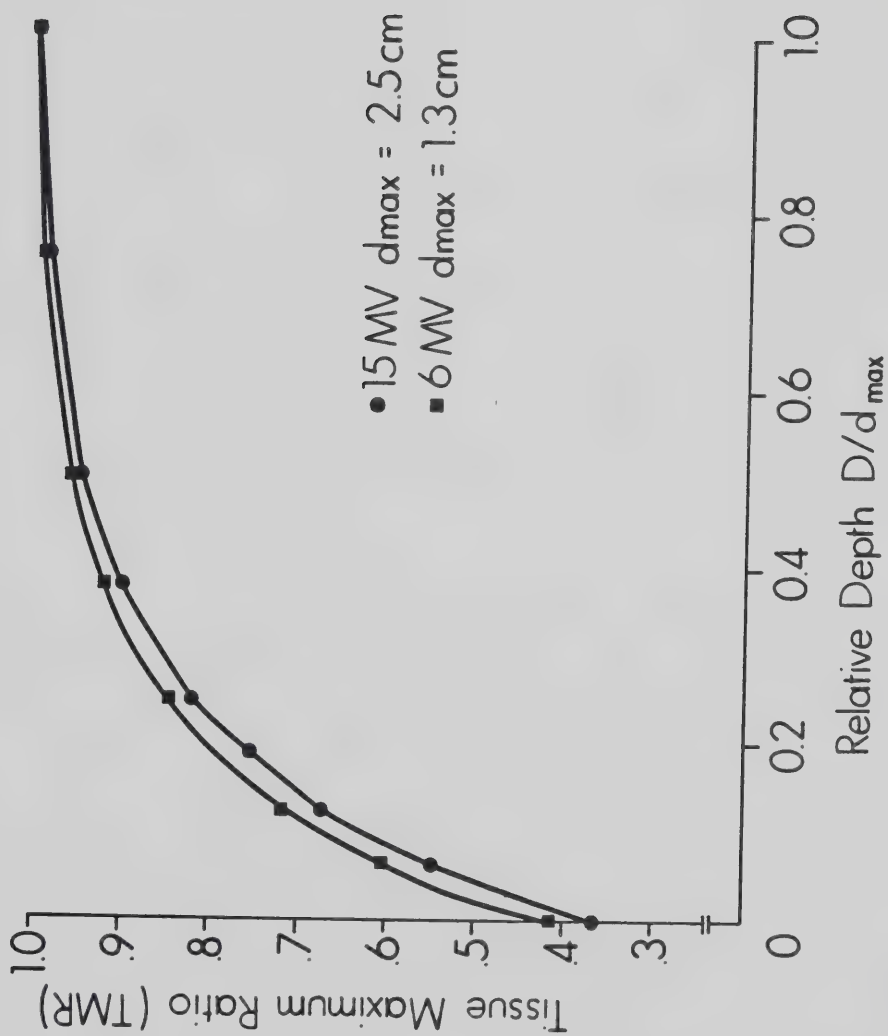


Figure 21. Comparison between 6 MV and 15 MV accessory build-up curves at 100 cm SPD.





### 2.3 Filtering the Electron Contamination

When at the surface, the chamber used has a sufficiently thin window to ensure that the build-up depth is approximately zero (5  $\mu\text{m}$  polystyrene equivalent). The window thickness has an equivalent thickness of less than a centimeter of air. Only very low energy photons would have had a reasonable probability of interaction with such a window. In order to be detected these photons would have had to have been produced within a few centimeters of the chamber, otherwise they would have been rapidly attenuated in air. Primary photons with a low enough energy to have had a high probability of interaction with the window would have been completely attenuated when the beam emerged from the beam defining head. Therefore, the surface dose is not due to low energy forward directed photons. Some of the dose at the surface is attributable to backscatter, but most of the dose is due to contaminant electrons.

Filtering of electron contamination produced by accessories is rarely practiced for megavoltage energies above those of  $\text{Co}^{60}$ . The efficacy of electron filtering for materials of various atomic numbers at 6 MV and 15 MV was studied.

Placing a filter beneath an accessory produces a number of effects; the intensity of the primary beam is reduced, the number of interactions to produce electron contamination is increased and there is increased attenuation and scattering of electrons. The reduction of the primary beam can be taken into account by normalizing the readings taken at the surface to readings taken at  $d_{\text{max}}$  under the same conditions of filtration; in other words, by taking a tissue maximum ratio under conditions of filtration.



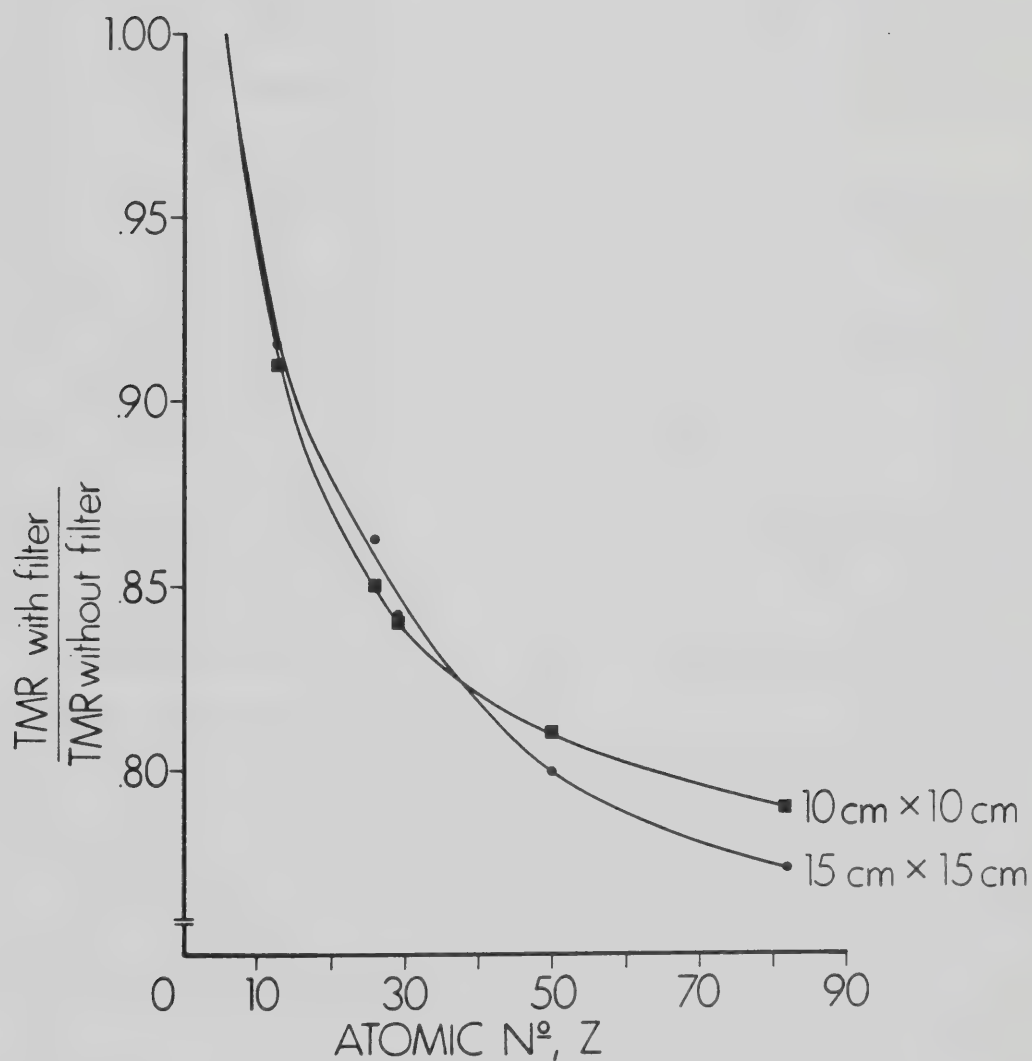


Figure 22. Reduction in the 15 MV surface dose when electron filters with materials of various atomic numbers are placed beneath the accessory tray. In all cases, an equilibrium thickness of filter was used.



It is unlikely that filtration changes the amount of electron contamination present in the beam because the amount of electron contamination did not continue to increase with thickness of accessory after 0.64 cm of Lucite at 15 MV (see Section 2.2 and Figure 16). This was verified by placing the filter material above the accessory tray (thickness = 0.64 cm of Lucite). The reading at the surface with the filter material above the accessory compared to  $d_{\max}$  was no different within experimental error from that with the accessory tray in the field alone.

There was some reduction in the surface TMR when a filter with an atomic number higher than that of Lucite was placed beneath the accessory tray. The ratio of the TMR of the accessory tray alone to the TMR with a filter underneath the tray is shown in Figure 22 for 15 MV at field sizes of 10 cm x 10 cm and 15 cm x 15 cm with an SPD of 100 cm. High atomic number materials produce the most filtering although the effect is not very significant. Lead will reduce the surface dose by about 20%. An increased amount of electron scatter and absorption can be the only cause of the filtering effect.

Similar results were obtained at 6 MV for a field size of 15 cm x 15 cm at an SPD of 100 cm (see Figure 23). Again, lead proved to be the most effective filtering material at this energy. It reduced the surface dose by about 20% as well.



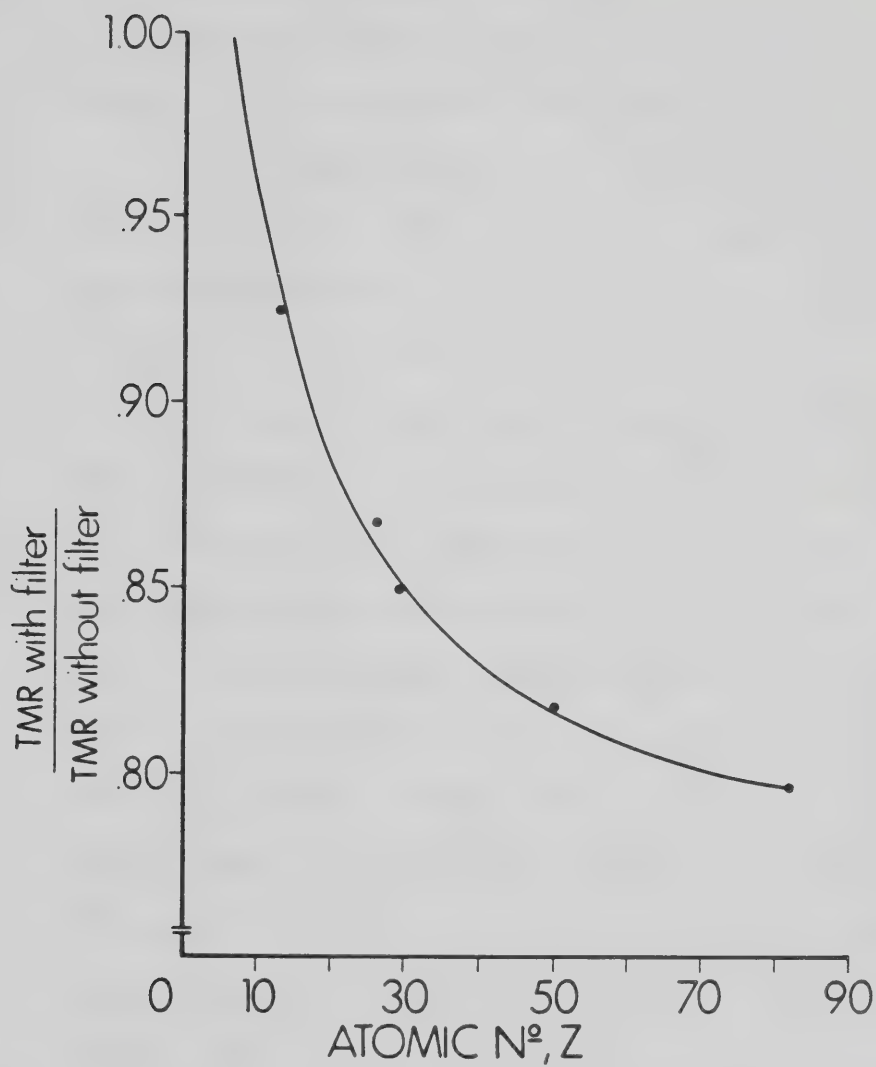


Figure 23. Reduction in the 6 MV surface dose when electron filters with materials of various atomic numbers are placed beneath the accessory tray for a field size of 15 cm x 15 cm.





## 2.4 Distance Distribution of the Surface Dose

### 2.4.1 SPD Dependence of the Surface Dose

The surface maximum ratio is defined to be the tissue maximum ratio measured with the chamber at the surface (i.e.  $d=0$ ). Figure 24 illustrates that the surface maximum ratio in the open 15 MV beam increases rapidly as the source-to-probe distance decreases for both 20 cm x 20 cm and 30 cm x 30 cm field sizes.

The curves for field size collimated to 20 cm x 20 cm show the effect of a thin accessory. The Siemens Mevatron -20 is equipped with a removable 1 mm thick Lucite cross-hair tray which can be inserted at 40 cm from the source. When the source-to-probe distance is less than 75 cm, the surface dose with the cross-hairs in place is greater than when it is removed. However, the cross-hairs, when in place, reduce the surface dose in the clinical region of SPD greater than 75 cm. This is an exception to previous observations that accessories in the field increased the surface dose.

### 2.4.2 Determination of the Apparent Source of Contamination Electrons

As the source-to-probe distance increases, the volume of air between the target and probe increases. For  $\text{Co}^{60}$ , Nilsson and Brahme (46) have predicted an increase in absorbed dose as a function of source-to-probe distance due to  $\text{Co}^{60}$  photon interactions with air. In these experiments the reverse appears to be the case and a decrease in the dose as a function of increasing source-



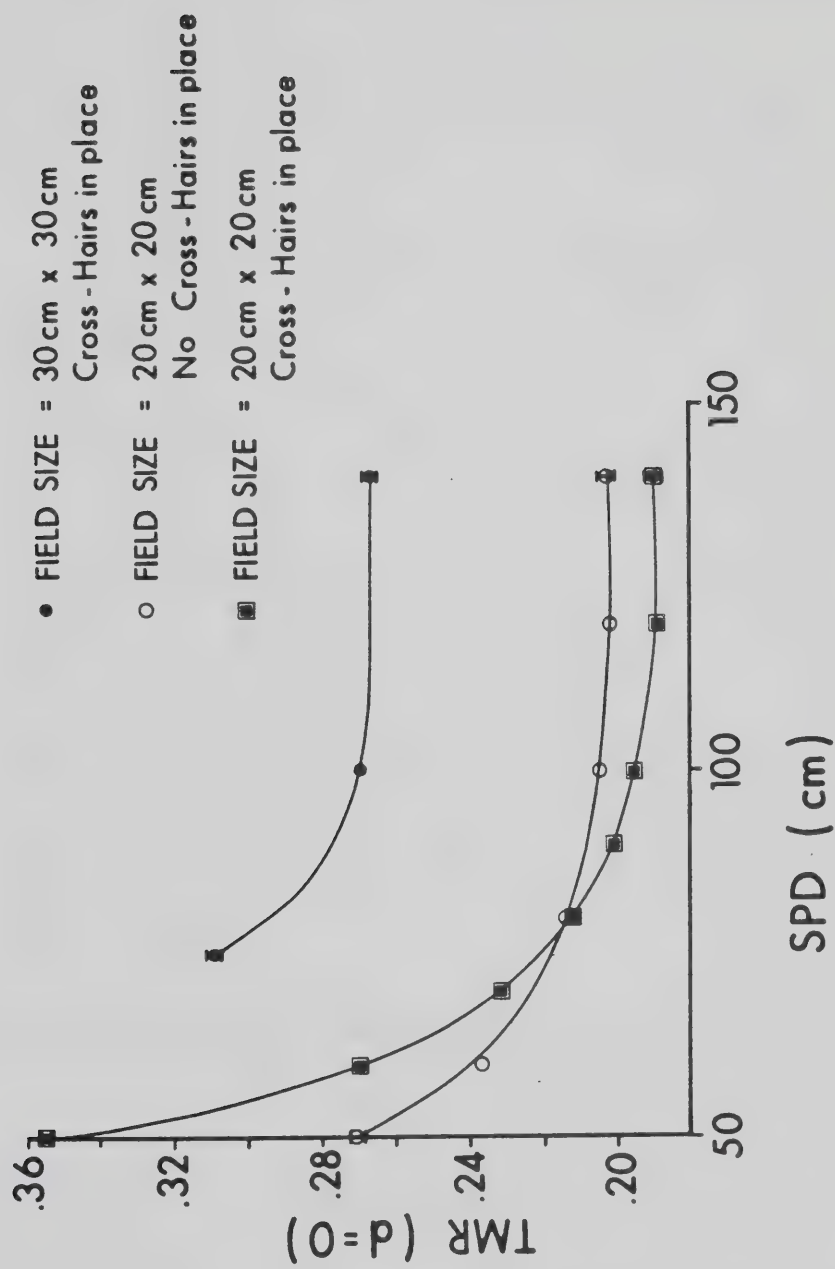


Figure 24. Distribution of the surface dose as a function of source-to-probe distance at 15 MV.



to-probe distance has been observed. This implies that at 15 MV, for a field size of 30 cm x 30 cm, the interaction of the primary photon beam with air is not the major source of electron contamination.

The surface maximum ratio is normalized to the dose measured at  $d_{\max}$  within a polystyrene phantom. The maximum dose in a phantom is due almost entirely to primary photons for which the variation with distance falls off as  $1/(\text{SPD})^2$ . However, the electron contamination does not necessarily arise at the source of primary photons. Instead of normalizing the surface dose at a given SPD to the dose at  $d_{\max}$ , each surface dose at the same SPD is normalized to the dose measured at a convenient point inside a phantom using a standard field size and photon source-to-probe distance. The isocentric normalized dose, IND, is defined as:

$$\text{IND} = \frac{\text{Dose delivered to a point at an arbitrary } d, \text{ SPD, field size}}{\text{Dose delivered at the isocenter}} \quad (2.3.1)$$

The isocenter point was at  $d_{\max}$  at SPD = 100 cm with a field size of 10 cm x 10 cm.

The apparent source of contamination electrons can be located assuming that it is a point source and there is no attenuation of electrons by air. Therefore, the isocenter normalized dose at the surface is directly proportional to the inverse square of the distance to the source of the



electron contamination, or:

$$\text{IND}(d=0) \propto \frac{1}{(\text{SPD}-d_0)^2} \quad (2.3.2)$$

where  $d_0$  is the distance of the source of contamination electrons below the primary photon source.

Figure 25 is a graph of  $\sqrt{1/\text{IND}(d=0)}$  versus SPD. The graph yields a straight line except for very large source-to-probe distances. Therefore, the source must be small and the inverse square approximation valid for source-to-probe distances less than 120 cm. The x-intercept of the graph yields a distance,  $d_0$ , of 12 cm below the primary source of photons. This corresponds approximately to the position of the bottom of the fixed head assembly which consists of the field flattening filter and the beam monitor ion chamber. The bottom surface of the field flattening filter is 3.1 cm in width, which at distances greater than 50 cm, subtends an angle no larger than  $3.5^\circ$  which would approximate a point source.

The dependence of the surface isocentric normalized dose,  $\text{IND}(d=0)$ , on SPD, was investigated for a 6 MV beam. The inverse root of the isocentric normalized dose,  $1/\sqrt{\text{IND}}$ , versus SPD is plotted in Figure 26. The intercept appears to be between 30 and 40 cm beneath the target, however, the line is not straight (in contrast to that obtained at 15 MV) indicating that a  $1/r^2$  dependence from a localized source of contamination is not the entire explanation for the presence of the surface dose.





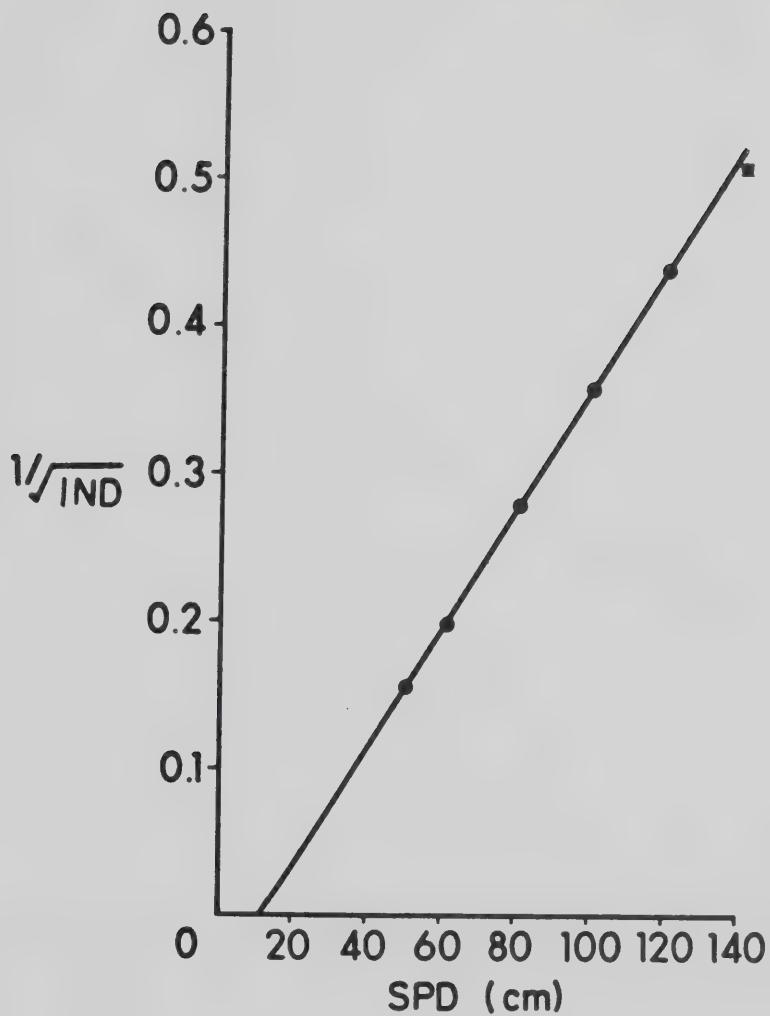


Figure 25. Graph illustrating the inverse square dependence of the surface dose on the distance to the source of contamination at 15 MV.



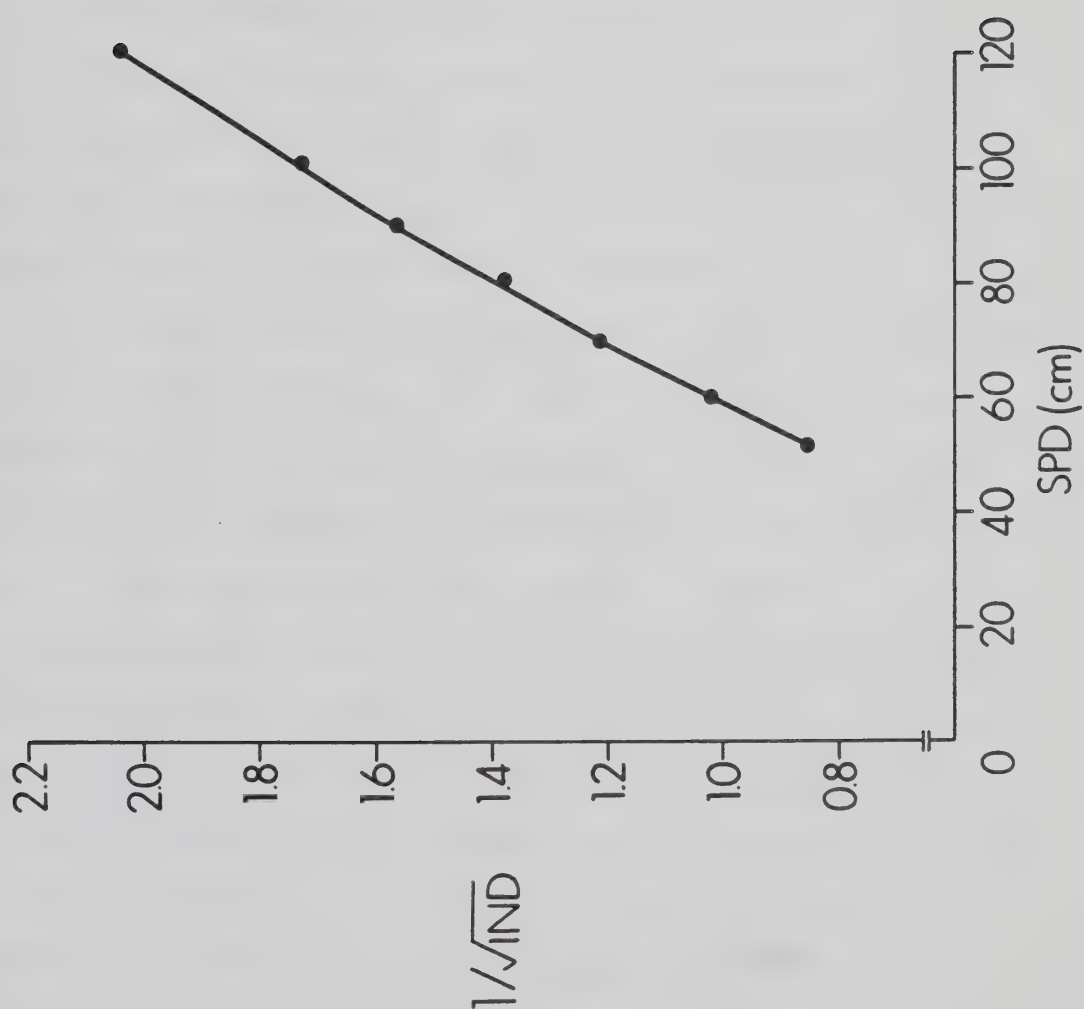


Figure 26. Graph illustrating the failure at 6 MV of the inverse square dependence to a localized source of contamination.



## 2.5 Lateral Distribution of the Surface Dose

The magnitude of surface dose as a function of lateral displacement from the central axis was measured for several source-to-probe distances. The central axis angle, C.A.A., was defined to be the angle between the central axis and a line joining the probe to the apparent source of electrons. This established parameters for the lateral direction in order to compare the distribution at various source-to-probe distances (see inset on Figure 27). In each case, the surface dose at any central axis angle and source-to-probe distance is normalized to the dose at  $d_{\max}$  on the central axis (C.A.A.=0). The curves in Figure 27 follow a Gaussian distribution.

At all points across the field, a smaller SPD results in a larger electron contamination dose. This agrees with the surface dose dependence measured along the central axis. Both the lateral distribution and the dependence on the distance from the source of the electron contamination agree with the work of Almond (5).

The lateral surface dose distribution for 6 MV and 15 MV beams at SPD=100 cm is shown in Figure 28. The distribution for each beam has been normalized to the maximum surface dose. Since the distribution at 6 MV was mapped for only one source-to-probe distance the abscissa is left as the distance from the central axis. The ordinate is defined as the surface dose at some distance away from the central axis normalized to the dose at  $d_{\max}$  measured at the central axis. There are two differences between the 6 and 15 MV lateral distributions. First, the maximum dose does not occur at the central axis but from 4 to 6 cm off the central axis. These "horns" in the surface dose are a very small but real effect. Secondly, there is a more rapid decrease in



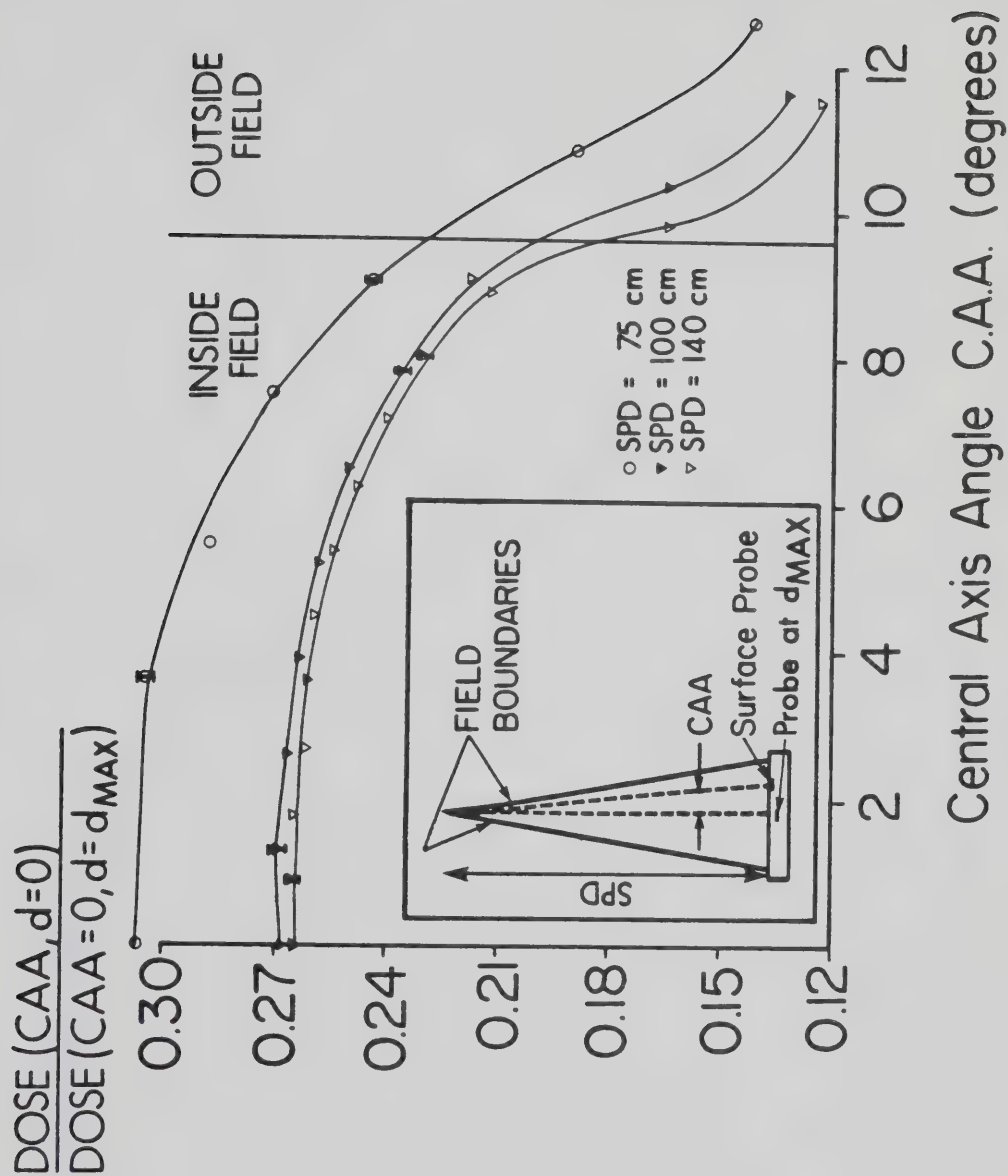


Figure 27. Gaussian distribution of the surface dose at 15 MV. The inset is a schematic diagram of the experimental arrangement.





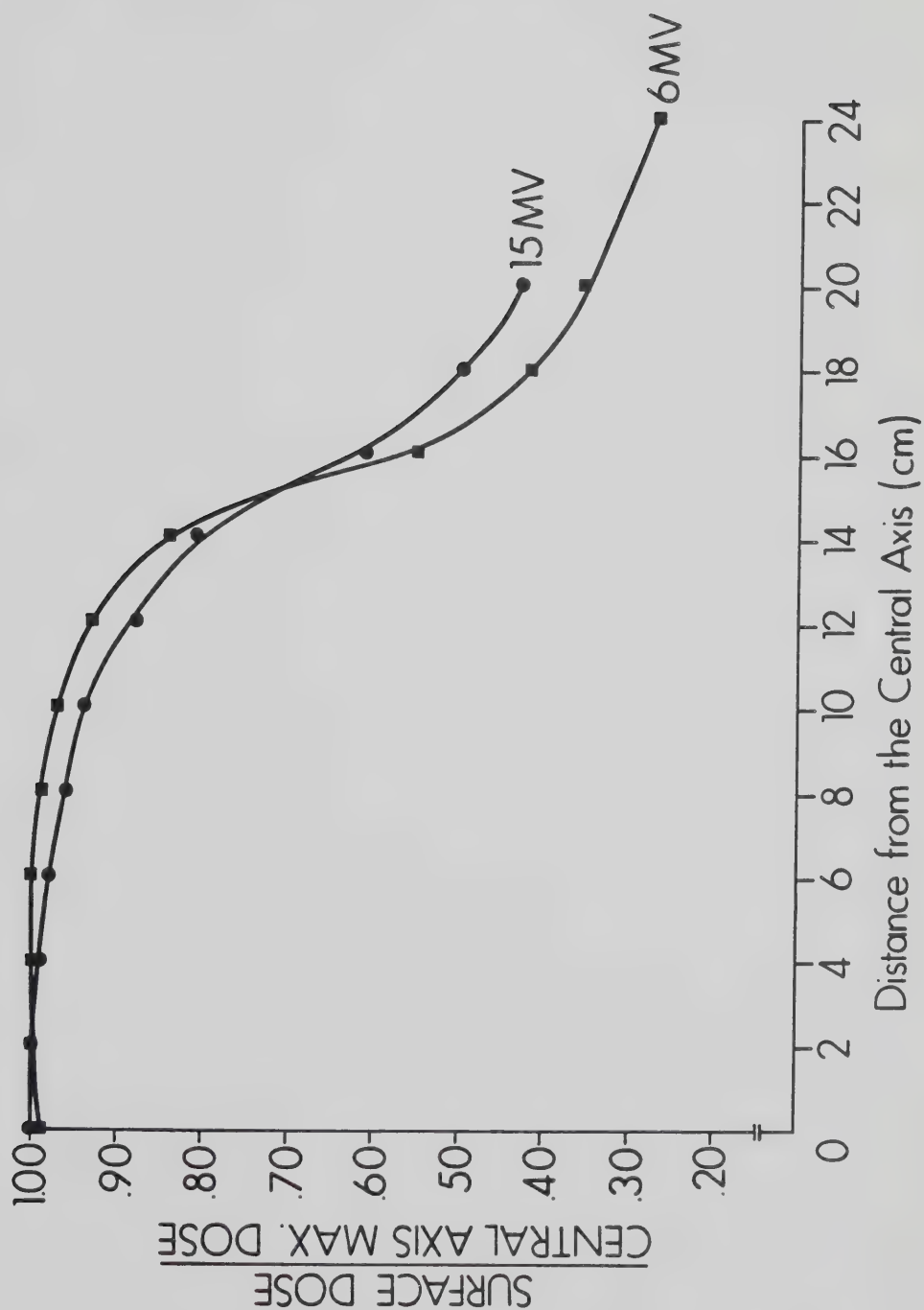


Figure 28. Comparison between 6 MV and 15 MV of the lateral distribution of the surface dose at 100 cm SPD. The lateral distribution is not Gaussian at 6 MV. The field size is 30 cm x 30 cm.



the surface dose of the 6 MV beam near the field edge compared to the 15 MV beam. The lateral distribution at 6 MV is not Gaussian.



## 2.6 Surface Dose Measured for Rectangular Fields

The surface isocentric normalized dose was measured for rectangular and square fields. Both collimator openings were varied by 5 cm increments at 100 cm SPD so that the dose at all such fields between 5 cm x 5 cm and 30 cm x 30 cm were determined. Table 2 illustrates the results.

The surface isocentric normalized dose as measured at SPD = 100 cm depends on which collimator defines the long or short axis. If Field A (upper collimator) is the long axis (lower left hand part of Table 2) the surface dose tends to be greater than if Field B (lower collimator) is the long axis for the same field dimension. For example, the surface isocentric normalized dose at A = 10 cm and B = 25 cm is .106 whereas the dose at B = 10 cm and A = 25 cm is .109.

In general, the larger the field area, the greater the surface dose. If a square and rectangular field have the same area the square field will have the greater surface isocentric normalized dose. For example, if A = 10 cm and B = 10 cm, the surface dose is .071 but if A = 5 cm and B = 20 cm, the surface dose is .063 (if A = 20 cm and B = 5 cm, the dose is .064).

The equivalent square field dose for a rectangular field was determined by plotting the dose as a function of square field width and finding the square field that has the same dose as the rectangular field. Table 2 also lists the results of the equivalent square determination. For large fields (greater than 10 cm x 15 cm) the equivalent square field area is approximately equal to the geometric field area. For example, if A = 20 cm and B = 10 cm, the equivalent square area is  $(13.8 \pm 4)\text{cm} \times (13.8 \pm 4)\text{cm} = (190 \pm 10)\text{cm}^2$  and the



Table 2      Surface Normalized Dose For  
Rectangular Fields

|              |      | Field B (cm) |       |       |       |       |       |
|--------------|------|--------------|-------|-------|-------|-------|-------|
|              |      | 5.0          | 10.0  | 15.0  | 20.0  | 25.0  | 30.0  |
| Field A (cm) | 5.0  | 0.037        | 0.049 | 0.057 | 0.062 | 0.067 | 0.070 |
|              | 10.0 | 0.049        | 0.071 | 0.087 | 0.098 | 0.106 | 0.112 |
|              | 15.0 | 0.057        | 0.088 | 0.109 | 0.125 | 0.138 | 0.147 |
|              | 20.0 | 0.064        | 0.100 | 0.126 | 0.146 | 0.161 | 0.173 |
|              | 25.0 | 0.069        | 0.109 | 0.139 | 0.163 | 0.181 | 0.195 |
|              | 30.0 | 0.072        | 0.116 | 0.150 | 0.176 | 0.196 | 0.211 |

Equivalent Square Fields For The  
Surface Dose

|              |      | Field B (cm) |      |      |      |      |      |
|--------------|------|--------------|------|------|------|------|------|
|              |      | 5.0          | 10.0 | 15.0 | 20.0 | 25.0 | 30.0 |
| Field A (cm) | 5.0  | 5.0          | 6.6  | 7.7  | 8.5  | 9.1  | 9.5  |
|              | 10.0 | 6.6          | 10.0 | 11.9 | 13.5 | 14.7 | 15.5 |
|              | 15.0 | 7.7          | 12.0 | 15.0 | 17.3 | 19.1 | 20.4 |
|              | 20.0 | 8.7          | 13.8 | 17.5 | 20.0 | 22.5 | 24.2 |
|              | 25.0 | 9.3          | 15.0 | 19.3 | 22.7 | 25.0 | 27.3 |
|              | 30.0 | 9.8          | 16.0 | 20.9 | 24.7 | 27.5 | 30.0 |





geometric area is  $(20.0 \pm .1) \text{ cm} \times (10.0 \pm .1) \text{ cm} = (200 \pm 3) \text{ cm}^2$ .

However, for small fields the equivalent square field area is less than the geometric field area. The surface equivalent square field is very different from the equivalent square field at  $d_{\text{max}}$ .



## 2.7 Penetration Curves Outside the Field

### 2.7.1 Transmission Through the Collimators

The transmission of primary photons through the collimators was studied by placing a Capintec 0.6 cc cylindrical ion chamber (Model PR-06C) at  $d_{\max}$ . A measurement was taken at the central axis with a field size of 20 cm x 20 cm. All subsequent readings were normalized to this measurement.

Transmission measurements were made with one or both collimator sets closed. Figures 29a) to d) illustrate the position of the upper and lower collimators and the relative dose received. The percentage transmission at the field boundary through one collimator is about 1% and about 0.1% through both collimators.

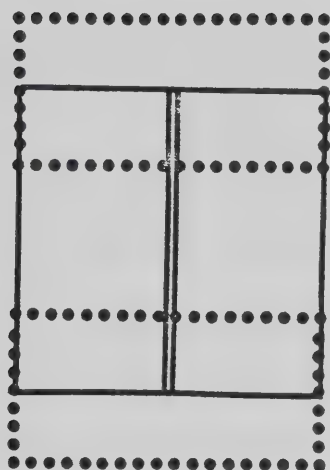
### 2.7.2 Determination of the Penetration Curves Outside the Field

By definition, except for transmission through the collimators, the primary photon dose outside the field boundary is zero. Only contamination electrons and scattered photons can contribute to this dose. This was studied experimentally.

Nilsson and Brahme have shown that the scattered photon spectrum at the field edge is almost identical to the photon spectrum at the central axis for a 20 cm x 20 cm field for nominal beam energies of 6 MV and 21 MV. It is unlikely that the electron contamination spectrum changes appreciably between the center and edge of the field.

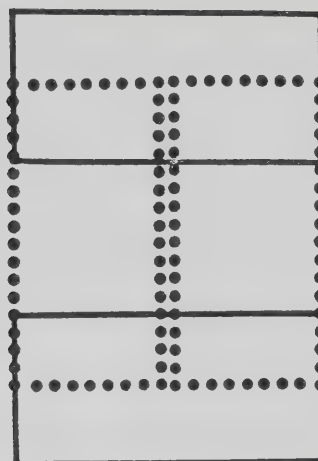
In order to get as close as possible to the field





a)

PT = 1.1

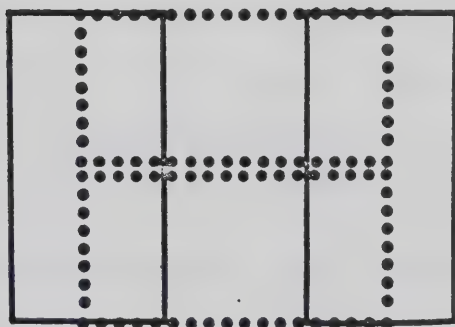


b)

PT = 1.0

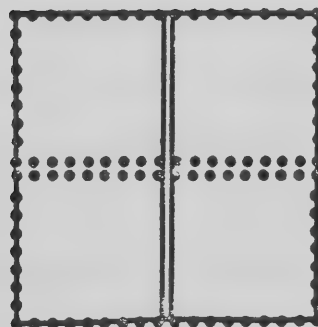
PT = 1.0

c)



PT = 0.1

d)



Percent Transmission = PT

..... Upper      ————— Lower Collimator

Figure 29. Transmission measurements on the Mevatron -20. a) Lower collimator closed, upper open; b) Upper collimator closed, lower open with collimator assembly rotated 90°; c) As in b) but collimator assembly not rotated; d) Both collimator sets closed.



boundary, the thin-window parallel-plate probe was placed near the edge of the phantom (see Figure 30). The phantom was tilted at an angle of  $8.5^{\circ}$ \* so that the position of the phantom surface would not move closer or further from the field boundary with the addition of build-up layers. This also reduced the number of particles incident at oblique angles upon the phantom at oblique angles.

Figure 31 illustrates the penetration curve 3 cm outside a 30 cm x 30 cm field. The penetration curve has a peak at a shallow depth (1-2 mm) then falls off rapidly at depths greater than 1 cm. The curve has a relatively slow fall-off at depths beyond about 2 cm. The general shape of the curve agrees with the work of Scrimger and Kolitsi (30) for 8 MV x-rays.

The penetration curve 3 cm outside the field was measured at 6 MV for the same field size (30 cm x 30 cm) and SPD (100 cm) as the comparable experiment carried out at 15 MV. The phantom was again tilted at  $8.5^{\circ}$ . Figure 32 illustrates a rapid decrease in the penetration curve at shallow depths with a levelling out at greater depths. The maximum dose is at the surface at 6 MV rather than at a shallow depth beneath the surface. This suggests the dose at shallow depths is again due mainly to contamination electrons while the dose at deeper depths is due to scattered photons.

The relative dose in the plateau region ( $d_{\text{max}}$ ) for both the 6 MV and 15 MV curves outside the field is approximately 0.3 of the maximum dose received.

\* The angle of tilt =  $\tan^{-1} \frac{\text{Field Width}}{2 \text{ SPD}}$





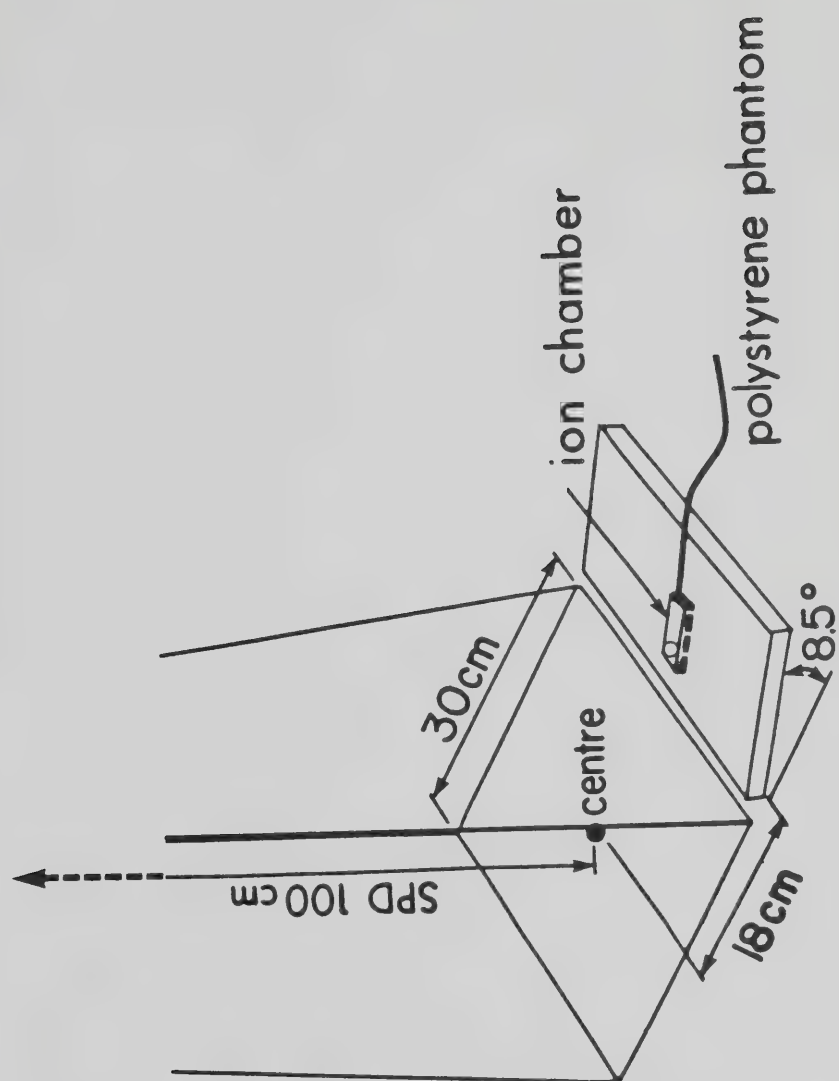


Figure 30. Diagram of the experimental arrangement to determine the penetration curve outside the field.



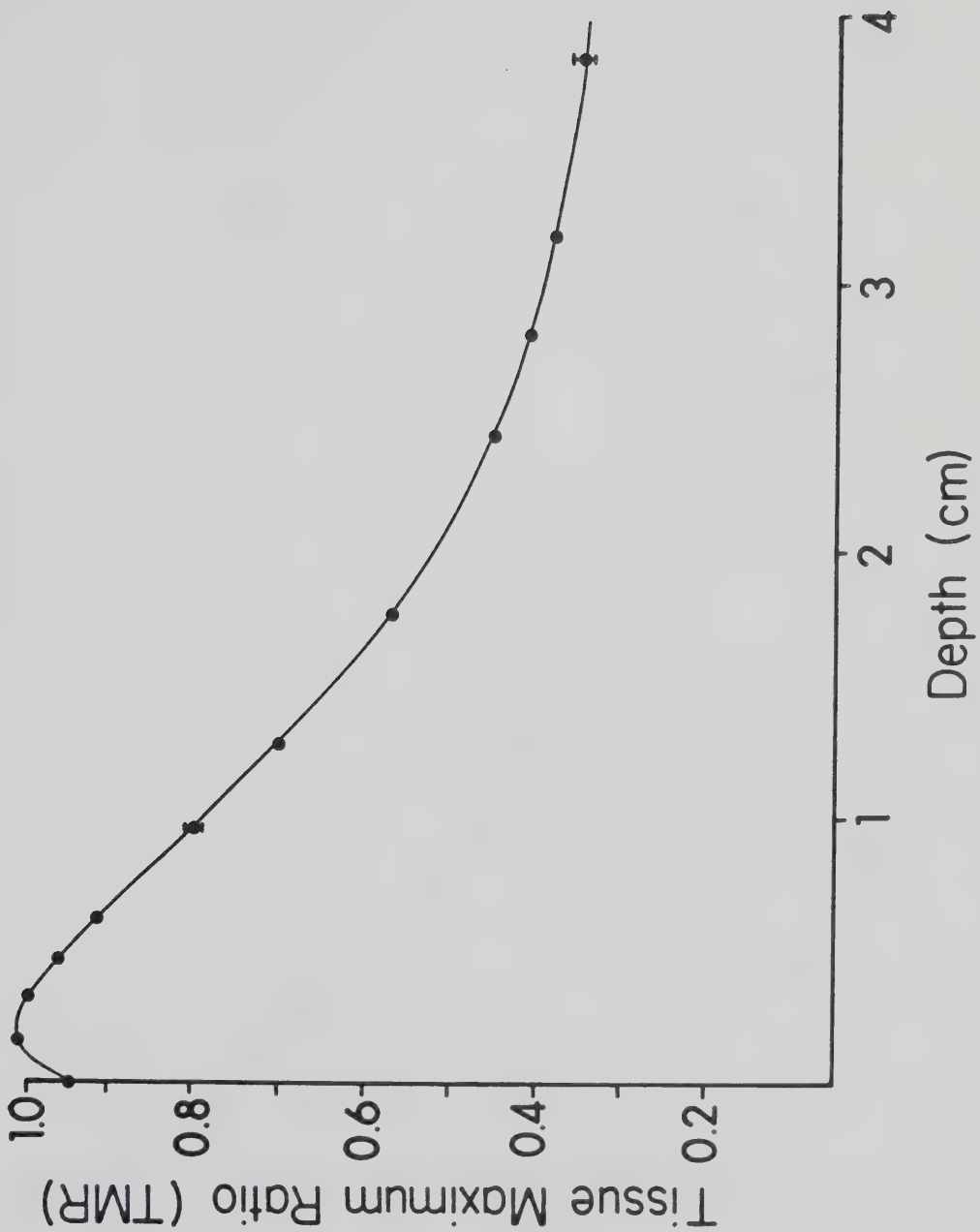


Figure 31. Penetration curve at 15 MV obtained 3 cm outside of a 30 cm x 30 cm field (see Figure 30 for the experimental arrangement).



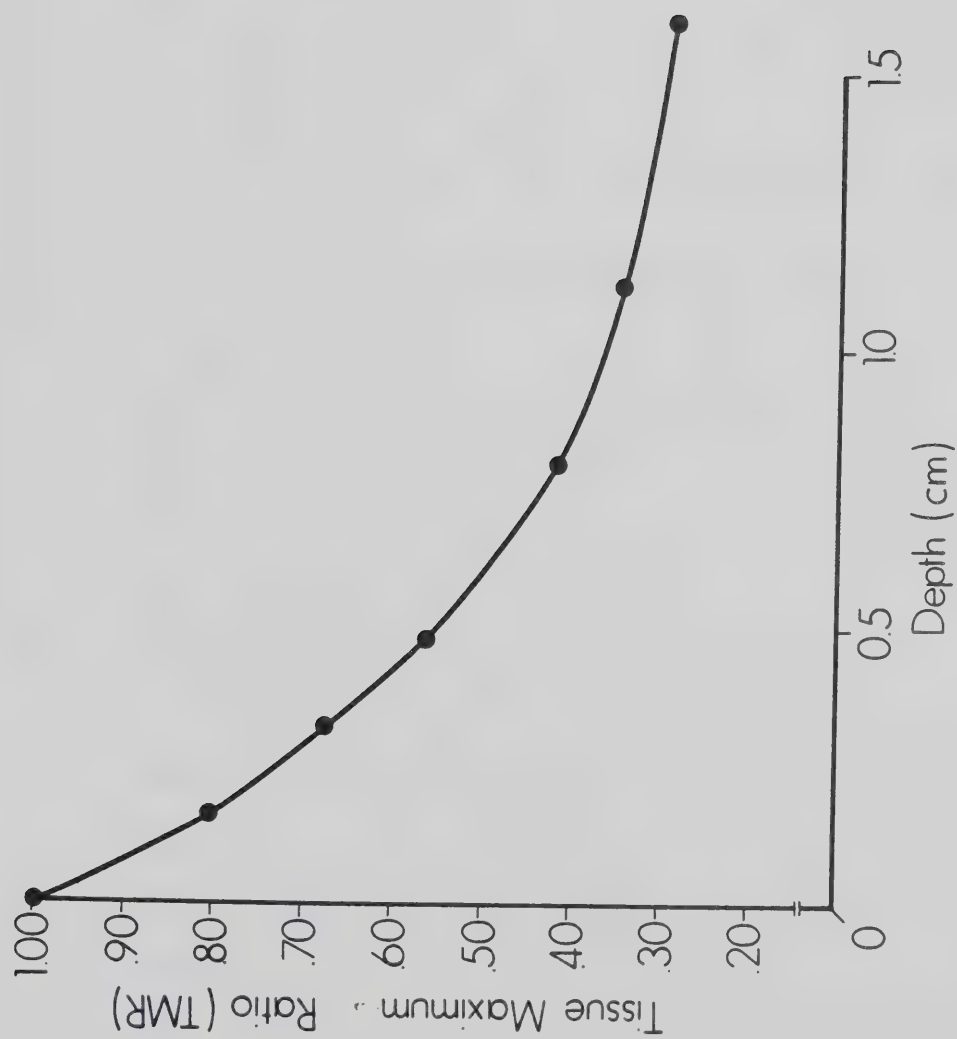


Figure 32. Penetration curve at 6 MV obtained 3 cm outside of a 30 cm x 30 cm field.



## 2.8 Increase in Dose with Increasing Field Width

### 2.8.1 Measurement of the Stem Effect

Exposure to ionizing radiation may cause a spurious signal attributable to the ion chamber cable such as a leakage current which is mistaken for ionization in the chamber volume. These phenomena are called the stem effects. A stem effect, if present, should increase with increasing field size. The manufacturer's claim that the stem effect for their thin window ion chamber is less than 1%.

The stem effect was measured by exposing the chamber at  $d_{\max}$  in a phantom to a rectangular field as wide as the chamber volume and as long as the phantom. One measurement was taken with the cable completely in the field and another with the cable completely outside the field. The stem effect was found to be less than 0.5%.

### 2.8.2 Increase in Dose with Increasing Field Width

A number of authors (15-21,25,28,29,31-35) have commented on the dependence of the surface dose on the square root of field width both with and without accessories present in the beam. Many of these authors calculated TMR surface doses, in other words, normalized the surface dose at each field size to the dose at  $d_{\max}$  for the same field size. However, since the dose at  $d_{\max}$  increases with field size (as expressed by the output factor), such a plot would not unambiguously express the dependence of surface dose on field size.





A more general form of the isocentric normalized dose can be used to more clearly describe the dose dependence on field size. The ionization readings at some field size and a given source-to-probe distance are normalized to the maximum ionization readings (at  $d_{\max}$ ) obtained at a field size of 10 cm x 10 cm at the same source-to-probe distance. This quantity will be called the normalized dose, ND. It is given by:

$$ND = \frac{\text{Dose delivered to a point at an arbitrary } d, \text{ SPD, field size}}{\text{Dose delivered to } d_{\max} \text{ at the same SPD at a field size of 10 cm x 10 cm}} \quad (2.8.1)$$

The normalized dose is equal to the isocentric normalized dose at 100 cm SPD.

The tissue maximum ratio is directly proportional to the normalized dose. The constant of proportionality is the output factor. The relationship is given by:

$$ND(d, SPD, W) = \text{Output Factor}(SPD, W) \times TMR(d, SPD, W) \quad (2.8.2)$$

where W represents the field size.

The normalization reading (the denominator of Equation 2.8.1) is not field size dependent so ND clearly illustrates dependence of the reading (the numerator of Equation 2.8.1) on field size.\*

\* Data acquisition is simpler using the concept of normalized dose. Only one set of measurements at  $d_{\max}$  for a field size of 10 cm x 10 cm need be taken. A set of readings at  $d_{\max}$  at all field sizes is not required. If an output factor curve has been determined, the TMR value may be obtained, if desired, using Equation 2.8.2.



The normalized dose, ND, for a variety of conditions at  $d=0$  is plotted as a function of field width in Figure 33. Field width is defined as the square root of field area for square fields. Under these conditions, at 15 MV there is a linear increase in the surface dose with respect to field width. Note that either decreasing the SPD or placing the accessories in the field increases the slope of the curve. Since the surface dose for any given field size is proportional to the slope of the line, the slope is also a measure of the electron contamination, but with the advantage that it is not dependent on the field width.

A small phantom was placed completely within the field so that an increase in detected signal due to increasing field size could only be attributed to beam contamination. To obtain the dose as a function of depth for as many field widths as possible, the phantom lateral dimensions were kept as small as possible (i.e. 10 cm x 10 cm) which in turn dictated a minimum field size used in the determination of the contamination depth-dose curve of 15 cm x 15 cm. The maximum square field size attainable for the machine studied was 30 cm x 30 cm. These field sizes defined the range of the study.

The dose as a function of field width was measured for a number of depths with the limited polystyrene phantom of the type illustrated in Figure 34. Since there was build-up material on top of the ion chamber, it could not be assumed that all of the contamination



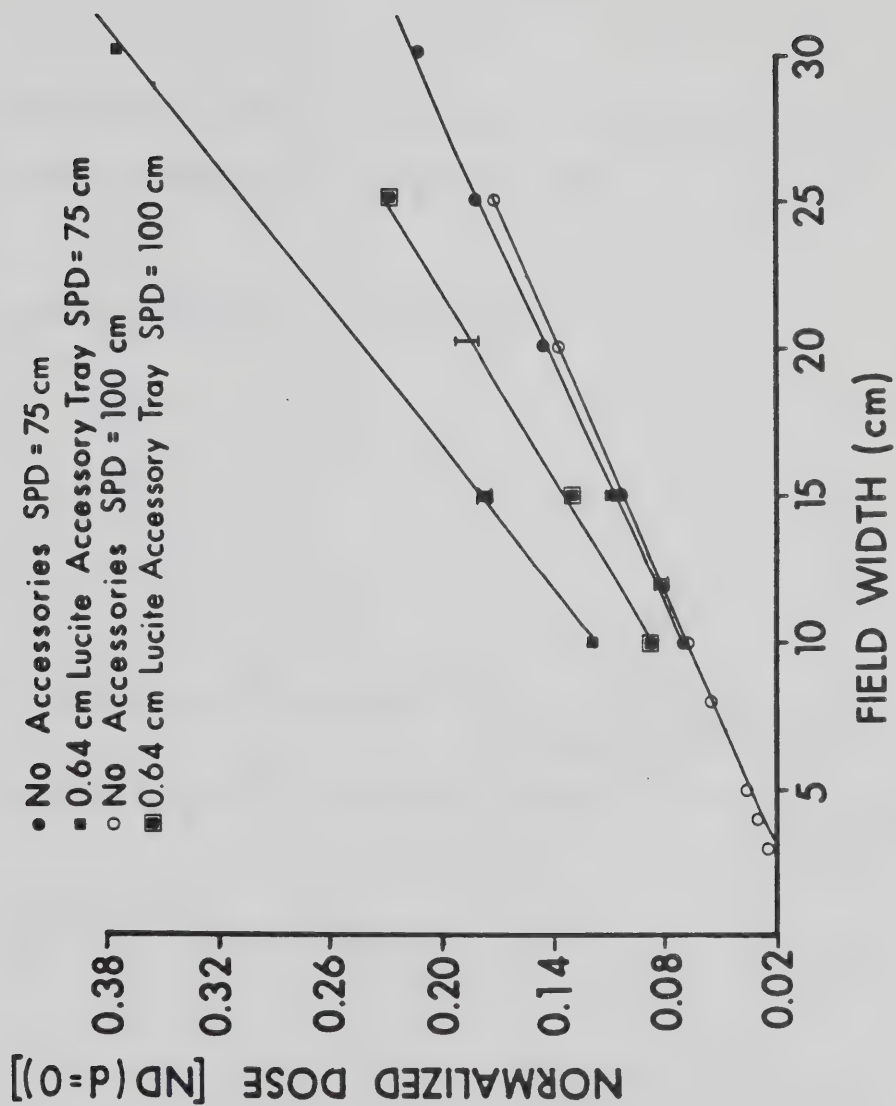


Figure 33. Linearity of the surface dose with respect to field width under a variety of conditions at 15 MV.



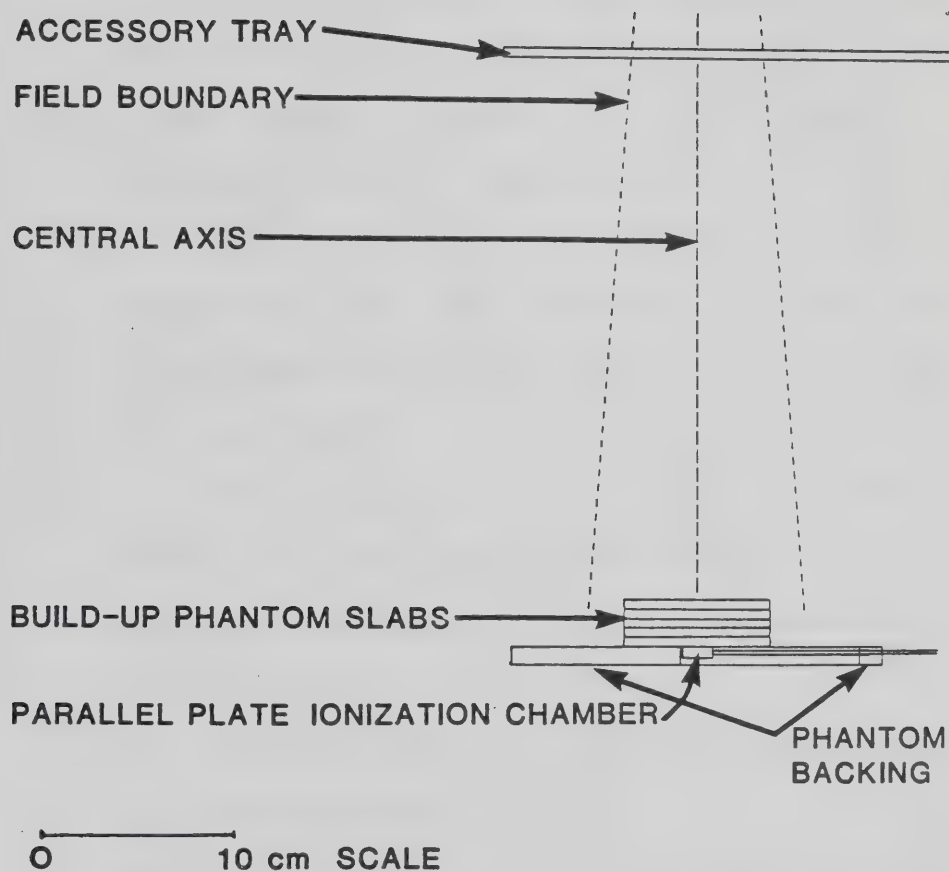


Figure 34. Diagram of the experimental arrangement to measure the increase in contamination with increasing field width. The phantom slab cross-section was  $100 \text{ cm}^2$  and the slabs were always within the field boundary.





contributing to the dose was due to electrons.

Figure 35 illustrates that at 100 cm SPD for various depths in the phantom less than  $d_{\max}$  there is a linear dependence of normalized dose on field width. Qualitatively, the slope at shallow depths is greater than the slope at deeper depths. As has been discussed for the dose at the surface, the slope of normalized dose versus field width is a measure of the magnitude of the contamination penetrating to the depth specified. Therefore, there is a greater magnitude of contamination at shallow depths than at deeper depths.

Figure 36 is a graph of normalized dose versus field width at 75 cm SPD for various depths into the limited phantom. The linear fit at 75 cm SPD is nearly as good as that obtained at 100 cm SPD.

Normalized dose measurements were made on the 15 MV accelerator at field sizes of 15 cm x 15 cm, 20 cm x 20 cm and 25 cm x 25 cm at 100 cm SPD when Lucite accessories of 0.64 cm and 3.18 cm were placed in the field at the accessory tray position. There is approximately a linear increase in dose as a function of field width with a 3.18 cm accessory in place (see Figure 37).

Figure 38 is a graph of normalized dose versus field width for various depths at 100 cm SPD for the 6 MV accelerator. Like the curves at 15 MV, the linear fit is good.



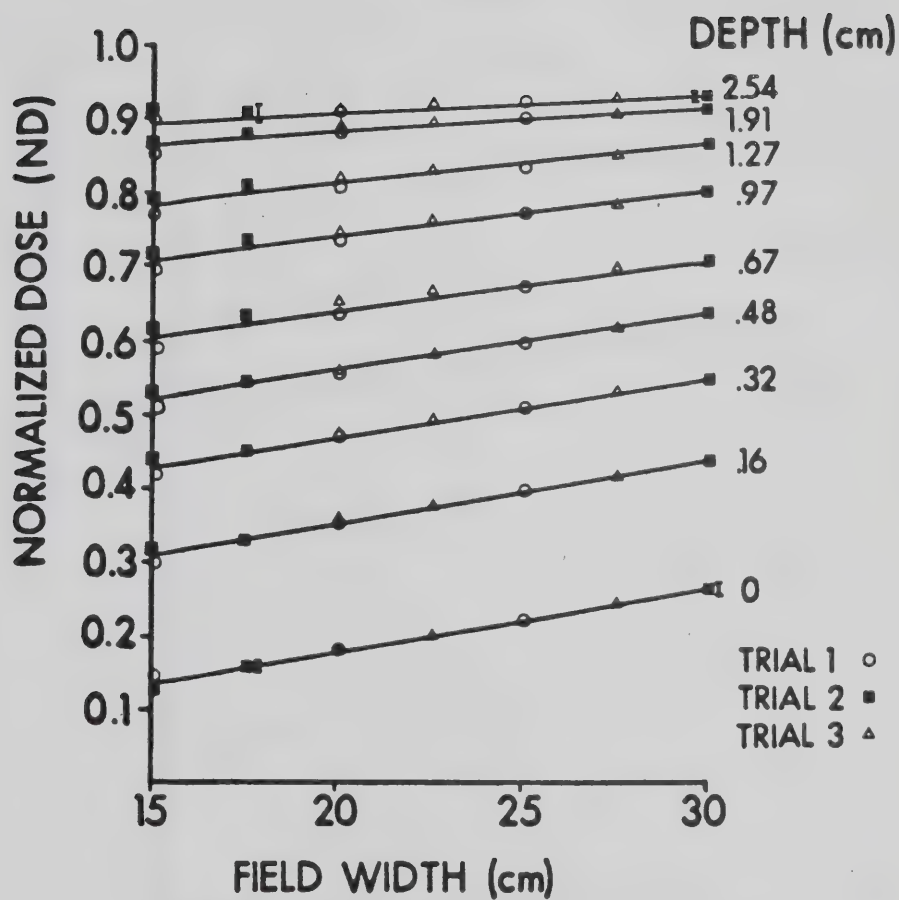


Figure 35. The increase in normalized dose with respect to field width for various depths beneath the surface of the phantom in an open field at 100 cm SPD for the 15 MV beam. The increase can only be attributed to contamination because the phantom was completely within the field boundary (see Figure 34).



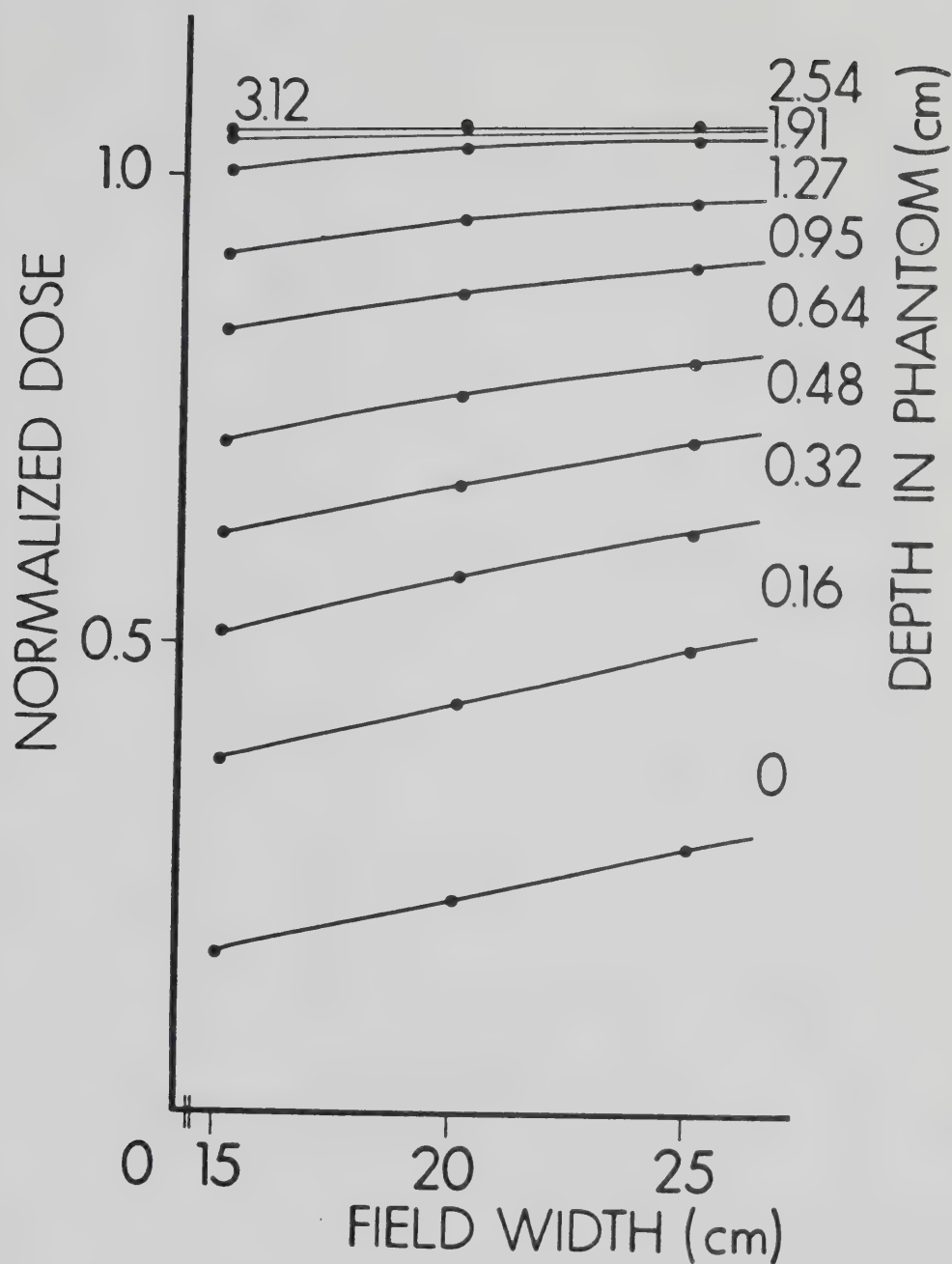


Figure 36. The increase in normalized dose with respect to field width for various depths beneath the phantom surface in an open field at 75 cm SPD at 15 MV.



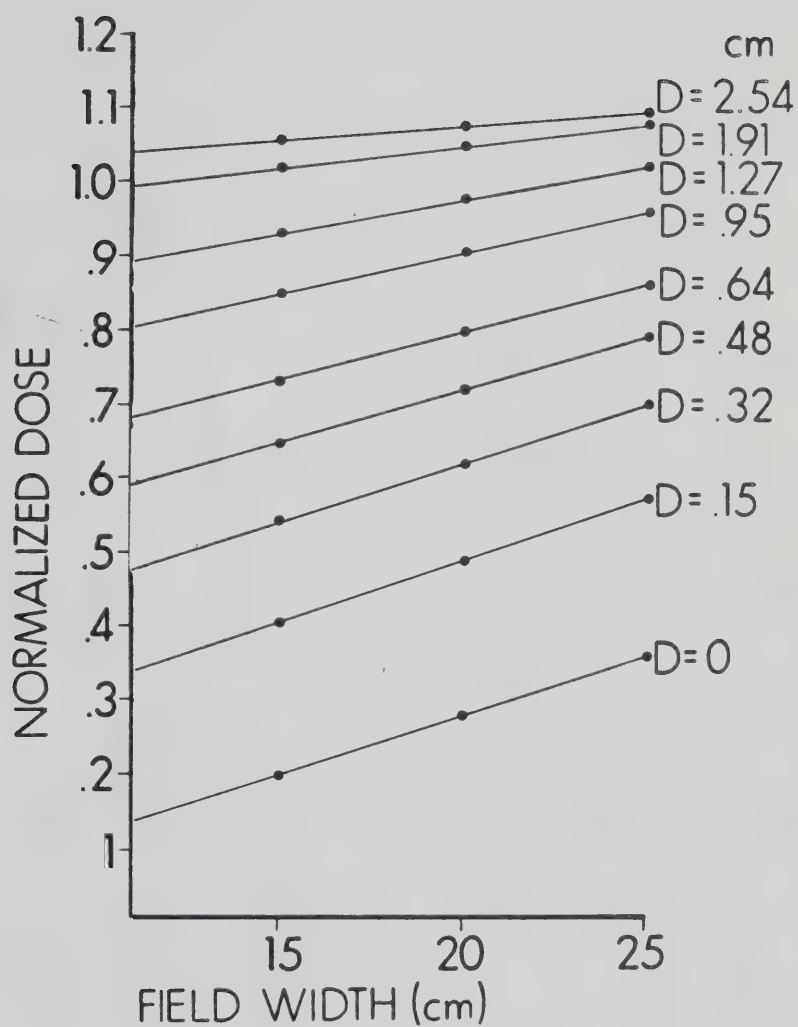


Figure 37. The increase in normalized dose at 15 MV with respect to field width for various depths beneath the phantom surface with the probe at 100 cm from the source with a 3.18 cm accessory in place.





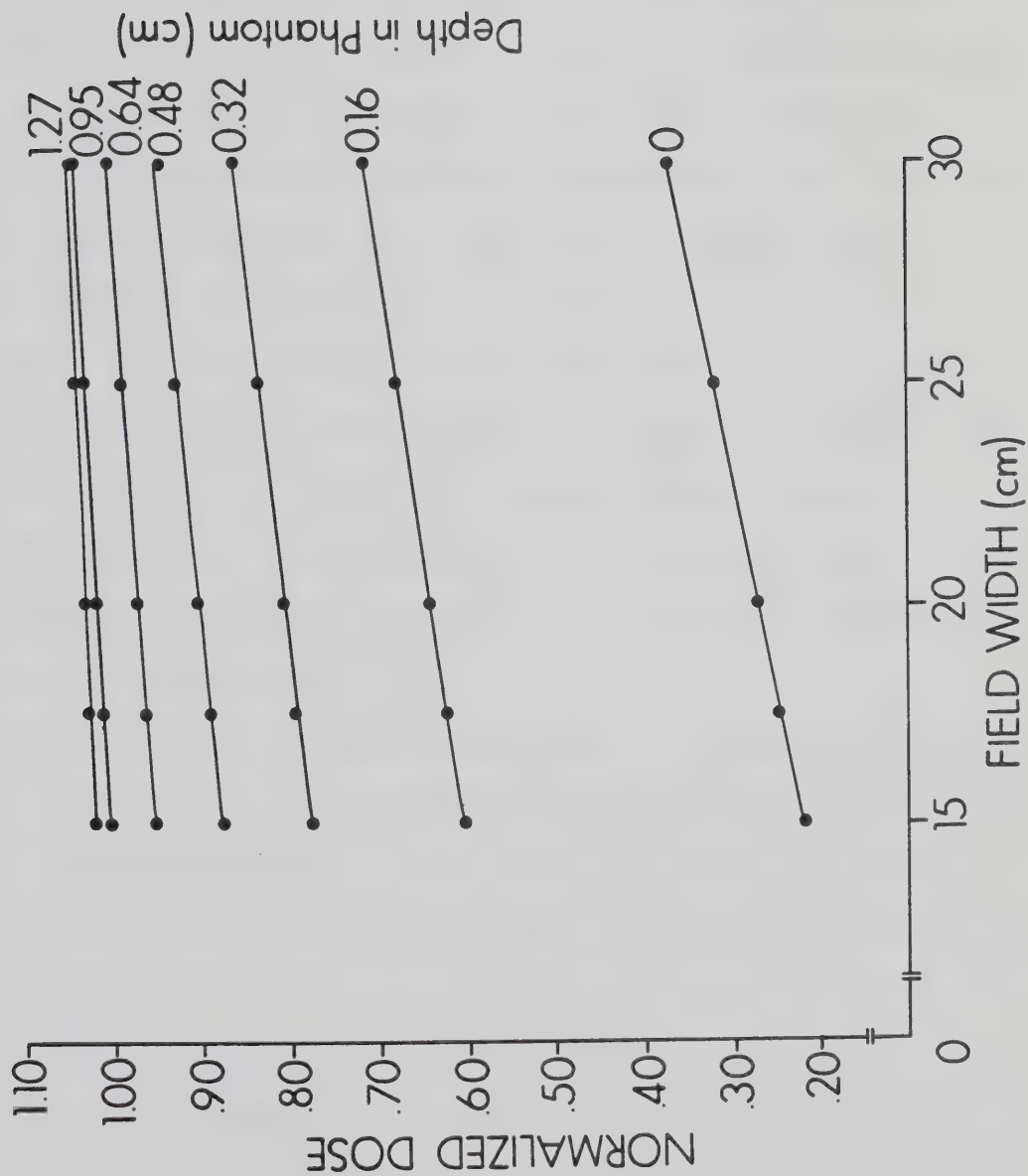


Figure 38. The increase in normalized dose with respect to field width for various depths beneath the phantom surface in an open field at 100 cm SPD at 6 MV.



## 2.9 Determination of the Amount of Photon Backscatter from the Phantom

The surface dose is the sum of backscatter from the phantom and contamination produced outside the phantom. By the definition of phantom generated radiation (Section 1.5), backscatter is part of this component of the beam. Backscatter photons are any photons scattered through  $90^\circ$  or more so that they have a sense in the direction component normal to the phantom that is opposite to the sense of the primary photons. A determination of the amount of backscatter dose is essential in order to isolate the dose due to contamination at the surface.

The amount of backscatter due to photons generated in the phantom was measured. The thin window parallel-plate chamber was first placed on a thick slab of polystyrene ( $>20$  cm thick) which had a cross-section larger than any field size used. The surface dose was measured for field sizes between 3.5 cm x 3.5 cm and 20 cm x 20 cm and source-to-probe distances between 80 cm and 120 cm. The normalized dose, N.D. (Equation 2.8.1) was obtained.

The full phantom was replaced with various thicknesses of backscatter. The thinnest layer was approximately  $1.5 \text{ mg/cm}^2$  and the thickest layer was  $480 \text{ mg/cm}^2$  of unit density material. There was virtually no difference between the readings at  $1.5 \text{ mg/cm}^2$  and  $480 \text{ mg/cm}^2$  indicating that there is little contribution from charged particles set in motion near the surface of the phantom which scatter backwards. The normalized dose difference was obtained between the normalized doses with full phantom and with  $1.5 \text{ mg/cm}^2$ . The normalized dose difference represents the normalized dose due to backscatter photons. The results are shown in Figures 39 and 40 as a function of field width for 6 and 15 MV at various source-to-probe distances.



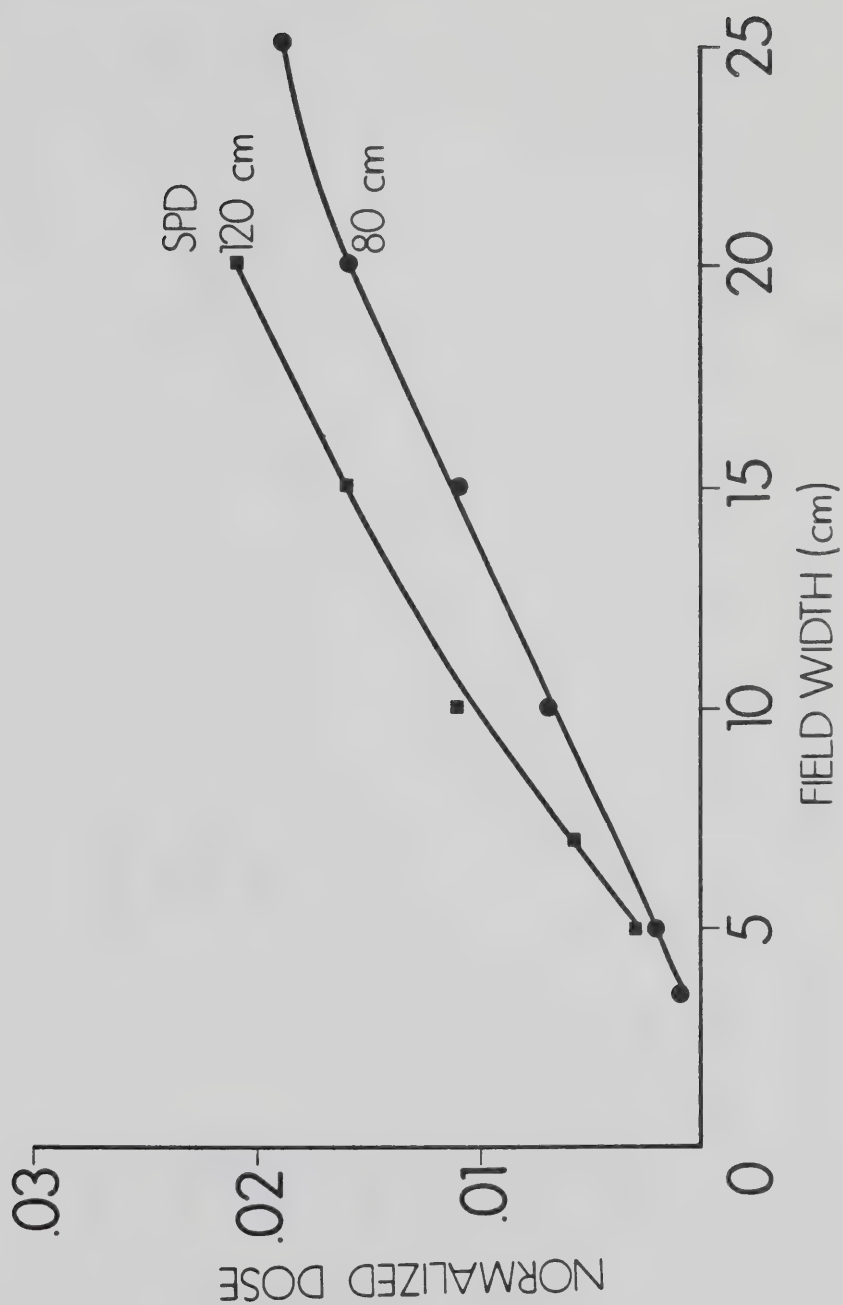


Figure 39. The normalized dose due to backscatter photons as a function of field width for source-to-probe distances of 80 cm and 120 cm at 6 MV.



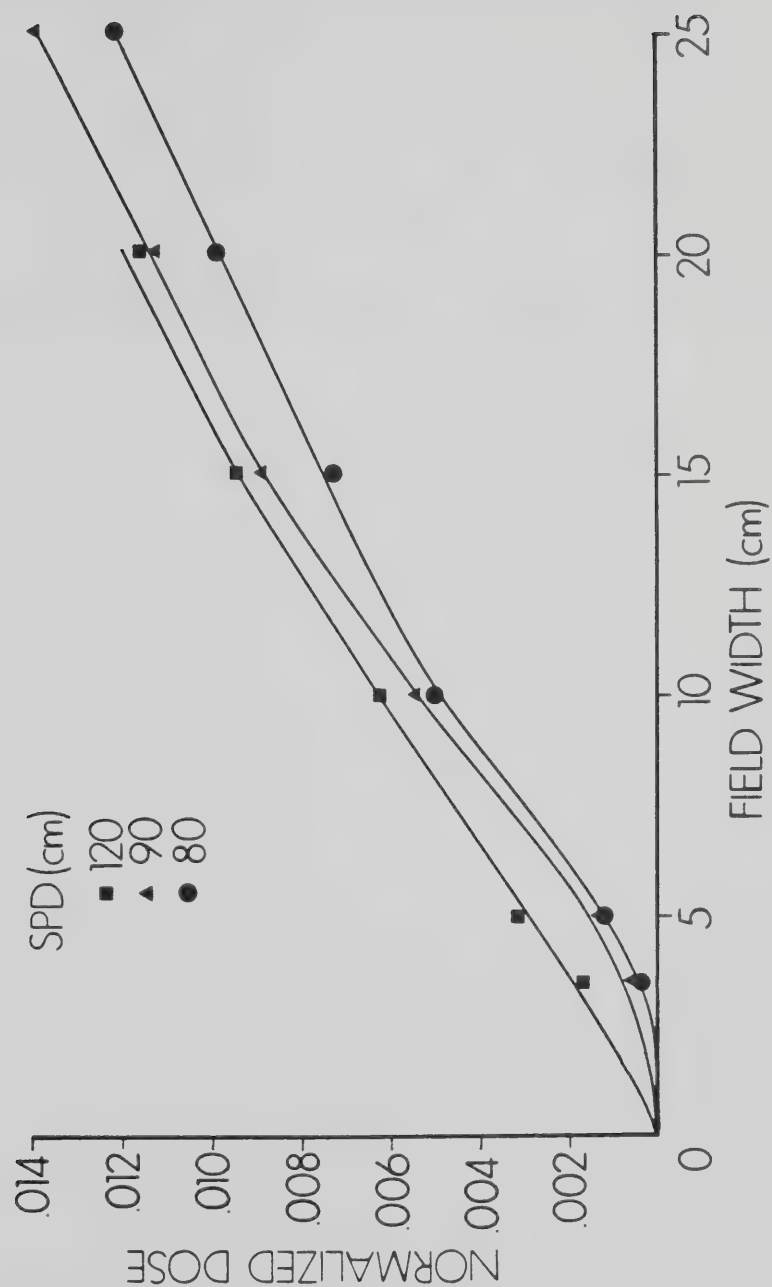


Figure 40. The normalized dose due to backscatter photons as a function of field width for source-to-probe distances of 80 cm, 90 cm and 120 cm at 15 MV.





Between field widths of 5 cm and 20 cm, the amount of backscatter increases with field width for all source-to-probe distances. The amount of photon backscatter at 6 MV is about 50% greater than at 15 MV for the same field width and source-to-probe distance. At all field sizes and source-to-probe distances for both accelerators, the amount of dose due to photon backscatter was much less than the amount of dose due to contamination electrons at the surface of the phantom.



## 2.10 Sweeping Electrons from the Field Using a Permanent Magnet

### 2.10.1 Determination of the Field Distribution of the Magnet

A survey of the literature (41, 42, 43, 44, 45) has shown that the central field magnetic strength must be somewhere between 1 and 3 kG in order to sweep a 10 cm x 10 cm field free of contamination electrons produced by photons in the energy range of 4 MV to 25 MV when the source-to-probe distance, SSD, is about 85 cm.

The magnetic field strength distribution of a discarded magnetron magnet was determined using a Rawson-Lush Rotating Coil Gaussmeter Type 820 Probe and a Type 501 Indicator manufactured by Rawson Electrical Instruments Co. of Cambridge, Massachusetts.

The uncertainty in the strengths at maximum field strength was  $\pm 30$  G. The magnet was a permanent type with the pole gap fixed at 7.5 cm. The maximum central field was found to be 1340 G. Figure 41 illustrates the measured magnetic field distribution. The central distribution was mapped every 2 cm until the magnetic field fell to 60 G.

### 2.10.2 Verifying Electrons are Swept by the Magnet

If the amount of bending is small, to a first approximation, the electrons will travel along the central axis in and near the magnet. The angle of deflection (in radians) for an electron travelling a distance,  $d$ , in a uniform magnetic field is given by (see Figure 42):

$$\phi_{\text{deflect}} = \frac{d}{r} = \frac{deBc}{m_0 c^2} \frac{1}{\left[ \left( (T + m_0 c^2) / m_0 c^2 \right)^2 - 1 \right]^{1/2}} \quad (2.10.1)$$



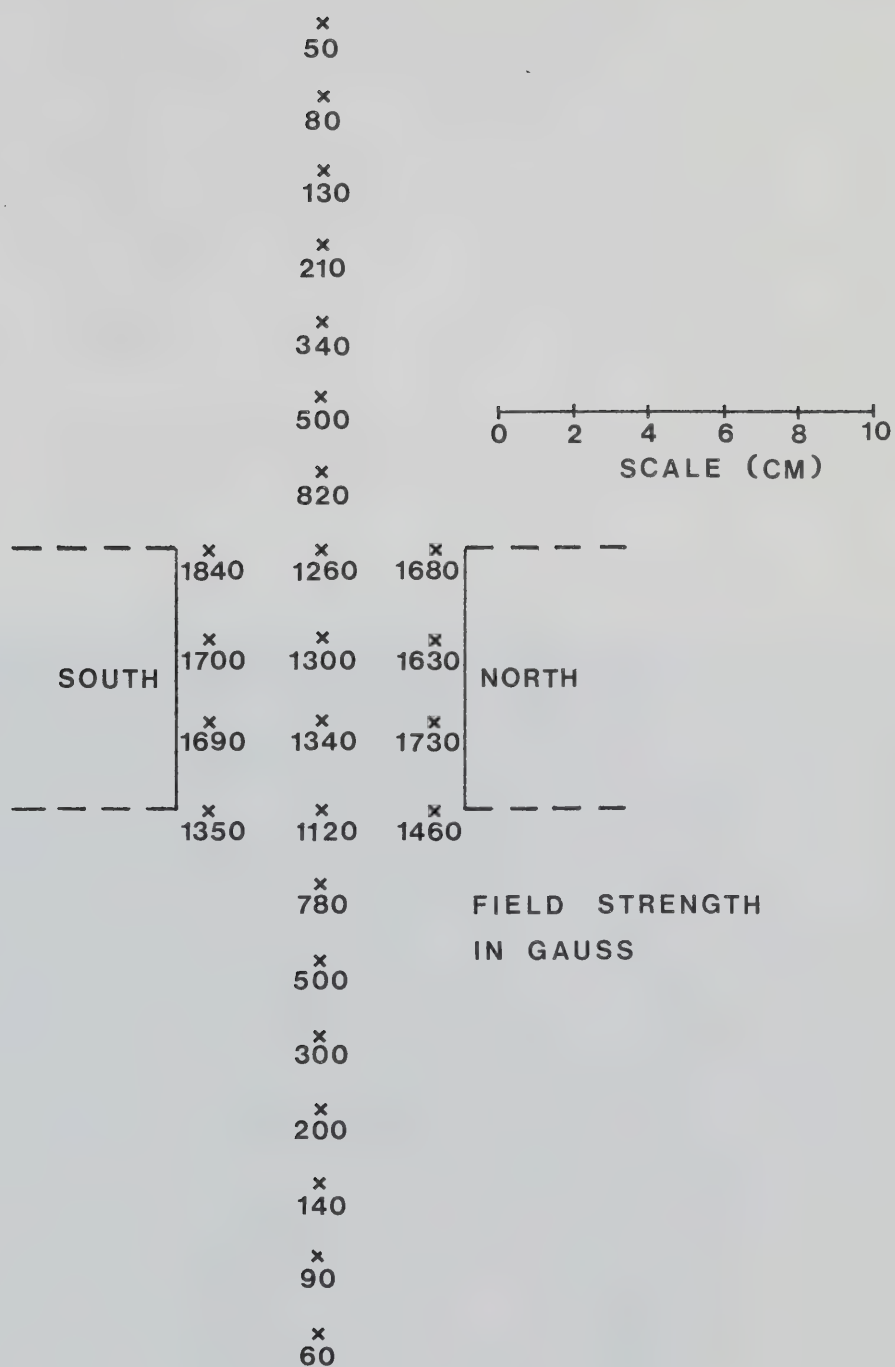
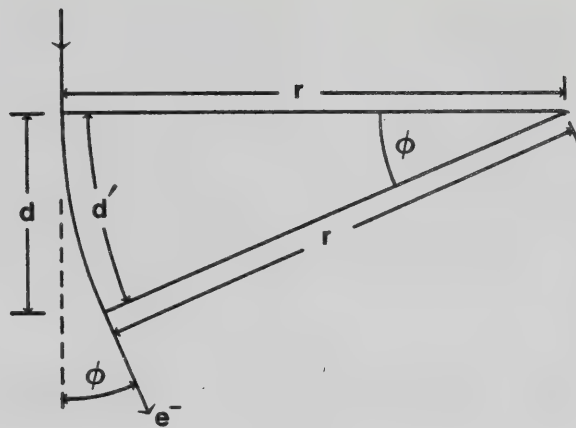


Figure 41. The measured magnetic field distribution along the direction of the photon beam.





Constant Magnetic Field  
 Direction Out Of The Plane  
 If  $\phi$  Is Small,  $d \approx d'$

Figure 42. The angle of deflection of an electron in a uniform magnetic field (above) and the measured deflection of 18 MeV electrons (below).





The above equation uses the definition of a radius of curvature (Equation 1.4.1). The total amount of deflection can be found by summing the amount of angular deflection occurring along the central axis:

$$\left[ \phi_{\text{deflect}} \right]_{\text{total}} = \frac{ec}{m_0 c^2} \frac{1}{\left[ (T+m_0 c^2)/m_0 c^2 \right]^2 - 1}^{\frac{1}{2}} \sum d_i B_i \quad (2.10.2)$$

The field,  $B_i$ , was measured every 2 cm so  $d_i$  is a constant ( $d_i = \text{const} = 2 \text{ cm}$ ). The Mevatron -20 can produce mono-energetic 18 MeV electrons. The electron contamination of the 15 MV beam will not have kinetic energies this high so that if the 18 MV beam can be deflected then the electron contamination can also be swept. The amount of deflection predicted by Equation 2.10.2 for 18 MeV electrons in the measured magnetic field distribution is approximately  $17^\circ$ .

The magnet was mounted 65 cm from the source, so the largest field size (measured at SPD=100 cm) that can be swept is 10 cm x 10 cm. This defines a central axis angle of  $2.9^\circ$ . Clearly, this simple theory predicts enough deflection will occur.

The analysis was verified semi-qualitatively by experiment. A sheet of film (Kodak XV-2) was placed parallel to a beam of electrons. An equal amount of exposure was delivered with an open electron applicator



with and without the magnet beneath the applicator. Figure 42 illustrates the results. The angle of deflection between the image of the beams is about  $20^{\circ}$ .

The deflection of contamination electrons was directly verified by placing a half cylinder of film beneath the magnet. Figure 43 illustrates the setup. The contamination electrons produced a broad hazy patch on the film (see Figure 44). The width of the image increased as a function of angle swept. This is to be expected because the amount of bending and the amount of scatter increases with decreasing electron energy. The overexposed central patch is mainly due to photons. Transmission through the collimator can be discerned. There is no direct evidence of positron contamination which would be deflected in the opposite direction.



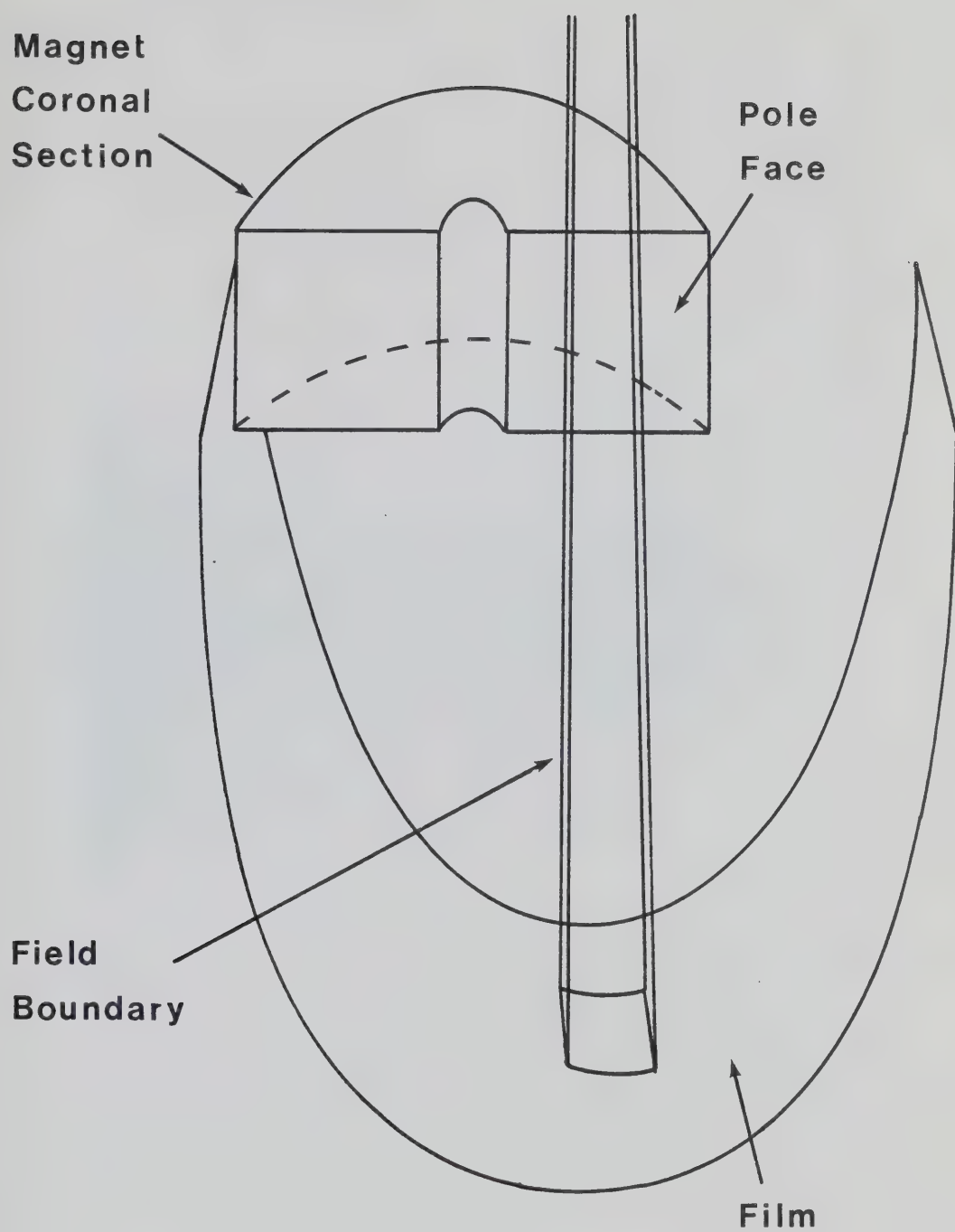


Figure 43. The set-up to verify that contamination electrons were being swept from the field of the 15 MV beam.



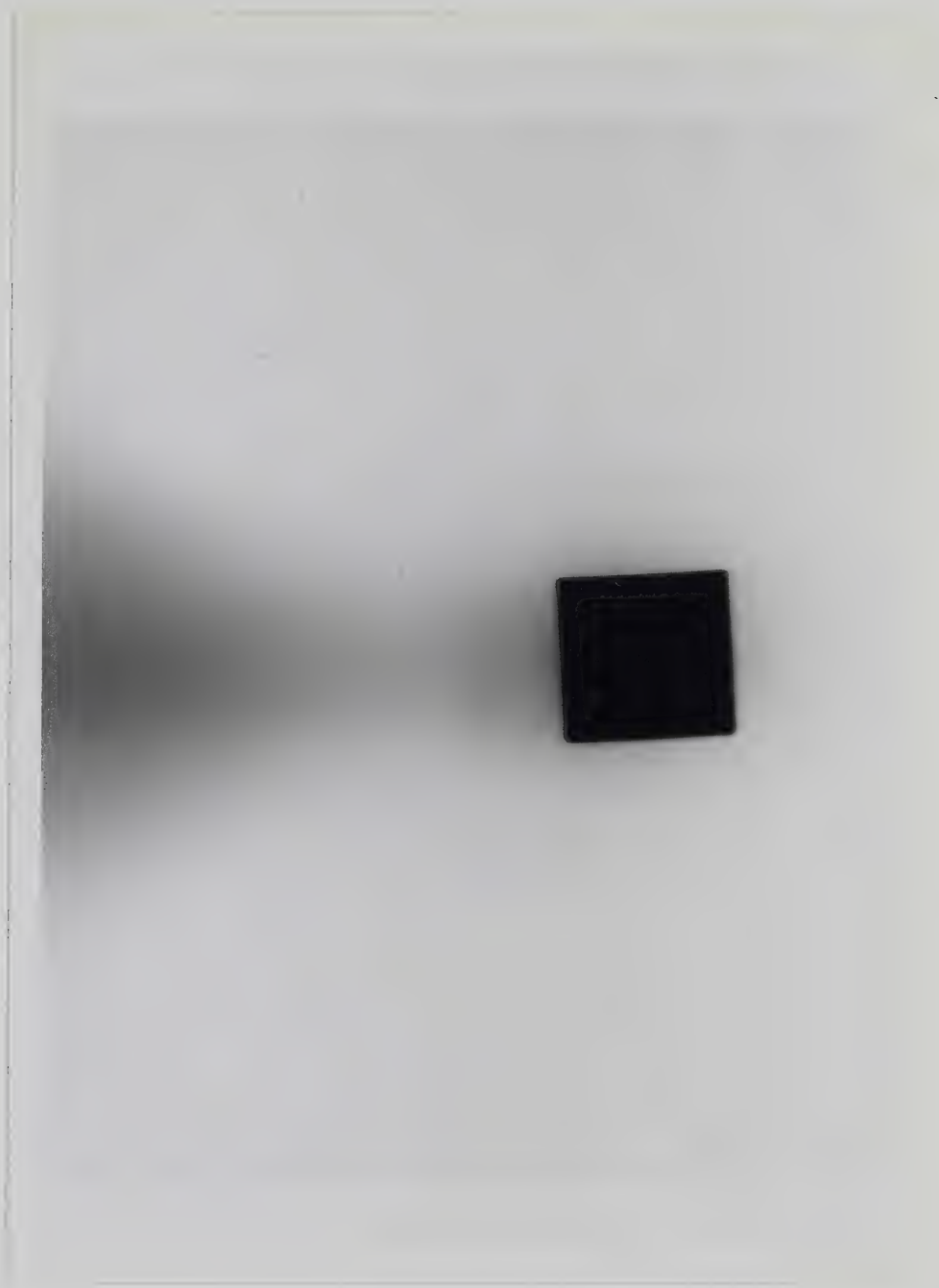


Figure 44. Image of the swept electron contamination.





### 2.10.3 The Surface Dose With and Without the Magnet in Place

The magnet was mounted on a holder so that it could be placed just beneath the accessory holder position. The holder had a square hole cut in it enabling a 10 cm x 10 cm beam to pass through without interacting with it. A photograph of the magnet attached to its holder is shown in Figure 45. Figure 46 shows the magnet mounted from the accessory holder position.

With the magnet in place the electron contamination produced between the target and magnet is swept from the beam. The surface dose under this condition is due to electron contamination produced between the magnet and phantom and photon backscatter produced from the phantom. Since air is the only material in the beam between the magnet and phantom, the electron contamination with the magnet in place is produced by interactions of the photon beam with air between the magnet and phantom.

The dose was measured at the surface of a full phantom (>20 cm thick and with a cross-sectional area greater than the width of the beam). The measurements were taken under various conditions of field size and SPD and presence of accessories. The small magnet pole separation meant that the target field could be no greater than 10 cm x 10 cm.

Figure 47 illustrates the dependence of the normalized dose at the surface, when the magnet is in place, on field width for various accessory configurations at an SPD of 100 cm. The maximum doses used to normalize these curves





Figure 45. The magnet attached to its holder.





Figure 46. The magnet mounted from the accessory holder position.



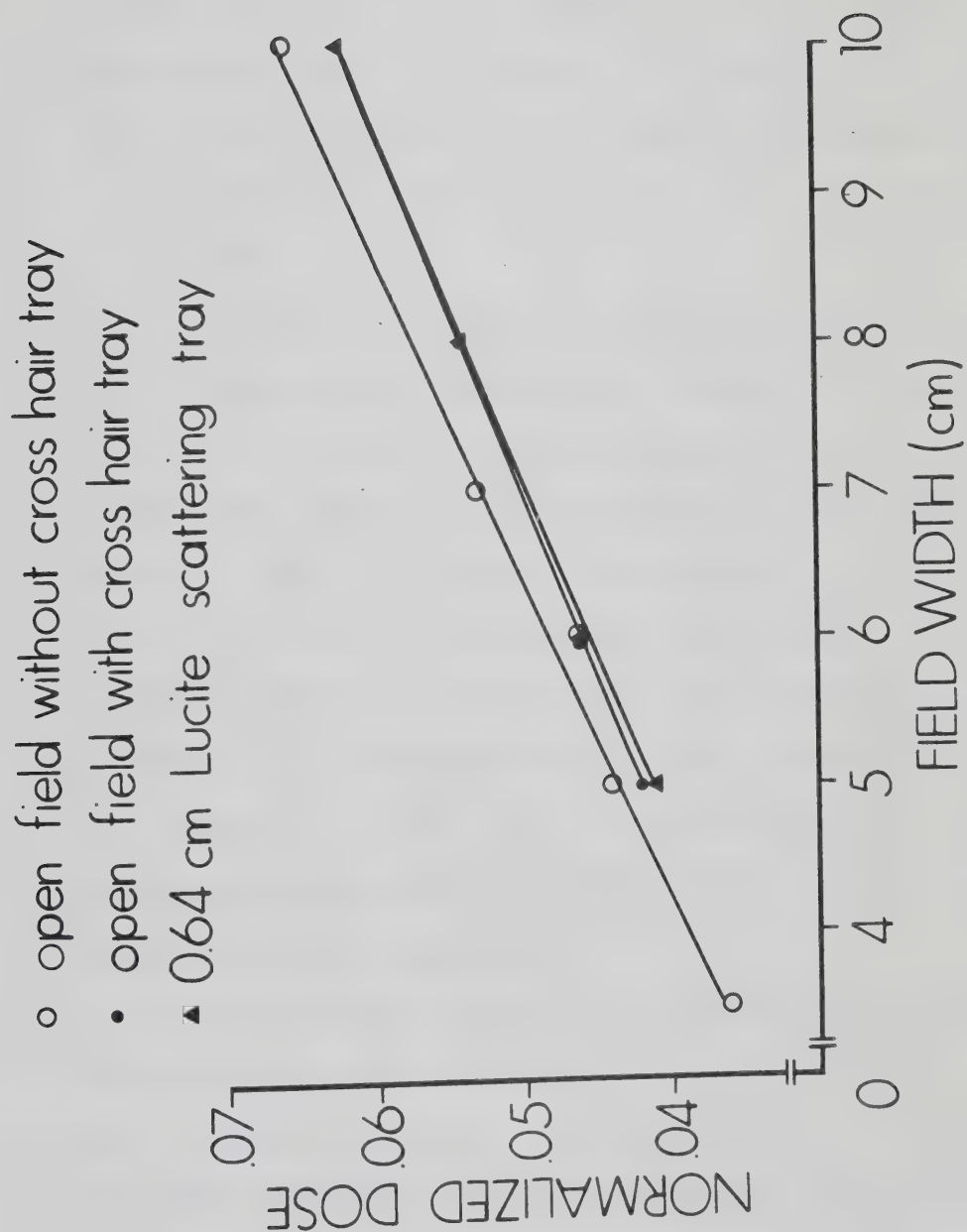


Figure 47. The surface normalized dose with the magnet in place for various conditions at 100 cm SPD for the 15 MV beam.





were measured at an SPD of 100 cm at a depth of  $d_{\max}$  for a field size of 10 cm x 10 cm under the same accessory configuration. The normalized dose curves are the same within 0.005. This is to be expected because electron contamination produced by the accessories is swept from the field by the magnet. The normalization procedure takes into account the reduction in the primary dose available for the production of electron contamination in air and photon backscatter.

The dose due to photon backscatter can be subtracted from the surface dose with the magnet in place to leave the dose due to electron contamination produced in air\* as the only component. Figures 48 and 49 illustrate the normalized dose due to contamination produced in air as a function of field width for various source-to-probe distances when an open field is used (with cross-hair tray in place) for a 15 MV and 6 MV photon beam, respectively. At each source-to-probe distance the normalized dose increased as a function of field width. This increase was larger for smaller field widths.

The measurements suggest that curves taken at various source-to-probe distances converge to a zero normalized dose at a zero field width. The behavior at field sizes less than the chamber diameter cannot easily be determined.

The difference between readings with and without the magnet in place can only be due to what is being swept by the magnet when it is in place; namely electron

\* This refers to air between the magnet and phantom.



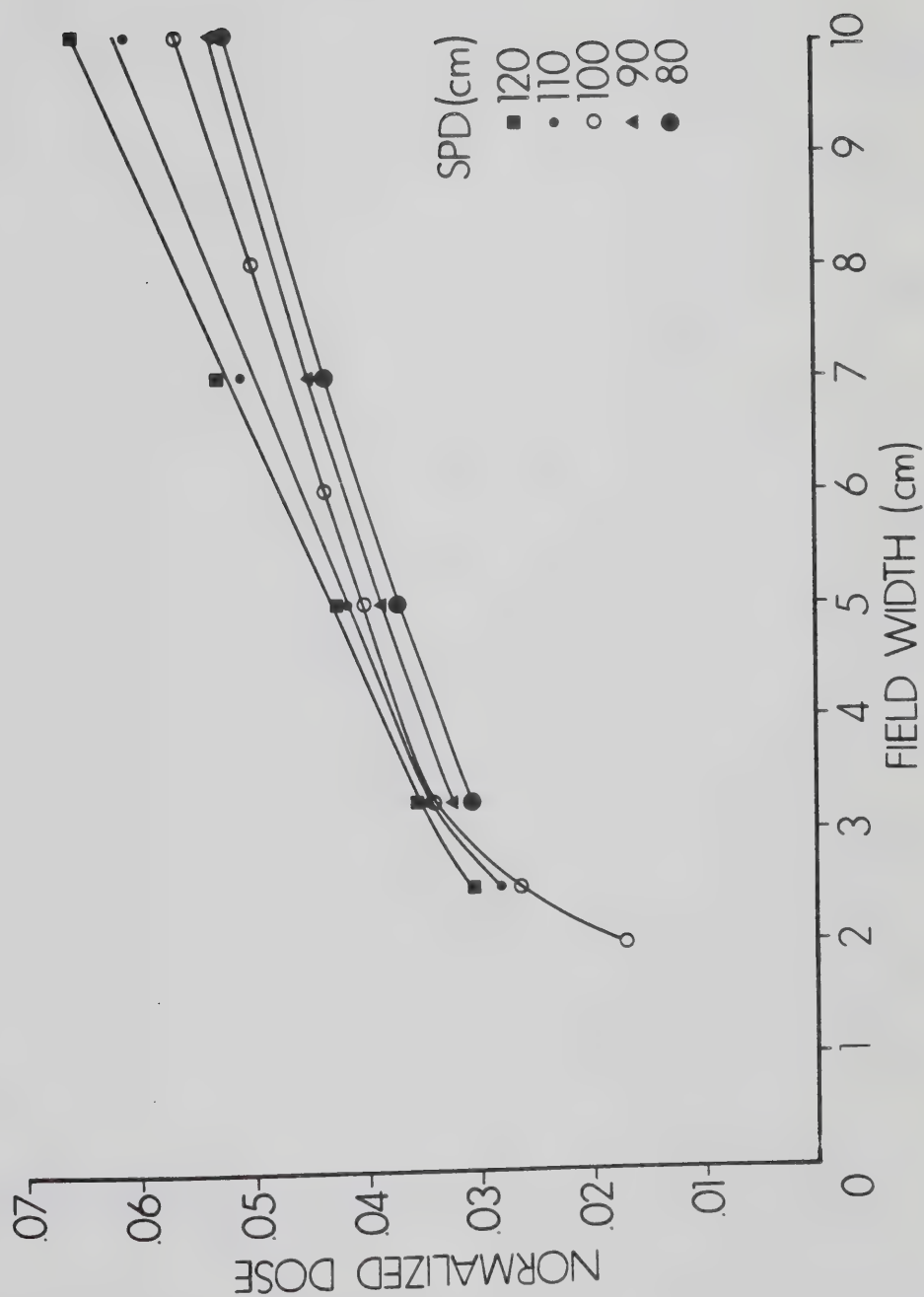


Figure 48. Normalized dose due to contamination produced in air as a function of field width for various source-to-probe distances for an open field at 15 MV.



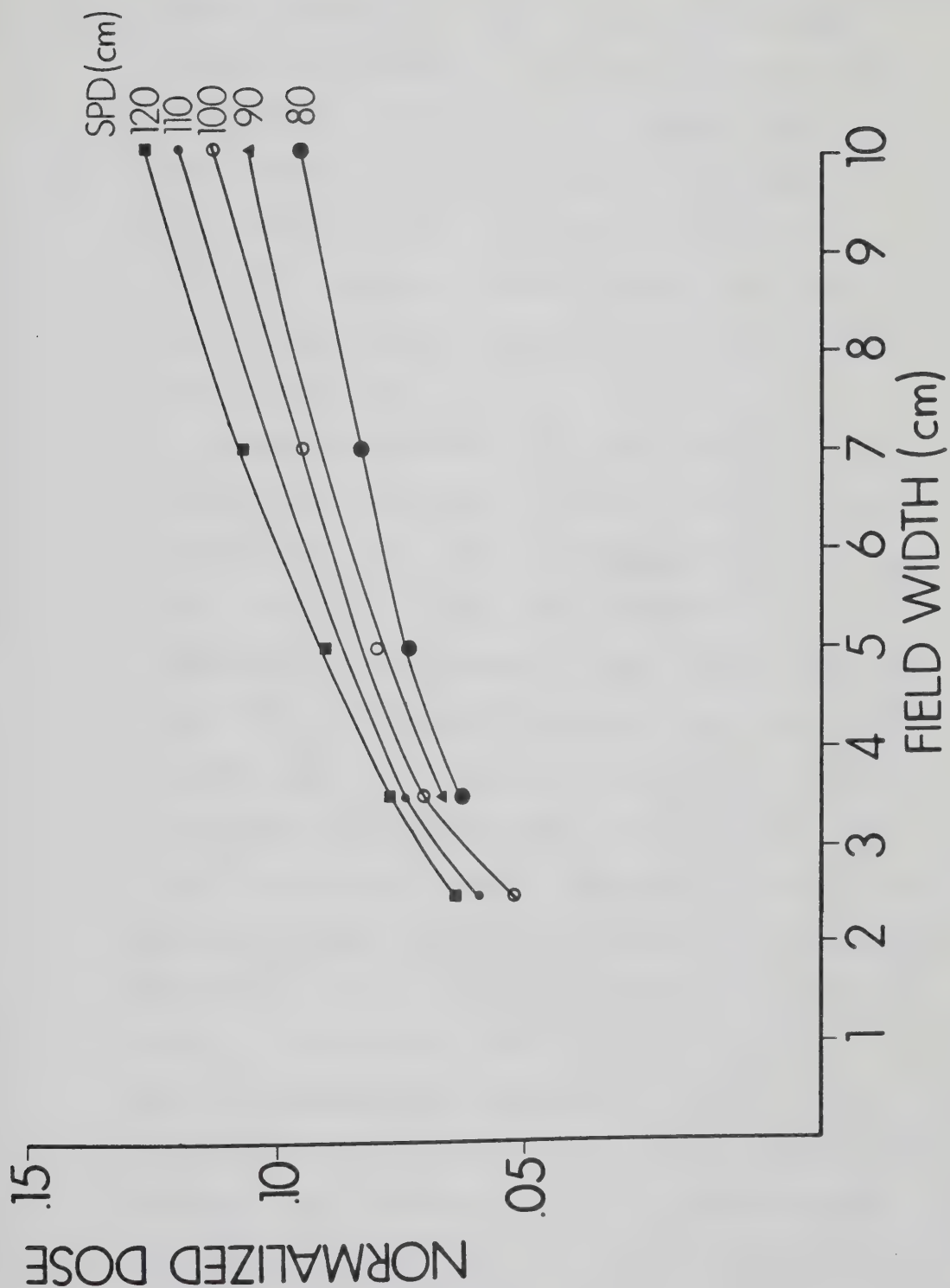


Figure 49. Normalized dose due to contamination produced in air as a function of field width for various source-to-probe distances for an open field at 6 MV.



contamination produced between the target and magnet.\*

Figures 50 and 51 are graphs of the normalized dose difference between magnet in and out for 15 MV and 6 MV photon beams, respectively. The normalized dose is very small at small field sizes, but increases rapidly as a function of field size. The normalized dose due to contamination produced between the magnet and target increases approximately in direct proportion to the beam cross-sectional area.

There is considerable difference between the electron contamination contributions due to air and due to interactions between the target and phantom at small field sizes. (less than 10 cm x 10 cm). The contributions due to air exceed those of contributions produced between target and magnet for both 6 MV and 15 MV photon beams at all source-to-probe distances. The increase in dose as a function of field width at very small field sizes (less than 5 cm x 5 cm) is greater for electron contamination produced in air than for electron contamination produced between the target and magnet. The most interesting difference between these curves is that the normalized dose for air-produced electron contamination is greater for large SPD whereas the target-to-magnet electron contamination is greater for smaller source-to-probe distances. The source-to-probe

\* It did not matter if normalization measurements were done with the magnet in or out. The difference at  $d_{\max}$  between readings taken with the magnet in place compared to readings with the magnet not in place was less than 0.5%. This indicates that few contamination electrons produced between the target and magnet penetrate to  $d_{\max}$ .





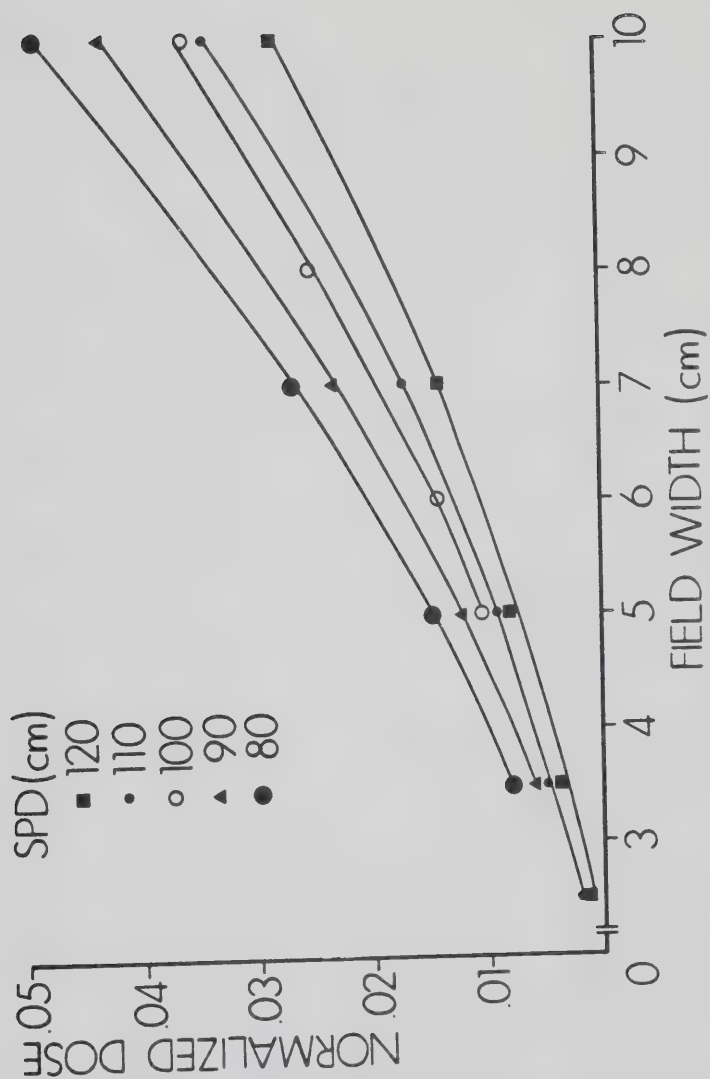


Figure 50. Normalized dose difference between magnet in place and out of place for a 15 MV beam as a function of field width for various source-to-probe distances for an open field.



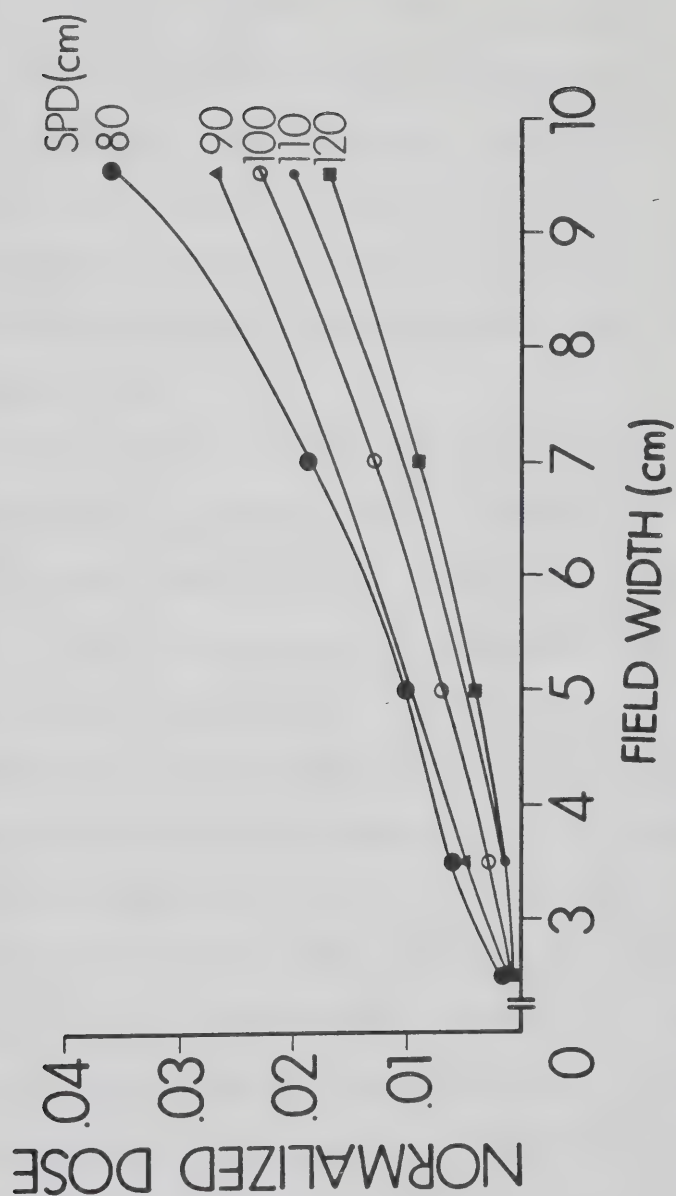


Figure 51. Normalized dose difference between magnet in place and out of place for a 6 MV beam as a function of field width for various source-to-probe distances for an open field.



dependence of the surface dose is better illustrated in Figures 52 to 55. Figures 52 and 53 are graphs of normalized dose versus SPD at 15 MV for air contamination and contamination between the target and magnet, respectively, for a family of field widths. Figures 54 and 55 are for contamination produced in air and between the target and magnet, respectively, under the same measurement conditions as 15 MV but done at 6 MV.

If an assumption is made that the location where the contamination is produced between the target and magnet is a point source, then the same procedure used in Section 2.4.3 to locate the apparent source of contamination electrons can be used again. The difference in the absolute readings taken with the magnet not in place and magnet in place is a measure of the contamination dose produced between the target and magnet. If the readings were taken at nearly the same time, then the difference in absolute readings need not be normalized. Figure 56 is a graph of the square root of the difference in absolute readings versus SPD at 15 MV for a number of field sizes. The apparent source of electron contamination is at 40 cm SPD. The electron contamination appears to be coming from the cross-hair tray. A similar result was obtained at 6 MV (see Figure 57).

The cross-hair tray was removed and the readings repeated at 15 MV. Figure 58 illustrates that the apparent source of contamination is shifted to between 30 cm and



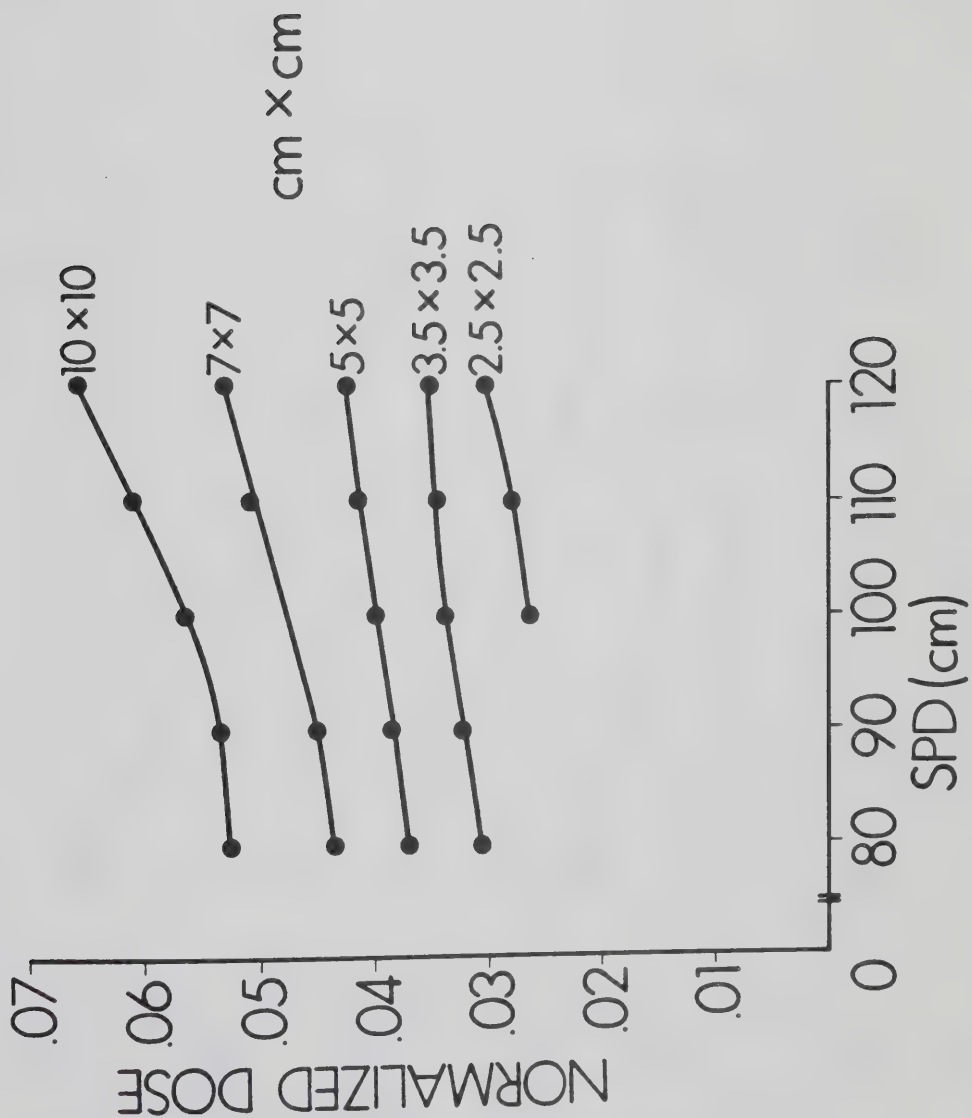


Figure 52. Normalized dose due to contamination produced in air as a function of source-to-probe distance for various field widths for an open field at 15 MV.





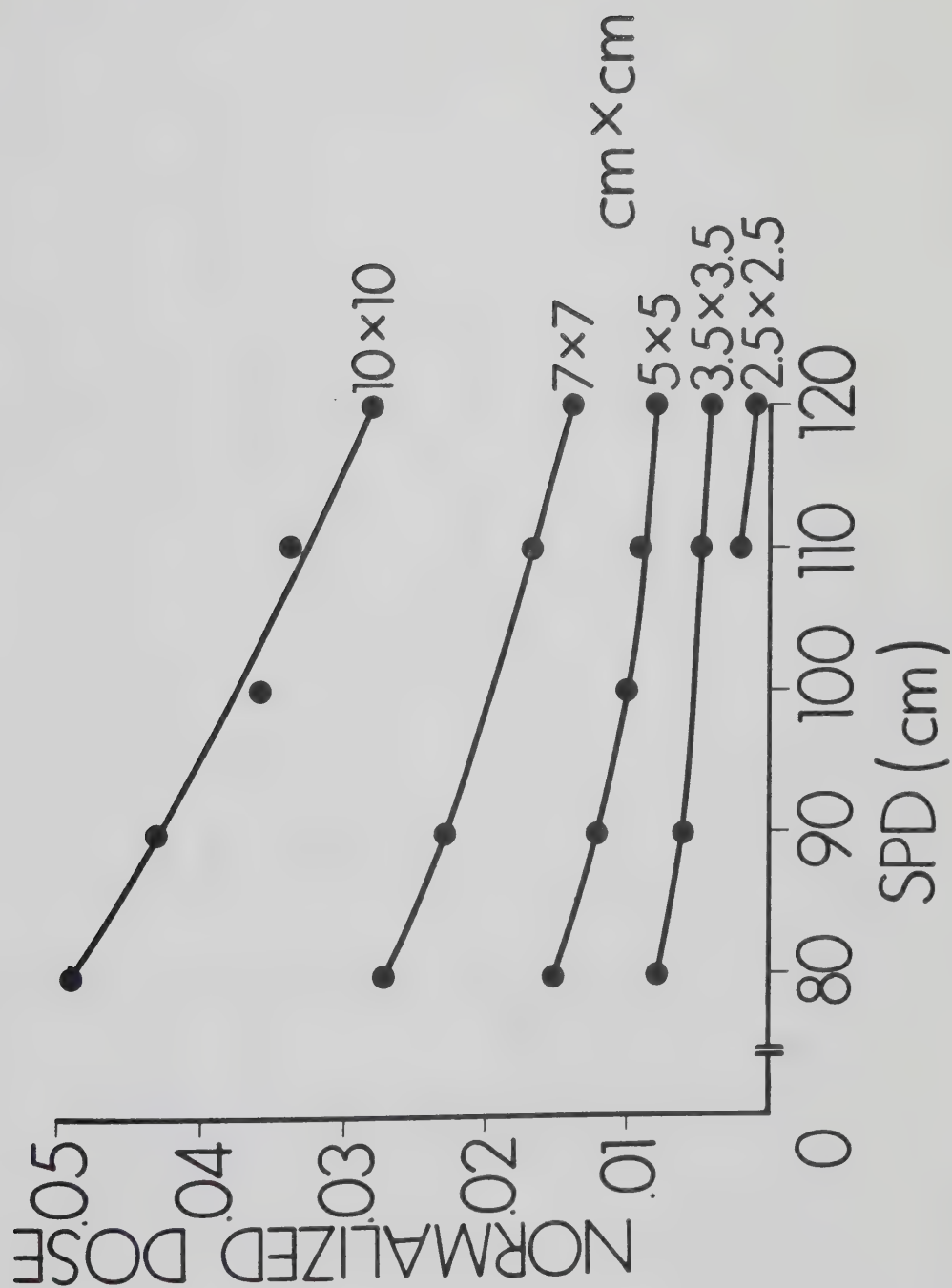


Figure 53. Normalized dose produced between the target and magnet in a 15 MV beam as a function of source-to-probe distances for various field widths for an open field.



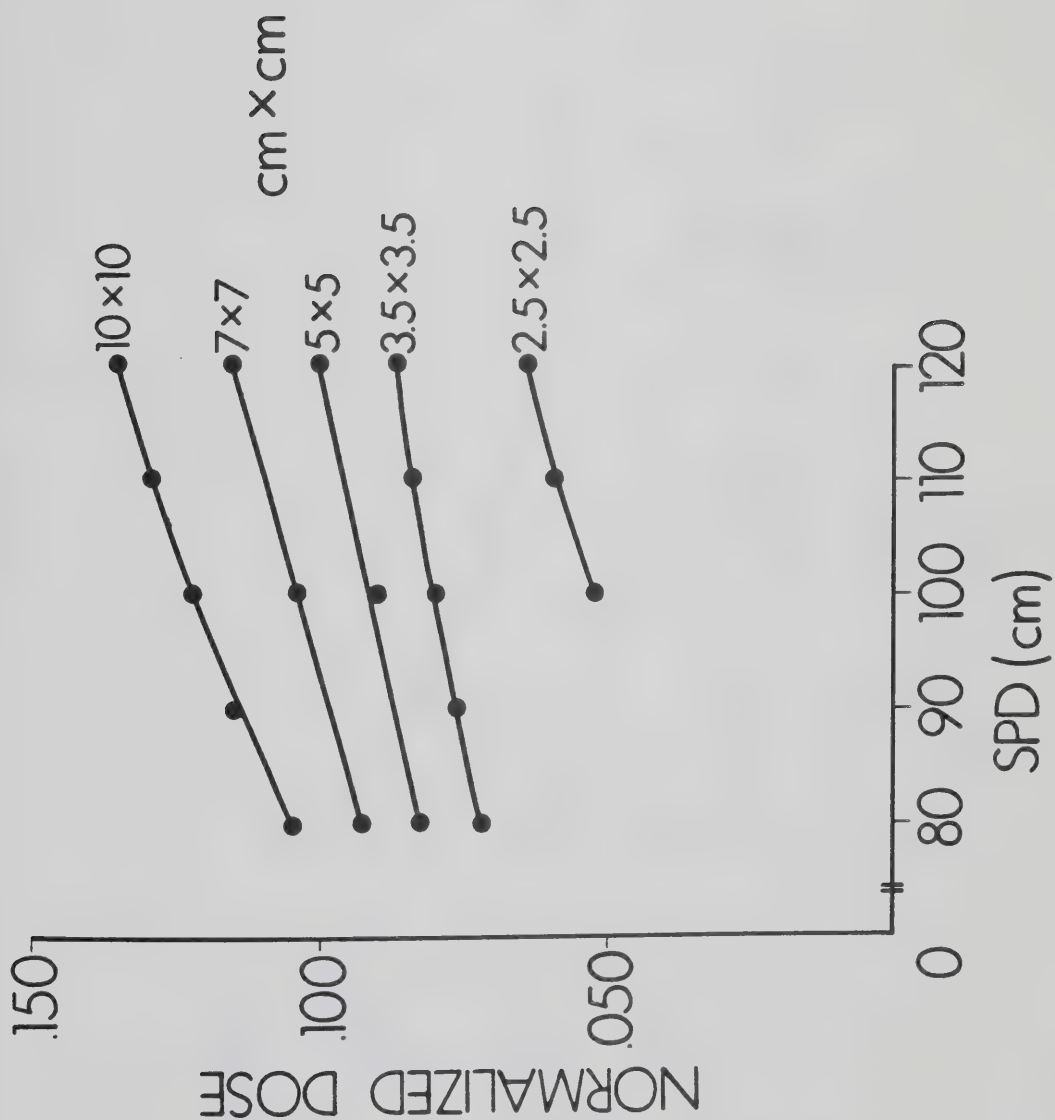


Figure 54. Normalized dose due to contamination produced in air as a function of source-to-probe distance for various field widths for an open field at 6 MV.



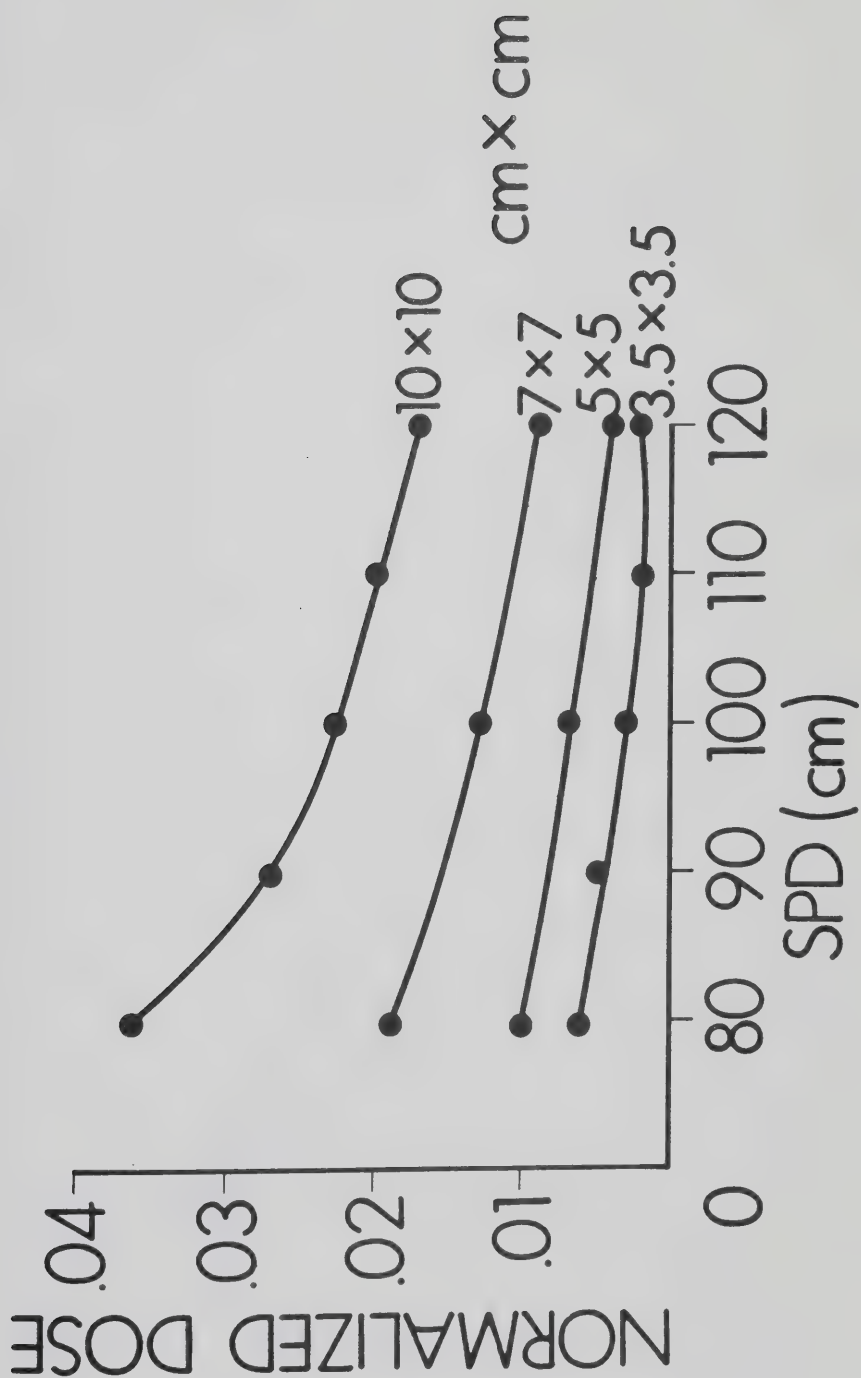


Figure 55. Normalized dose produced between the target and magnet in a 6 MV beam as a function of source-to-probe distances for various field widths for an open field.



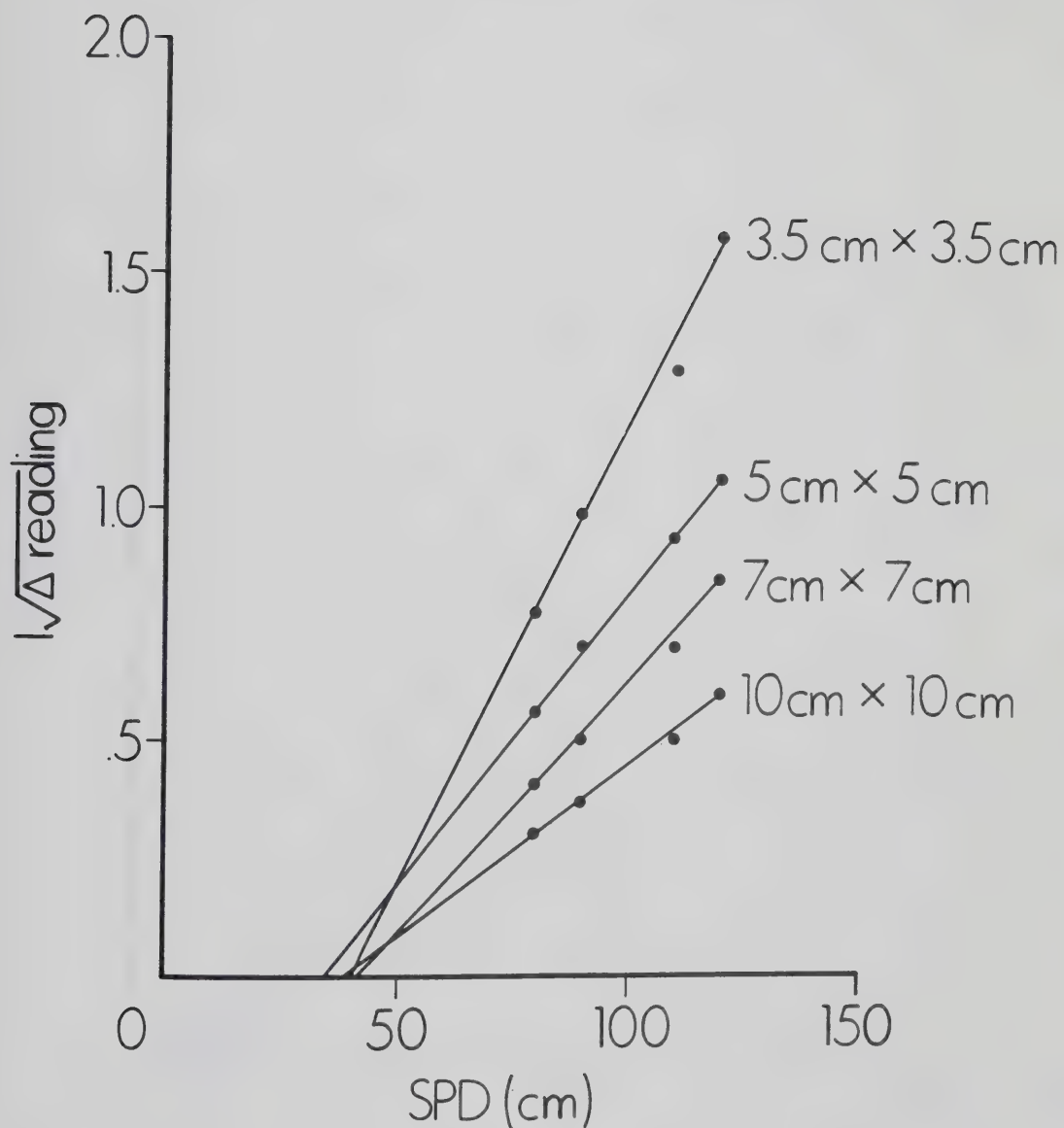


Figure 56. Dependence of the dose produced between the target and magnet on the inverse square of the distance from the apparent source at 15 MV when the cross-hair tray was in place.





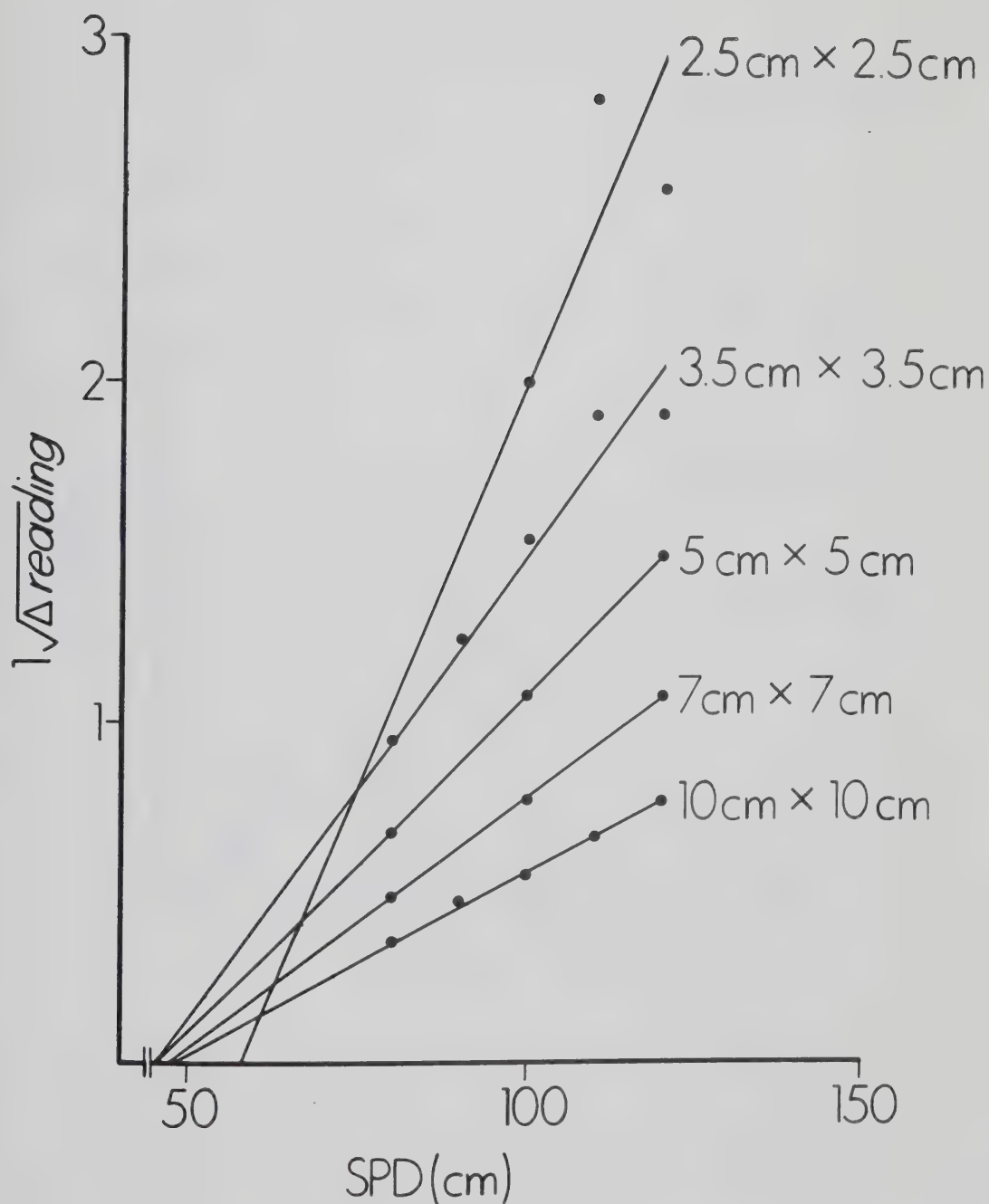


Figure 57. Dependence of the dose produced between the target and magnet on the inverse square of the distance from the apparent source at 6 MV when the cross hair tray was in place.



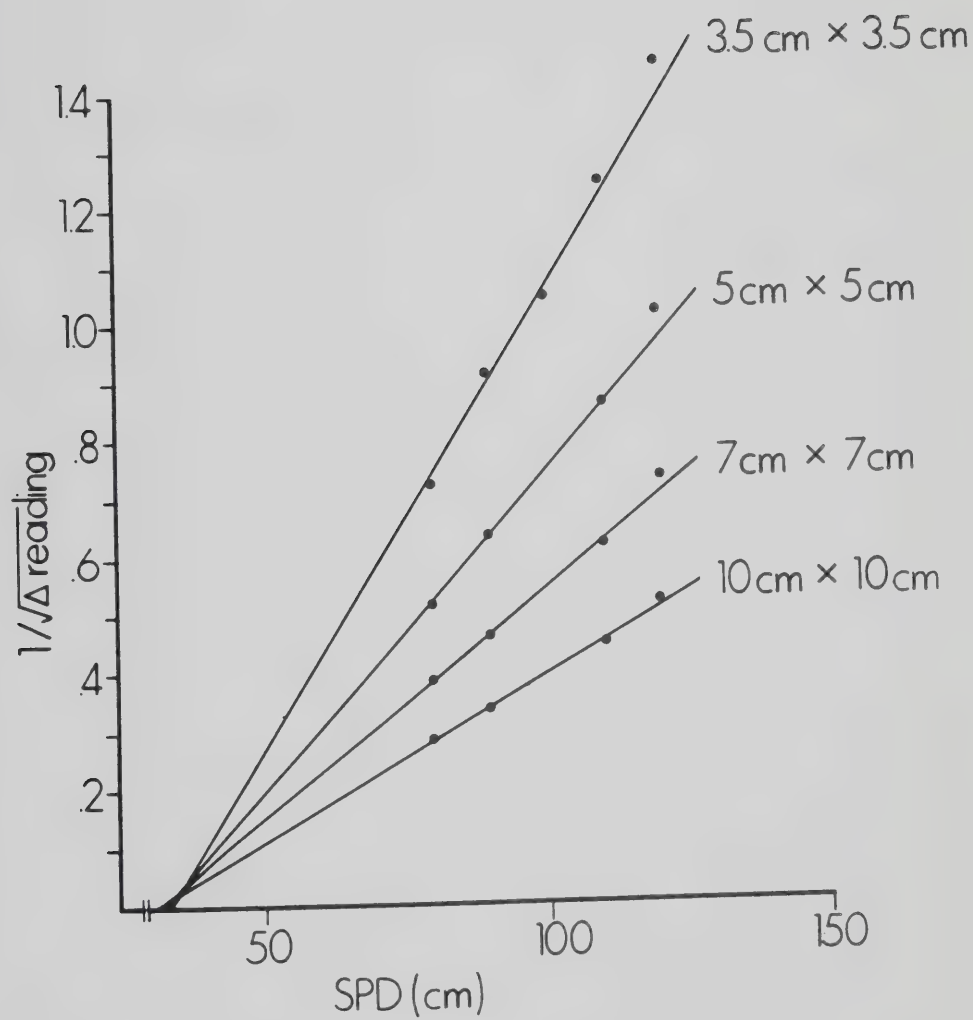


Figure 58. Dependence of the dose produced between the target and magnet on the inverse square of the distance from the apparent source at 15 MV when the cross-hair tray was not in place.



35 cm. The range of x-intercepts corresponds approximately to the position of the collimators.



#### 2.10.4 Determination of the Penetration Curves of Electron Contamination Produced Between the Target and Magnet

Electrons produced by interactions between the target and magnet should penetrate some distance into a phantom. The penetration curve can be obtained by measuring the difference between readings taken without and with the magnet in place when the same thickness of overlying material is placed over the ion chamber.

Figure 59 illustrates the central axis penetration curve for electron contamination produced by the 15 MV beam between the target and magnet as measured by a probe at 100 cm SPD in a 10 cm x 10 cm field. This penetration curve has its maximum at about 0.15 cm in the phantom and a relative plateau in dose of about 1 cm. From 1 cm to 3.5 cm the dose drops rapidly as a function of depth. At 2.9 cm the dose deposited is only 20% of the dose deposited at 0.15 cm.

An almost identical penetration curve was produced when the probe was 3 cm outside a field with a size of 10 cm x 10 cm at 100 cm SPD for a 15 MV beam (see Figure 60). The phantom setup was similar to the inset in Figure 30 except the phantom was tilted at  $5.7^{\circ}$ .

Figure 61 illustrates the penetration curve for electron contamination produced between the target and magnet for the 6 MV beam. The shape of the curve is similar to the result at 15 MV except that the maximum dose occurs at the surface at 6 MV and this beam reaches its 20% level at 1.3 cm instead of 2.9 cm. Figure 62 compares the penetration curves for electron





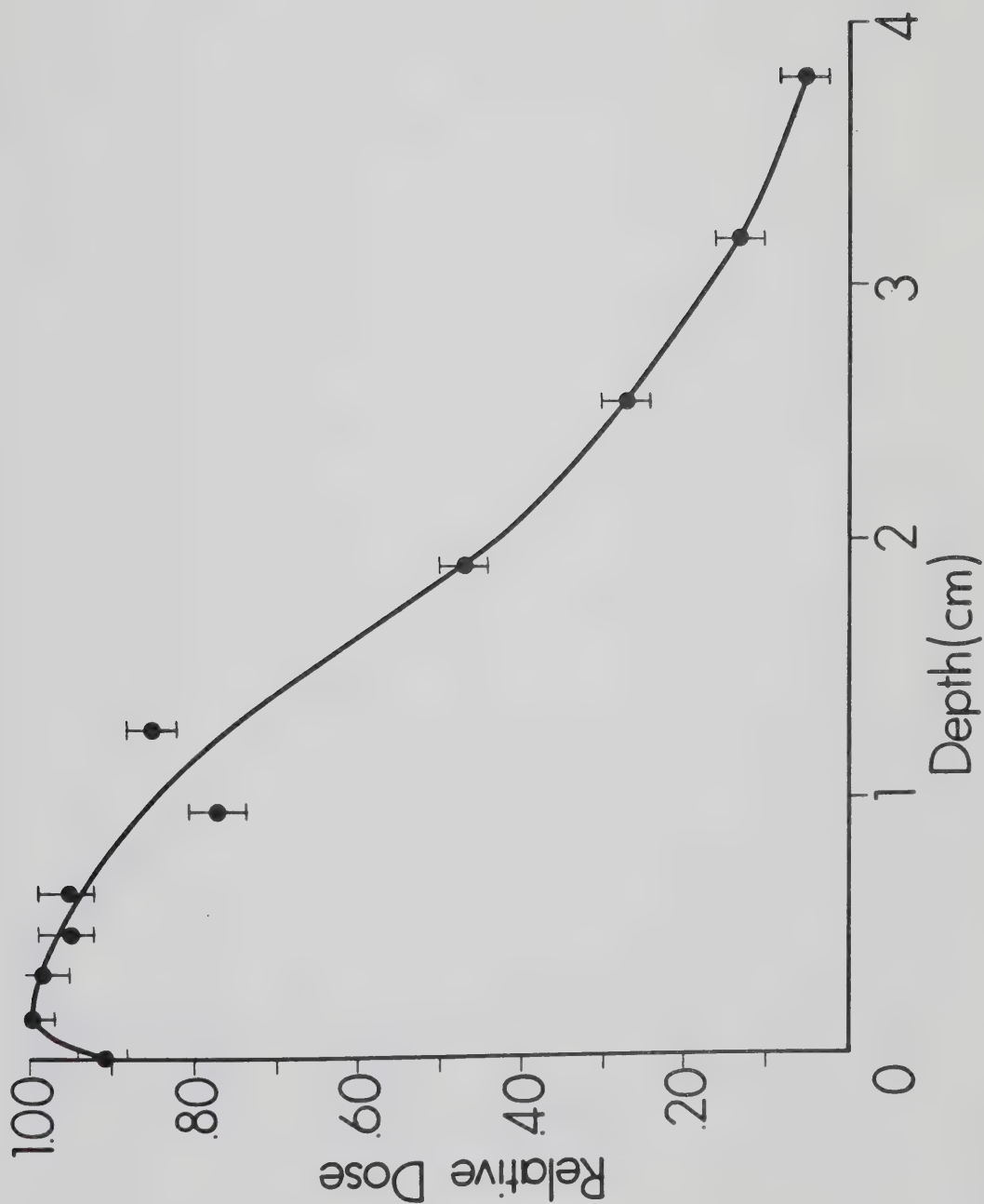


Figure 59. Central axis penetration curve for electron contamination produced between the target and magnet by the 15 MV beam at 100 cm SPD for a field size of 10 cm x 10 cm.



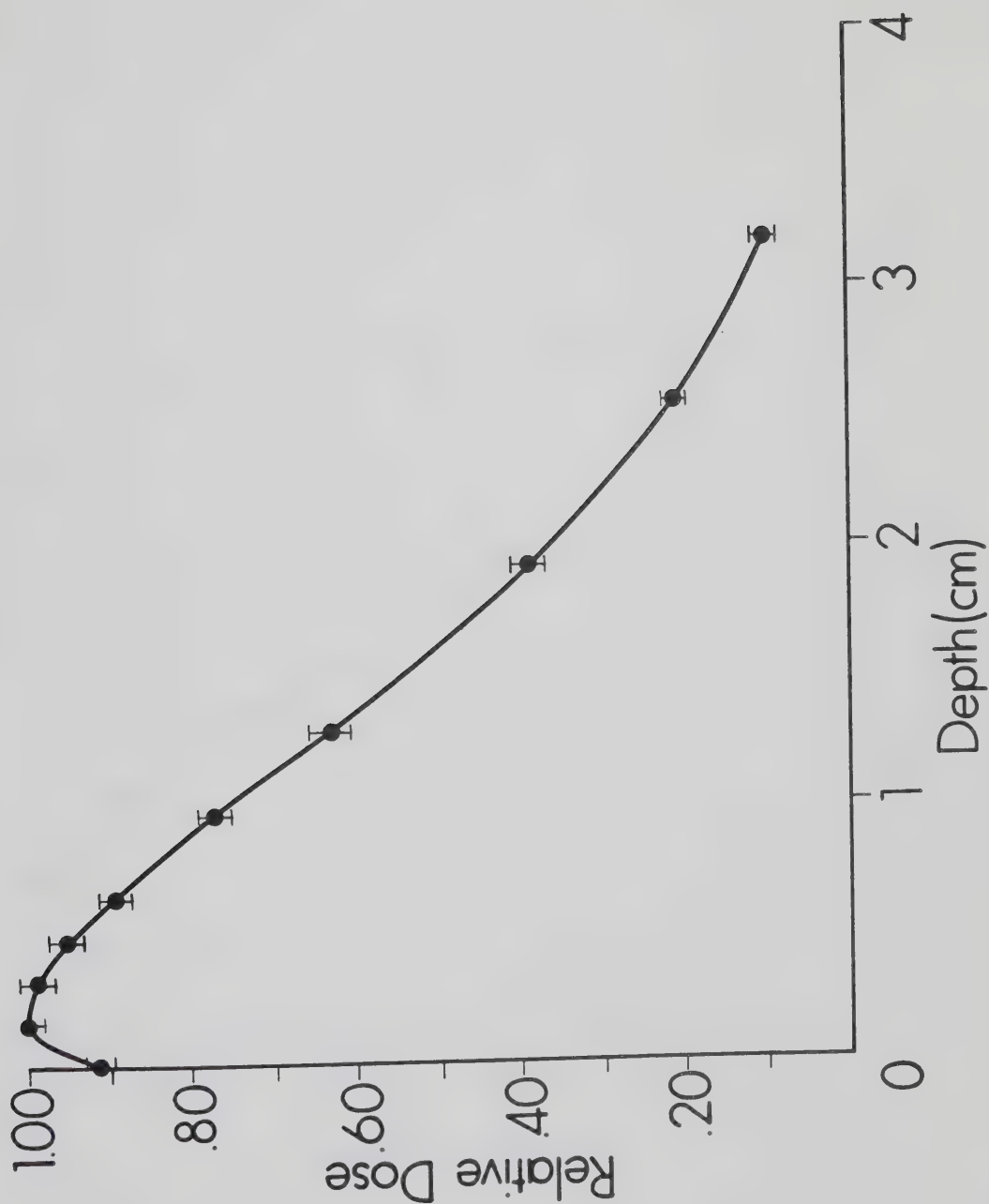


Figure 60. Penetration curve for electron contamination between the target and magnet measured 3 cm outside a 10 cm x 10 cm field at 100 cm SPD for a 15 MV beam.



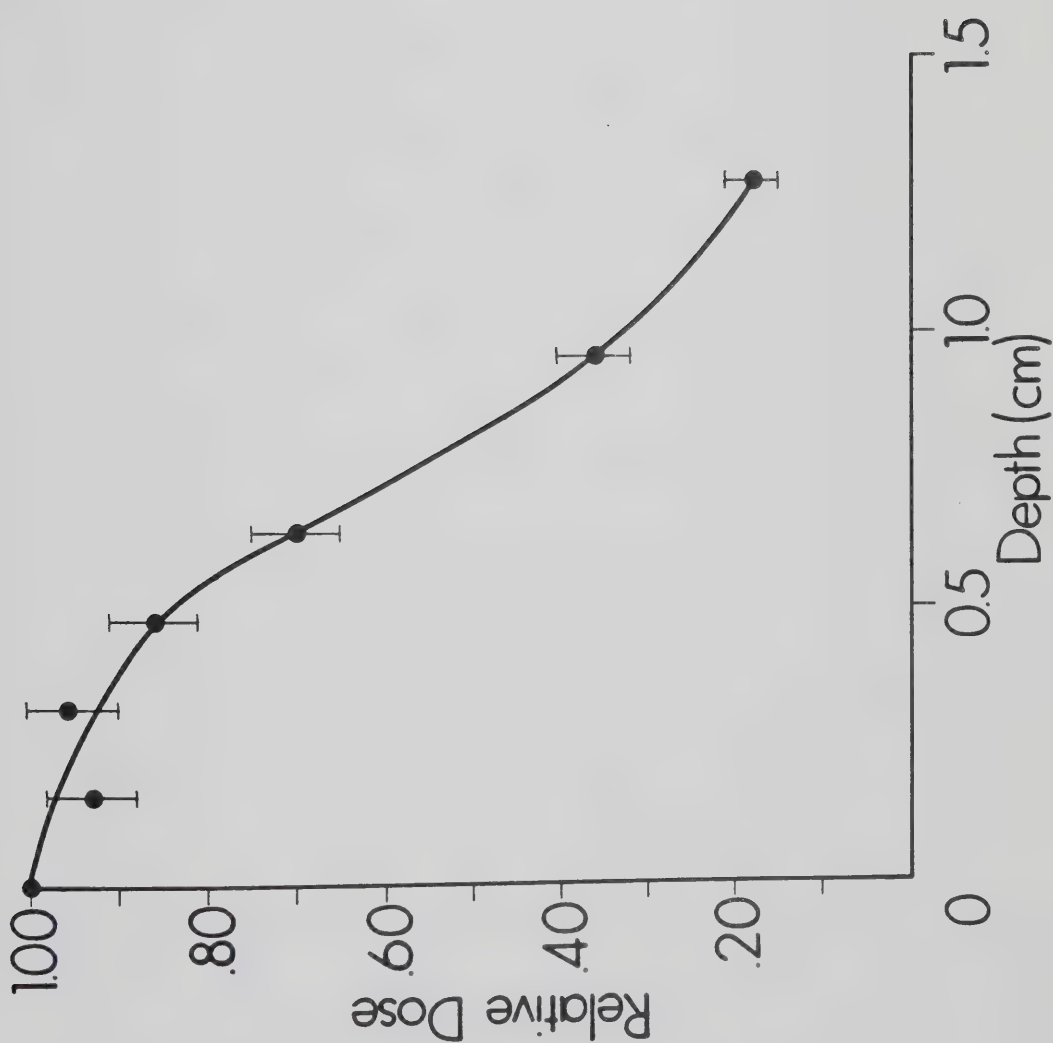


Figure 61. Central axis penetration curve for electron contamination produced between the target and magnet by the 6 MV beam at 100 cm SPD for a field size of 10 cm x 10 cm.



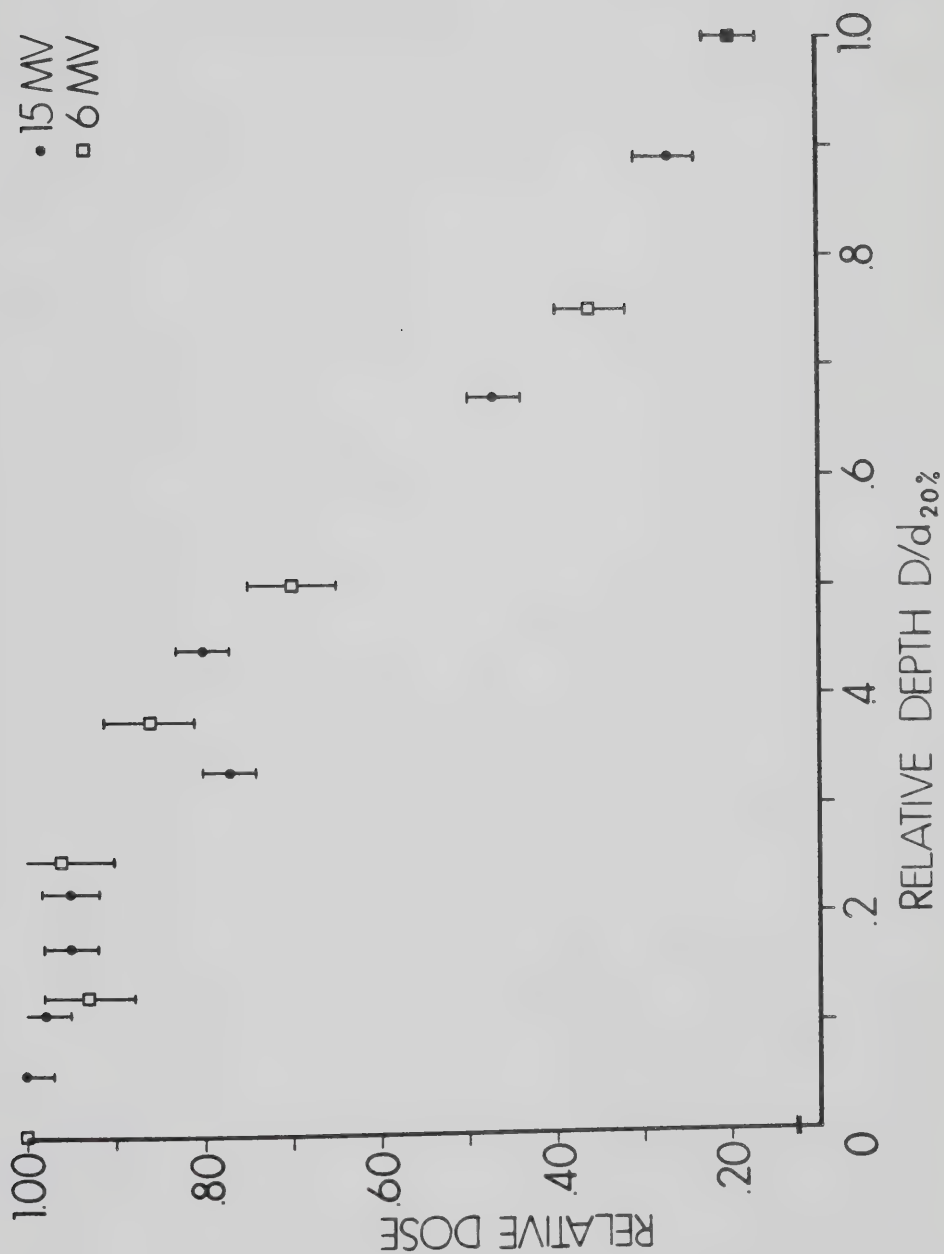


Figure 62. Comparison between the 15 MV and 6 MV contamination penetration curves produced between the target and magnet in a 10 cm x 10 cm beam at 100 cm SPD.





contamination produced between the target and magnet for 6 MV and 15 MV by normalizing the depth of penetration with respect to the depth required to reach the 20% level.

The curves are almost identical.



## 2.11 A Method for Separating Contamination from Phantom Generated Penetration Curves

### 2.11.1 Determination of the Contamination Penetration Curves

The graphs of normalized dose versus field width allow one to separate the dose due to contamination from the dose due to photons interacting in the phantom. The total dose,  $T(d, SPD, W)$ , is a sum of the phantom generated dose,  $P(d, SPD)$ , and the contamination dose,  $C(d, SPD, W)$ . The phantom generated dose is not a function of the field width,  $W$ , when measured with a limited phantom (see Figure 34). The phantom generated dose is due to primary photons interacting with the phantom and scattered photons generated by the primary interactions in the phantom. The phantom generated dose is due to the primary photon component of the beam, Mathematically.

$$T(d, SPD, W) = P(d, SPD) + C(d, SPD, W) \quad (2.11.1)$$

$$\text{where } T(d, SPD, W) = \frac{\text{Total Reading}}{\text{Standard Reading}}$$

$$P(d, SPD) = \frac{\text{Reading Due To Primary Photons}}{\text{Standard Reading}}$$

$$C(d, SPD, W) = \frac{\text{Reading Due To Contamination}}{\text{Standard Reading}}$$

The standard reading used is the same as in Equation 2.8.1.

$$\frac{dT(d, SPD, W)}{dW} = \frac{dP(d, SPD)}{dW} + \frac{dC(d, SPD, W)}{dW} \quad (2.11.2)$$

$$\text{but } \frac{dP(d, SPD)}{dW} = 0$$



Therefore,

$$\frac{dT(d,SPD,W)}{dW} = \frac{dC(d,SPD,W)}{dW} \quad (2.11.3)$$

where  $\frac{dT(d,W)}{dW}$  is the slope of the line of normalized dose versus field width at a depth,  $d$ , source-to-probe distance,  $SPD$ , and field width,  $W$ . The normalized dose due to contamination,  $C(d,SPD,W)$ , is found by integrating Equation 2.8.3. This makes an assumption that the nature of the contamination does not change as a function of field width, but the magnitude of contamination does. Mathematically,

$$C(d,SPD,W) = \int_{W_1}^{W_2} \frac{dT(d,SPD,W)dW}{dW} \quad (2.11.4)$$

If  $\frac{dT(d,SPD,W)}{dW}$  is not a constant then,

$$C(d,SPD,W_1,W_2) \propto T(d,SPD,W_2) - T(d,SPD,W_1) \quad (2.11.5)$$

If  $\frac{dT(d,SPD,W)}{dW}$  is a constant then,

$$C(d,SPD) \propto \text{Slope of Line} \quad (2.11.6)$$

where the last equation does not have any dependence on field width. An assumption is implicit that dose increase of small field size is the same as dose increases for larger sizes.



The slopes in Figures 35 to 38 were linear so Equation 2.11.6 can be used. Therefore, the amount of contamination is independent of field width. Table 3 lists the amount of contamination as a function of depth normalized to the maximum amount of contamination for the 15 MV beam. The penetration characteristics of the contamination are relatively independent of the thickness of accessory and source-to-probe distance. Therefore, to a good approximation, the relative amount of contamination only depends on the depth of measurement in the phantom. A plot of the contamination penetration curve at SPD = 100 cm is shown in Figure 63.

The open field penetration behaviour at 100 cm SPD was obtained for the 6 MV accelerator also by using the increase in normalized dose versus field width. The normalized contamination penetration curve is shown in Figure 64.

The contamination penetration curves are equivalent to the tissue maximum ratio of the contaminant component if they were the only component in the beam.

#### 2.11.2. Determination of the Phantom Generated Build-Up Curves

The phantom generated build-up contribution is obtained by subtracting the contamination component from the total build-up curve. The total build-up curve is measured with a full phantom (that is, the





Table 3 Contamination Dose Normalized To The  
Maximum Contamination Dose At 15 MV

| Depth<br>(cm) | SPD = 100cm<br>No<br>Accessory | SPD = 100cm<br>0.64cm Lucite<br>Accessory | SPD = 100cm<br>3.18cm Lucite<br>Accessory | SPD = 75cm<br>No<br>Accessory |
|---------------|--------------------------------|---|---|-------------------------------|
| 0.00          | 0.94                           | 0.98                                      | 0.95                                      | 0.99                          |
| 0.16          | 1.00                           | 1.00                                      | 1.00                                      | 1.00                          |
| 0.32          | 0.94                           | 0.96                                      | 0.95                                      | 0.92                          |
| 0.48          | 0.89                           | 0.88                                      | 0.88                                      | 0.84                          |
| 0.64          | 0.83                           | 0.79                                      | 0.80                                      | 0.78                          |
| 0.95          | 0.69                           | 0.64                                      | 0.67                                      | 0.63                          |
| 1.27          | 0.61                           | 0.51                                      | 0.55                                      | 0.50                          |
| 1.91          | 0.48                           | 0.34                                      | 0.36                                      | 0.31                          |
| 2.54          | 0.28                           | 0.23                                      | 0.24                                      | 0.21                          |
| 2.86          | 0.23                           | 0.19                                      | 0.21                                      | 0.16                          |
| 3.18          | 0.21                           | 0.16                                      | 0.18                                      | 0.18                          |
| 3.49          | 0.18                           | 0.14                                      | 0.17                                      | 0.16                          |
| 3.81          | 0.15                           | 0.13                                      | 0.15                                      | 0.17                          |
| 4.13          | 0.15                           | 0.12                                      | 0.14                                      | 0.11                          |



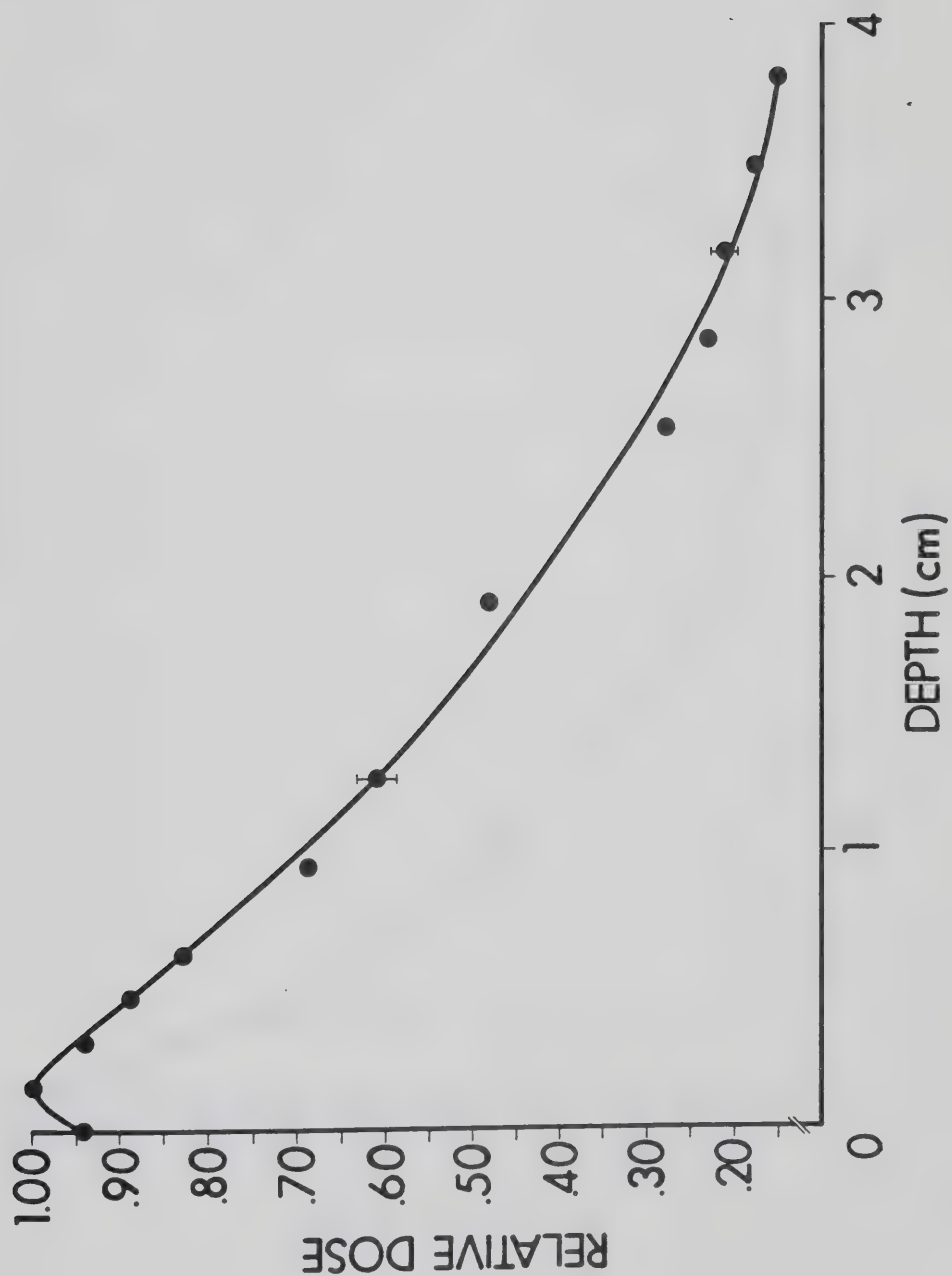


Figure 63. Contamination penetration curve determined by the increase in dose in a limited phantom as a function of field width at 100 cm SPD for a 15 MV beam.



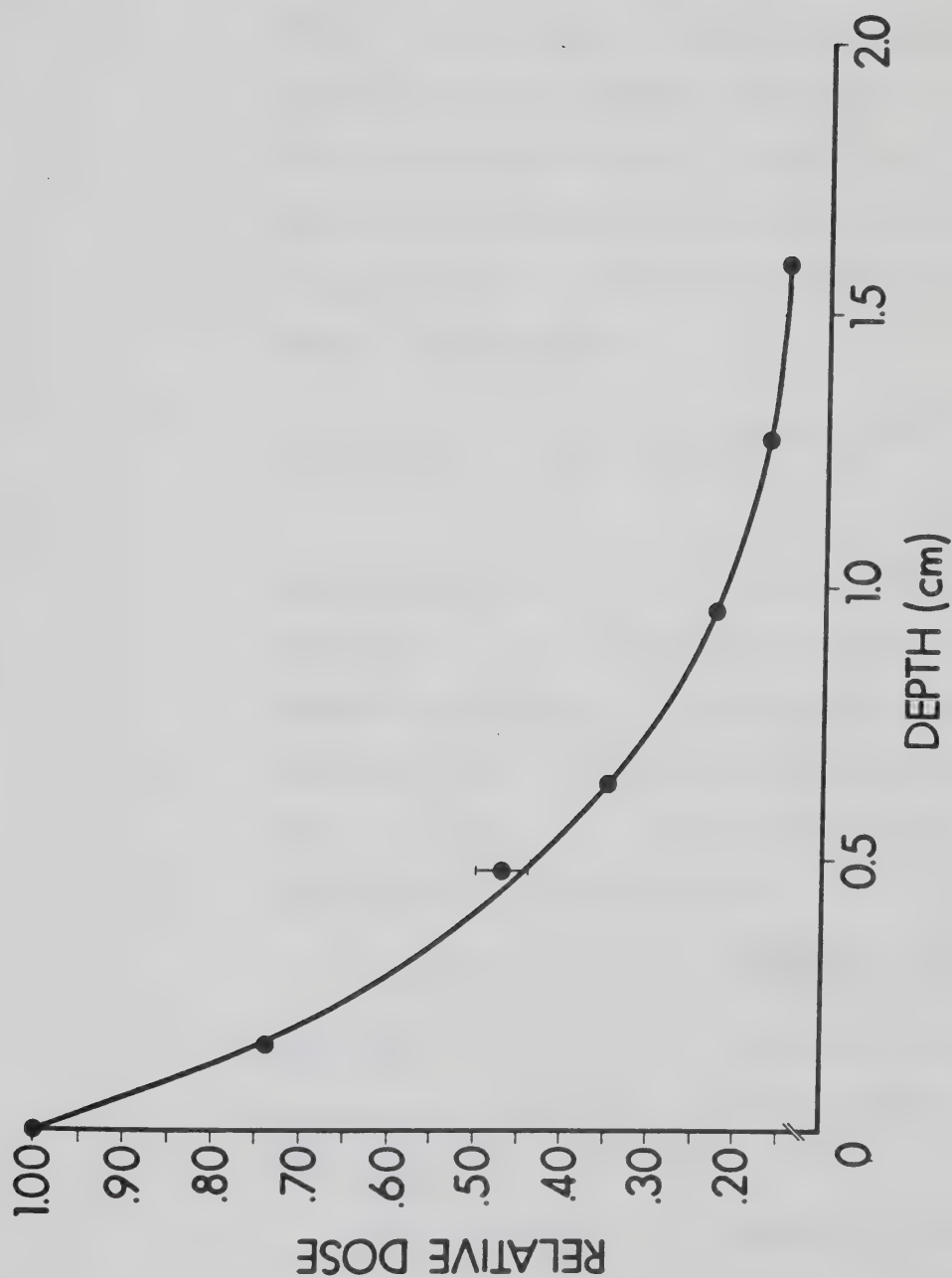


Figure 64. Contamination penetration curve determined by the increase in dose in a limited phantom as a function of field width at 100 cm SPD for a 6 MV beam.



cross-sectional area is greater than the field width). The magnitude of contamination under any condition is determined by equating the difference between the total build-up curve and the photon backscatter at the surface with the magnitude of the contamination dose at the surface. Mathematically,

$$C(d=0, SPD, W) = T(d=0, SPD, W) - PBS(d=0, SPD, W) \quad (2.11.7)$$

where  $PBS(d=0, SPD, W)$  is the amount of photon backscatter at the surface of the phantom. The amount of contamination at any depth is determined from a knowledge of the amount of contamination there is at the surface and the penetration characteristics. Mathematically,

$$C(d, SPD, W) = C(d=0, SPD, W) \frac{CTMR(d)}{CTMR(d=0)} \quad (2.11.8)$$

where  $CTMR(d)$  is the value of the normalized contamination penetration curve at a depth,  $d$ , in the phantom.

Having established the magnitude of contamination at any depth in the phantom, the contamination component is subtracted from the total build-up component to yield the phantom generated build-up curve.





A computer program called `Seprimary.For*` (for a listing and documentation of `Seprimary.For` see Appendix 5) calculates the phantom generated build-up curves. The input data lists the normalized contamination penetration data as a function of depth, the photon backscatter normalized dose at the surface as a function of field size as well as SPD and the total build-up normalized dose as a function of field size, SPD, depth and amount of accessories in the field.

The "pseudo-unit" of the output is normalized dose. This can be converted to the tissue maximum ratios of the phantom generated build-up curves by dividing the curves by the maximum normalized dose value of each curve.

An estimate of the limit errors in the calculated quantities is also computed. The errors in the measured quantities are entered with the input data.

Tables 4 to 15 list the phantom generated normalized dose and tissue maximum ratio curves as a function of depth along with their associated limit errors for a variety of conditions of field size, SPD and presence of accessories for the 15 MV and 6 MV accelerators. The phantom generated normalized dose at  $d_{\max}$  increases as a function of

\* The suffix, '.For', indicates an executable Fortran program. The suffix, '.Dat', indicates a data file storing constant values.



Table 4

15 MV    SPD = 100cm  
 No Accessories  
 Field Size = 3.0cm X 3.0cm  
 Photon Backscatter N.D. = 0.001

| Depth<br>(cm) | ND    | Error in ND | TMR  | Error in TMR |
|---------------|-------|-------------|------|--------------|
| 0.00          | 0.001 | 0.000       | 0.00 | 0.00         |
| 0.16          | 0.168 | 0.008       | 0.21 | 0.01         |
| 0.32          | 0.290 | 0.008       | 0.36 | 0.01         |
| 0.48          | 0.388 | 0.008       | 0.48 | 0.01         |
| 0.64          | 0.456 | 0.008       | 0.56 | 0.01         |
| 0.95          | 0.577 | 0.007       | 0.71 | 0.01         |
| 1.27          | 0.663 | 0.007       | 0.82 | 0.01         |
| 1.91          | 0.759 | 0.006       | 0.93 | 0.01         |
| 2.54          | 0.802 | 0.005       | 0.99 | 0.01         |
| 2.86          | 0.811 | 0.005       | 1.00 | 0.01         |
| 3.18          | 0.813 | 0.005       | 1.00 | 0.01         |
| 3.50          | 0.813 | 0.005       | 1.00 | 0.01         |
| 3.81          | 0.812 | 0.005       | 1.00 | 0.01         |

15 MV    SPD = 100cm  
 No Accessories  
 Field Size = 4.0cm X 4.0cm  
 Photon Backscatter N.D. = 0.001

| Depth<br>(cm) | ND    | Error in ND | TMR  | Error in TMR |
|---------------|-------|-------------|------|--------------|
| 0.00          | 0.001 | 0.000       | 0.00 | 0.00         |
| 0.16          | 0.173 | 0.009       | 0.20 | 0.01         |
| 0.32          | 0.303 | 0.009       | 0.34 | 0.01         |
| 0.48          | 0.402 | 0.008       | 0.46 | 0.01         |
| 0.64          | 0.486 | 0.008       | 0.55 | 0.01         |
| 0.95          | 0.614 | 0.008       | 0.70 | 0.01         |
| 1.27          | 0.706 | 0.007       | 0.80 | 0.01         |
| 1.91          | 0.818 | 0.006       | 0.93 | 0.01         |
| 2.54          | 0.862 | 0.006       | 0.98 | 0.01         |
| 2.86          | 0.872 | 0.005       | 0.99 | 0.01         |
| 3.18          | 0.881 | 0.005       | 1.00 | 0.01         |
| 3.50          | 0.882 | 0.005       | 1.00 | 0.01         |
| 3.81          | 0.880 | 0.005       | 1.00 | 0.01         |



Table 5

15 MV SPD = 100cm

No Accessories

Field Size = 5.0cm X 5.0cm

Photon Backscatter N.D. = 0.002

| Depth<br>(cm) | ND    | Error in ND | TMR  | Error in TMR |
|---------------|-------|-------------|------|--------------|
| 0.00          | 0.002 | 0.001       | 0.00 | 0.00         |
| 0.16          | 0.173 | 0.010       | 0.19 | 0.01         |
| 0.32          | 0.304 | 0.010       | 0.33 | 0.01         |
| 0.48          | 0.407 | 0.010       | 0.44 | 0.01         |
| 0.64          | 0.504 | 0.009       | 0.55 | 0.01         |
| 0.95          | 0.633 | 0.009       | 0.69 | 0.01         |
| 1.27          | 0.728 | 0.008       | 0.79 | 0.01         |
| 1.91          | 0.840 | 0.007       | 0.91 | 0.01         |
| 2.54          | 0.897 | 0.006       | 0.97 | 0.01         |
| 2.86          | 0.910 | 0.006       | 0.99 | 0.01         |
| 3.18          | 0.917 | 0.006       | 1.00 | 0.01         |
| 3.50          | 0.922 | 0.006       | 1.00 | 0.01         |
| 3.81          | 0.920 | 0.005       | 1.00 | 0.01         |

15 MV SPD = 100cm

No Accessories

Field Size = 8.0cm X 8.0cm

Photon Backscatter N.D. = 0.004

| Depth<br>(cm) | ND    | Error in ND | TMR  | Error in TMR |
|---------------|-------|-------------|------|--------------|
| 0.00          | 0.004 | 0.001       | 0.00 | 0.00         |
| 0.16          | 0.194 | 0.012       | 0.20 | 0.01         |
| 0.32          | 0.332 | 0.012       | 0.34 | 0.01         |
| 0.48          | 0.439 | 0.011       | 0.46 | 0.02         |
| 0.64          | 0.532 | 0.011       | 0.55 | 0.02         |
| 0.95          | 0.669 | 0.010       | 0.69 | 0.02         |
| 1.27          | 0.765 | 0.010       | 0.79 | 0.02         |
| 1.91          | 0.881 | 0.008       | 0.91 | 0.01         |
| 2.54          | 0.940 | 0.007       | 0.98 | 0.01         |
| 2.86          | 0.953 | 0.007       | 0.99 | 0.01         |
| 3.18          | 0.957 | 0.007       | 0.99 | 0.01         |
| 3.50          | 0.964 | 0.007       | 1.00 | 0.01         |
| 3.81          | 0.963 | 0.006       | 1.00 | 0.01         |



Table 6

15 MV SPD = 100cm

No Accessories

Field Size = 10.0cm X 10.0cm

Photon Backscatter N.D. = 0.006

| Depth<br>(cm) | ND    | Error in ND | TMR  | Error in TMR |
|---------------|-------|-------------|------|--------------|
| 0.00          | 0.006 | 0.001       | 0.01 | 0.00         |
| 0.16          | 0.191 | 0.013       | 0.19 | 0.01         |
| 0.32          | 0.333 | 0.013       | 0.34 | 0.02         |
| 0.48          | 0.443 | 0.012       | 0.45 | 0.02         |
| 0.64          | 0.540 | 0.012       | 0.55 | 0.02         |
| 0.95          | 0.677 | 0.011       | 0.69 | 0.02         |
| 1.27          | 0.774 | 0.010       | 0.79 | 0.02         |
| 1.91          | 0.897 | 0.009       | 0.91 | 0.02         |
| 2.54          | 0.955 | 0.008       | 0.97 | 0.01         |
| 2.86          | 0.970 | 0.007       | 0.99 | 0.01         |
| 3.18          | 0.977 | 0.007       | 0.99 | 0.01         |
| 3.50          | 0.983 | 0.007       | 1.00 | 0.01         |
| 3.81          | 0.983 | 0.007       | 1.00 | 0.01         |

15 MV SPD = 100cm

No Accessories

Field Size = 12.0cm X 12.0cm

Photon Backscatter N.D. = 0.007

| Depth<br>(cm) | ND    | Error in ND | TMR  | Error in TMR |
|---------------|-------|-------------|------|--------------|
| 0.00          | 0.007 | 0.001       | 0.01 | 0.00         |
| 0.16          | 0.205 | 0.015       | 0.21 | 0.02         |
| 0.32          | 0.349 | 0.014       | 0.35 | 0.02         |
| 0.48          | 0.462 | 0.014       | 0.47 | 0.02         |
| 0.64          | 0.556 | 0.013       | 0.56 | 0.02         |
| 0.95          | 0.699 | 0.012       | 0.70 | 0.02         |
| 1.27          | 0.796 | 0.012       | 0.80 | 0.02         |
| 1.91          | 0.914 | 0.010       | 0.92 | 0.02         |
| 2.54          | 0.973 | 0.009       | 0.98 | 0.02         |
| 2.86          | 0.987 | 0.008       | 0.99 | 0.02         |
| 3.18          | 0.993 | 0.008       | 1.00 | 0.02         |
| 3.50          | 0.992 | 0.008       | 1.00 | 0.02         |
| 3.81          | 0.993 | 0.008       | 1.00 | 0.02         |





Table 7

15 MV    SPD = 100cm  
 No Accessories  
 Field Size = 15.0cm X 15.0cm  
 Photon Backscatter N.D. = 0.009

| Depth<br>(cm) | ND    | Error in ND | TMR  | Error in TMR |
|---------------|-------|-------------|------|--------------|
| 0.00          | 0.009 | 0.001       | 0.01 | 0.00         |
| 0.16          | 0.207 | 0.017       | 0.21 | 0.02         |
| 0.32          | 0.354 | 0.016       | 0.35 | 0.02         |
| 0.48          | 0.463 | 0.016       | 0.46 | 0.02         |
| 0.64          | 0.560 | 0.015       | 0.56 | 0.02         |
| 0.95          | 0.704 | 0.014       | 0.70 | 0.02         |
| 1.27          | 0.806 | 0.013       | 0.80 | 0.02         |
| 1.91          | 0.921 | 0.011       | 0.92 | 0.02         |
| 2.54          | 0.975 | 0.010       | 0.97 | 0.02         |
| 2.86          | 0.991 | 0.010       | 0.99 | 0.02         |
| 3.18          | 0.997 | 0.009       | 0.99 | 0.02         |
| 3.50          | 1.002 | 0.009       | 1.00 | 0.02         |
| 3.81          | 1.004 | 0.009       | 1.00 | 0.02         |

15 MV    SPD = 100cm  
 No Accessories  
 Field Size = 20.0cm X 20.0cm  
 Photon Backscatter N.D. = 0.012

| Depth<br>(cm) | ND    | Error in ND | TMR  | Error in TMR |
|---------------|-------|-------------|------|--------------|
| 0.00          | 0.012 | 0.002       | 0.01 | 0.00         |
| 0.16          | 0.205 | 0.020       | 0.20 | 0.02         |
| 0.32          | 0.353 | 0.020       | 0.35 | 0.02         |
| 0.48          | 0.462 | 0.019       | 0.46 | 0.02         |
| 0.64          | 0.565 | 0.018       | 0.56 | 0.02         |
| 0.95          | 0.708 | 0.017       | 0.70 | 0.02         |
| 1.27          | 0.802 | 0.016       | 0.80 | 0.02         |
| 1.91          | 0.922 | 0.014       | 0.92 | 0.02         |
| 2.54          | 0.982 | 0.012       | 0.98 | 0.02         |
| 2.86          | 0.997 | 0.011       | 0.99 | 0.02         |
| 3.18          | 1.001 | 0.011       | 0.99 | 0.02         |
| 3.50          | 1.004 | 0.011       | 1.00 | 0.02         |
| 3.81          | 1.007 | 0.011       | 1.00 | 0.02         |



Table 8

15 MV    SPD = 100cm  
 No Accessories  
 Field Size = 25.0cm X 25.0cm  
 Photon Backscatter N.D. = 0.015

| Depth<br>(cm) | ND    | Error in ND | TMR  | Error in TMR |
|---------------|-------|-------------|------|--------------|
| 0.00          | 0.015 | 0.002       | 0.01 | 0.00         |
| 0.16          | 0.208 | 0.024       | 0.21 | 0.03         |
| 0.32          | 0.357 | 0.023       | 0.36 | 0.03         |
| 0.48          | 0.471 | 0.022       | 0.47 | 0.03         |
| 0.64          | 0.565 | 0.022       | 0.56 | 0.03         |
| 0.95          | 0.710 | 0.020       | 0.71 | 0.03         |
| 1.27          | 0.802 | 0.019       | 0.80 | 0.03         |
| 1.91          | 0.919 | 0.016       | 0.92 | 0.03         |
| 2.54          | 0.977 | 0.014       | 0.97 | 0.03         |
| 2.86          | 0.994 | 0.014       | 0.99 | 0.03         |
| 3.18          | 0.999 | 0.013       | 0.99 | 0.03         |
| 3.50          | 1.001 | 0.013       | 1.00 | 0.03         |
| 3.81          | 1.004 | 0.013       | 1.00 | 0.03         |



Table 9

15 MV SPD = 75cm

No Accessories

Field Size = 10.0cm X 10.0cm

Photon Backscatter N.D. = 0.007

| Depth<br>(cm) | ND    | Error in ND | TMR  | Error in TMR |
|---------------|-------|-------------|------|--------------|
| 0.00          | 0.007 | 0.001       | 0.01 | 0.00         |
| 0.16          | 0.202 | 0.014       | 0.21 | 0.02         |
| 0.32          | 0.339 | 0.013       | 0.35 | 0.02         |
| 0.48          | 0.449 | 0.013       | 0.46 | 0.02         |
| 0.64          | 0.539 | 0.012       | 0.55 | 0.02         |
| 0.95          | 0.682 | 0.011       | 0.69 | 0.02         |
| 1.27          | 0.777 | 0.011       | 0.79 | 0.02         |
| 1.91          | 0.896 | 0.009       | 0.91 | 0.02         |
| 2.54          | 0.959 | 0.008       | 0.98 | 0.02         |
| 2.86          | 0.971 | 0.008       | 0.99 | 0.02         |
| 3.18          | 0.978 | 0.008       | 1.00 | 0.02         |
| 3.50          | 0.981 | 0.007       | 1.00 | 0.02         |
| 3.81          | 0.982 | 0.007       | 1.00 | 0.01         |

15 MV SPD = 75cm

0.64cm Lucite Accessory

Field Size = 10.0cm X 10.0cm

Photon Backscatter N.D. = 0.007

| Depth<br>(cm) | ND    | Error in ND | TMR  | Error in TMR |
|---------------|-------|-------------|------|--------------|
| 0.00          | 0.007 | 0.001       | 0.01 | 0.00         |
| 0.16          | 0.202 | 0.019       | 0.21 | 0.02         |
| 0.32          | 0.342 | 0.018       | 0.35 | 0.02         |
| 0.48          | 0.449 | 0.018       | 0.47 | 0.02         |
| 0.64          | 0.538 | 0.017       | 0.56 | 0.02         |
| 0.95          | 0.679 | 0.016       | 0.70 | 0.02         |
| 1.27          | 0.765 | 0.015       | 0.79 | 0.02         |
| 1.91          | 0.880 | 0.013       | 0.91 | 0.02         |
| 2.54          | 0.942 | 0.011       | 0.97 | 0.02         |
| 2.86          | 0.955 | 0.011       | 0.99 | 0.02         |
| 3.18          | 0.961 | 0.011       | 0.99 | 0.02         |
| 3.50          | 0.963 | 0.010       | 1.00 | 0.02         |
| 3.81          | 0.966 | 0.010       | 1.00 | 0.02         |



Table 10

15 MV SPD = 75cm

No Accessories

Field Size = 30.0cm X 30.0cm

Photon Backscatter N.D. = 0.018

| Depth<br>(cm) | ND    | Error in ND | TMR  | Error in TMR |
|---------------|-------|-------------|------|--------------|
| 0.00          | 0.018 | 0.002       | 0.02 | 0.00         |
| 0.16          | 0.210 | 0.029       | 0.21 | 0.03         |
| 0.32          | 0.353 | 0.028       | 0.35 | 0.03         |
| 0.48          | 0.462 | 0.027       | 0.46 | 0.03         |
| 0.64          | 0.551 | 0.026       | 0.55 | 0.03         |
| 0.95          | 0.692 | 0.024       | 0.69 | 0.03         |
| 1.27          | 0.782 | 0.023       | 0.78 | 0.03         |
| 1.91          | 0.900 | 0.020       | 0.90 | 0.03         |
| 2.54          | 0.967 | 0.017       | 0.97 | 0.03         |
| 2.86          | 0.984 | 0.016       | 0.99 | 0.03         |
| 3.18          | 0.991 | 0.016       | 0.99 | 0.03         |
| 3.50          | 0.995 | 0.016       | 1.00 | 0.03         |
| 3.81          | 0.998 | 0.015       | 1.00 | 0.03         |

15 MV SPD = 75cm

0.64cm Lucite Accessory

Field Size = 30.0cm X 30.0cm

Photon Backscatter N.D. = 0.018

| Depth<br>(cm) | ND    | Error in ND | TMR  | Error in TMR |
|---------------|-------|-------------|------|--------------|
| 0.00          | 0.018 | 0.002       | 0.02 | 0.00         |
| 0.16          | 0.180 | 0.045       | 0.19 | 0.05         |
| 0.32          | 0.302 | 0.043       | 0.32 | 0.05         |
| 0.48          | 0.390 | 0.042       | 0.41 | 0.05         |
| 0.64          | 0.463 | 0.041       | 0.49 | 0.06         |
| 0.95          | 0.599 | 0.037       | 0.63 | 0.06         |
| 1.27          | 0.680 | 0.035       | 0.72 | 0.06         |
| 1.91          | 0.816 | 0.031       | 0.86 | 0.05         |
| 2.54          | 0.901 | 0.027       | 0.95 | 0.05         |
| 2.86          | 0.927 | 0.026       | 0.98 | 0.05         |
| 3.18          | 0.936 | 0.026       | 0.99 | 0.05         |
| 3.50          | 0.946 | 0.025       | 1.00 | 0.05         |
| 3.81          | 0.948 | 0.024       | 1.00 | 0.05         |





Table 11

15 MV      SPD = 100cm  
 3.18cm Lucite Accessory  
 Field Size = 30.0cm X 30.0cm  
 Photon Backscatter N.D. = 0.013

| Depth<br>(cm) | ND    | Error in ND | TMR  | Error in TMR |
|---------------|-------|-------------|------|--------------|
| 0.00          | 0.013 | 0.002       | 0.01 | 0.00         |
| 0.16          | 0.171 | 0.028       | 0.17 | 0.03         |
| 0.32          | 0.319 | 0.027       | 0.31 | 0.03         |
| 0.48          | 0.433 | 0.026       | 0.42 | 0.03         |
| 0.64          | 0.537 | 0.025       | 0.52 | 0.03         |
| 0.95          | 0.686 | 0.023       | 0.67 | 0.03         |
| 1.27          | 0.782 | 0.022       | 0.76 | 0.03         |
| 1.91          | 0.914 | 0.019       | 0.89 | 0.03         |
| 2.54          | 0.987 | 0.017       | 0.96 | 0.03         |
| 2.86          | 1.004 | 0.016       | 0.98 | 0.03         |
| 3.18          | 1.014 | 0.016       | 0.99 | 0.03         |
| 3.50          | 1.019 | 0.015       | 1.00 | 0.03         |
| 3.81          | 1.024 | 0.015       | 1.00 | 0.03         |

15 MV      SPD = 140cm  
 No Accessories  
 Field Size = 30.0cm X 30.0cm  
 Photon Backscatter N.D. = 0.017

| Depth<br>(cm) | ND    | Error in ND | TMR  | Error in TMR |
|---------------|-------|-------------|------|--------------|
| 0.00          | 0.017 | 0.002       | 0.02 | 0.00         |
| 0.16          | 0.194 | 0.035       | 0.20 | 0.04         |
| 0.32          | 0.339 | 0.034       | 0.34 | 0.04         |
| 0.48          | 0.445 | 0.033       | 0.45 | 0.04         |
| 0.64          | 0.540 | 0.032       | 0.55 | 0.04         |
| 0.95          | 0.678 | 0.029       | 0.69 | 0.04         |
| 1.27          | 0.749 | 0.028       | 0.76 | 0.04         |
| 1.91          | 0.876 | 0.024       | 0.89 | 0.04         |
| 2.54          | 0.949 | 0.021       | 0.96 | 0.04         |
| 2.86          | 0.965 | 0.020       | 0.98 | 0.04         |
| 3.18          | 0.969 | 0.020       | 0.98 | 0.04         |
| 3.50          | 0.976 | 0.019       | 0.99 | 0.04         |
| 3.81          | 0.986 | 0.019       | 1.00 | 0.04         |



Table 12

6 MV SPD = 100cm

No Accessories

Field Size = 5.0cm X 5.0cm

Photon Backscatter N.D. = 0.002

| Depth<br>(cm) | ND    | Error in ND | TMR  | Error in TMR |
|---------------|-------|-------------|------|--------------|
| 0.00          | 0.002 | 0.001       | 0.00 | 0.00         |
| 0.16          | 0.391 | 0.011       | 0.42 | 0.02         |
| 0.32          | 0.581 | 0.010       | 0.62 | 0.02         |
| 0.48          | 0.698 | 0.009       | 0.75 | 0.02         |
| 0.64          | 0.785 | 0.008       | 0.84 | 0.02         |
| 0.95          | 0.878 | 0.008       | 0.94 | 0.02         |
| 1.27          | 0.917 | 0.007       | 0.99 | 0.02         |
| 1.91          | 0.930 | 0.007       | 1.00 | 0.02         |

6 MV SPD = 100cm

No Accessories

Field Size = 10.0cm X 10.0cm

Photon Backscatter N.D. = 0.009

| Depth<br>(cm) | ND    | Error in ND | TMR  | Error in TMR |
|---------------|-------|-------------|------|--------------|
| 0.00          | 0.009 | 0.001       | 0.01 | 0.00         |
| 0.16          | 0.420 | 0.014       | 0.43 | 0.02         |
| 0.32          | 0.617 | 0.012       | 0.63 | 0.02         |
| 0.48          | 0.739 | 0.011       | 0.76 | 0.02         |
| 0.64          | 0.831 | 0.010       | 0.85 | 0.02         |
| 0.95          | 0.926 | 0.009       | 0.95 | 0.02         |
| 1.27          | 0.968 | 0.009       | 0.99 | 0.02         |
| 1.91          | 0.978 | 0.009       | 1.00 | 0.02         |



Table 13

6 MV SPD = 100cm

No Accessories

Field Size = 20.0cm X 20.0cm

Photon Backscatter N.D. = 0.018

| Depth<br>(cm) | ND    | Error in ND | TMR  | Error in TMR |
|---------------|-------|-------------|------|--------------|
| 0.00          | 0.018 | 0.002       | 0.02 | 0.00         |
| 0.16          | 0.437 | 0.019       | 0.43 | 0.02         |
| 0.32          | 0.640 | 0.017       | 0.64 | 0.02         |
| 0.48          | 0.766 | 0.016       | 0.76 | 0.02         |
| 0.64          | 0.859 | 0.014       | 0.85 | 0.02         |
| 0.95          | 0.954 | 0.013       | 0.95 | 0.02         |
| 1.27          | 0.994 | 0.012       | 0.99 | 0.02         |
| 1.91          | 1.005 | 0.012       | 1.00 | 0.02         |

6 MV SPD = 100cm

No Accessories

Field Size = 30.0cm X 30.0cm

Photon Backscatter N.D. = 0.026

| Depth<br>(cm) | ND    | Error in ND | TMR  | Error in TMR |
|---------------|-------|-------------|------|--------------|
| 0.00          | 0.026 | 0.003       | 0.03 | 0.00         |
| 0.16          | 0.445 | 0.024       | 0.44 | 0.03         |
| 0.32          | 0.647 | 0.022       | 0.64 | 0.03         |
| 0.48          | 0.772 | 0.020       | 0.77 | 0.03         |
| 0.64          | 0.865 | 0.018       | 0.86 | 0.03         |
| 0.95          | 0.957 | 0.016       | 0.95 | 0.03         |
| 1.27          | 0.996 | 0.015       | 0.99 | 0.03         |
| 1.91          | 1.005 | 0.015       | 1.00 | 0.03         |



Table 14

6 MV SPD = 75cm

No Accessories

Field Size = 30.0cm X 30.0cm

Photon Backscatter N.D. = 0.029

| Depth<br>(cm) | ND    | Error in ND | TMR  | Error in TMR |
|---------------|-------|-------------|------|--------------|
| 0.00          | 0.029 | 0.003       | 0.03 | 0.00         |
| 0.16          | 0.468 | 0.026       | 0.46 | 0.03         |
| 0.32          | 0.667 | 0.023       | 0.66 | 0.03         |
| 0.48          | 0.789 | 0.021       | 0.78 | 0.03         |
| 0.64          | 0.878 | 0.019       | 0.87 | 0.03         |
| 0.95          | 0.966 | 0.017       | 0.96 | 0.03         |
| 1.27          | 1.003 | 0.016       | 0.99 | 0.03         |
| 1.91          | 1.011 | 0.016       | 1.00 | 0.03         |

6 MV SPD = 75cm

0.64cm Lucite Accessory

Field Size = 30.0cm X 30.0cm

Photon Backscatter N.D. = 0.029

| Depth<br>(cm) | ND    | Error in ND | TMR  | Error in TMR |
|---------------|-------|-------------|------|--------------|
| 0.00          | 0.029 | 0.003       | 0.03 | 0.00         |
| 0.16          | 0.481 | 0.038       | 0.49 | 0.05         |
| 0.32          | 0.658 | 0.034       | 0.67 | 0.05         |
| 0.48          | 0.763 | 0.032       | 0.78 | 0.05         |
| 0.64          | 0.852 | 0.029       | 0.87 | 0.05         |
| 0.95          | 0.937 | 0.026       | 0.96 | 0.05         |
| 1.27          | 0.973 | 0.025       | 0.99 | 0.05         |
| 1.91          | 0.981 | 0.024       | 1.00 | 0.05         |





Table 15

6 MV SPD = 75cm  
 3.18cm Lucite Accessory  
 Field Size = 30.0cm X 30.0cm  
 Photon Backscatter N.D. = 0.029

| Depth<br>(cm) | ND    | Error in ND | TMR  | Error in TMR |
|---------------|-------|-------------|------|--------------|
| 0.00          | 0.029 | 0.003       | 0.03 | 0.00         |
| 0.16          | 0.497 | 0.040       | 0.49 | 0.05         |
| 0.32          | 0.678 | 0.036       | 0.67 | 0.05         |
| 0.48          | 0.784 | 0.033       | 0.78 | 0.05         |
| 0.64          | 0.877 | 0.030       | 0.87 | 0.05         |
| 0.95          | 0.963 | 0.027       | 0.96 | 0.05         |
| 1.27          | 0.999 | 0.026       | 0.99 | 0.05         |
| 1.91          | 1.006 | 0.025       | 1.00 | 0.05         |

6 MV SPD = 100cm  
 3.18cm Lucite Accessory  
 Field Size = 10.0cm X 10.0cm  
 Photon Backscatter N.D. = 0.009

| Depth<br>(cm) | ND    | Error in ND | TMR  | Error in TMR |
|---------------|-------|-------------|------|--------------|
| 0.00          | 0.009 | 0.001       | 0.01 | 0.00         |
| 0.16          | 0.420 | 0.014       | 0.43 | 0.02         |
| 0.32          | 0.621 | 0.013       | 0.64 | 0.02         |
| 0.48          | 0.742 | 0.012       | 0.76 | 0.02         |
| 0.64          | 0.832 | 0.011       | 0.85 | 0.02         |
| 0.95          | 0.925 | 0.010       | 0.95 | 0.02         |
| 1.27          | 0.965 | 0.009       | 0.99 | 0.02         |
| 1.91          | 0.976 | 0.009       | 1.00 | 0.02         |



field size. The ratio of the phantom generated normalized dose at  $d_{\max}$  to the phantom generated normalized dose at a field size of 10 cm x 10 cm are the phantom generated output factors. Figures 65 and 66 illustrate the phantom generated output factors compared to the total output factors for 6 MV and 15 MV, respectively, as a function of field width. The phantom generated output factor increases as a function of field width due only to increased scatter to  $d_{\max}$  as a function of field width. The increase in output as a function of field width due to contamination has been removed. There is only a few percent difference between the total and phantom generated output factors because there is little contamination present at  $d_{\max}$ . However, the phantom generated output curve is greater than the total output curve at small field sizes and reaches a plateau at a field size greater than 20 cm x 20 cm.

Tables 4 to 8, 12 and 15 indicate that the phantom generated TMR curve is independent of field size. Tables 9 to 11, 14 and 15 illustrate that the phantom generated TMR curve is independent of SPD and the presence of accessories.



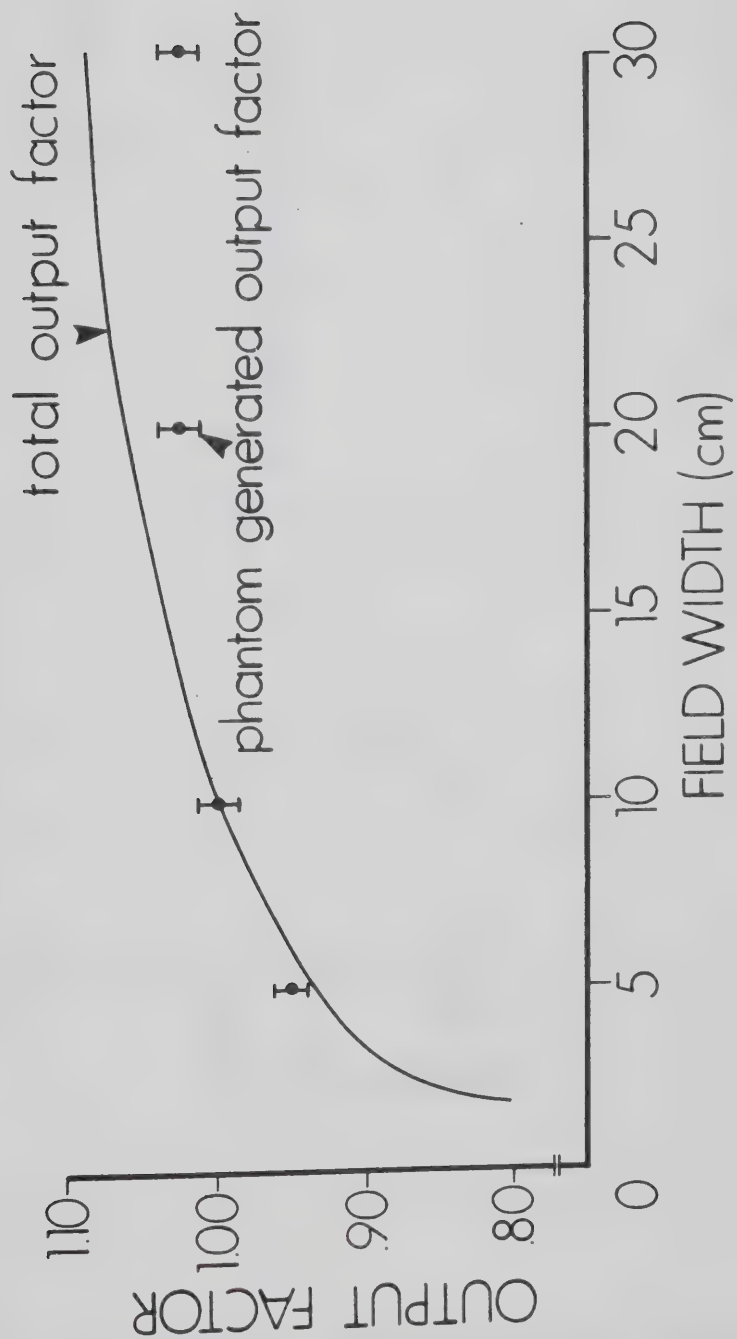


Figure 65. The phantom generated output factor curve compared to the total output factor curve at 6 MV.



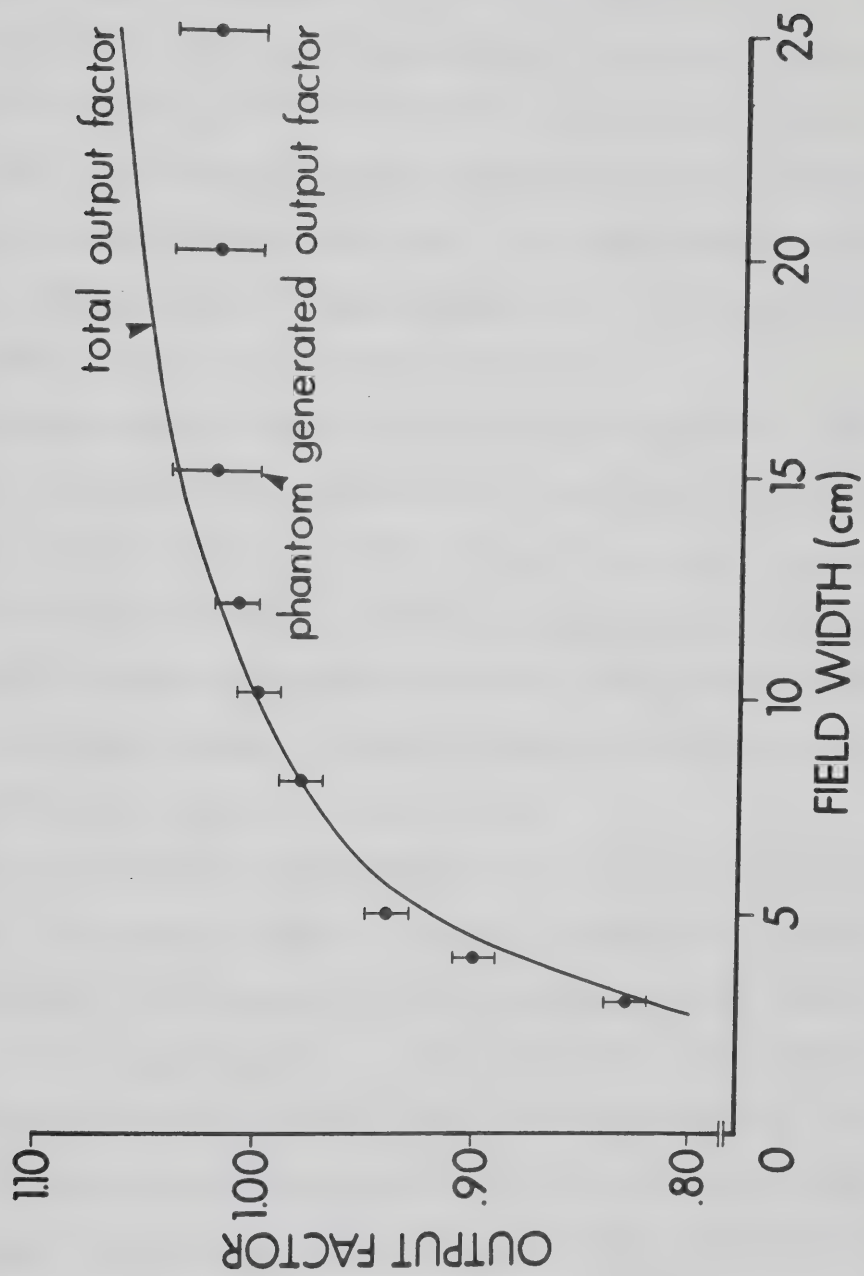


Figure 66. The phantom generated output factor curve compared to the total output factor curve at 15 MV.





## 2.12 Blocking the Primary Beam

A conical ingot of cerrobend or Lippowitz's metal (an alloy of lead, tin and bismuth which will attenuate half the dose in a thickness of 1.05 cm at 6 MV and 1.7 cm at 15 MV) 10 cm in length was produced such that the sides of the ingot were parallel to the beam direction when it was placed on the accessory tray. The ingot blocked the primary beam from a conical region of space underneath it. At 100 cm SPD the maximum diameter of the blocked region was 4.3 cm.

If the surface dose with the block in and out is constant, then the electron contamination and photon backscatter are not perturbed by the addition of the beam block. Table 16 lists the surface normalized dose at 100 cm SPD both with and without the beam block in place and the difference between these conditions under a variety of circumstances. There is a difference between the surface dose with the block in and out so the block does modify the surface dose.

A field size at 100 cm approximately 4 cm x 4 cm\* is being blocked by the ingot. The surface normalized dose for a beam of 4 cm x 4 cm with an accessory tray in place is listed in Table 16. The surface dose for a 4 cm x 4 cm field size is almost the same as the difference between the dose with the beam block in and the beam block out. The remainder is the contribution to the surface dose due to photon backscatter between 4 cm x 4 cm to the field size listed. Therefore, the beam block stops an amount of electron contamination corresponding to the projected area of the block at SPD = 100 cm as well as blocking the primary beam.

The normalized dose as a function of depth in a phantom was

\* The area of a 4.3 diameter circle is approximately the same as the area of a square with sides measuring 4 cm.



Table 16

Surface Normalized Dose At 100cm SPD  
 With And Without A Cerrobend Primary  
 Beam Block Present On The Accessory Tray

| Energy | Field Size  | Block<br>Out | Block<br>In | Difference        |
|--------|-------------|--------------|-------------|-------------------|
| 6 MV   | 10cm X 10cm | 0.169        | 0.071       | $0.098 \pm 0.007$ |
| 6 MV   | 20cm X 20cm | 0.300        | 0.204       | $0.096 \pm 0.007$ |
| 15 MV  | 20cm X 20cm | 0.271        | 0.220       | $0.051 \pm 0.004$ |

Surface Normalized Dose At 100cm SPD  
 With The Accessory Tray In Place For  
 A 4cm X 4cm Field Size

| Energy | Surface Normalized Dose |
|--------|-------------------------|
| 6 MV   | $0.092 \pm 0.005$       |
| 15 MV  | $0.048 \pm 0.003$       |



obtained with the block in and the block out. The difference between these readings is due to both a lack of the primary beam and a partial loss of contamination.

The loss of electron contamination is reflected by the loss of surface dose. If it is assumed that the scattered photon component of the contamination is attenuated by the beam block to the same extent as the electron component, then the contamination TMR curve obtained in Section 2.11.1 can be used to obtain the phantom generated N.D. and TMR for the portion of the beam blocked. This was obtained using the program Seprimary.For described in Section 2.11.2. The result is shown in Table 17. The phantom generated TMR values agree with the phantom generated TMR values obtained in Section 2.11.2.



Table 17      Difference Between The Primary Beam  
Blocked And Not Blocked With The  
Contamination Dose Removed

15 MV      SPD = 100cm  
0.064 Lucite Accessory Tray Left In When Block Removed  
Field Size = 20.0cm X 20.0cm  
Photon Backscatter N.D. = 0.003

| Depth<br>(cm) | ND    | Error in ND | TMR  | Error in TMR |
|---------------|-------|-------------|------|--------------|
| 0.00          | 0.003 | 0.003       | 0.00 | 0.00         |
| 0.16          | 0.200 | 0.017       | 0.21 | 0.02         |
| 0.32          | 0.336 | 0.016       | 0.36 | 0.02         |
| 0.48          | 0.447 | 0.016       | 0.47 | 0.02         |
| 0.64          | 0.543 | 0.015       | 0.58 | 0.02         |
| 0.95          | 0.675 | 0.014       | 0.72 | 0.02         |
| 1.27          | 0.765 | 0.013       | 0.81 | 0.02         |
| 1.91          | 0.874 | 0.011       | 0.93 | 0.02         |
| 2.54          | 0.923 | 0.009       | 0.98 | 0.02         |
| 2.86          | 0.935 | 0.009       | 0.99 | 0.02         |
| 3.18          | 0.939 | 0.009       | 1.00 | 0.02         |
| 3.50          | 0.941 | 0.008       | 1.00 | 0.02         |
| 3.81          | 0.939 | 0.008       | 1.00 | 0.02         |





### 2.13 Penetration Curve Outside a Magnetically Swept Field

The techniques described in Section 2.7 (Penetration Curves Outside the Field), Section 2.10 (Sweeping Electrons from the Field using a Permanent Magnet) and Section 2.11 (A Method for Separating Contamination from Phantom Generated Penetration Curves) can be used to determine the penetration curve of the scattered photon contamination component.

An ion chamber in a partial phantom as illustrated in Figure 30 was placed 3 cm outside an open 10 cm x 10 cm field. Readings as a function of the thickness of overlying phantom were obtained with the magnet in place. The probe was placed on the side of the field opposite to the direction of deflection of the electrons. The only contribution to the dose under these conditions is due to scattered photons and electrons produced in air between the magnet and the partial phantom. The readings as a function of overlying phantom normalized to the maximum reading obtained is shown in Figure 67. This curve is characteristic of photons. If it is assumed that the surface dose is entirely due to electrons produced in air (in other words, neglecting the backscatter surface dose produced by the scattered photons), then this contribution can be subtracted using the technique of Section 2.11. The result is also shown in Figure 67. The scattered photon build-up curve is characteristic of a megavoltage photon beam between 6 MV and 15 MV. The depth of the maximum dose is at approximately 2.5 cm compared to 1.6 cm for 6 MV and 3.5 cm for 15 MV.



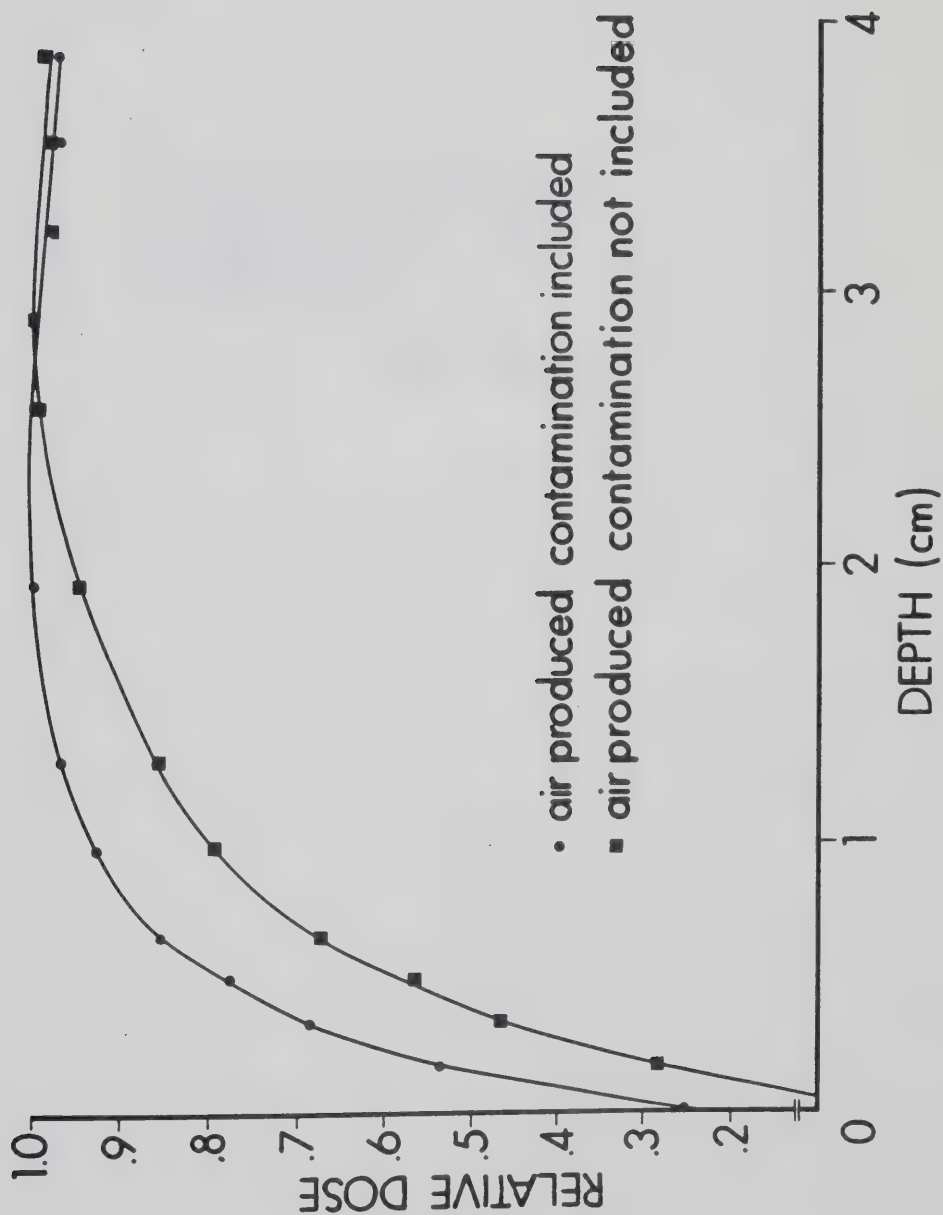


Figure 67. The scattered photon contamination build-up curve obtained 3 cm outside a magnetically swept 10 cm x 10 cm field at 100 cm SPD for the 15-MV beam.



### 3. DISCUSSION

It is truth very certain that,  
when it is not in our power  
to determine what is true  
we ought to know,  
what is probable.

René Descartes



### 3.1 Independent Modelling of the Phantom Generated Build-Up Curves

#### 3.1.1 Introduction

The phantom generated build-up curves were determined using a computer model. This was done to verify the phantom generated build-up curves produced by the subtraction of the contamination contribution from the total build-up curves. The computer program called Buildup3.For was written in Fortran -77 to run on the VMS operating system of a VAX 11/760 computer. Buildup3 is listed in Appendix 6. Buildup3 models the generation of charged particles set in motion in water from megavoltage photon spectra and has the capability to harden the spectra. The charged particles are followed through the phantom using the Monte Carlo method and the dose absorbed by the phantom is determined.

#### 3.1.2 Data Preparation Programs

Two additional programs prepared the look-up Tables for the program, Buildup3. The program, Quadint3.For, interpolates the total scattering and stopping power data. The program, Normdist.For, generates the value of the error function,  $\text{erf}(x)$ .

The amount of energy lost per unit path length, stopping power, and the root mean square angular scattering power for representative energies are stored in a data file called Master.Dat. Quadint3.For interpolates using the quadratic method (47), the scattering and stopping power data from Master.Dat. The output of Quadint3.For is a listing of the stopping and scattering power data for 0.1 MeV increments





in energy from 0.2 MeV to 18.0 MeV. This listing is stored in a file called Quadint3.Dat. Buildup3 reads the value of Quadint3.Dat before execution.

Normdist.For generates the error function, erf(x):

$$\text{erf}(x) = \frac{1}{\sqrt{\pi}} \int_{-x}^x e^{-(t^2)/2} dt \quad (3.1.1)$$

Normdist.For is listed in Appendix 7. The value of erf(x) represents the probability of a value of t being within the limits of integration,  $[-x, x]$ , if t follows a Gaussian distribution with a mean equal to 0 and a standard deviation equal to 1.

The file named Gaus.Dat lists the inverse error function from 0.00 to 0.99 in increments of 0.01. It was generated by interpolation of the inverse error function from the above values of the error function. Gaus.Dat is used to determine a normally distributed random scattering angle from a uniformly distributed random number between 0 and 1. Figure 68 graphically illustrates the procedure used in a number of places in the program and will be discussed further in the following section.

### 3.1.3 Generation of Charged Particles Set In Motion by Photons

Buildup3 requires the photon number spectrum to be entered as a function of photon energy. The number spectrum was not measured but was interpolated from spectra published in a paper by C.W. Sandifer and M. Taherzadeh of



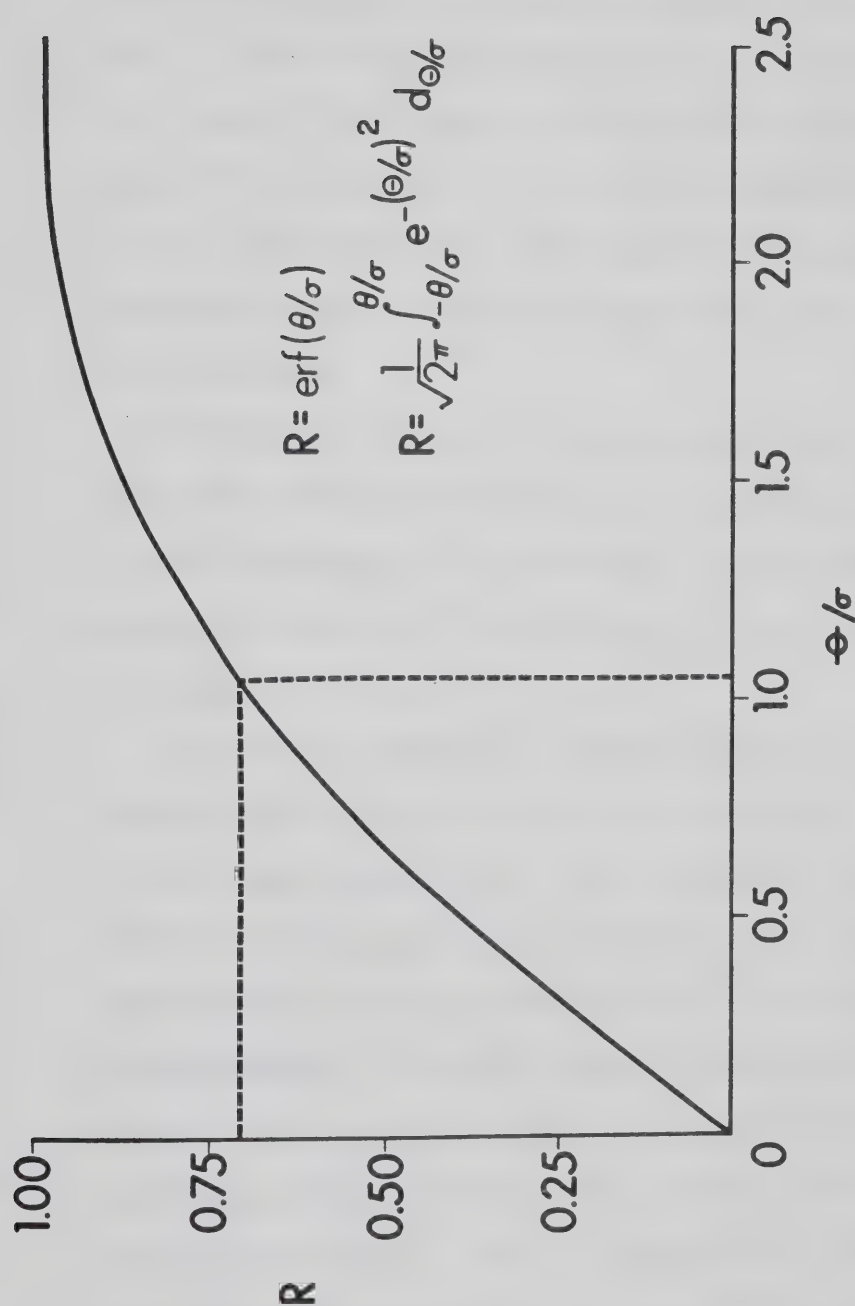


Figure 68. The probability of an angle,  $\theta$ , occurring when the root mean scattering angle,  $\sigma$ , is equal to  $R$ . Conversely, if a random number,  $R$ , between 0 and 1 is chosen, a ratio,  $\theta/\sigma$ , can be found. Knowing  $\sigma$ , then  $\theta$  is determined. This figure illustrates that a random number of 0.71 results in a value of  $\theta/\sigma$  of 1.06.



E.G. and G. Inc. (48). They measured thick-target bremsstrahlung spectra produced by electrons impinging on a 0.2 radiation-length gold-tungsten ( $Z$  of gold = 79,  $Z$  of tungsten = 74) target for electron energies in the range of 5.3 to 20.9 MeV. The electrons were accelerated by a  $90^\circ$  bent beam linac. An aluminum block was placed behind the target to absorb low energy electrons emerging from the target.

The Siemens Mevatron -20 and Mevatron -6 are similar except for a number of features. The target is pure gold in both the Mevatron -20 and Mevatron -6. The Siemens accelerators have a  $270^\circ$  bend instead of the research accelerator's  $90^\circ$  bend.

Sandifer and Taherzadeh measured spectra produced by electron energies very close to the nominal photon energies of the Siemens accelerators; 5.3 MV compared to the Siemens 6 MV and 14.8 MV compared to the Siemens 15 MV. The desired Siemens nominal energy was determined by normalizing the nearest measured differential energy spectra greater than and less than the desired energy to unity and linearly interpolating between these spectra to obtain the spectrum at the desired energy. Table 18 summarizes the determination of the 6 MV differential spectrum. The number spectrum, which is the number of photons in discrete bins as a function of energy, is determined by multiplying the value of the differential spectrum of an energy bin by the energy



Table 18      Determination of the 6 MV Differential  
Spectrum from Measured Spectra

| Maximum<br>Bin<br>Energy<br>(MeV) | Experimental                     |                                   | Derived                          |
|-----------------------------------|----------------------------------|-----------------------------------|----------------------------------|
|                                   | 5.3 MV<br>dN/dh $\nu$<br>(1/MeV) | 10.0 MV<br>dN/dh $\nu$<br>(1/MeV) | 6.0 MV<br>dN/dh $\nu$<br>(1/MeV) |
| 0.16                              | 5.34 X 10 <sup>-1</sup>          | 2.53 X 10 <sup>-1</sup>           | 4.92 X 10 <sup>-1</sup>          |
| 0.25                              | 1.00                             | 1.00                              | 1.00                             |
| 0.36                              | 7.00 X 10 <sup>-1</sup>          | 6.76 X 10 <sup>-1</sup>           | 6.96 X 10 <sup>-1</sup>          |
| 0.49                              | 6.51 X 10 <sup>-1</sup>          | 6.05 X 10 <sup>-1</sup>           | 6.44 X 10 <sup>-1</sup>          |
| 0.64                              | 5.49 X 10 <sup>-1</sup>          | 4.94 X 10 <sup>-1</sup>           | 5.41 X 10 <sup>-1</sup>          |
| 0.81                              | 4.86 X 10 <sup>-1</sup>          | 4.39 X 10 <sup>-1</sup>           | 4.79 X 10 <sup>-1</sup>          |
| 1.00                              | 4.11 X 10 <sup>-1</sup>          | 3.58 X 10 <sup>-1</sup>           | 4.03 X 10 <sup>-1</sup>          |
| 1.21                              | 2.83 X 10 <sup>-1</sup>          | 2.74 X 10 <sup>-1</sup>           | 2.82 X 10 <sup>-1</sup>          |
| 1.44                              | 2.37 X 10 <sup>-1</sup>          | 2.38 X 10 <sup>-1</sup>           | 2.37 X 10 <sup>-1</sup>          |
| 1.69                              | 1.92 X 10 <sup>-1</sup>          | 2.18 X 10 <sup>-1</sup>           | 1.96 X 10 <sup>-1</sup>          |
| 1.96                              | 1.62 X 10 <sup>-1</sup>          | 1.98 X 10 <sup>-1</sup>           | 1.67 X 10 <sup>-1</sup>          |
| 2.25                              | 1.40 X 10 <sup>-1</sup>          | 1.80 X 10 <sup>-1</sup>           | 1.46 X 10 <sup>-1</sup>          |
| 2.56                              | 1.09 X 10 <sup>-1</sup>          | 1.59 X 10 <sup>-1</sup>           | 1.16 X 10 <sup>-1</sup>          |
| 2.89                              | 1.00 X 10 <sup>-1</sup>          | 1.37 X 10 <sup>-1</sup>           | 1.06 X 10 <sup>-1</sup>          |
| 3.24                              | 8.34 X 10 <sup>-2</sup>          | 1.32 X 10 <sup>-1</sup>           | 9.06 X 10 <sup>-2</sup>          |
| 3.61                              | 6.43 X 10 <sup>-2</sup>          | 1.14 X 10 <sup>-1</sup>           | 7.17 X 10 <sup>-2</sup>          |
| 4.00                              | 5.63 X 10 <sup>-2</sup>          | 9.80 X 10 <sup>-2</sup>           | 6.25 X 10 <sup>-2</sup>          |
| 4.41                              | 4.17 X 10 <sup>-2</sup>          | 1.01 X 10 <sup>-1</sup>           | 5.05 X 10 <sup>-2</sup>          |
| 4.81                              | 2.51 X 10 <sup>-2</sup>          | 8.67 X 10 <sup>-2</sup>           | 3.43 X 10 <sup>-2</sup>          |
| 5.29                              | 8.20 X 10 <sup>-3</sup>          | 7.61 X 10 <sup>-2</sup>           | 1.83 X 10 <sup>-2</sup>          |
| 5.76                              | 2.67 X 10 <sup>-3</sup>          | 7.24 X 10 <sup>-2</sup>           | 1.31 X 10 <sup>-2</sup>          |





width of the bin:

$$N_i = \left( \frac{dn}{dh\nu} \right)_i (\Delta h\nu)_i \quad (3.1.2)$$

where  $(\Delta h\nu)_i$  is the width of the bin

$\left( \frac{dn}{dh\nu} \right)_i$  is the value of the differential energy spectrum at the bin energy

$N_i$  is the number of photons in the energy bin

The number spectrum is smoothed graphically (see Figures 69 and 70) and is normalized so that the sum of the bins is unity:

$$F_i = \frac{\tilde{N}_i}{\sum_i \tilde{N}_i} \quad (3.1.3)$$

where  $\tilde{N}_i$  is the smoothed value of number spectrum at the bin energy

$F_i$  is the smoothed normalized number spectrum at the bin energy

The mean energy of the photon number spectrum is determined by a linear weighting with respect to energy:

$$\overline{h\nu} = \frac{\sum_i F_i (h\nu)_i}{\sum_i F_i} = \sum_i F_i (h\nu)_i \quad (3.1.4)$$

because  $\sum_i F_i = 1$

where  $\overline{h\nu}$  is the mean value of the photon number spectrum

The mean value of the 6 MV photon beam is 1.5 MeV and the mean value of the 15 MV photon beam is 3.9 MeV.

The central energy of the photon bin, the value of the number spectrum,  $F_i$ , the total attenuation coefficient,



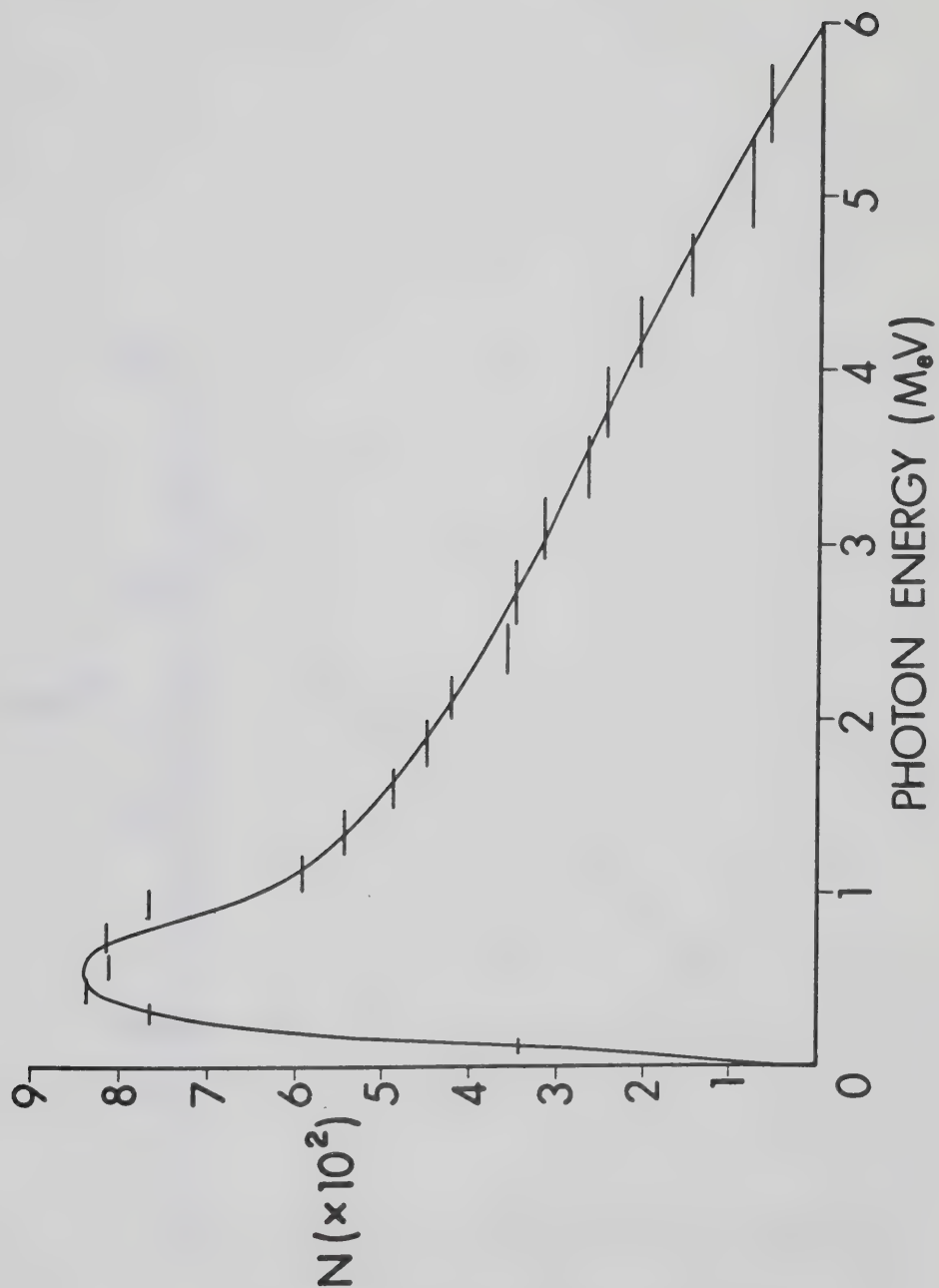


Figure 69. The smoothed and unsmoothed unnormalized primary photon number spectrum at 6 MV.



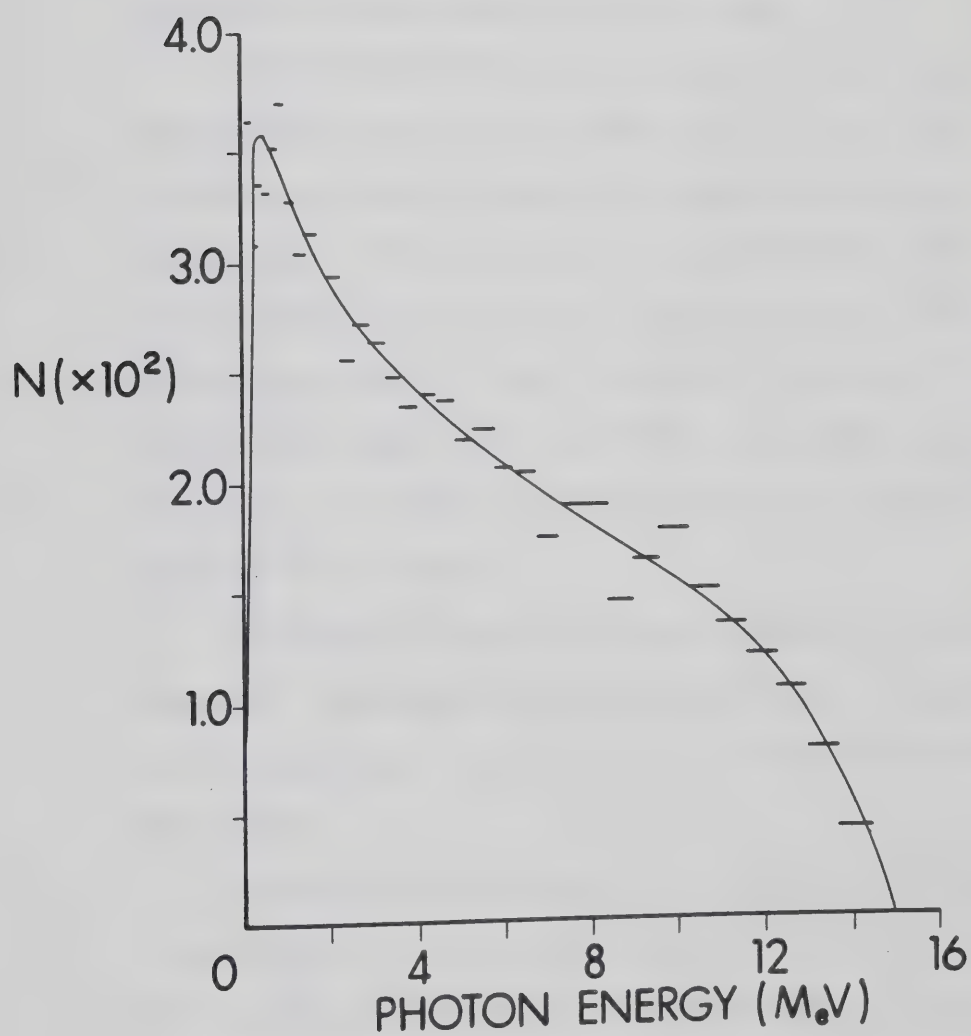


Figure 70. The smoothed and unsmoothed unnormalized primary photon number spectrum at 15 MV.



$\mu_{\text{tot}}/\rho$  for water, and the total Compton absorption coefficient,  $\sigma_{\text{tot}}/\rho$  for water, are listed in files named Photon6 for 6 MV and Photon15 for 15 MV.

The subroutine, Impulse, generates the charged particle set in motion spectrum due to photon interactions in a 1 mm slab of water. The photons are assumed to be initially directed normally into the slab.

The maximum photoelectric attenuation coefficient for the spectrum occurs at the lowest energy bin (0.13 MeV) and is the only 2% of the value of the Compton attenuation coefficient. The ratio between the photoelectric and Compton attenuation coefficients for the center of the second energy bin (0.21 MeV) is only 0.5% and the ratio for the third energy bin (0.31 MeV) is less than 0.1% (9). Therefore, the photoelectric effect need not be and was not taken into account.

A flow chart of the subroutine, Impulse, is shown in Figure 71. The loop at the left of the figure is repeated for both the Compton and, if required, the pair production interactions.

The number of photons from each photon energy bin in a 1 mm slab,  $N_i'$ , (the variable used in the program for  $N_i'$  is  $\text{nteract}(i)$ , that is,  $N_i' \rightarrow \text{nteract}(i)*$ ), is determined knowing the number fluence incident on the slab,  $F_i$ , and the total mass attenuation coefficient,  $(\mu_t/\rho)_i$

$((\mu_t/\rho)_i \rightarrow \text{mu}(i)*):$

\* The arrow indicates a transformation from a mathematical variable to a variable or array element defined in a program if the variables are different.





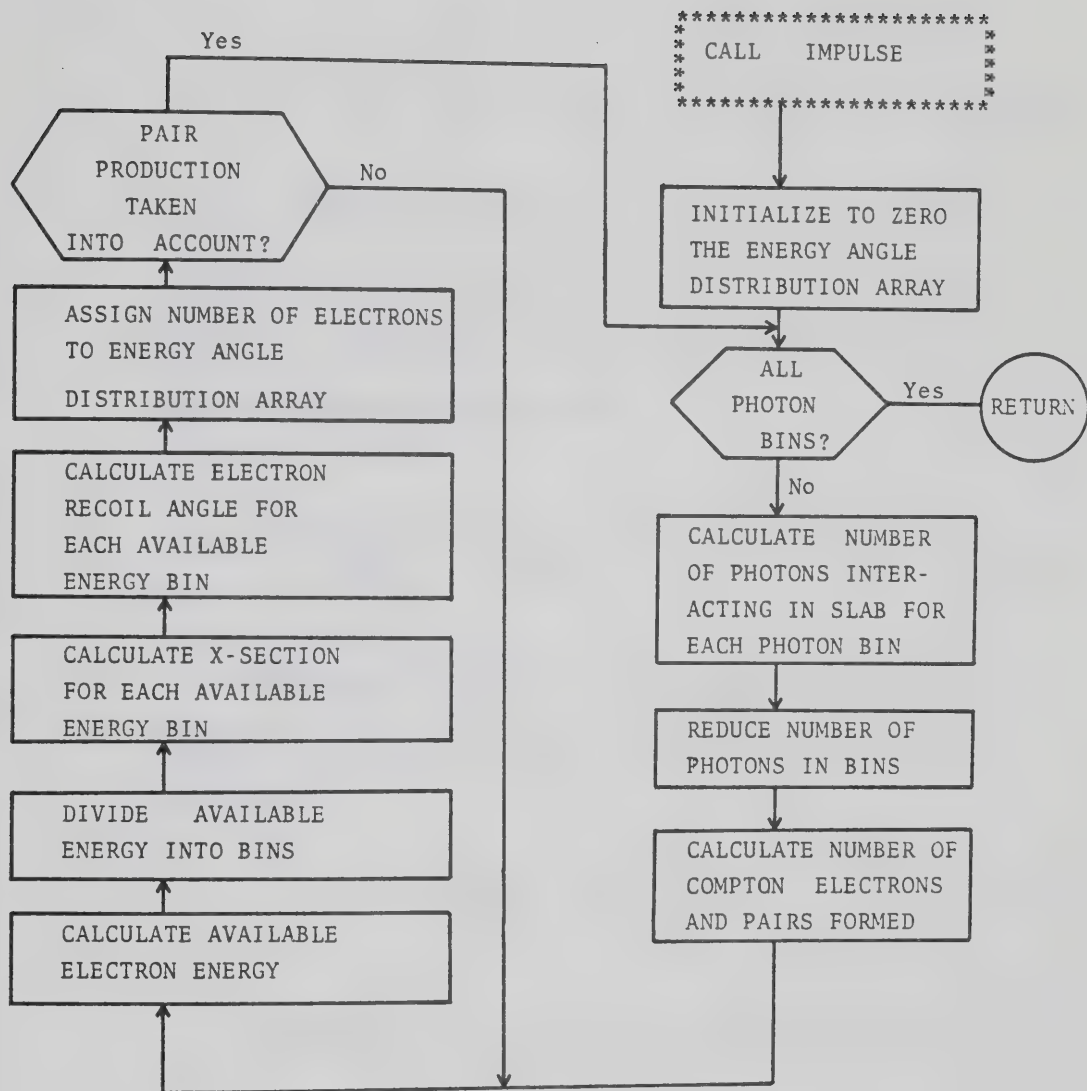


Figure 71. A flow chart for the subroutine, Impulse. The loop at the left is repeated for both Compton and pair production interactions.



$$N_i' = F_i (1 - e^{-(\mu_t/\rho)_i (0.1 \text{ g/cm}^2)}) \quad (3.1.5)$$

If the Compton scattered photons do not interact again (corresponding to narrow beam geometry), then the only photon bin which needs to be modified is the bin from which the primary photon came:

$$(F_i)_{\text{slab after}} = (F_i)_{\text{slab before}} e^{-(\mu_{\text{tot}}/\rho)_i (0.1 \text{ g/cm}^2)} \quad (3.1.6)$$

The number of the interacting photons at a given energy bin due to the Compton interaction,  $\text{NCOMP}_i$ , is given by:

$$\text{NCOMP}_i = \frac{(\sigma_{\text{tot}}/\rho)_i}{(\mu_{\text{tot}}/\rho)_i} N_i' \quad (3.1.7)$$

The number due to pair production,  $\text{NPP}_i$ , is given by:

$$\text{NPP}_i = 2(N_i' - \text{NCOMP}_i) \quad (3.1.8)$$

The above expression assumes that positrons can be treated like electrons. Additionally, the total attenuation coefficient takes into account pair production in the field of atomic electrons, "triplet production", however, the factor 2 does not take this completely into account. At the mean photon energy of the 15 MV beam ( $\sim 4 \text{ MeV}$ ), the



triplet cross-section is about 3% of the pair production cross-section and the pair production cross-section is, in turn, only about 6% of the total attenuation cross-section (9). This results in slightly fewer charged particles with a slightly larger mean energy. The failure to take into account triplet production rigorously will not significantly affect the distribution of charged particles set in motion.

The kinetic energy available to a charged particle is always less than the photon energy,  $h\nu(h\nu \rightarrow \text{xnrg}(i))$ . The maximum energy of a Compton electron,  $T_{\text{max}}$ , ( $T_{\text{max}} \rightarrow \text{nrgmax}$ ), can be derived from the conservation of energy and momentum:

$$T_{\text{max}} = \frac{2\alpha_0}{2\alpha_0 + 1} h\nu \quad (3.1.9)$$

The electron may have any energy up to and including the energy,  $T_{\text{max}}$ . The difference between the photon energy and the kinetic energy of the recoil electron,  $T$ , is the energy of the scattered photon.

The available kinetic energy of the pair production interaction,  $T_A$  ( $T_A \rightarrow \text{nrgmax}$ ), must be shared between the electron and positron:

$$T_A = h\nu - 1.022 \text{ MeV} \quad (3.1.10)$$

where 1.022 MeV represents the combined rest mass of the electron and positron.

The available kinetic energy is divided evenly into



20 bins. The kinetic energy dependent part of the differential cross-section with respect to kinetic energy is calculated at each of the 20 kinetic energy bins. The kinetic energy differential cross-section for the Compton effect  $d\sigma/dT$  is given by the Klein-Nishina equation (see Equations 1.2.5 and 1.2.6).

The absolute differential cross-section is not calculated because it is not needed. The number of photons interacting by the Compton effect is known (see Eqn. 3.1.7). The relative number interacting at each available kinetic energy bin is determined by normalizing each cross-section factor,  $C(h\nu, T_i)$ , to the sum,  $\sum_i C(h\nu, T_i)$ , where the sum is carried out over all 20 available kinetic energy bins.

The differential cross-section for the pair production interaction,  $d\pi/dT$ , is given by Equations 1.2.7, 1.2.8 and 1.2.9. When considering the Compton interaction calculation, the kinetic energy dependent part of the differential cross-section,  $P(h\nu, T)$ , needs to be calculated. The sum,  $\sum_i P(h\nu, T_i)$ , is used to normalize the cross-section so that the appropriate number of electrons is set in motion at each energy,  $T_i$ .

The initial zenith direction of the Compton recoil electron, with respect to the primary photon direction,  $\theta$ , is given by Equation 1.2.4. If Equations 1.2.3 and 1.2.4 are combined with Equation 3.1.9, the Compton





electron, with respect to the primary photon direction,  $\theta$ , is given by Equation 1.2.4. If Equations 1.2.3 and 1.2.4 are combined with Equation 3.1.9, the Compton electron recoil angle,  $\theta$ , can be determined:

$$\theta = \arctan \left( \frac{1}{1+\alpha_0} \frac{\sqrt{(T_{\max} - T)(2\alpha_0 + 1)}}{\sqrt{T}} \right) \quad (3.1.11)$$

An element of the energy-angle distribution array is incremented by an amount corresponding to the number of electrons set in motion at that kinetic energy and zenith angle:

$$S_{k\ell} = S_{k\ell} + N_{\text{COMP}} \frac{C(h\nu, T_i)}{\sum_i C(h\nu, T_i)} \quad (3.1.12)$$

where  $S_{k\ell}$  ( $S_{k\ell} \rightarrow \text{SPECTR}(k, \ell)$ ) is the energy-angle distribution array

$k$  is the energy bin number

$\ell$  is the angle bin number

The available kinetic energy bins, represented by  $i$  for the calculation of the number of interactions at each available energy, is not the same as the energy-angle distribution kinetic energy bin, represented by  $k$ , in the above expression. There are 90 energy bins for the energy-angle distribution array spaced evenly between 0.0 and 18.0 MeV. Each energy bin of the energy-angle distribution is 0.2 MeV wide. Therefore, if the primary photon energy is low, many available kinetic energy bins may be mapped into one energy bin of the energy-angle distribution array.

There are 36 angle bins, represented by  $\ell$ , in



Equation 3.1.12 to cover any zenith angle between 0 and  $180^\circ$ . The 36 bins are distributed uniformly so that each bin is  $5^\circ$  wide. It is assumed that the initial zenith angle for the bin equals the center of the bin. Therefore, the possible initial zenith angles are ( $2.5^\circ$ ,  $7.5^\circ$ ,  $12.5^\circ$ ...  $177.5^\circ$ ). The maximum zenith angle for an electron produced by a Compton photon interaction is  $90^\circ$ , however, there is a small possibility of a charged particle having an angle greater than  $90^\circ$  when produced by the pair production effect.

The root mean square zenith angle,  $\langle \phi^2 \rangle^{\frac{1}{2}}$ , between the trajectory of a charged particle and that of the primary photon is given by Equation 1.2.11. It is assumed that the distribution is Gaussian (5).

The zenith scattering angle is chosen by the direct or inversion method of random sampling. The cumulative probability,  $P(t)$ , associated with a random variable,  $T$ , is:

$$P(t) = \text{Probability } (T < t) \quad (3.1.13)$$

If  $P(t)$  is normalized, then  $0 < P(t) < 1$ . By generating a random number,  $R$ , such that  $0 < R < 1$ , and identifying  $R$  with  $P(t)$ , a random sample,  $T$ , may be obtained from the distribution,  $P(t)$ , by inversion (49). The cumulative probability for a particle having a zenith angle,  $\phi$  ( $\phi \rightarrow g$ ), when the root mean square angle is  $\langle \phi^2 \rangle^{\frac{1}{2}}$ , is given by:

$$P(t) = \text{erf}(t) = \frac{1}{\sqrt{2\pi}} \int_0^t e^{-t'^2/2} dt' \quad (3.1.14)$$



where  $t = \phi / \langle \phi^2 \rangle^{1/2}$

A numerical method was chosen to invert the above expression.  $P(t)$  was generated for values of  $t$  between 0 and 3.0. The value of  $t$  as a function of  $P(t)$  is listed in the file, Gaus.Dat. A random number,  $R$ , is chosen and is identified with  $P(t)$ . A value,  $t$ , corresponding to  $P(t)$  is obtained from a look-up table (see Figure 68).

After the charged particles have been set in motion by photons from all the photon bins, the energy-angle distribution is passed back to the main program of Buildup3. The angular distribution is shown in Figure 72 for a 15 MV beam interacting in a slab 0.1 cm thick. The mean charged particle energy (in MeV) is indicated as the numbers in the bins. The characteristic bilobal forward peaked distribution is evident. The forward directed charged particles have a much higher energy than the charged particles set in motion at larger angles. There are very few electrons set in motion at angles greater than  $60^\circ$  from the initial photon direction.

#### 3.1.4 The Monte Carlo Program

Monte Carlo methods are applied to the solution of physical problems when the microscopic behaviour is better understood than the macroscopic behaviour or the geometry of the problem does not lend itself to a closed analytic solution. The process to be studied must have some intrinsic random nature. In the case of charged particle interactions with matter, the slowing down and



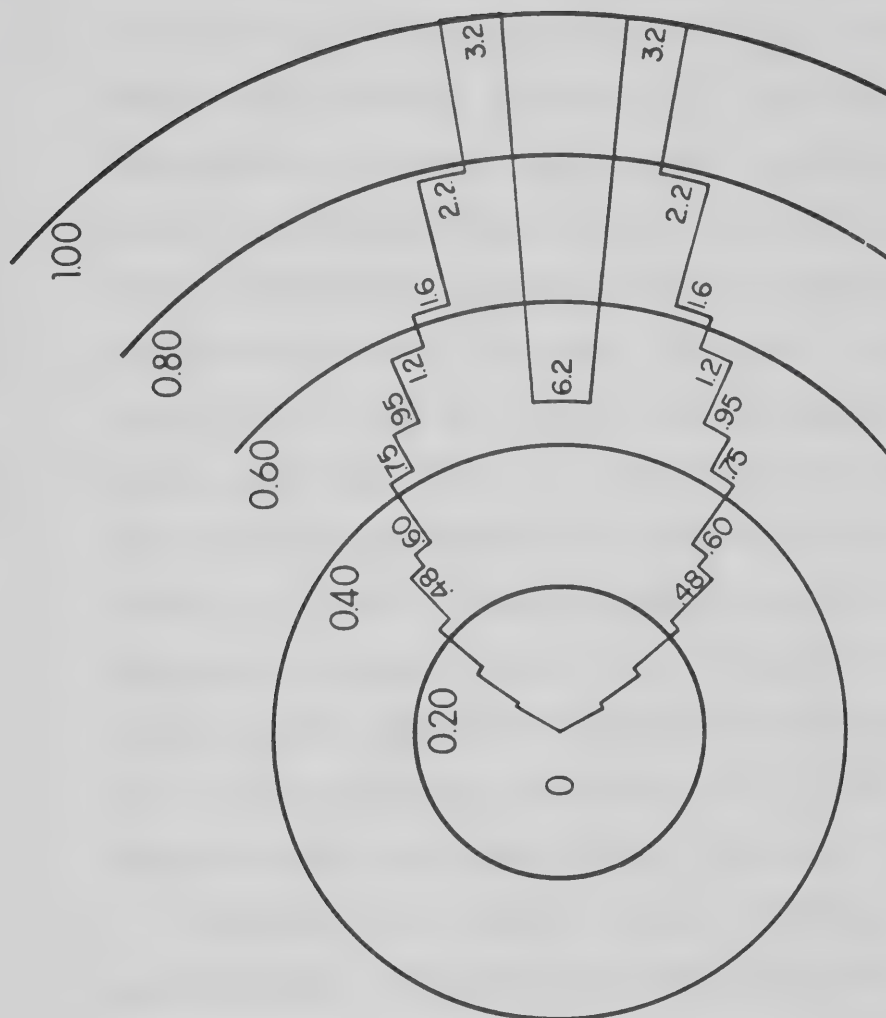


Figure 72. The angular distribution of charged particles interacting in a 0.1 cm slab at 15 MV. The mean charged particle energy (in MeV) is indicated by the numbers in the histogram. Each angle bin is  $5^\circ$  wide.





the scattering direction is microscopically indeterminate.

The number of Coulomb interactions resulting in ionization and excitation of water molecules per centimeter of path length is as high as  $10^5$ . It would be impractical to model every interaction. The total path length of an electron (the distance required to come to rest in the phantom) is approximated by a number of sub-path lengths or steps. Each step, therefore, is part of a random walk. At the end of each step the combined effects of many collisions are taken into account. The amount of energy lost and, therefore, the dose deposited in the phantom, the amount of scattering and the position of the electron is evaluated for each step. The electron is considered to have stopped when its kinetic energy falls below the cut-off energy which was chosen to be 0.2 MeV.\* The remaining energy is deposited in the slab where this occurs.

This Monte Carlo algorithm employs two major approximations: the continuous slowing down approximation, C.S.D.A., and the Gaussian scattering approximation. In the C.S.D.A., fluctuations of energy loss are disregarded and the particle is taken to be a deterministic function of the path length travelled. In the Gaussian approximation, the net angular multiple scattering deflections are the result of the combined effect of many small individual deflections. This leads to a Gaussian distribution of the zenith scattering angle.

\* The mean range at this energy is much less than the slab thickness of 0.1 cm.



The flow chart of the Monte Carlo algorithm is illustrated in Figure 73. The number of histories followed at a given energy and angle depends on the value of the energy-angle distribution as calculated by the subroutine, Impulse. The value of the energy-angle distribution, a floating-point array, is converted to an integer. This integer is decremented by one for each history followed.

The initial position and the cosine and sine of the zenith and azimuthal angles of the charged particles are determined. It is assumed that all the charged particles generated in a slab are set in motion half way through the slab. The initial sine and cosine of the zenith scattering angle are determined by the angle bin number that specifies the energy-angle distribution array. The initial azimuthal angle is randomly distributed through  $2\pi$  radians.

A history can end only if one of two conditions are met; the energy of the particle falls below 0.2 MeV or the particle leaves the phantom. The first condition is top tested in the Monte Carlo step loop (see Figure 73). The test to see if the particle has left the phantom is bottom tested. Since the phantom is semi-infinite in extent, a particle can only leave the phantom from the top surface.

The energy lost in each step is a constant fraction of the energy at the beginning of the step. Such an



THE FOLLOWING IS REPEATED FOR ALL HISTORIES AT EACH  
ELECTRON ENERGY AND ANGLE

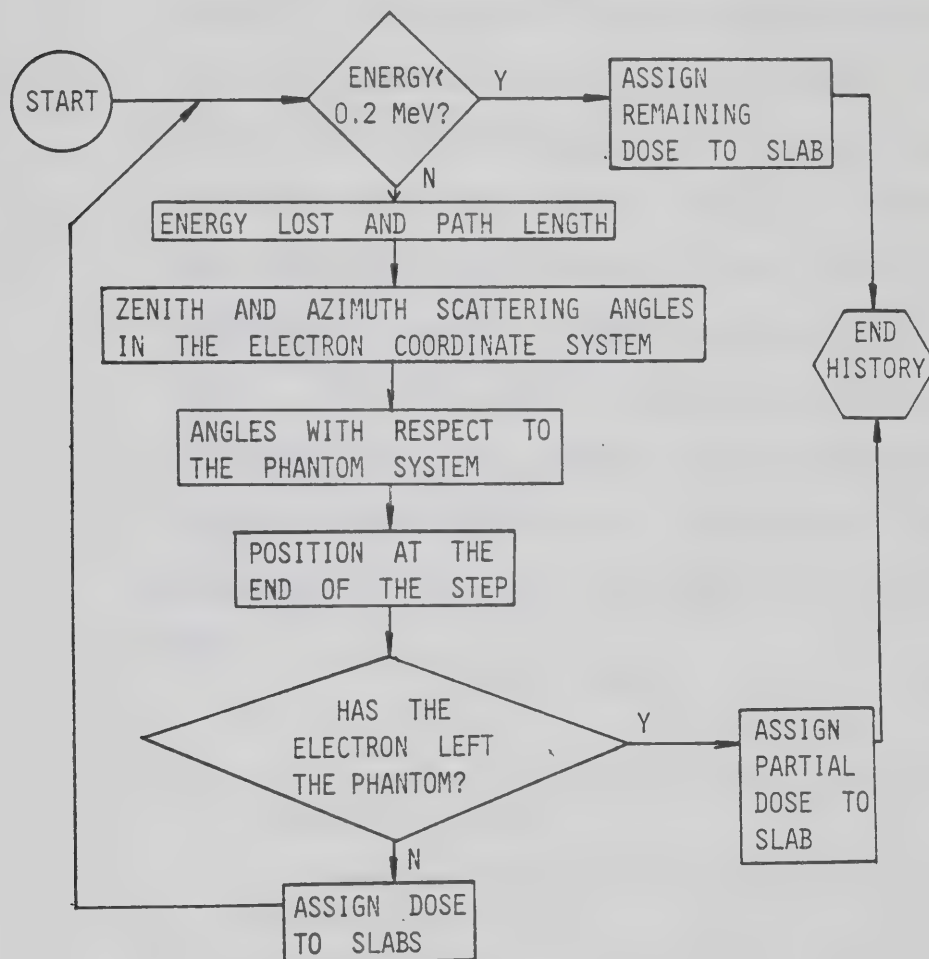


Figure 73. A flow chart for the Monte Carlo section of the main program of Buildup3.For.



energy loss criteria is called logarithmic spacing because the length of the step,  $\Delta S$ , decreases logarithmically as a function of path length traversed through the phantom. Logarithmic spacing has the advantage that the average zenith angle changes little from step to step. The smaller the fraction of energy lost per step the greater the number of steps required to model the history. This will result in a more accurate depiction of the history, but it will require more time to execute. A fractional energy loss factor of 0.1 was chosen as a compromise between the contradictory demands of accuracy and speed:

$$(\Delta T)_j = 0.1 T_j \quad (3.1.15)$$

where  $(\Delta T)_j$  is the particle kinetic energy lost in the  $j^{\text{th}}$  step  $((\Delta T)_j \rightarrow EP)$

$T_j$  is the particle kinetic energy at the beginning of the step  $(T_j \rightarrow E)$

The number of steps required to complete a history is:

$$\frac{\text{Number of Steps}}{\text{History}} = 15.3 + \frac{\ln(T_o)}{0.105} \quad (3.1.16)$$

where  $T_o$  ( $T_o \rightarrow E0$ ) is the initial energy of the particle (Note: the number of steps/history is an integer. The result of the previous expression must be rounded up to the nearest integer.) Therefore, a particle with an initial energy of 1.0 MeV will require 16 steps and a





particle with  $T_0 = 10$  MeV will require 38 steps to complete its history.

The path length traversed in a step is given by:

$$(\Delta S)_j = \frac{(\Delta T)_j}{\left[ \frac{dT}{dS} \right]_{T_j - ((\Delta T)_j)/2}} \quad (3.1.17)$$

where  $(\Delta S)_j$  is the path length

$$\left[ \frac{dT}{dS} \right]_{T_j - ((\Delta T)_j)/2} \quad \text{is the stopping power for the particle energy half way through the step}$$

The zenith scattering angle is the cumulative amount of scatter that occurs in a step so the angle is measured with respect to the direction of the particle at the beginning of the step.

The scattering angle is obtained by:

$$\phi = \langle \phi^2 \rangle^{1/2} t \quad (3.1.18)$$

where  $t$  is determined from random sampling (see Figure 68, Sections 3.1.2 and 3.1.3 for more details).

The azimuthal angle of scattering in the step, with respect to the direction at the beginning of the step, is chosen at random to lie in any  $2\pi$  direction.

The subroutine, Geom, transforms the zenith and azimuthal angle in the coordinate system travelling with the particle to the coordinate system "attached" to the phantom. The algorithm will be discussed in more detail later (see Section 3.1.5).



The distance travelled in the  $z$ , or depth direction, (the direction perpendicular to the phantom face with the sense directed into the phantom) in the step is given by:

$$z = (\Delta S)\cos(\phi) \quad (3.1.19)$$

where  $\phi$  ( $\cos\phi \rightarrow \text{cal}$ ) is the zenith angle in the phantom coordinate system

The depth traversed in the step is added to the cumulative depth,  $z_s$ , (the phantom surface is  $z_s = 0.0$ ).

A test is made to see if the particle has left the phantom. The particle has left the phantom if the cumulative depth is negative. If the particle has not left the phantom, the dose it deposited in slabs through which it traversed are assigned. If it did leave the phantom, the dose in the slabs before it left are deposited. The subroutine, Assign, assigns the absorbed dose to the phantom slabs (see Section 3.1.6 on Assign). If the particle did not leave the phantom, the control of the calculation is passed to the test to see if the energy is above the cut-off energy. If it did leave, control is passed to the statement controlling the number of histories at each initial energy and angle. If the particle does come to the end of its range its remaining energy is assigned to the slab it last entered.

After all the histories are followed, for all charged particles' energies and angles generated in all the slabs,



the dose is deposited as a function of depth and then normalized to the maximum dose received. The normalized dose as a function of depth is printed as the output of the calculation.

The Monte Carlo program was run, without the charged particle set in motion part of the program (in other words, without Subroutine Impulse) with a set of initially monoenergetic, monodirectional electrons. The energy of the electrons was varied between 2.0 MeV and 10.0 MeV. The penetration profile obtained was compared with results of a well-established analytic technique due to Spencer using the moments method (50). Spencer's method also employed continuous slowing down. This comparison is made in Figure 74.

### 3.1.5 Scattering Angle Transformation

The subroutine, Geom, transforms scattering angles from the coordinate system travelling with the particle to the coordinate system fixed to the phantom (see Figure 75). The direction with respect to the particle reference system in polar coordinates is specified by a zenith angle,  $\phi$ , ( $\phi \rightarrow g$ ), and an azimuthal angle,  $\psi$ , ( $\psi \rightarrow r$ ).

Directions in the phantom reference system are also in polar coordinates. The zenith direction in the phantom system is  $\alpha$  and the azimuthal angle is  $\beta$ . It is useful to specify the direction sine and cosines. The direction of the particle in the phantom system at the beginning of the step is specified by  $\cos \alpha$  ( $\cos \alpha \rightarrow \text{oldcal}$ ) or  $\sin \alpha$  ( $\sin \alpha \rightarrow \text{oldsal}$ ) and  $\cos \beta$  ( $\cos \beta \rightarrow \text{oldcbeta}$ ) or



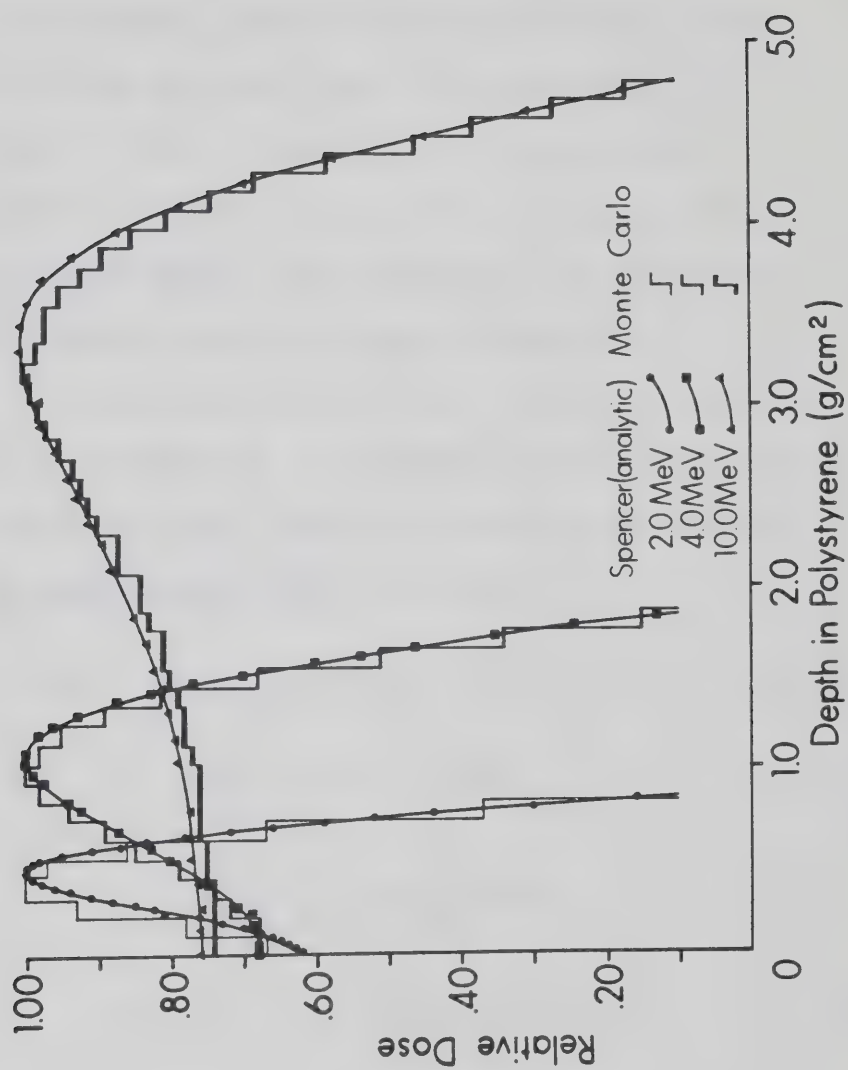


Figure 74. Comparison between the Monte Carlo program of Buildup3.For and Spencer's analytic formalism to predict the dose deposited by various monoenergetic electrons in water.





$\sin \beta$  ( $\sin \beta \rightarrow \text{oldsbeta}$ ). The direction of the particle in the phantom system at the end of the step (after scattering has taken place) is given by  $\cos \alpha'$  ( $\cos \alpha' \rightarrow \text{cal}$ ) or  $\sin \alpha'$  ( $\sin \alpha' \rightarrow \text{sals}$ ) and  $\cos \beta'$  ( $\cos \beta' \rightarrow \text{cbeta}$ ) or  $\sin \beta'$  ( $\sin \beta' \rightarrow \text{sbeta}$ ). The relationship between the directions in the particle and the phantom system are shown in Figure 75.

To determine the position of the charged particle inside the phantom, a transformation must be made to the coordinate system fixed with respect to the phantom. The transformation is given by (51)\*:

$$\cos(\alpha') = \sin(\phi)\cos(\psi)\sin(\alpha) + \cos(\phi)\cos(\alpha) \quad (3.1.20)$$

$$\sin(\alpha') = \sqrt{1 - \cos^2(\alpha')} \quad (3.1.21)$$

$$\sin(\beta' - \beta) = \frac{\sin(\phi)\sin(\psi)}{\sin(\alpha')} \quad (3.1.22)$$

$$\cos(\beta' - \beta) = \frac{\cos(\phi) - \cos(\alpha)\cos(\alpha')}{\sin(\alpha)\sin(\alpha')} \quad (3.1.23)$$

$\beta'$  can be found by taking the inverse sin or cos of the above expressions but it is more convenient to define  $\sin(\beta')$  and  $\cos(\beta')$  as:

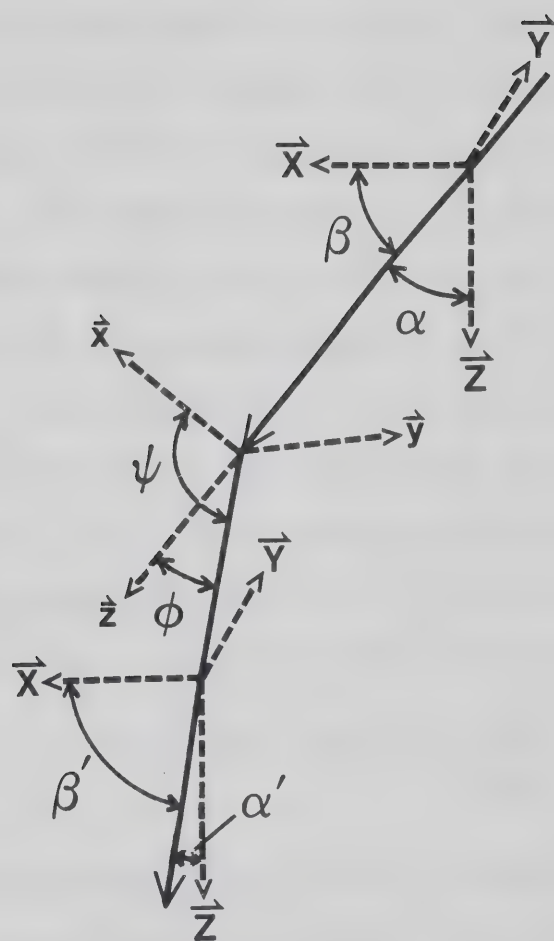
$$\sin(\beta') = \sin(\beta' - \beta)\cos\beta + \cos(\beta' - \beta)\sin\beta \quad (3.1.24)$$

$$\cos(\beta') = \cos(\beta' - \beta)\cos\beta - \sin(\beta' - \beta)\sin\beta \quad (3.1.25)$$

Having obtained  $\sin\alpha'$ ,  $\cos\alpha'$ ,  $\sin\beta'$  and  $\cos\beta'$ , these values are passed back to the main program.

\* The error in the formulation of Equation 3.1.22 in Bruce and Johns (51) has been corrected.





Phantom Coordinate System  $\vec{X}, \vec{Y}, \vec{Z}$

Particle Coordinate System  $\vec{x}, \vec{y}, \vec{z}$

Figure 75. Relationship between scattering angles in the particle and phantom coordinate system.



### 3.1.6 Assigning Dose

When called, the subroutine, Assign, deposits the required dose in the slab or slabs traversed between the beginning and end of the step. Dose is assigned for each of the following three situations: The particle energy is greater than or equal to the step cut-off energy (0.2 MeV), the particle energy is less than the step cut-off energy at the end of the step or the particle has left the phantom during the step.

The simplest possible case and the most often occurring case is when the particle does not leave the slab it was in at the beginning of the step. The total dose received by the slab, up to and including the step,  $Dose'(k)$ , ( $k \rightarrow k_{ay}$ ), should be given by:

$$Dose'(k) = Dose(k) + \frac{(\Delta T)_j}{\rho V_{slab}} \quad (3.1.26)$$

where  $Dose(k)$  is the total dose received by the slab up to and not including the step. Since the phantom is semi-infinite, the mass of the slab,  $\rho V_{slab}$ , is infinite! This difficulty is eliminated by redefining  $Dose'(k)$  as:

$$Dose'(k) = Dose(k) + (\Delta T)_j \quad (3.1.27)$$

Now  $Dose'(k)$  is not equal to the absolute dose. However, since the slabs have the same thickness,  $Dose'(k)$  is directly proportional to the absolute dose. The final output of the program is the dose at each slab normalized



to the maximum dose received by any slab in the phantom, so absolute dose is not required.

If the particle traverses more than one slab during a step, the energy lost is assigned to the slabs in proportion to the fraction of the path length spent in each slab.\*

If the particle traversed completely through one or more slabs, the dose deposited in those slabs will be:

$$\text{Dose}'(k) = \text{Dose}(k) + \frac{(\Delta T)_j}{z_j/0.1 \text{ cm}} \quad (3.1.28)$$

where 0.1 cm is the slab thickness. The denominator in the last term represents the number (floating point) of slabs traversed.

If the particle traverses only part of two slabs the fraction of the total dose deposited, Dose Fraction, (Dose Fraction  $\rightarrow$  Dosefrac), in one of the slabs due to a step is calculated. The remaining energy is deposited in the other slab.

Similar procedures are followed if the particle

\* The situation for which this will occur is at the top of the phantom and the particle has a large initial kinetic energy. For example, the distance travelled by a 15 MeV electron in its first step  $(\Delta S)_1$  is given by:

$$(\Delta S)_1 = \frac{1.5 \text{ MeV}}{2.306 \text{ MeV/cm}} = 0.65 \text{ cm}$$

Therefore, the dose imparted to 7 slabs will have to be calculated. The mean square angle of scattering will be:

$$\langle \phi^2 \rangle^{1/2} = \sqrt{3.95 \times 10^{-2} \text{ rad}^2/\text{cm}} (0.65 \text{ cm}) = .16 \text{ rad}$$

which is about  $9^\circ$ .





leaves the phantom, except that dose is not assigned for that portion of the path outside the phantom.

### 3.1.7 Results

The program was run to model 6 MV and 15 MV accelerators under narrow beam (or small field) and broad (or large field) beam conditions. The program was designed to calculate the energy-angle spectrum of charged particles set in motion in thin phantom slabs. The Monte Carlo part of the program follows the charged particles through the rest of the phantom. This procedure is common to both the small field and large field approximations. Figures 76 and 77 illustrate the dose delivered to a phantom due to charged particles set in motion in a 0.1 cm slab of water at the surface of the phantom by a 6 MV and 15 MV photon beam, respectively. To a good approximation, the dose due to charged particles set in motion in a thin slab attenuates exponentially with distance from the slab. The charged particle energy absorption coefficient,  $\mu_e^+$ , can be found by finding the slope of the line of a graph of  $\ln(1.0/D(x))$  versus depth where  $D(x)$  is the relative dose at a depth,  $x$  (the maximum dose = 1.0). The charged particle energy absorption coefficient is  $3.1 \text{ cm}^{-1}$  for 6 MV and  $1.15 \text{ cm}^{-1}$  for 15 MV photon beams.

In the broad beam, or large field approximation, the scattered photons generated in the phantom are not



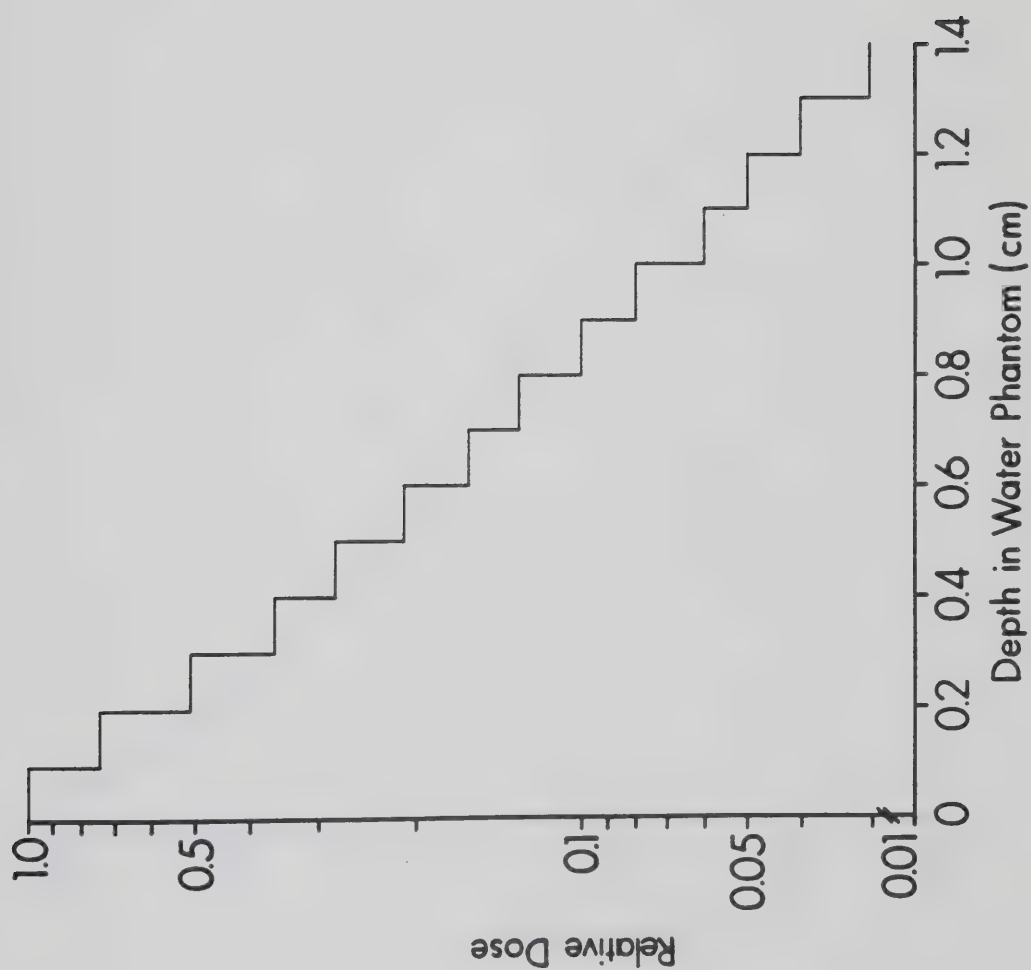


Figure 76. Distribution of dose in a semi-infinite water phantom due to electrons set in motion in the top 0.1 cm slab by a 6 MV photon beam.



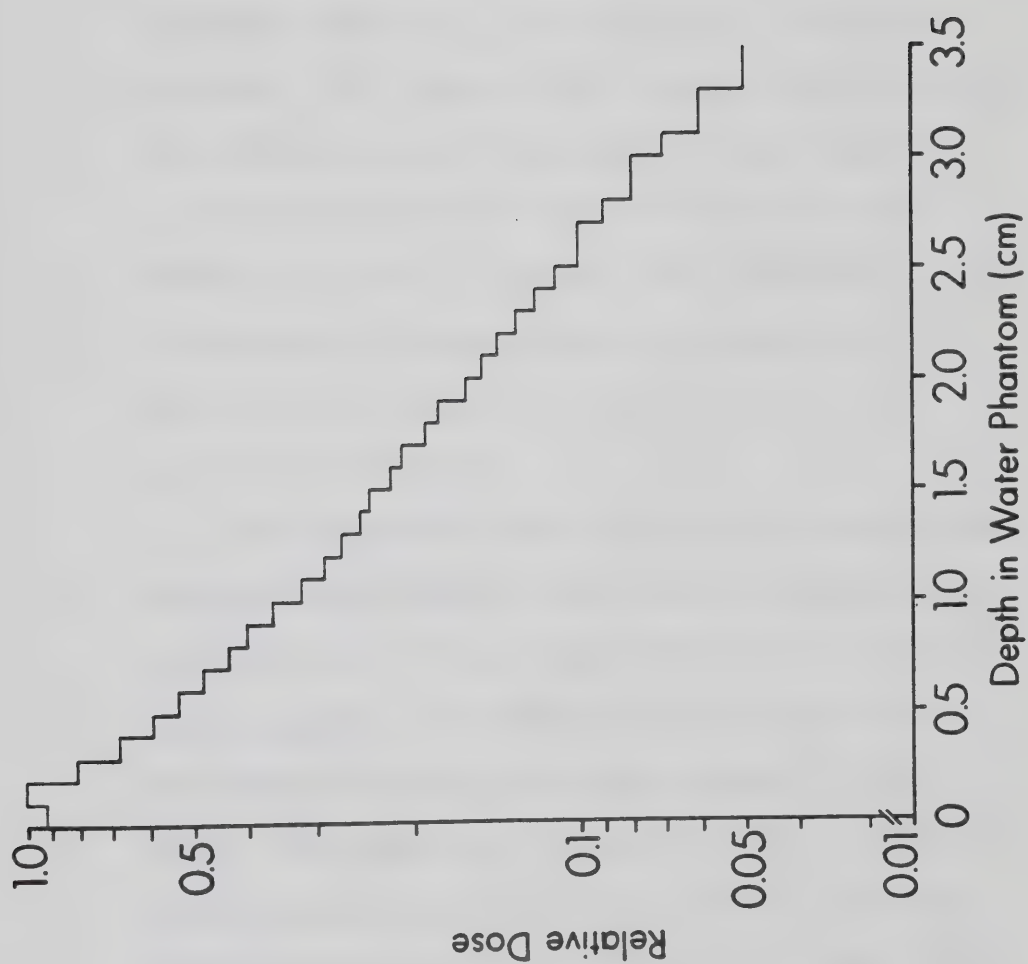


Figure 77. Distribution of dose in a semi-infinite water phantom due to electrons set in motion in the top 0.1 cm slab by a 15 MV photon beam.



lost from the beam. Scattered photons have a spectrum that has a similar shape, but an effective nominal energy lower than the primary beam (36). It was also seen in Section 2.13 that the depth of  $d_{\max}$  of the scattered radiation is less than that of the primary radiation. The primary photon spectrum tends to harden as it penetrates into the phantom. Lower energy scattered photons tend to replenish the low energy photons lost from the spectrum due to hardening. Large field geometry is approximated by assuming that the primary photon spectrum is unaltered as the beam penetrates the phantom.

With the primary photon spectrum remaining the same as a function of depth in the phantom, the penetration characteristics of the charged particles set in motion remain the same. The number of charged particles set in motion at any depth decreases exponentially with depth. The appropriate attenuation coefficient is the mean energy absorption coefficient which is an energy fluence weighted average normalized to the total energy fluence of the beam. Mathematically, the mean energy absorption coefficient is given by:

$$\bar{\mu}_{\text{en}} = \frac{\sum_i F_i(h\nu)_i (\mu_{\text{en}})_i}{\sum_i F_i(h\nu)_i} \quad (3.1.29)$$

Equation 3.1.29 has the same form as Equation 1.5.10. The mean attenuation coefficient for the 6 MV spectrum





is  $0.029 \text{ cm}^{-1}$  and  $0.021 \text{ cm}^{-1}$  for the 15 MV spectrum.

The dose deposited by the charged particles set in motion attenuates exponentially in the phantom and the primary photon beam attenuates exponentially. The assumption, therefore, that large field geometry can be modelled by keeping the primary spectrum constant with depth is identical to the build-up model presented in Section 1.5.

The method of computing the dose in the build-up region for broad beam geometry is to attenuate the dose due to charged particles set in motion in a thin slab at a depth,  $x$ , by a factor  $e^{-\mu_{en}x}$ . This is done for 100 thin slabs (each 0.1 cm thick). The dose received at any point in the phantom is a sum of the dose reaching the point from the charged particles set in motion from all the slabs above the point.

This procedure is done by the program, Addose.For. The input for this program is the thin slab charged particle set in motion dose penetration profiles shown in Figures 76 and 77. The depth of maximum dose,  $d_{\text{max}}$ , as predicted by the large field model computed by Buildup3.For and Addose.For, is the same as the  $d_{\text{max}}$  point predicted by Equation 1.5.11. The output for Addose.For is normalized by dividing the dose by the dose at  $d_{\text{max}}$ . The result is the broad beam TMR curve in the build-up region. Appendix 8 contains the listing and



documentation for Addose.For.

Small field geometry assumes that all the scattered photons produced by the beam in the phantom do not interact again. This is modelled by hardening the beam. Every photon that interacts in the phantom is removed from the number spectrum. This is accomplished by the subroutine of Buildup3.For called Impulse (see Equation 3.1.16). Small field geometry requires more computer time to model than large field geometry because the charged particle set in motion energy-angle distribution has to be recalculated for each slab. More importantly, each charged particle set in motion in the slab has to be followed through the rest of the phantom. The relative dose was calculated to a depth of 10 cm so the small beam geometry requires approximately 100 times (10 cm/0.1 cm) as much time to model as the large beam geometry.

The build-up curves of the small and large field, together with the experimental results from Section 2.11 are shown in Figures 78 and 79 for 6 MV and 15 MV photon beams, respectively. As was found experimentally, there is little difference between small and large field geometries in the build-up region. There is good agreement between the computer modelled and experimental build-up curves.



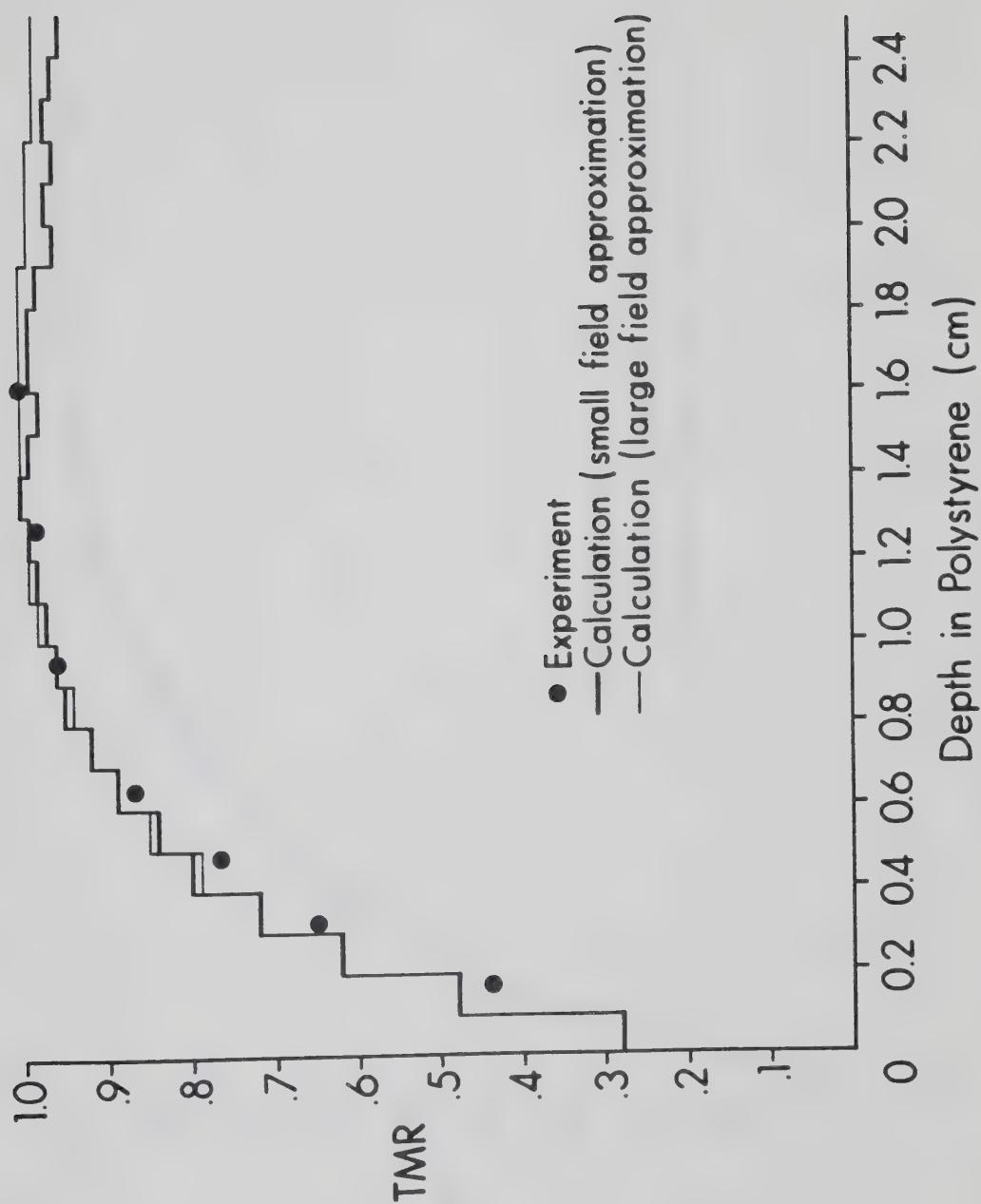


Figure 78. Comparison between experiment and computer modelling of the phantom generated TMR curve at 6 MV.



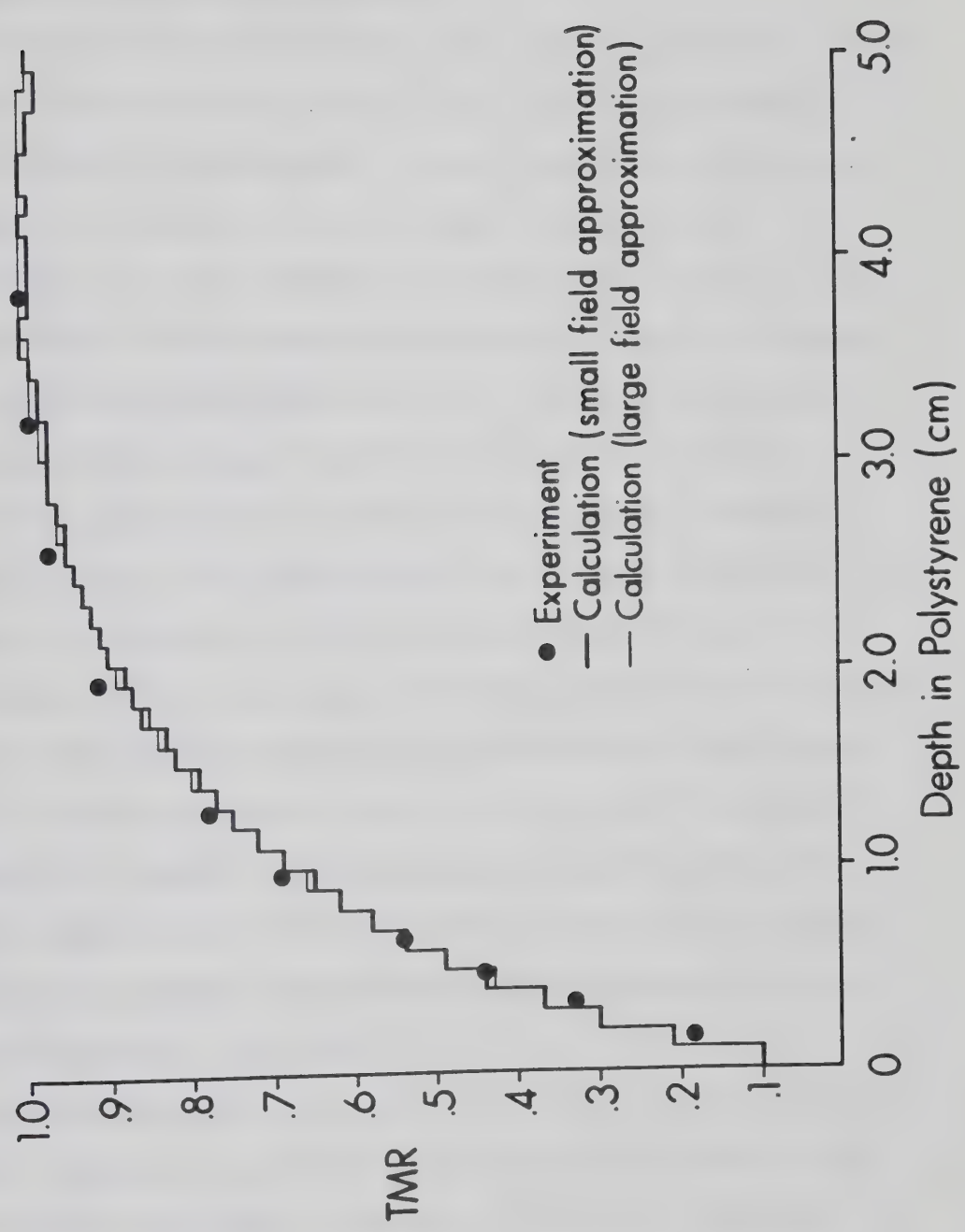


Figure 79. Comparison between experiment and computer modelling of the phantom generated TMR curve at 15 MV.





### 3.2 Nature and Source of Contamination

The definition of contamination stated in the introduction implies that radiation reaching the phantom, other than primary radiation\*, is to be considered as contamination. Primary radiation is the photon component of the beam that is directed away from the source.

The utility of this definition of contamination is that it allows one to determine the dose deposited by primary photons in a phantom. This is called the phantom generated dose. The phantom generated dose is deposited by charged particles set in motion by primary photons and scattered photons produced in the phantom. Therefore, contamination dose is exogenous whereas the phantom generated dose is endogenous to the phantom. Scatter, measured by an increase in dose with increasing field size using a full phantom in the build-up region, cannot be confused with contamination generated outside the phantom. Changes in the phantom generated dose can only be due to changes in the phantom size, density or configuration. A modification of the phantom in these respects will not affect the nature of the contamination component (although it will affect the interaction of the contamination component in the phantom).

The TMR build-up curves in Section 2.1 demonstrate a field size dependence, especially at or near the phantom surface, greater than can be expected from lateral scattering of photons and electrons generated in the phantom.

Adding small additional thicknesses of accessories increased the TMR in the build-up region. As the thickness of accessory increases,

\* The dose due to charged particles set in motion by neutrons is not considered.



the amount of contamination produced by the accessory increases.

However, contamination produced at shallow depths within the accessory is shielded by deeper layers of the accessory. At an equivalent thickness less than 3.2 cm of Lucite, there is a balance between production and absorption of contamination.

The surface dose displays the characteristics of electron contamination. High atomic number "filters" can reduce the surface normalized dose due to an accessory when placed beneath the accessory. When placed above the accessory the high atomic number material did not alter the surface normalized dose. The number of interactions produced by the high Z material above and below the accessory are approximately the same. The mass stopping power is relatively independent of atomic number and, indeed, the mass stopping power of Lucite, for example, is slightly higher than lead (5). Therefore, the only possible difference between the configurations of high Z material above and below Lucite resulting in a reduced surface normalized dose is the difference between the amount of scattering of contamination electrons outside the beam. This is not surprising considering that the scattering power of lead is nearly an order of magnitude higher than water\* (see Appendix 4). Therefore, nearly as many contamination electrons emerge from the bottom surface of the high Z "filter" as emerge from the bottom surface of the accessory, but fewer of the electrons are forward directed. Therefore, a high atomic number material placed in the beam should be called an electron scatterer rather than an electron filter.

The distance from the source distribution and lateral distribution

\* The scattering power of water and Lucite are within 10% at energies less than 15 MeV (5).



of the surface dose for large open fields at 15 MV are typical of electron distributions. The distance distribution of the surface dose falls off as  $1/r^2$  from a point 12 cm below the target which corresponds to the position of the field flattening filter. The field flattening filter has, at its thickest point, 5.4 cm of stainless steel in the beam. It is the only component present in an open field which has a sufficient thickness to produce a maximum fluence of contamination electrons\*, so it is likely to contribute to the dose due to contaminant electrons.

The lateral surface distribution is Gaussian. This indicates that the surface dose is due to electrons and indicates that the electrons could have been produced from a small source. Therefore, the surface dose at 15 MV for large fields behaves in accordance with Equation 1.3.4.

The situation at 6 MV is quite different. The assumption that the surface dose decays as  $1/r^2$  at large field sizes is not valid.\*\* Additionally, the lateral distribution is not Gaussian. The surface dose inside the field is larger than can be expected from a normal distribution and the surface dose outside the field is smaller. Both of these are contraindications that localized source is responsible for most of the electron contamination for large fields at 6 MV.

The source of electron contamination at small fields is better understood due to magnetic separation of the electrons produced by

\* A Lucite accessory with a thickness greater than 3.2 cm will not contribute to greater contamination. The equivalent thickness of steel is about 40 cm.

\*\* A  $1/r^2$  dose decay with distance from an apparent source of contamination is necessary although not a sufficient condition for identifying the source of contamination unequivocally.





two regions of the beam. The surface normalized dose was measured for various conditions of field size (the largest field size was 10 cm x 10 cm) and source to probe distance inside the field with the magnet in place and not in place at the accessory holder position. Air contributes most of the surface dose at 6 MV and 15 MV for these field sizes. At 15 MV, however, the increase in the dose, as a function of field width due to electron contamination produced between the target and magnet, suggests that at a field size of about 15 cm x 15 cm for a source to probe distance of 100 cm, this contribution will be greater than the contribution due to air.\* At 15 MV, when the SPD=100 cm for a field size of 30 cm x 30 cm, (which was the condition of the measurement of the distance distribution in Section 2.4), the contribution due to air will be a minority component. Therefore, the results obtained at small field sizes does not contradict the results at large field sizes at 15 MV. At 6 MV the surface dose for large field sizes is mostly due to air contamination (with the possible exception of small source to probe distances). This is why the source of electron contamination could not be localized to a small region for the 6 MV large field beam in Sections 2.4 and 2.5.

Qualitatively, the SPD dependence of the contamination components are easy to explain. The greater the thickness of air intervening between the magnet, the greater the dose due to contamination produced in air. Conversely, increasing the distance between the region of production of contamination between the target and magnet will result in a smaller normalized dose.

\* Based on a linear extrapolation of the increase in dose between a field width of 7 cm and 10 cm.





Plotting graphs of the square root of the reading due to contamination produced between target and magnet will determine the position of the source of contamination if the source is confined to a small region. At small fields at both 6 MV and 15 MV with the cross-hair tray in place, the source appears to be the cross-hair tray. At 15 MV, with the cross-hair tray not in place, the source appears to be the collimators. This agrees with the observation that the surface dose appears to be produced by the field flattening filter at 15 MV for large field sizes. At small field sizes the contamination produced by the field flattening filter is largely blocked by the collimators.

A general conclusion can be hypothesized by these findings. Electron contamination measured at a point tends to be produced by mass close to that point. Contamination produced further away is stopped or scattered by mass lying close to the measuring point. Therefore, air is a significant contributor under most conditions. Accessories and the cross hair tray when present contribute. Collimators at small field sizes produce some contamination\*. The field flattening filter can be the major source of electron contamination at large field sizes (therefore not blocked by the collimators) if the cross hair tray or accessories are not in the field.

All these possible sources of electron contamination result in a greater magnitude of electron contamination reaching the probe as a function of field size. A greater field size results in a greater interaction volume for air, accessory and cross hair tray sources. As the collimator jaws are opened a greater amount of contamination produced by the field flattening filter emerges through the collimator

\* At small field sizes the perimeter of the collimator compared to the field area is much larger than the same ratio at large field sizes.



opening.

The key to the separation of the contamination from the phantom generated dose is to know the contribution of contamination to the dose at one point. Except for the photon backscatter\* which can be independently measured, the surface dose is due to contamination electrons generated outside the phantom. Knowing the contamination contribution at the surface and the penetration characteristics of the contamination component, the phantom generated dose can be obtained by the subtraction of the dose due to contamination.

The same contamination penetration curve was used to determine the amount of contamination for each field width, SPD and accessory configuration. This assumes that different beam geometries or the presence of accessories in the field do not change the nature of the contamination. Justification for this assumption was provided at 15 MV by determining the contamination penetration curve at different SPD's and accessory configurations. The contamination penetration characteristics were within 5% (see Table 3). The surface dose is usually less than 40% of the maximum dose so an uncertainty in the correct amount of contamination at the surface will be less than 2% of the maximum dose. At deeper depths the uncertainty will be even less.

The validity of the contamination curve at 15 MV was verified in a number of other ways. The shape of the contamination penetration curve is characteristic of mixed electron and photon contamination. The surface contamination is established as being due to electrons. These electrons must penetrate to some depth beneath the phantom.

\* Some of the photon backscatter is due to scattered photon backscatter, but it need not be taken into account. The photon backscatter at most makes up about 20% of the electron contamination which usually makes up no more than 30% of the phantom generated dose, therefore, scattered photon backscatter will likely contribute less than 6% to photon backscatter. Photon backscatter is a small quantity so scattered photon backscatter is negligible.



The peak and rapid fall off at shallow depths are characteristic of electrons. The slow fall off at depths greater than 2 cm is characteristic of photons. Therefore, the contamination radiation appears to be a combination of an electron contribution primarily at shallow depths and photons contributing primarily at greater depths.

The derived contamination penetration curve, using the increase in dose in a limited phantom versus the increase in field width (greater than the phantom dimensions) at 15 MV, is similar in shape to the contamination curves measured outside the field. The difference in shape (see Figures 63 and 31) can be attributed to a difference between the relative amount of contamination electrons and photons present inside and outside the field boundary. Figure 27 demonstrated a Gaussian lateral distribution of the surface dose. Consequently, for a 30 cm x 30 cm field size there were about 45% fewer electrons present at 18 cm from the central axis as were present at the central axis. This largely accounts for the difference observed between Figures 31 and 63.

The most convincing evidence that the phantom generated build-up curves are correct is their agreement with computer modelling obtained independently (see Figure 79). The computer model also verifies that the phantom generated TMR curves are independent of field size.

The validity of subtracting the contamination component from the total build-up curve to yield the phantom generated build-up curve at 6 MV was tested as well. The contamination penetration had its maximum at the surface and decayed rapidly with depth at shallow depths (see Figure 64). The curve levelled off at deeper depths. This, as was found at 15 MV, is indicative of electrons contributing at shallow depths and scattered photons contributing at deeper depths. The contam-





ination curves derived inside the field (Figure 64) and measured outside the field (Figure 32) are in approximate agreement if the lateral surface dose distribution is taken into account. Approximately 60% fewer electrons are present 3 cm outside of a 30 cm x 30 cm, 6 MV field as compared to the central axis. This accounts for the difference in the shape of Figures 64 and 32. The computer model of the phantom generated dose as a function of depth agreed with the experimentally derived phantom generated dose build-up curve at 6 MV (see Figure 78).

The computer model established that the dose due to electrons set in motion in a thin phantom slab decays exponentially in the phantom as a function of depth from the slab. Therefore, Equations 1.5.8, 1.5.11 and 1.5.16 should be valid descriptions of the dose in the build-up region\*.

Values of  $\mu_e$  of  $3.1 \text{ cm}^{-1}$  and  $1.15 \text{ cm}^{-1}$  for the mean energy absorption coefficient of electrons set in motion by 6 MV and 15 MV photon beams, respectively, were found (see Section 3.1.7). The value of  $\mu_Y$  was found from Equation 3.1.29 to be  $0.029 \text{ cm}^{-1}$  for 6 MV and  $0.021 \text{ cm}^{-1}$  for 15 MV photon beams.

The  $d_{\text{max}}$  predicted by Equation 1.5.11 is 1.5 cm for 6 MV and 3.6 cm for 15 MV, respectively. This compares with the experimentally determined  $d_{\text{max}}$  values (after the contamination component has been removed) of 1.6 cm for 6 MV and 3.5 cm for 15 MV.

Table 19 lists the TMR dose for 6 MV and 15 MV beams in the build-up region as predicted by Equation 1.5.16. This agrees well with the phantom generated build-up TMR dose. Therefore, the simple differential Equation 1.5.6 is physically acceptable and accurately predicts\* the dose in the build-up region received by a homogeneous unit density phantom.

\* The model fails to predict the surface dose due to backscattered photons.





Table 19      Tissue Maximum Ratios in the Build-Up  
Region as Predicted By Equation 1.5.16

| Depth<br>(cm) | 6 MV  | 15 MV |
|---------------|-------|-------|
|               | TMR   | TMR   |
| 0.00          | 0.000 | 0.000 |
| 0.16          | 0.408 | 0.181 |
| 0.32          | 0.654 | 0.331 |
| 0.48          | 0.802 | 0.455 |
| 0.64          | 0.890 | 0.557 |
| 0.95          | 0.971 | 0.708 |
| 1.27          | 0.996 | 0.814 |
| 1.91          | 0.995 | 0.932 |
| 2.54          | -     | 0.982 |
| 3.18          | -     | 0.998 |
| 3.81          | -     | 1.000 |



region received by a homogeneous unit density phantom.

The contamination electrons are set in motion by matter between the target and magnet by the same processes that set electrons in motion in the phantom. The major difference between contamination electrons produced between the target and magnet that reach the phantom surface and electrons set in motion by primary photons interacting with the phantom near the surface is that the contamination electrons will be more forward directed. Those contamination electrons that were set in motion with a large zenith angle will have left the beam. Figure 72 illustrated that the forward directed electrons that are set in motion by a 15 MV beam have a higher average energy than those that are set in motion with large zenith angles. Therefore, contamination electrons have a higher average energy compared to electrons set in motion in the phantom. Having a higher average energy results in greater penetration of the contamination electrons compared to phantom generated electrons. Additionally, contamination electrons that are set in motion further away from the phantom are more likely to have been produced with a smaller zenith angle than contamination electrons produced closer to the phantom. Therefore, electrons produced further away from the phantom are likely to be more energetic\* and, therefore, more penetrating than those produced close to the phantom.

Figure 80 compares the relative dose imparted to a phantom from electrons set in motion in the top 0.1 cm of a phantom compared to the electron contamination penetration curve from a 15 MV photon beam and

\* The slowing down of electrons in air is insignificant. The stopping power of air for 3 MeV electrons is about  $1.8 \text{ MeV cm}^2/\text{g}$  (5). One hundred centimeters of air has a mass thickness of about  $0.13 \text{ g/cm}^2$  so an electron will lose about 0.2 MeV or 7% of its energy in traversing this distance. The range of 3 MeV electrons in air is about 11 m.



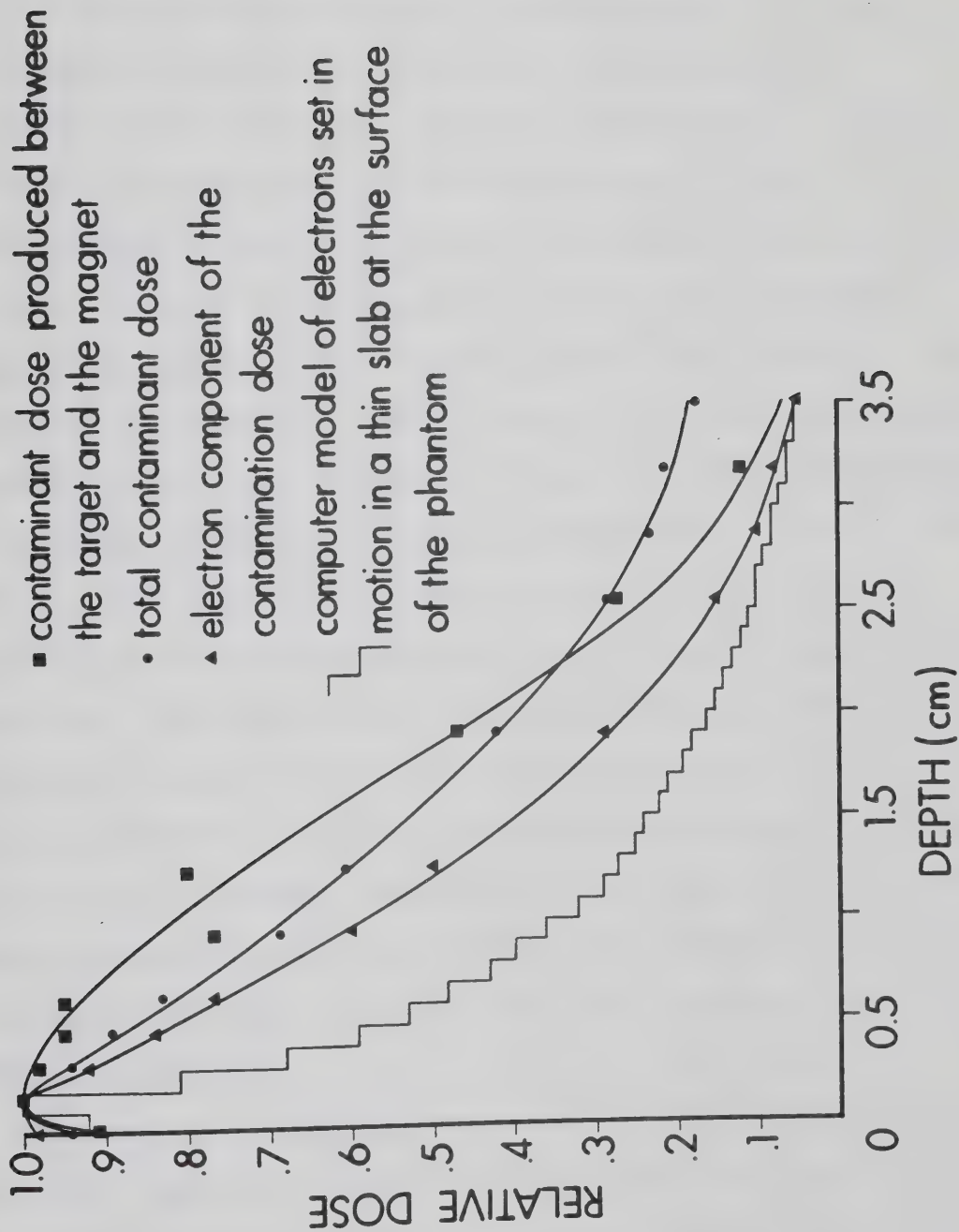


Figure 80. Comparison between various penetration curves at 15 MV.



the electron contamination produced between the target and magnet. The contamination penetration curve contains electrons as well as scattered photons so the comparison cannot be made fairly. In Section 2.13 the scattered photon build-up curve was obtained. The electron contamination component can be obtained by subtraction of the scattered photon contamination component. An assumption is made that there are no contamination electrons penetrating to a depth of 4.4 cm of polystyrene so the dose at this depth is entirely due to scattered photons. Figure 80 shows the result. The electron contamination component is more penetrating than the electrons set in motion in the phantom at shallow depths. This is because the electron contamination component contains fewer low energy electrons compared to the electrons set in motion in the photon which are stopped at shallow depths in the phantom. The electron contamination component produced between the target and magnet is more penetrating than the total electron contamination curve. The maximum range of the contamination electrons is approximately equal to the maximum range of the electrons set in motion by the phantom. This is because the maximum energy of contamination electrons produced at any position in the beam is the same as the maximum energy of electrons set in motion in the phantom. All the electron penetration curves in Figure 80 have their maximum at about 1.5 mm depth in the phantom.

Figure 81 is a comparison between the dose due to electrons set in motion in a thin slab at the top of the phantom and total dose due to contamination for the 6 MV beam. The contamination curve has not had the scattered photons removed. By comparing the total contamination and electron set in motion curves between 15 MV (Figure 80) and 6 MV (Figure





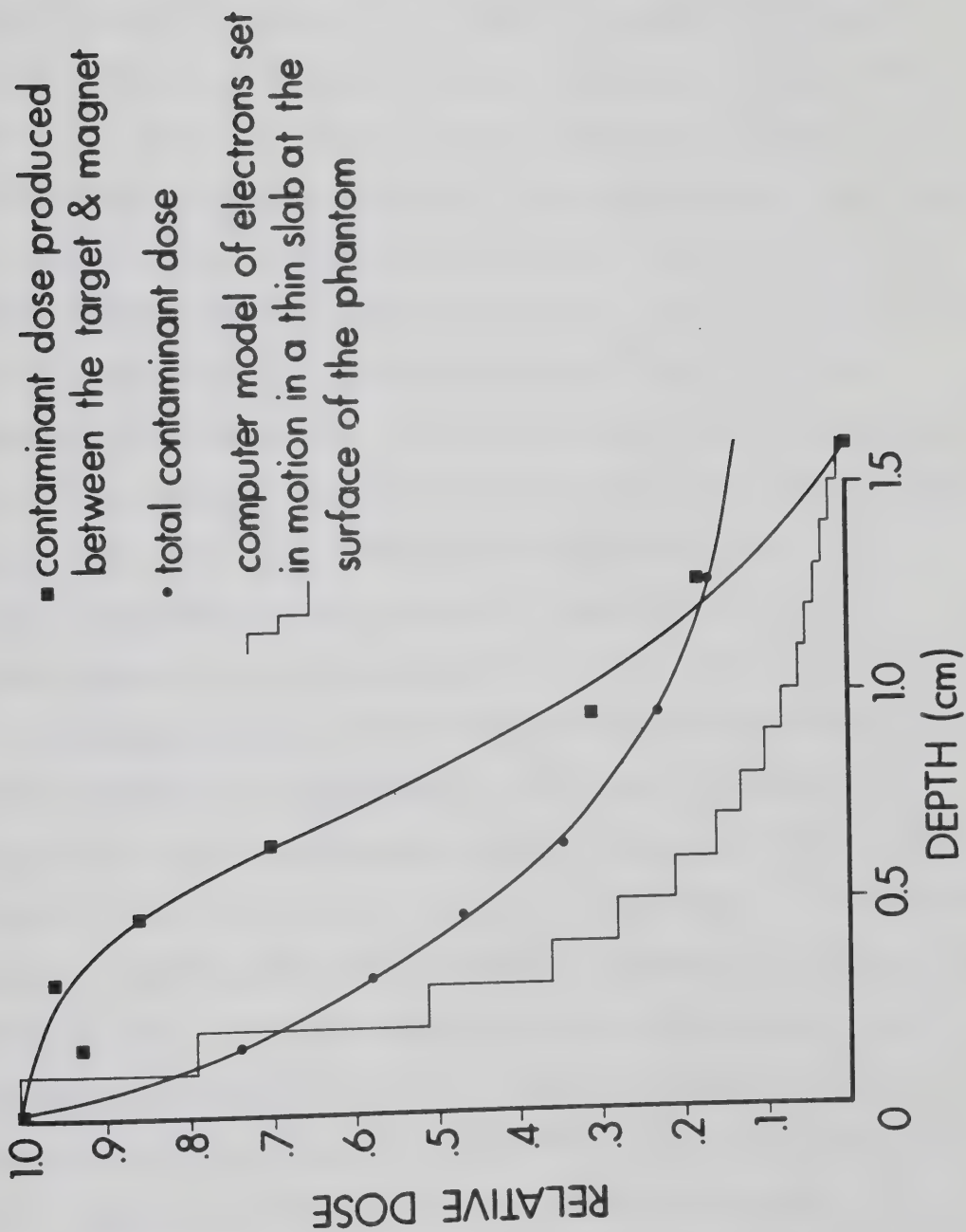


Figure 81. Comparison between various penetration curves at 6 MV.



81) it can be seen that the 6 MV curves would be very similar had the scattered photon component been removed. Therefore, the electron contamination component at 6 MV has similar penetration characteristics to electrons set in motion at the surface of a phantom implying that the contamination electrons are produced close to the phantom. This confirms the results of Section 2.10 which indicated that most of the contamination at 6 MV is produced in air between the magnet and phantom.

Figure 81 also illustrates the penetration curve of electrons produced between the target and magnet at 6 MV. The penetration of this fraction of the electron contamination is much greater at shallow depths than the electrons set in motion at the surface of the phantom, however, this component contributes very little to the total contamination at 6 MV. As at 15 MV, the maximum range of electrons set in motion at the surface of the phantom and contamination electrons produced between the target and magnet are almost identical.

Decreasing the source-to-probe distance increases the fraction of detected contamination produced between the target and magnet and decreases the amount of contamination produced by air between the magnet and phantom that arrives at the probe. Therefore, the relative proportion of electron contamination that is produced by these sources changes as a function of SPD. Since these sources each have different penetration characteristics measured at the same SPD, the penetration characteristics of the total electron contamination component could change as the SPD changes. However, as the source to probe distance decreases, more electrons produced between the target and magnet are going to be arriving at the probe produced with larger zenith angles. As the probe gets closer to a source of electron contamination more lower energy



electrons will arrive at the probe so the contamination component will be less penetrating at shallow depths. More lower energy electrons arriving from a source between the target and magnet will tend to compensate for fewer electrons produced in air. Therefore, the total penetration characteristics of contamination electrons likely does not change significantly as a function of source-to-probe distance.

At depths approaching  $d_{\max}$ , most of the contamination dose is due to scattered photons. The Compton effect produces a scattered photon for every recoil electron produced. Therefore, the sources of electrons are also going to be the sources of scattered photons.

Nilsson and Brahme, using computer Monte Carlo modelling, found that the field flattening filter and the collimator are the main sources of scattered photons (36). This can be qualitatively explained. The mean interaction distance for the scattered photons is of the order of the inverse of their mean energy absorption coefficient,  $1/\bar{\mu}_{\text{en}}$ . Section 3.2 illustrated that one could define an effective energy absorption coefficient for the dose deposited by electrons set in motion. The mean interaction distance is of the order of the inverse of this coefficient which is  $1/\bar{\mu}_{\text{e}} \pm$ . Scattered photons will emerge from a depth from a source of the order  $1/\bar{\mu}_{\text{en}}$  while contamination electrons will emerge from a depth of the order  $1/\bar{\mu}_{\text{e}} \pm$ . Both the collimators and the field flattening filter have thicknesses greater than  $1/\bar{\mu}_{\text{en}}$  so many more scattered photons will emerge compared to contamination electrons. Sources of contamination with a thickness of the order of  $1/\bar{\mu}_{\text{e}} \pm$ , like accessories and air, will produce approximately equal numbers of contamination electrons and scattered photons in the beam.

Contamination electrons produce a higher maximum dose illustrated



by the surface dose of Figures 63 and 64 than scattered photons illustrated by the dose plateau in the same figures. The ratio of the electron energy fluence produced by scattered photons deposited at any point is from Equation 1.5.8 and is approximately equal to:

$$\frac{\psi_{e^{\pm}}(x)}{(\psi_{\gamma})_0} \sim \frac{\mu_{\gamma}}{\mu_{e^{\pm}} - \mu_{\gamma}} \left( e^{-(\mu_{\gamma}/\rho)x} - e^{-(\mu_{e^{\pm}}/\rho)x} \right)$$

At  $d_{\max}$  the term  $(e^{-(\mu_{\gamma}/\rho)d_{\max}} - e^{-(\mu_{e^{\pm}}/\rho)d_{\max}})$  is approximately equal to

1. Since  $\mu_{\gamma}$  is much less than  $\mu_{e^{\pm}}$ :

$$\frac{\psi_{e^{\pm}}(d_{\max})}{(\psi_{\gamma})_0} \approx \frac{\mu_{\gamma}}{\mu_{e^{\pm}}} \quad (3.2.1)$$

It has been shown previously that contamination electrons penetrate somewhat further than electrons set in motion in the phantom by scattered photons, however, they are both of the same order of magnitude. Therefore, the relative energy fluence of contamination electrons compared to scattered photons is approximately:

$$\frac{(\psi_{e^-})_{\text{contamination}}}{(\mu_{\gamma})_{\text{scattered photon}}} \approx \frac{\text{Dose } (d=0)}{\text{Dose } (d_{\max} \text{ scattered photon})} \frac{\mu_{\gamma}}{\mu_{e^{\pm}}} \ll 1 \quad (3.2.2)$$

Therefore, despite the fact that the maximum dose due to contamination electrons is greater than the maximum dose due to scattered photons, the energy fluence arriving at the phantom surface of scattered photons is greater than the energy fluence due to contamination electrons.

The greater energy fluence of scattered photons compared to contamination electrons is due in part to thick sources like the collimators and the field flattening filter. Additionally, electrons





more readily multiple scatter\* out of the beam compared to photons.

The shift in  $d_{\max}$ , especially when accessories are present in the beam, can be attributed to electron contamination. Since the build-up curve for scattered photon contamination is similar to the primary photon build-up curve, scattered photons are unlikely to contribute significantly to the shift in  $d_{\max}$ . The peak in the contamination penetration curve due to electrons occurs at very shallow depths so increasing the magnitude of electron contamination results in a  $d_{\max}$  shift towards shallower depths. This also explains why the shift in  $d_{\max}$  is accompanied by an increased surface dose. These findings agree with Biggs and Ling (41) who observed that a shift in  $d_{\max}$  did not occur when electrons were swept from the beam.

\* For example, a 3 MeV electron in air has a mass angular scattering power of  $0.602 \text{ radians}^2 \cdot \text{cm}^2/\text{g}$  (5) which, after passage through 100 cm of air, corresponds to a mean scattering angle of  $16.0^\circ$ .



### 3.3 Clinical Uses of the Results

Low energy photon beams (isotope sources with an energy less than or equal to  $m_0c^2$  or accelerator sources less than about 1 MV) produce a maximum dose at the surface of a patient. If these photon sources were used to treat tumors at a depth under the patient's skin surface, skin reactions could occur.

Skin reactions may be minor such as erythema (reddening of the skin) or more serious such as moist desquamation (peeling of the skin with blistering). The type of reaction, if it occurs, varies considerably as a function of dose from patient to patient (7). Skin reactions are similar to sunburns in morphology and histology, however, the onset of the ionizing radiation induced skin reaction occurs several days after exposure rather than a few hours.

Few skin reactions occur to patients undergoing megavoltage radiation therapy. The main reason is that the maximum dose is received at a depth well below the skin. The dose due to contamination electrons reduces this skin sparing effect.

Another effect produced by contamination electrons and scattered photons is an elevated dose outside the field boundary. A situation where this may be clinically important arises when the eyes lie just outside the field. The lens of the eye is susceptible to the formation of radiation induced cataracts. Cataracts are likely to form if the total dose received over 30 days is 1500 rads (52).

The amount of contamination increases with accessories in the field, greater field size and smaller SPD. Skin reactions or high dose outside the field may result even at megavoltage energies if two or more of these conditions are encountered.



Passing the beam through the poles of a magnet could be effective in reducing the electron contamination arriving at a patient. To ensure that few electrons are produced in air between the magnet and patient, the magnet would have to be placed as close to the patient as possible. In a clinical situation the contamination electrons should not strike the patient outside of the treatment area, therefore, the electrons should be swept through at least  $90^{\circ}$ . A magnetic field of nearly 1 Tesla would be required. Electron contamination increases as a function of field size so the pole gap should be as wide as possible. The field gradient should be steep enough to ensure that the dose distribution, due to electrons set in motion in the patient is not affected. These requirements could only be met with an electromagnet. In addition, such a magnet would likely have to be liquid cooled.

When an accessory is in place, the surface dose inside the field can be reduced by about 20% if a lead (or other high atomic number material) sheet is placed underneath the accessory. The "filter" scatters electrons out of the field so a reduction of surface dose inside the field would be concomitant with an increase in the surface dose outside the field. The "filter" would then be clinically acceptable only if the increased dose outside the field would not cause complications and if the reduced dose inside the field significantly reduced the probability of the occurrence of skin reactions.

A useful, immediately applicable feature of the removal of the contamination component is that the TMR in the build-up region is independent of field size, SPD and presence of accessories and, therefore, is amenable to data storage in computers. Instead of listing all of the values of the TMR curves in the build-up region for field widths, SPD's and presence of accessories applicable to treatment planning, only



two TMR curves; one, the phantom generated TMR curve and the other, the contamination TMR curve and the surface dose as a function of these conditions need be listed. The surface dose dictates the magnitude of the dose received in the build-up region due to contamination.

The separation of the contamination component of dose and the phantom generated dose may prove to be important for treatment planning in the build-up region in the presence of inhomogeneities. The treatment planning algorithms most often employed (developed by Dr. Jack Cunningham) separate the contribution to the dose to a point into primary and scattered photon contributions. In the build-up region, the phantom generated scattered contribution can be confused with the contamination contribution.

The primary dose at a given depth is determined by extrapolating a curve of TMR versus field width to the y-axis. The TMR value at the y-axis is called the zero-area TMR value at that depth. The difference between the TMR value at any other field width is assumed to be due to scatter generated within the phantom.

The usual measure of the amount of phantom generated scatter contributing to a point at energies of 6 MV or higher is the scatter maximum ratio or SMR. The scatter maximum ratio is the difference between the TMR at a given field width and depth and the zero-area TMR at the same depth.

Since the amount of contamination also increases with field width, some of the contamination is attributed to scatter in this scheme. This is merely an academic distinction in treatment planning of homogeneous phantoms. In treatment planning of inhomogeneous regions, the scatter contribution from a region is increased if the inhomogeneity has a high electron density and it is decreased if the electron density is low. This





reflects the direct proportionality of the Compton cross-section with electron density. If the inhomogeneity is in the build-up region, then the contamination dose erroneously attributed to phantom generated scatter will be similarly modified. In fact, the electron component of the contamination dose should be reduced if high electron density inhomogeneities are present in the build-up region and increased if low electron densities are present, which is opposite to the treatment planning for phantom generated scatter.



#### 4. CONCLUSIONS

Conclusions are usually  
consolidated guesses.

Anonymous



#### 4.1 Conclusions

The Mevatron -6 and Mevatron -20 accelerators produce photon beams which were found to be contaminated by electrons and scattered photons. The dose measured at the surface of a phantom was due mainly to electron contamination. The magnitude of the surface tissue maximum ratio varied greatly under the conditions studied between 0.05 (in an open 5 cm x 5 cm 15 MV field at an SPD of 100 cm) to 0.60 (in a 30 cm x 30 cm field with a 3.2 cm Lucite accessory in place in a 6 MV beam). The other contribution to the surface dose due to photon backscatter was usually an order of magnitude lower.

The electron component of the surface dose was clearly evident. The magnitude of the displacement of the TMR curves with increasing field width was greatest at the surface. Under the same conditions of field width, SPD and accessory configuration, the 6 MV accelerator had a greater dose than the 15 MV accelerator at the same relative depth.

Adding additional thicknesses of accessories increased the surface TMR up to a thickness approximately equal to or greater than the electron range in the accessory ( $\sim 1/\mu_e$ ) when increases in the accessory thickness did not cause further increases in the surface TMR.

Electron "filters" reduced the surface dose when an accessory was in place by as much as 20% if the atomic number of the "filter" was equal to lead. The "filter" acted by scattering electrons out of the field. A reduction of dose inside the field accompanies an increase in dose outside the field.

The surface dose increased rapidly when the source-to-probe distance decreased. At 15 MV the isocentric normalized dose dependence on SPD for a 30 cm x 30 cm field size was consistent with the field flattening filter being the source of contamination. At 6 MV the isocentric



normalized dose did not decrease according to the inverse square dependence so the source was not localized.

The lateral distribution of the surface dose for a field size of 30 cm x 30 cm at 15 MV was Gaussian. This further suggested that the surface contamination was due to electrons which emanate from a localized source. The surface dose in a 30 cm x 30 cm field at 6 MV was not normally distributed which was consistent with a source or sources of electron contamination that are not localized.

The measurements were always taken with square fields except in Section 2.6 where the surface dose of a 15 MV beam was measured for rectangular fields. The surface dose was somewhat greater if the upper collimator defined the long axis compared to the situation when the lower collimator defined the long axis. The surface equivalent square field was very different from the equivalent square field at  $d_{\text{max}}$ .

The surface dose has been shown to be a useful measure of the amount of electron contamination incident on the phantom. The amount of contamination at the surface of a phantom was more accurately assessed by determining the amount of dose due to photons backscattering from the phantom.

Contamination electrons produced between the target and accessory tray were swept from the field by passing the beam through the poles of a permanent magnet positioned at the accessory tray. The surface dose with the magnet in place and the photon backscatter dose taken into account, was due to electrons produced in air between the magnet and phantom. This source of electron contamination was the most important at 6 MV and for small field sizes at 15 MV. The air produced electron contamination increased rapidly as a function of field size at small field sizes and increased as a function of SPD.





Electron contamination produced between the target and magnet, as indicated by surface dose with the photon backscatter removed, increased approximately in direct proportion to the cross-sectional area of the beam. This contribution to electron contamination decreased as a function of SPD.

The inverse square fall-off in the surface dose produced between the target and magnet along with the SPD dependence of the surface dose at large fields with no magnet in place suggested that electron contamination tended to be produced by mass close to the phantom and this material attenuated or scattered electrons produced further from the phantom.

The clinical aspects of an electromagnet to sweep contamination electrons from the field were discussed. The requirements for such a magnet were contradictory and would be difficult to achieve in practice.

The penetration of contamination into polystyrene, both inside and outside the field, had similar characteristics. The contamination inside the field was obtained by equating the increase in the dose as a function of field size in a limited phantom (where the field size is greater in extent than the phantom) at various depths in the phantom with the amount of contamination penetrating to that depth. The contamination as a function of depth in a phantom outside the field was measured by tilting the phantom so that the phantom would not change its relative distance from the field boundary as the phantom thickness increased. Both penetration characteristics illustrated that electrons deposit their energy at shallow depths in the phantom and scattered photons contributed at deeper depths. The difference between the shape of the curves was due to a difference in the relative proportion of electrons and scattered photons inside and outside the field.



The penetration curve of electrons produced between the target and magnet and a penetration curve of electrons set in motion in a thin slab at the surface of the phantom were also obtained. Electrons which were produced further away from the phantom were more penetrating at shallow depths and, therefore, more energetic than those produced close to or at the phantom surface. However, the maximum range of the electrons was independent of where they were produced.

The contamination penetration curves normalized to their own maxima were approximately independent of the configuration of the beam or the condition of measurement. Only the amount of contamination varied as a function of field width, SPD and presence of accessories. The phantom generated normalized dose at any depth was found by subtracting the amount of contamination penetrating to that depth. Since the shape of the contamination penetration curve was invariant, the amount subtracted at any depth was determined by the amount of electron contamination at the surface.

The output factor for the phantom generated normalized dose was larger at small field sizes and plateaued to a smaller value at larger field sizes compared to the total output factor. The phantom generated normalized dose curves were divided by the maximum normalized dose of each curve to obtain the phantom generated tissue maximum ratio curve. The phantom generated tissue maximum ratios were independent of field width, SPD and presence of accessories.

The phantom generated dose in the build-up region was computer modelled independently of experiment. The calculated results agreed with the experimental phantom generated tissue maximum ratios and were independent of field width.



The computer model showed that electrons set in motion in a thin layer produced a dose in the phantom which decreased exponentially. Therefore, an analytic model of the phantom generated dose in the build-up region could be adopted in which the primary photons and electrons set in motion fall exponentially, each with their own characteristic attenuation constant.

The separation of contamination from phantom generated contributions could reduce the data storage requirements of small computer treatment planning systems. Large computer planning systems could employ the results to produce a more accurate model of dose deposition when inhomogeneities are present in the build-up region.

The energy fluence of scattered photons is greater than the energy of electron contamination even though the maximum dose of contamination electrons is greater than the maximum dose of scattered photons. The shift in  $d_{\max}$  is due to contamination electrons.



## REFERENCES

- (1) Fitzgerald, J.J., Mathematical Theory of Radiation Dosimetry, Gordon and Breach Science Publishers, Inc., New York, 1967.
- (2) Johns, H.E., Laughlin, J.S., "Interaction of Radiation with Matter", Chapter 2 of Radiation Dosimetry, Gerald J. Hine, Gordon L. Brownell, Ed., Academic Press, New York, 1956.
- (3) Nelms, Ann T., Graphs of the Compton Energy-Angle Relationship and the Klein-Nishina Formula from 10 keV to 500 MeV, N.B.S. Circular, 542, U.S. Department of Commerce, 1953.
- (4) Rossi, Bruno, High Energy Particles, Prentice-Hall Inc., Englewood Cliffs, New Jersey, 1952.
- (5) Almond, P.R., "Dosimetry Considerations of Electron Beams", In: Kramer, S., Suntharalingam, N., Zinniger, G.F., Ed., High-Energy Photons and Electrons, J. Wiley and Sons, New York, 1976: 129-168.
- (6) Karzmark, C.J., Morton, R.J., A Primer on Theory and Operation of Linear Accelerators in Radiation Therapy, U.S. Department of Health and Human Services, 1981.
- (7) Cunningham, J.R., Johns, H.E., The Physics of Radiology, Charles C. Thomas, Publisher, 1974.
- (8) ICRU Report 24, Determination of Absorbed Dose in a Patient Irradiated by Beams of X- or Gamma Rays in Radiotherapy Procedures, International Commission on Radiation Units and Measurements, Washington, D.C., 1976.
- (9) Hubbell, J.H., Photon Cross-Sections, Attenuation Coefficients, and Energy Absorption Coefficients from 10 keV to 100 GeV, NSRDA - NBS 29, U.S. Department of Commerce, 1969.
- (10) Cassen, B., Corrigan, K.E., Hayden, H.S., Attenuation and Transition Effects in the Absorption of Supervoltage Radiation, Radiology, 31, 319-324, (1938).
- (11) Koch, H.W., Kerst, D.W., Morrison, P., "Experimental Depth Dose for 5, 10, 15 and 20 - Million - Volt X-Rays", Radiology, 40, 120-127, (1943).
- (12) Laughlin, J.S., Beattie, J.W., Lindsey, J.E., Harvey, R.A., "Dose Distribution Measurements with the University of Illinois 25 MeV Medical Betatron", American Journal of Roentgenology, 65, 787-799, (1951).





## REFERENCES (CONT'D)

- (13) Johns, H.E., Darby, E.K., Haslam, R.N.H., Katz, L., Harrington, E.L., "Depth Dose Data and Isodose for Radiations from a 22 MeV Betatron", American Journal of Roentgenology, 62, 257-268, (1949).
- (14) Johns, H.E., Epp, E.R., Cormack, D.V., Fedoruk, S.O., "Depth Dose Data and Diaphragm Design for the Saskatchewan 100 Curie Cobalt Unit", British Journal of Radiology, 25, 302-308, (1952).
- (15) Richardson, J.E., Kerman, H.O., Brucer, M., "Skin Dose from a Cobalt 60 Teletherapy Unit", Radiology, 63, 25-36, (1951).
- (16) Kemp, L.A.W., Burns, J.E., "Physical Measurements on the London Hospital Picker C 3000 Cobalt Unit", Acta Radiologica, 49, 471-484, (1958).
- (17) Saylor, W.L., Quillin, R.M., "Methods for the Enhancement of Skin Sparing in Cobalt 60 Teletherapy", American Journal of Roentgenology, 111, 174-179, (1971).
- (18) Velkley, D., Manson, D.J., Purdy, J.A., Oliver, G.D., "Build-Up Region of Megavoltage Photon Radiation Sources", Medical Physics, 2, 14-19, (1975).
- (19) Gagnon, W.F., Grant, W.G., "Surface Dose from Megavoltage Therapy Machines", Radiology, 117, 705-708, (1975).
- (20) Leung, P.M.K., Sontag, M.R., Maharaj, H., Chenery, S., "Dose Measurements in the Build-Up Region for Cobalt-60 Therapy Units", Medical Physics, 3, 169-172, (1976).
- (21) Smith, C.W., Sutherland, W.H., "Electron Contamination of Telecobalt Beams", British Journal of Radiology, 49, 562-563, (1976).
- (22) Khan, F.M., "Use of Electron Filters to Reduce Skin Dose in Cobalt Teletherapy", American Journal of Roentgenology, 111, 180-181, (1971).
- (23) Wilson, C.W., Perry, B.J., "Secondary Electron Emission Generated by X-Rays", British Journal of Radiology, 24, 293, (1951).
- (24) Hughes, H.A., "Measurements of Superficial Absorbed Dose with 2 MV X-Rays used at Glancing Angles", British Journal of Radiology, 32, 255-258, (1959).
- (25) Gray, L., "Relative Surface Doses from Supervoltage Radiation", Radiology, 109, 437-442, (1973).
- (26) Ibbott, G.S., Hendee, W.R., "Beam-Shaping Platforms and the Skin Sparing Advantage of Co<sup>60</sup> Radiation", American Journal of Roentgenology, 111, 193-196, (1970).



## REFERENCES (CONT'D)

- (27) Leung, P.M.K., Johns, H.E., "Use of Electron Filters to Improve the Build-Up Characteristics of Large Fields from Cobalt-60 Beams", Medical Physics, 4, 441-444, (1977).
- (28) Rao, P.S., Pillai, K., Gregg, E.C., "Effect of Shadow Trays on Surface Dose and Build-Up for Megavoltage Radiation", American Journal of Roentgenology, 117, 168-174, (1973).
- (29) Wu, A., "Effects of an Acrylic Resin Tray on Relative Surface Doses for 10 MV X-Ray Beams", International Journal of Radiation Oncology, Biology and Physics, 6, 1257-1260, (1980).
- (30) Scrimger, J., Kolitsi, Z., "Scattered Radiation from Beam Modifiers Used with Megavoltage Therapy Units", Radiology, 130, 233-236, (1979).
- (31) Baily, N.A., Beyer, N.S., "Surface and Entrance Dose for a 2 MV<sub>p</sub> X-Ray Beam", Radiology, 69, 553-557, (1957).
- (32) Chamberlain, E.C., Baily, N.A., "Entrance and Exit Absorbed Dose Characteristics for a 6 MeV X-Ray Generator", Radiology, 82, 267-271, (1964).
- (33) Bagne, F., "Physical Aspects of Supervoltage X-Ray Therapy", Medical Physics, 1, 266-274, (1974).
- (34) Dawson, D.J., "Percent Depth Doses for High Energy X-Rays", Physics in Medicine and Biology, 21, 226-235, (1976).
- (35) Dawson, D.J., "Tissue-Maximum Ratios for High Energy X-Rays", Medical Physics, 4, 423-430, (1977).
- (36) Nilsson, B., Brahme, A., "Absorbed Dose from Secondary Electrons in High Energy Photon Beams", Physics in Medicine and Biology, 24, 901-912, (1979).
- (37) Marbach, J.R., Almond, P.R., "Scattered Photons as the Cause for the Observed  $d_{\max}$  Shift with Field Size in High-Energy Photon Beams", Medical Physics, 4, 310-314, (1977).
- (38) Tolbert, D.D., Lane, R.G., Paliwal, B.R., Frost, S.W., Chin, K.B., Dercks, J., "Characteristics of Clinac-18 Wedged Fields for 10 MV X-Rays", Medical Physics, 4, 419-422, (1977).
- (39) Almond, P., Van Roosenbeck, E., "Variation in the Position of the Central Axis Maximum Build-Up Point with Field Size for High-Energy Photon Beams", British Journal of Radiology, 43, 911, (1970).
- (40) Bagne, F., "A Method for Calculating Megavoltage X-Ray Dose and Dose Parameters", Medical Physics, 7, 664-671, (1980).



## REFERENCES (CONT'D)

- (41) Biggs, P.J., Ling, C.C., "Electrons as the Cause of the Observed  $d_{\max}$  Shift with Field Size in High Energy Photon Beams", Medical Physics, 6, 291-295, (1979).
- (42) Padikal, T.N., Deye, J.A., "Electron Contamination of a High-Energy X-Ray Beam", Physics in Medicine and Biology, 23, 1086-1092, (1978).
- (43) Ling, C., Private Correspondence, (1981).
- (44) Ling, C., Rustgi, S., Gromadzki, Z., "Production of Secondary Radiation by 10 MV Photons", Presented to the American Association of Physicists in Medicine Meeting, August 1981, Boston, Mass.
- (45) Ling, C.C., Schell, M.C., Rustgi, S.N., "Magnetic Analysis of the Radiation Components of a 10 MV Photon Beam", Medical Physics, 9, 20-26, (1982).
- (46) Nilsson, B., Brahme, A., "Contamination of High-Energy Photon Beams by Scattered Photons", Strahlentherapie, 157, 181-186, (1981).
- (47) Tremblay, J.P., Bunt, R.B., "An Introduction to Computer Science, An Algorithmic Approach", McGraw-Hill Book Company, New York, 1979.
- (48) Sandifer, C.W., Taherzadeh, M., "Measurement of Linac Thick-Target Bremsstrahlung Spectra using a large NaI Scintillation Spectrometer", Published by E.G. and G. Inc., Goleta, California.
- (49) Raeside, D.E., "Monte Carlo Principles and Applications", Physics in Medicine and Biology, 21, 181-197, (1976).
- (50) Spencer, L.V., "Energy Dissipation by Fast Electrons, National Bureau of Standards Monograph 1", United States Department of Commerce, (1959).
- (51) Bruce, W.R., Johns, H.E., "The Use of the Monte Carlo Method", Section II in British Journal of Radiology, Supplement Number 9, (1960).
- (52) Hall, E.J., Radiobiology for the Radiologist, Harper and Row, New York, 1978.
- (53) Nahum, A.E., "Water/Air Mass Stopping Power Ratios for Megavoltage Photon and Electron Beams", Physics in Medicine and Biology, 23, 24-38, (1978).
- (54) Cohen, M. Jones, D.E.A., Greene, D., "Central Axis Depth Dose Data for Use in Radiotherapy", British Journal of Radiology, Supplement No. 11, The British Institute of Radiology, London, (1972).



## APPENDICES

All the mathematical sciences are founded on relations between physical laws and laws of numbers, so that the aim of exact sciences is to reduce the problem of nature to the determination of quantities by operations with numbers.

James Clerk Maxwell





# 5.1 Appendix 1 Numerical Values For Constants

|                   |                           |                |
|-------------------|---------------------------|----------------|
| $e$               | $= 1.602 \times 10^{-19}$ | Coulomb        |
| $h$               | $= 6.626 \times 10^{-34}$ | Joule-second   |
| $\hbar$           | $= 1.055 \times 10^{-34}$ | Joule-second   |
| $m_0$             | $= 9.110 \times 10^{-31}$ | kilogram       |
| $c$               | $= 2.998 \times 10^8$     | meter/second   |
| $m_0 c^2$         | $= 0.5110$                | MeV            |
| $r_0$             | $= 2.818 \times 10^{-15}$ | meter          |
| $N_0$             | $= 6.022 \times 10^{22}$  | molecules/mole |
| $I(\text{water})$ | $\sim 70$                 | eV             |
| $W(\text{water})$ | $\sim 34$                 | eV/ion pair    |

The quantity  $q(T, h\nu, Z)$  for water (see Equation 1.2.11) is listed below as a function of  $\nu$  (see Equation 1.2.8)

|                 |     |     |     |     |     |     |     |     |     |     |
|-----------------|-----|-----|-----|-----|-----|-----|-----|-----|-----|-----|
| $\nu$           | 0.0 | 0.1 | 0.2 | 0.3 | 0.4 | 0.5 | 0.6 | 0.7 | 0.8 | 0.9 |
| $q(T, h\nu, Z)$ | 5.0 | 3.5 | 1.9 | 1.3 | 1.1 | .88 | .77 | .69 | .62 | .58 |



5.2 Appendix 2      Total and Compton Attenuation  
Coefficients for Water (9)

| Energy<br>(MeV) | Total<br>Attenuation<br>Coefficient<br>(1/cm) | Compton<br>Attenuation<br>Coefficient<br>(1/cm) |
|-----------------|---|---|
| 0.10            | 0.168   | 0.165   |
| 0.15            | 0.149   | 0.148   |
| 0.20            | 0.136   | 0.136   |
| 0.30            | 0.118   | 0.118   |
| 0.40            | 0.106   | 0.106   |
| 0.50            | 0.0967  | 0.0967  |
| 0.60            | 0.0895  | 0.0895  |
| 0.80            | 0.0786  | 0.0786  |
| 1.00            | 0.0707  | 0.0706  |
| 1.50            | 0.0575  | 0.0574  |
| 2.00            | 0.0494  | 0.0490  |
| 3.00            | 0.0397  | 0.0385  |
| 4.00            | 0.0340  | 0.0322  |
| 5.00            | 0.0303  | 0.0278  |
| 6.00            | 0.0277  | 0.0245  |
| 8.00            | 0.0243  | 0.0201  |
| 10.00           | 0.0220  | 0.0171  |
| 15.00           | 0.0194  | 0.0127  |
| 20.00           | 0.0181  | 0.0102  |



5.3 Appendix 3      Total Stopping Power of Electrons  
in Water (5)

| Energy<br>(MeV) | Stopping<br>Power<br>(MeV/cm) | Energy<br>(MeV) | Stopping<br>Power<br>(MeV/cm) |
|-----------------|-------------------------------|-----------------|-------------------------------|
| 0.10            | 4.202                         | 1.00            | 1.893                         |
| 0.15            | 3.304                         | 2.00            | 1.889                         |
| 0.20            | 2.850                         | 3.00            | 1.931                         |
| 0.25            | 2.580                         | 4.00            | 1.974                         |
| 0.30            | 2.401                         | 5.00            | 2.014                         |
| 0.35            | 2.280                         | 6.00            | 2.051                         |
| 0.40            | 2.190                         | 7.00            | 2.085                         |
| 0.45            | 2.123                         | 8.00            | 2.119                         |
| 0.50            | 2.071                         | 9.00            | 2.152                         |
| 0.55            | 2.032                         | 10.00           | 2.183                         |
| 0.60            | 2.000                         | 15.00           | 2.327                         |
| 0.65            | 1.975                         | 20.00           | 2.470                         |
| 0.70            | 1.955                         |                 |                               |
| 0.75            | 1.939                         |                 |                               |
| 0.80            | 1.926                         |                 |                               |
| 0.85            | 1.915                         |                 |                               |
| 0.90            | 1.906                         |                 |                               |
| 0.95            | 1.899                         |                 |                               |



5.4 Appendix 4      Mean Square Mass Angular Scattering  
Power of Electrons in Water and Lead \*

| Energy<br>(MeV) | Water<br>(rad <sup>2</sup> g/cm <sup>2</sup> ) | Lead<br>(rad <sup>2</sup> g/cm <sup>2</sup> ) |
|-----------------|--|---|
| 0.10            | 1.31 × 10 <sup>2</sup>                         | 9.15 × 10 <sup>2</sup>                        |
| 0.15            | 6.59 × 10 <sup>1</sup>                         | 4.68 × 10 <sup>2</sup>                        |
| 0.20            | 4.10 × 10 <sup>1</sup>                         | 2.95 × 10 <sup>2</sup>                        |
| 0.30            | 2.14 × 10 <sup>1</sup>                         | 1.56 × 10 <sup>2</sup>                        |
| 0.40            | 1.37 × 10 <sup>1</sup>                         | 1.00 × 10 <sup>2</sup>                        |
| 0.50            | 9.71   | 7.17 × 10 <sup>1</sup>                        |
| 0.60            | 7.36   | 5.45 × 10 <sup>1</sup>                        |
| 0.80            | 4.75   | 3.55 × 10 <sup>1</sup>                        |
| 1.00            | 3.39   | 2.55 × 10 <sup>1</sup>                        |
| 1.50            | 1.82   | 1.38 × 10 <sup>1</sup>                        |
| 2.00            | 1.16   | 8.83  |
| 3.00            | 6.00 × 10 <sup>-1</sup>                        | 4.63  |
| 4.00            | 3.72 × 10 <sup>-1</sup>                        | 2.89  |
| 5.00            | 2.55 × 10 <sup>-1</sup>                        | 1.99  |
| 6.00            | 1.87 × 10 <sup>-1</sup>                        | 1.46  |
| 8.00            | 1.13 × 10 <sup>-1</sup>                        | 8.87 × 10 <sup>-1</sup>                       |
| 10.00           | 7.61 × 10 <sup>-2</sup>                        | 6.00 × 10 <sup>-1</sup>                       |
| 15.00           | 3.67 × 10 <sup>-2</sup>                        | 2.91 × 10 <sup>-1</sup>                       |
| 20.00           | 2.17 × 10 <sup>-2</sup>                        | 1.73 × 10 <sup>-1</sup>                       |

\* From "ICRU Report 21, Electrons with Initial Energies Between 1 and 50 MeV", International Commission on Radiation Units and Measurements, Washington, D.C., 1972





## 5.5 Appendix 5 Listing and Documentation For

'Seprimary.For'

program seprimary

```

C *****
C *
C * This program subtracts the contamination normalized dose from *
C * the total normalized dose to yield the phantom generated norm- *
C * alized dose. The amount of contamination arriving at the phan- *
C * tom is the proportional to the difference between the total *
C * and photon backscatter normalized doses. The phantom generated *
C * TMR curve is calculated after a search has found the maximum *
C * normalized dose. The error in the normalized dose and TMR *
C * values are calculated.
C *
C *****

integer i,n
real depth(20),ctmr(20),w,nd(20),bsnd
real ernd,ebsnd,cmax,pnd(20),epnd(20)
real recmax,max,remax,ptmr(20),eptmr(20)

C *****
C *
C * depth(20) is the depth in the phantom.
C * ctmr(20) is the contamination tissue maximum ratio,TMR, as a
C * function of depth.
C * w is the field width.
C * nd(20) is the total normalized dose as a function of depth.
C * bsnd is the backscatter normalized dose.
C * ernd is the error in the normalized dose.
C * ebsnd is error in the backscatter normalized dose.
C * cmax is the value of maximum contamination normalized dose
C * pnd(20) is the phantom generated normalized dose as a function
C * of depth.
C * epnd(20) is the error in the phantom generated normalized
C * dose as a function of distance.
C * recmax is the relative error in cmax.
C * max is the maximum phantom generated normalized dose.
C * remax is the relative error in max.
C * ptmr(20) is phantom generated normalized dose as a function
C * of depth.
C * eptmr(20) is the error in the phantom generated normalized
C * dose as a function of depth.
C *
C *****

open(unit=1,status='old',file='contam15.dat')
open(unit=2,status='old',file='nd15no16.dat')
open(unit=3,status='new',file='prim15.dat')

C *****
C *
C * contam.dat stores contamination TMR values as a function of
C * depth.
C * nd15no16.dat stores the total normalized dose curve as a func-
C * tion of depth and the value of the photon back-
C * scatter normalized dose for a particular config-
C * uration of field size and SPD at 15 MU.
C * prim15.dat is the output file that lists the phantom generated
C * normalized dose and TMR values along with their
C * associated errors.
C *

```



```

C *****
      read (1,100) n
      do 5 i=1,n
5         read (1,500) depth(i),ctmr(i)
          read (1,600) ectmr
          read (2,700) w
          do 10 i=1,n
10         read (2,1000) nd(i)
           read (2,1100) ernd,bsnd,ebsnd

C *****
C *
C * The following statements calculates the maximum amount of con- *
C * tamination and the amount of contamination occurring as a *
C * function of depth. The contamination is removed from the total *
C * normalized dose. The relevant errors are calculated as well. *
C *
C *****

      cmax=(nd(1)-bsnd)/ctmr(1)
      recmax=(ernd+ebsnd)/(nd(1)-bsnd)+ectmr/ctmr(1)
      pnd(1)=bsnd
      epnd(1)=ebsnd
      do 20 i=2,n
20         pnd(i)=nd(i)-cmax*ctmr(i)
           epnd(i)=ernd+(recmax+ectmr/ctmr(i))*cmax*ctmr(i)

C *****
C *
C * The maximum phantom generated normalized dose is found and the *
C * phantom generated TMR is calculated along with the associated *
C * errors. These quantities are then tabulated. *
C *
C *****

      max=pnd(1)
      do 30 i=1,n
          if(pnd(i) .ge. max) then
              max=pnd(i)
              remax=epnd(i)/pnd(i)
          end if
30      continue
      do 40 i=1,n
          ptmr(i)=pnd(i)/max
40      eptmr(i)=(remax+epnd(i)/pnd(i))*ptmr(i)
      write (3,1200) 'Field Size =',w,'cm X',w,'cm'
      write (3,1300) 'Photon Backscatter N.D. =',bsnd
      write (3,*) ' '
      write (3,1500) 'Depth','ND','Error in ND','TMR','Error in TMR'
      write (3,1600) '(cm)'
      do 50 i=1,n
50      write(3,1700) depth(i),pnd(i),epnd(i),ptmr(i),eptmr(i)

100     format(' ',i2)
500     format(' ',f4.2,2x,f4.2)
600     format(' ',f4.2)
700     format(' ',f4.1)
1000    format(' ',f5.3)
1100    format(' ',3(f5.3,2x))
1200    format(' ',a12,f4.1,a4,f4.1,a2)

```



```
1300      format(' ',a25,1x,f5.3)
1500      format(' ',a5,5x,a2,4x,a11,2x,a3,3x,a12)
1600      format(' ',a4)
1700      format(' ',f4.2,5x,f5.3,5x,f5.3,5x,f4.2,5x,f4.2)

      close(1)
      close(2)
      close(3)

      stop
      end
```



## 5.6 Appendix 6 Listing and Documentation For

## 'Buildup3.For'

program buildup3

```

C *****
C * Electron Monte-Carlo program to determine the electron dose *
C * in a semi-infinite water phantom for polyenergetic electrons using *
C * the Rossi Gaussian lateral scattering approximation. *
C *****

C *****
C ** Complete variable documentation appears in file Buildup3.doc *
C *****

      integer l,i1,nerg
      real r,zs,cal,sal,cbeta,sbeta
      real stop(179),tha(179),ep,cay
      real eo,e,dose(200),pl,gaus(100),g
      real z,max,ang,en(36),spectr(90,36)
      integer i,j,m,p,kay
      real xnrq(36),mu(36),sig(36),local,que(10)

      common /blk1/xnrq,en,mu,sig,local,spectr,que
      common /blk2/zs,z,ep,dose

C *****
C * Gaus.dat stores a table of x's as a function of erf(x). *
C * Quadint3.dat stores values of interpolated scattering and stopping *
C * power data in step sizes of 0.1 MeV. *
C * Dose.dat stores normalized absorbed dose as a function of depth *
C * in millimeters. *
C * Photon15.dat stores the normalized number of photons/bin,total *
C * absorption and Compton absorption coefficients as a *
C * function of bin energy. At the end of this file is *
C * a coefficient array which is used in Stearn's *
C * determination of a pair production electron trajectory.*
C *****

      open(unit=1,status='old',file='gaus.dat')
      open(unit=2,status='old',file='quadint3.dat')
      open(unit=4,status='new',file='dose.dat')
      open(unit=11,status='old',file='photon6.dat')

C *****
C * The following statements read the look-up tables and initializes. *
C *****

      do 2 l=1,179
        read(2,420) tha(l),stop(l)
2      continue
      do 10 i=1,36
        read(11,340) xnrq(i),en(i),mu(i),sig(i)
10      en(i)=en(i)*1000.0
        read(11,350) (que(i),i=1,10)
      do 30 l=1,100
30      read(1,422) gaus(l)
        i1=285019
        cay=0.90

C *****
C * Subroutine Impulse is called to determine the electron-set-in-motion *
C * number spectrum,'spectr(t,theta)',where 't' is the electron energy *

```





```

c      * and 'theta' is the original direction with respect to the photon      *
c      * direction. The program is repeated at all electron energies and      *
c      * angles for all histories as specified by 'spectr(t,theta)'. The      *
c      * following statements count histories and initializes the electron      *
c      * energy and angle.                                                    *
c      ****

      do 120 kay=10,100
        call impulse
        dose(kay)=dose(kay)+local
        do 120 j=1,75
          eo=floatj(j)/5.0+.1
          do 120 p=1,18
            ang=floatj(p)*5.0-2.5
            do 120 l=1,jnint(spectr(j,p))
              e=eo
              zs=floatj(kay)/10.0-.05
              cal=cos(ang/57.296)
              sal=sin(ang/57.296)
              r=6.2832*ran(i1)
              cbeta=cos(r)
              sbeta=sin(r)

c      ****
c      * 'Tha(nerg)' and 'stop(nerg)' are arrays that contain the      *
c      * mass angular scattering and mass stopping powers respec-      *
c      * tively. 'E' is the kinetic energy of the electron and      *
c      * 'ep' is the amount deposited in the path length 'pl'.      *
c      * 'Gaus(rg+1)' contains equally probable scattering angles      *
c      * for a Gaussian distribution with mean=0 and standard dev-      *
c      * iation=1. When this distribution is multiplied by the      *
c      * mean scattering angle the result is 'g', the zenith scat-      *
c      * tering angle. The final value of 'r' in each scattering      *
c      * event represents the scattering azimuth angle. The Sub-      *
c      * routine Geom determines the angles in the coordinate      *
c      * system fixed with respect to the phantom.                        *
c      ****

33      do 110 while(e .gt. 0.2)
          ep=(1-cay)*e
          nerg=e*10.0-ep*5.0
          pl=ep/stop(nerg)
          e=e-ep
          g=sqrt(tha(nerg)*pl)*gaus(jifix(100.0*ran(i1))+1)
          r=6.2832*ran(i1)
          call geom(r,g,cal,sal,cbeta,sbeta)
          z=pl*cal
          zs=zs+z

c      ****
c      * The following statement checks for the edge of the phantom. *
c      ****

          if (zs .lt. 0.0 ) go to 115

c      ****
c      * The energy loss is assigned to the cumulative dose      *
c      * received by the phantom using the Subroutine Assign.      *
c      ****

      call assign

```



```

110      continue

C      *****
C      * At this point the primary electron has an energy less than *
C      * 0.2 MeV. The remainder of the energy is assigned to the dose *
C      * at last depth interval. *
C      *****

115      call assign
120      continue

C      *****
C      * The following statements normalize the dose to the maximum *
C      * dose encountered and write the normalized dose. *
C      *****

      max=0.0
      do 122 i=1,100
        if (dose(i) .gt. max) max=dose(i)
122      continue
      do 125 i=1,100
        write(4,250) i,dose(i)/max
125      continue

250      format(' ',i3,2x,f6.2)
340      format(' ',f5.2,2x,f5.3,2x,2(f5.2,2x))
350      format(' ',10(f4.2,2x))
420      format(' ',e10.4)
422      format(e10.4)

      close(1)
      close(2)
      close(3)
      close(4)
      close(11)

      stop
      end

      subroutine geom(r,g,cal,sal,cbeta,sbeta)

      real r,g,cal,sal,cbeta,sbeta
      real ss,cc,oldcal,oldsal,oldcbeta,oldsbeta

C      *****
C      * 'Sal' and 'cal' are the sine and cosine respectively of *
C      * the zenith angle in the phantom system. 'Sbeta' and *
C      * cbeta are the sine and cosine respectively of the azi- *
C      * muth angle in the phantom system. *
C      *****

      oldsal=sal
      oldcal=cal
      oldcbeta=cbeta
      oldsbeta=sbeta
      cal=cal*cos(g)+sal*sin(g)*cos(r)
      if (abs(cal) .ge. 1.0) then
        cal=1.0*sign(1.0,cal)
        sal=0.0

```



```

        cbeta=cos(r)
        sbeta=sin(r)
        go to 400
    end if
    sal=sqrt(1.0-cal**2)
    if (oldsal .eq. 0.0) then
        cbeta=cos(r)
        sbeta=sin(r)
        go to 400
    end if
    ss=sin(g)*sin(r)/sal
    cc=(cos(g)-oldcal*cal)/oldsal/sal
    if (abs(ss) .ge. 1.0) ss=1.0*sign(1.0,ss)
    if (abs(cc) .ge. 1.0) cc=1.0*sign(1.0,cc)
    cbeta=cc*oldcbeta-ss*oldsbeta
    sbeta=ss*oldcbeta+cc*oldsbeta
    if (abs(cbeta) .ge. 1.0) cbeta=1.0*sign(1.0,cbeta)
    if (abs(sbeta) .ge. 1.0) sbeta=1.0*sign(1.0,sbeta)
400    continue

    return
end

```

#### subroutine impulse

```

real en(36),spectr(90,36)
real xnrg(36),mu(36),sig(36),local
integer i,j
real nteract(36),ncomp(36),npp(36)
real nrgmax,sum,que(10),q
real kinrg(20),nrgdif,a,b,c,dsigdt(20),arg
real theta(20),v,vee,g1,g2,g(20),nbin,angle,prob
integer binang,binum,vint

common /blk1/xnrg,en,mu,sig,local,spectr,que

c *****
c * The following statements determine the number of photons that *
c * interact in the phantom slice and the number due to the Compton *
c * and pair production interactions in each photon energy bin. *
c *****

    do 5 i=1,90
        do 5 j=1,36
5            spectr(i,j)=0.0
        local=0.0
        do 40 i=1,36
            q=en(i)*exp(-mu(i)*.001)
            nteract(i)=en(i)-q
            en(i)=q
            ncomp(i)=sig(i)/mu(i)*nteract(i)
            npp(i)=2*(nteract(i)-ncomp(i))

c *****
c * The following statements generate the electrons-set-in-motion *
c * due to the Compton interaction. *
c *****

    nrgmax=(2*xnrg(i)/.511)*xnrg(i)/(2*xnrg(i)/.511+1)

```



```

sum=0.0
do 10 j=1,20
  kinrg(j)=(float(j)-.5)*nrgmax/20.0
  nrgdif=xnrg(i)-kinrg(j)
  a=(.511*kinrg(j)/(xnrg(i)**2)**2
  b=2*(nrgdif/xnrg(i))**2
  c=((kinrg(j)-.511)**2-.261)*nrgdif/(xnrg(i))**3
  dsigdt(j)=(a+b+c)/nrgdif**2
  sum=sum+dsigdt(j)
  arg=(nrgmax-kinrg(j))*(2*xnrg(i)/.511+1)/kinrg(j)
  theta(j)=57.296*atan(sqrt(arg)/(1+xnrg(i)/.511))
10 continue
do 12 j=1,20
  dsigdt(j)=dsigdt(j)/sum
  nbin=dsigdt(j)*ncomp(i)
  binang=jifix(theta(j)*.2)+1
  if (kinrg(j) .lt. .2) then
    local=local+nbin*kinrg(j)
  else
    binum=jifix(kinrg(j)*5.0)
    spectr(binum,binang)=spectr(binum,binang)+nbin
  end if
12 continue

c *****
c * The following statements generates the electrons-set-in-motion *
c * due to the pair production interaction. *
c *****

nrgmax=xnrg(i)-1.022
sum=0.0
if (npp(i) .gt. 0) then
  do 15 j=1,20
    kinrg(j)=(float(j)-.5)*nrgmax/20.0
    v=(kinrg(j)+.511)/xnrg(i)
    vee=1-v
    g1=v**2+vee**2+2.0*v*vee/3.0
    g2=alog(2.0*xnrg(i)*v*vee/.511)-.5
    g(j)=g1*g2
    sum=sum+g(j)
    vint=jifix(v*10.0)+1
    theta(j)=57.296*que(vint)*alog(xnrg(i)/.511)*.511/xnrg(i)
15 continue
  do 17 j=1,20
    g(j)=g(j)/sum
    nbin=g(j)*npp(i)
    binum=jifix(kinrg(j)*5.0)
    do 17 binang=1,36
      angle=float(j(binang)*.08727-.04363
      prob=.06963/theta(j)*exp(-(angle/theta(j))**2/2.0)
      spectr(binum,binang)=spectr(binum,binang)+nbin*prob
17 continue
  end if
40 continue
return
end

subroutine assign
integer i,j,k,kp,dk
real zs,z,dosefrac,ep,dose(200)

```





```

common /blk2/zs,z,ep,dose

c *****
c * The fractions of dose to be assigned to all elements traversed *
c * are calculated. *
c *****

      k=10.0*zs
      kp=10.0*(zs-z)
      if (k .lt. 0) then
5         do 5 i=1,kp
            dose(kp+1-i)=dose(kp+1-i)-ep/z/10.0
            dose(kp+1)=dose(kp+1)+ep*((z-zs)+floatj(kp)/10.0)/z
            go to 55
        end if
        dk=k-kp
        j=0
        if (jiabs(dk) .gt. 1) then
            j=jiabs(dk)-1
            do 10 i=1,j
10             dose(kp+1+sign(i,dk))=dose(kp+1+sign(i,dk))+abs(ep/10.0/z)
        end if
        if (dk) 40,45,50
40         dosefrac=(zs-floatj(k+1)/10.0)/z
            dose(k+1)=dose(k+1)+ep*dosefrac
            dose(kp+1)=dose(kp+1)+ep*(1-floatj(j)/10.0/z-dosefrac)
            go to 55

45         dose(k+1)=dose(k+1)+ep
            go to 55

50         dosefrac=(zs-floatj(k)/10.0)/z
            dose(k+1)=dose(k+1)+ep*dosefrac
            dose(kp+1)=dose(kp+1)+ep*(1-floatj(j)/10.0/z-dosefrac)

55      continue
      return
      end

```



## Variable Documentation For Buildup3.For

## Main Program

## Integer

i,j,l,p, Dummy indices.  
 il, Random number seed.  
 kay, Slab number (1 is the top slab) in which the photon beam interacts.  
 nerg, Energy parameter specifying locations in look-up tables.

## Real

tha(179), A look-up array storing the scattering power of water in  $\text{radian}^2/(\text{cm}^2/\text{g})$ .  
 stop(179), A look-up array storing the stopping power of water in  $\text{MeV}/(\text{cm}^2/\text{g})$ .  
 xnrg(36), An array storing the photon bin energy.  
 en(36), The normalized number (in %) of photons in the bin.  
 mu(36), The total attenuation coefficient for water.  
 sig(36), The total Compton absorption coefficient for water.  
 que(10), Stearn's coefficients used in the determination of pair production electron trajectory.  
 gaus(100), Values of the inverse of  $\text{erf}(x)$ .  
 cay, Represents the fractional amount of energy retained by the electron after each step.  
 dose(200), The accumulated dose received by the slab.  
 local, Dose deposited in the slab by electrons set in motion with an energy  $< 0.2 \text{ MeV}$ .  
 eo, The initial energy of the electrons.  
 e, The energy of the electron.  
 ang, The zenith angle (degrees) at which the electrons are set in motion.  
 spectr(90,36), Generated by Subroutine Impulse, this array contains the number of electrons set in motion as a function of energy (90 bins) and zenith angles (36 bins).  
 zs, The depth of penetration into the phantom.  
 cal, The cosine of the zenith angle in the phantom coordinate system.  
 sal, The sine of the zenith angle in the phantom coordinate system.  
 r, The azimuth scattering angle (radian) in the electron frame.  
 cbeta, The cosine of the azimuth angle in the phantom coordinate system.  
 sbeta, The sine of the azimuth angle in the phantom coordinate system.  
 ep, The energy absorbed by the phantom in a step.  
 pl, The path length ( $\text{g}/\text{cm}^2$ ) travelled by the electron during the step.  
 g, The zenith scattering angle (radian) in the electron frame.  
 z, The change in the penetration during the step.  
 max, The maximum dose received by the phantom.

Subroutine Geom (Variables listed only where different from the Main Program.)

## Real

oldsal, The value of sal at the end of the previous step.



oldscal, The value of cal at the end of the previous step.  
 oldcbeta, The value of cbeta at the end of the previous step.  
 oldsbeta, The value of sbeta at the end of the previous step.  
 ss,cc, Parameters used to simplify geometric calculations.

Subroutine Impulse (Variables listed only where different from the Main Program.)

#### Integer

binang, Parameter specifying angle bin.  
 binum, Parameter specifying energy bin.  
 vint, Parameter used to specify Stearn's coefficient.

#### Real

q, The number of photons transmitted through the slab.  
 interact(36), The total number of photons in the bin interacting in the slab.  
 ncomp(36), The number of electrons set in motion by photons in the bin that interact in the slab due to the Compton effect.  
 npp(36), The number of electrons or positrons set in motion by photons in the bin interacting in the slab due to pair production.  
 nrgmax, The energy that is available to transfer to charged particles.  
 sum, Sum of the cross-section parameters. Used for normalization.  
 kinrg(20), Electron kinetic energy.  
 nrgdif, Difference between photon and electron kinetic energy.  
 a,b,c, Terms used to calculate the parameter proportional to the Klein-Nishina differential cross-section with respect to electron energy.  
 dsigdt(20), A parameter proportional to the Klein-Nishina differential cross-section.  
 arg, The argument used to simplify the calculation of recoil electron zenith angle for the Compton effect.  
 theta(20), The charged particle recoil zenith angle.  
 nbin, Product of normalized cross-section and number of charged particles set in motion.  
 v, Ratio of total electron energy to photon energy.  
 vee, Ratio of difference between total electron energy and photon energy compared to photon energy.  
 g1,g2, Terms used to calculate the parameter proportional to the pair production differential cross-section with respect to charged particle energy.  
 g(20), A parameter proportional to the pair production differential cross-section.

Subroutine Assign (Variables listed only where different from the Main Program)

#### Integer

k, The slab number (counting from the top down; the first slab is labelled 0) the electron is in at the end of the step.  
 kp, The slab number the electron was in at the end of the previous step.  
 dk, The number of slab boundaries crossed.



Real

dosefrac, The fraction of dose deposited to slabs across boundaries.





# 5.7 Appendix 7 Listing and Documentation For 'Normdist.For'

```

program normdist

c *****
c * This program calculates erf(x) using a modified approximation of the *
c * formulae listed in Dwight's Tables Of Integrals And Other *
c * Mathematical Data page 136. *
c *****

integer*4 factor
do 10 tea=0.0001,2.6,0.0001
  n = 1
  sum = 0.0
  test = 1.0
  do 9 while (test.ge.0.0001)
    term=(-1)**(n-1)*(tea**n-1)/n*factor(n-1)
    sum=sum+term
    test=term/sum
    n=n+1
    sum=sum/1.25331
  9 print 11,tea,sum
  10 format (f8.5,10x,f8.5)
  11 stop
end

function factor (i)

c *****
c * The subroutine Factor calculates the factorial of an integer. *
c *****

integer factor
factor=1
if (i.le.1) return
do 13 j=2,i
  13 factor=factor*j
return
end

```



## 5.8 Appendix B Listing and Documentation For

'Addose.For'

```

program addose

c *****
c * Addose.for calculates the dose as a function of depth in a *
c * phantom from electrons set in motion in 0.1cm slabs. The photon *
c * energy fluence is attenuated exponentially. The result is the *
c * broad beam TMR build-up values at 0.1cm intervals of depth. *
c *****

integer i,j,k
real dose(100),max,adose(100)

open(unit=1,status='old',file='dose.dat')
open(unit=2,status='new',file='addose.dat')

do 10 i=1,100
10  read(1,100) k,dose(k)

c *****
c * The following statements attenuates the photon energy fluence *
c * at the depth at which the electrons are being set in motion. *
c * The attenuation coefficient is 0.029/cm which is the average *
c * energy absorption coefficient at 6 MV. *
c *****

do 45 i=1,100
  do 40 j=1,i
    adose(i)=adose(i)+dose(j)*exp(-.029*(float(j(i+j-1)*.1-.05))
40  continue
45  print*,i,i,'adose(i)=',adose(i)
  max=0.0
  do 50 k=1,100
    if (adose(k) .gt. max) max=adose(k)
50  do 60 k=1,100
60  write(2,100)k,adose(k)/max

100 format(' ',i3,2x,f6.2)

close(1)
close(2)
stop
end

```



Thomas R. Mackie, B.Sc.  
John W. Scrimger, Ph.D.

## Contamination of a 15-MV Photon Beam by Electrons and Scattered Photons<sup>1</sup>

The 15-MV photon beam of a linear accelerator (Siemens Mevatron 20) was studied for electron and scattered photon contamination. The surface dose, attributable almost entirely to contamination electrons, has a Gaussian lateral distribution, a linear dependence on field width for square fields, and an inverse square dependence on distance from the bottom of the fixed head assembly. This geometrical dependence is consistent with the proposal that the field flattening filter is the main source of electron contamination when accessories are absent. A tissue-maximum-ratio curve in the build-up region for the electron and photon contamination was produced utilizing the linearity of dose with respect to field width. The derived contamination curve inside was similar to the measured build-up curve outside the field. The primary photon component, obtained by subtracting the contaminant contribution, showed no dependence on field size, source-to-probe distance, or presence of accessories.

**Index terms:** Electrons • Linear accelerator • Radiations, measurement • Therapeutic Radiology, instrumentation

Radiology 144: 403-409, July 1982

AN understanding of the role of electron and secondary photon contamination in megavoltage therapy machines is required to characterize dosimetry in the build-up region. Clinically, high-energy x-ray build-up produces a skin-sparing effect and contamination tends to reduce this effect.

Electron contamination has been identified as the major source of dose at the surface of a phantom for <sup>60</sup>Co (1, 2) and a wide range of accelerator energies (1-7). Most of these studies have employed thin-window parallel-plate chambers to measure the surface dose. Padikal and Deye, and Biggs and Ling, have measured the electron contamination directly by sweeping the electrons magnetically from the beam (3, 4).

There has been widespread disagreement concerning the origin of the contamination electrons. The collimator jaws (1-3, 5), field flattening filter (1, 2), and intervening air between the source and detector (2, 8) have been cited as possible sources. It is generally agreed that the presence of accessories in the field of the beam will increase the magnitude of electron contamination (1, 5, 6, 8-10). Bagne as well as Nilsson and Brahme, have derived expressions for dose in the build-up region by assuming that the surface dose is due to the presence of contamination electrons (8, 11).

Although electrons provide most of the contamination at the surface, contamination should be defined to include secondary photons generated outside the phantom. Throughout this paper the contamination component of the beam is defined as electrons and scattered photons produced by interactions of the primary photon beam with material outside the phantom. The primary photon beams are photons emerging through the collimator which have been produced by bremsstrahlung interactions in the target and modified by the fixed head assembly (Fig. 1).

### I. OPEN-FIELD BUILD-UP CURVES

#### Materials and Methods

Build-up curves were measured for a 15-MV photon beam from a Siemens Mevatron 20 linear accelerator. A schematic diagram of the beam defining head is shown in Figure 1. All measurements were made at constant source-to-probe distances (SPD) using 0.16-cm ( $\frac{1}{16}$ -in.) thick and 0.64-cm ( $\frac{1}{4}$ -in.) thick square polystyrene slabs as illustrated in Figure 2. The phantom slabs used in the determination of the open-field build-up curves each had a cross-sectional area of 625 cm<sup>2</sup>.

The detector used was a Capintec 192A electrometer with a PS-033

<sup>1</sup> From the Physics Department, University of Alberta and Cross Cancer Institute, Edmonton, Alberta, Canada. Received July 24, 1981; accepted and revision requested Nov. 13; revision received Feb. 16, 1982. jr



Figure 1

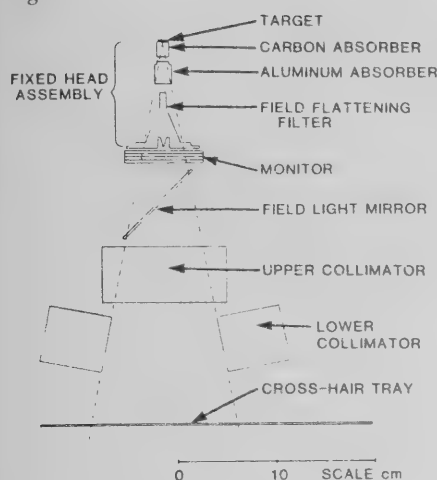


Diagram of the head assembly.

Figure 2

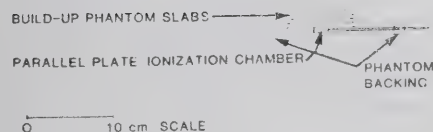


Diagram of the experimental arrangement. When determining the contamination depth dose, the phantom slab cross-sectional area was  $100 \text{ cm}^2$  and the slabs were always within the field boundary. The phantom slab cross-sectional area for all other measurements was  $625 \text{ cm}^2$ .

thin-window parallel-plate ionization chamber with an effective volume of  $0.5 \text{ ml}$ . The entrance window was aluminized polyester film  $0.5 \text{ mg/cm}^2$  thick. The tissue maximum ratio (TMR) is defined to be the dose at some depth,  $d$ , in the phantom normalized to the maximum dose occurring at a depth  $d_{\max}$ , for the same field area  $A$  and energy  $E$ .

$$\text{TMR} = \frac{\text{Dose}(d, A, E)}{\text{Dose}(d_{\max}, A, E)} \quad [1]$$

Throughout this paper the field size is referred to as the lateral field dimensions defined at  $100 \text{ cm}$ . Only square fields were used.

## Results

The central axis build-up curves for various field sizes are illustrated in Figure 3. These build-up curves demonstrate a dependence on field size. The TMRs for all depths below  $d_{\max}$  increase with increasing field size. The greatest relative difference between these curves occurs at or near the surface.

## Discussion

The spread in the curves is greater than can be expected from lateral scattering of photons and electrons generated in the phantom. Indeed, in the absence of backscatter or contamination, the TMR at the surface for all field sizes should approach zero. The field size dependence and the finite surface dose can be attributed to contamination since backscatter is negligible at the energy investigated.

## II. ACCESSORY BUILD-UP CURVES

### Materials and Methods

Various thicknesses of Lucite (density  $1.18 \text{ g/cm}^3$ ) alone or Lucite and lead (density  $11.4 \text{ g/cm}^3$ ) slabs were placed in the beam to determine their effect on the build-up curves. The distal surface of the slabs was placed at the accessory tray holder position  $56 \text{ cm}$  from the source. In all cases a Lucite surface was distal to the source. The build-up curves were measured as in Part I.

### Results

Figures 4 and 5 show the build-up at an SPD of  $100 \text{ cm}$  and  $75 \text{ cm}$ , respectively. The field size in both cases is  $30 \text{ cm} \times 30 \text{ cm}$ . When accessories are placed in the field at the tray holder position, a larger TMR for all depths less than  $d_{\max}$  is observed. There is also a shift in the point of  $d_{\max}$  to shallower depths. This is more pronounced at SPD =  $75 \text{ cm}$  (Fig. 5). There is virtually no difference in the build-up curves between a  $3.2\text{-cm}$  ( $1\frac{1}{4}\text{-in.}$ ) Lucite accessory and a  $0.30\text{-cm}$  lead slab on top of a  $0.64\text{-cm}$  lucite accessory.

At smaller SPDs, there is a greater

Figure 3

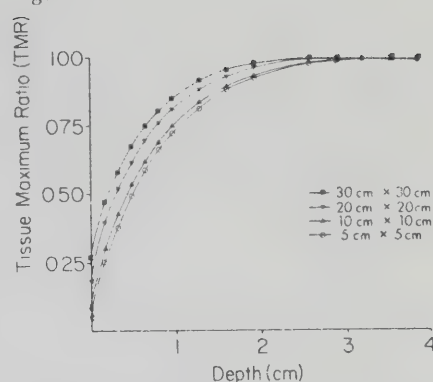
Open-field build-up curves at  $100\text{-cm}$  source-probe distance for various field sizes.

Figure 4

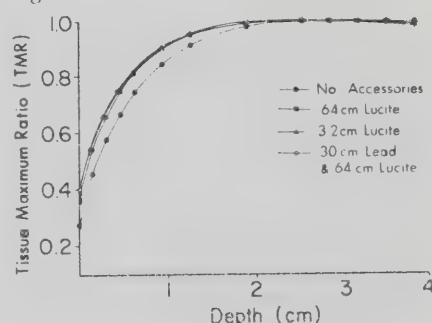
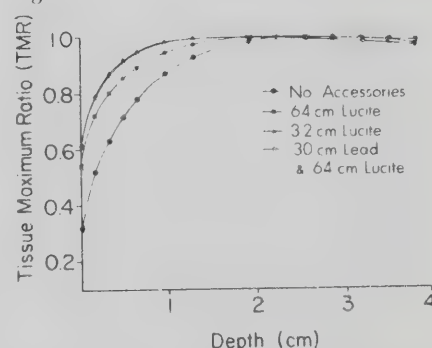
Effect of accessories on the build-up curves for a field size of  $30 \text{ cm} \times 30 \text{ cm}$ . Source-probe distance =  $100 \text{ cm}$ .

Figure 5

Effect of accessories on the build-up curves for a field size of  $30 \text{ cm} \times 30 \text{ cm}$ . Source-probe distance =  $75 \text{ cm}$ 

difference between the TMR with and without accessories. Therefore, as the distance to the source of contamination decreases, the dose increases. The TMR for SPD =  $75 \text{ cm}$  (Fig. 5) is greater than that for SPD =  $100 \text{ cm}$  (Fig. 4) at all depths and for all accessory conditions.





The difference between the TMR as a function of SPD is most pronounced at the surface.

## Discussion

As the thickness of accessory increases, the amount of contamination it produces increases. However, contamination produced at shallow depths within the accessory is shielded by the deeper layers. At a thickness equivalent to 3.2 cm (1¼ in.) of Lucite, there is a balance between production and absorption of contamination.

These observations agree qualitatively with those of Velkley *et al.* (5) for 25 MV x-rays collimated to a 10-cm × 10-cm field and Gray (1) for 4 MV x-rays.

## III. DISTANCE DISTRIBUTION OF SURFACE DOSE

### Materials and Methods

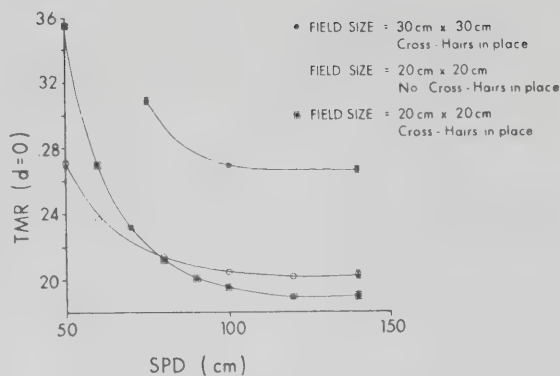
The surface maximum ratio is defined as the TMR measured with the chamber at the surface (*i.e.*  $d = 0$ ). When at the surface, the chamber used has a sufficiently thin window to ensure that the build-up depth is approximately zero (5 µm polystyrene equivalent). The window thickness has an equivalent mass stopping power of less than one centimeter of air. Only very low energy photons have a reasonable probability of interacting with such a window. In order to be detected, such photons have to be produced within a few centimeters of the chamber, otherwise they will be rapidly attenuated in air. Primary photons of low enough energy to interact with the window are completely attenuated when the beam emerges from the beam defining head. Therefore, most of the dose at the surface is attributable to contaminant electrons.

### Results

Figure 6 illustrates that the surface maximum ratio in the open beam increases rapidly as the SPD decreases for both 20-cm × 20-cm and 30-cm × 30-cm fields.

The curves for a collimated field size of 20 cm × 20 cm show the effect of a thin accessory. The Siemens Mevatron 20 is equipped with a removable, 1-mm thick, Lucite cross-hair tray which can be inserted at 40 cm from the source. When the SPD is less than 75 cm, the

Figure 6



Distribution of the surface dose as a function of source-probe distance. TMR = tissue maximum ratio

surface dose with the cross-hairs in place is greater than when it is removed. However, the cross-hairs, when in place, reduce the surface dose in the clinical region of SPD greater than 75 cm.

### Discussion

The reduction in dose when the cross-hairs are in place is a notable exception to previous observations that accessories in the field increased the surface dose. If it is assumed that all the electrons set in motion in the thin Lucite accessory by the incident photon beam emerge, they will be fewer than the number of incident electrons stopped. This is because the probability of production of electrons increases with increasing slab thickness whereas the survival of electrons already produced decreases with increasing thickness.

As the SPD increases, the volume of air between the target and probe increases. For  $^{60}\text{Co}$ , Nilsson and Brahme (8) predicted an increase in dose as a function of SPD due to  $^{60}\text{Co}$  photon interactions with air. In these experiments, the reverse appears to be the case and a decrease in dose as a function of increasing SPD has been observed. This implies that at 15 MV the interaction of the primary photon beam with air is not the major source of electron contamination.

The surface maximum ratio is normalized to the dose measured at  $d_{max}$  within a polystyrene phantom. The maximum dose in a phantom is due almost entirely to primary photons for which the variation with distance falls

off as  $1/(\text{SPD})^2$ . However, the electron contamination does not necessarily arise at the source of primary photons. Instead of normalizing the surface dose at a given SPD to the dose at  $d_{max}$ , each surface dose at the same SPD is normalized to the dose measured at a convenient point inside a phantom using a standard field size and photon SPD. The normalized dose is defined as:

$$\text{ND} = \frac{\text{Dose to point at arbitrary } d, \text{ SPD, field size,}}{\text{Dose to standard point}} \quad [2]$$

The standard point chosen was at the  $d_{max}$  point at SPD = 100 cm and field size = 10 cm × 10 cm.

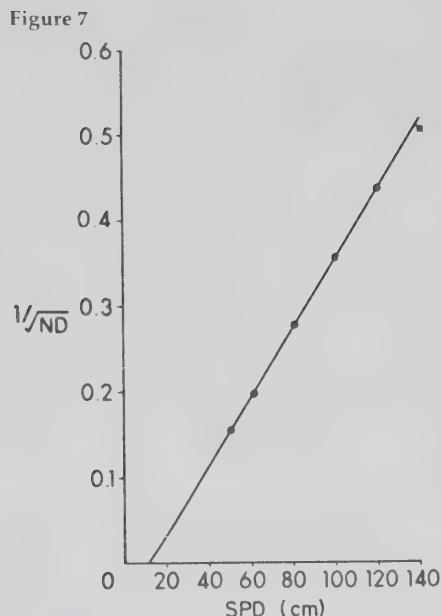
The apparent source of contamination electrons can be located assuming that it is a point source and there is no attenuation of electrons by air. Therefore, the normalized dose at the surface is directly proportional to the inverse square of the distance to the source of the electron contamination, or:

$$\text{ND}(d = 0) \propto \frac{1}{(\text{SPD} - d_0)^2} \quad [3]$$

where  $d_0$  is the distance of the source of contamination electrons below the primary photon source.

Figure 7 is a graph of the inverse square root of the normalized surface dose versus SPD. The graph yields a straight line except for very large SPDs. Therefore, the source must be small and the inverse square approximation valid for SPDs less than 120 cm. The x-intercept of the graph yields a dis-





Graph illustrating the inverse square dependence of the surface dose ( $ND$ ) on the distance to the source of contamination ( $SPD$ ).

tance  $d_0$  of 12 cm below the primary source of photons. This corresponds approximately to the position of the bottom of the fixed head assembly which consists of the field flattening filter and the beam monitor. The bottom surface of the field flattening filter is 3.1 cm wide; at distances greater than 50 cm this subtends an angle no larger than  $3.5^\circ$ , which approximates a point source.

The field flattening filter has a maximum thickness of 5.4 cm of stainless steel, which represents the largest interaction cross-section of any component in the beam defining head. The beam monitor is the last major component completely in the beam before the phantom, so it is likely to contribute to the dose due to contaminant electrons.

#### IV. GAUSSIAN LATERAL DISTRIBUTION OF SURFACE DOSE

##### Materials and Methods

The magnitude of surface dose as a function of lateral displacement from the central axis was measured for several SPDs. The central axis angle (CAA) was defined as the angle between the central axis and a line joining the probe to the apparent source of electrons.

This established parameters for the lateral direction in order to compare the distribution at various SPDs (Fig. 8, inset). In each case, the surface dose at any CAA and SPD is normalized to the dose at  $d_{max}$  on the central axis (CAA = 0).

##### Results

The curves in Figure 8 approximate a Gaussian distribution. At all points across the field, a smaller SPD results in a larger electron contamination dose.

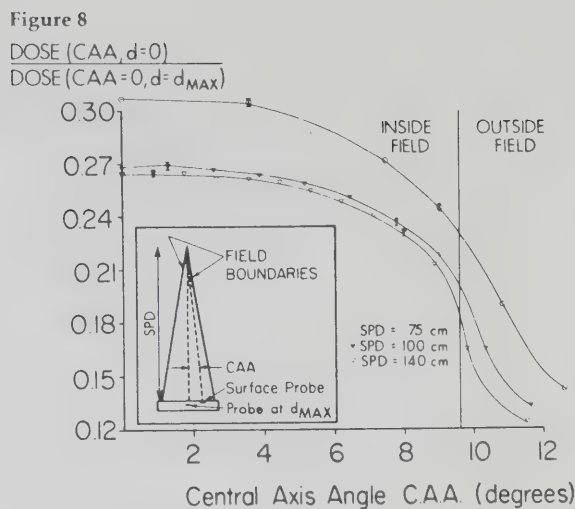
##### Discussion

The surface dependence measured along the central axis is in agreement with the finding at all points across the field that a larger electron contamination dose is the result of a smaller SPD. Both the lateral distribution and the dependence on the distance from the source of the electron contamination agree with the work of Almond (12).

#### V. BUILD-UP CURVES OUTSIDE THE FIELD

##### Materials and Methods

The primary photon dose outside the field boundary is very small (ap-



The Gaussian distribution of the surface dose. The inset is a schematic diagram of the experimental arrangement.

proximately 1% of the central axis dose at  $d_{max}$ ). Contamination electrons and scattered photons provide the largest contribution to the dose outside the field. This was studied experimentally. In order to get as close as possible to the field boundary, the probe was placed near the edge of the phantom (Fig. 9). The phantom was tilted at an angle<sup>2</sup> so that its surface would not move closer to or farther from the field boundary with the addition of build-up layers. This also reduced the number of particles incident at oblique angles upon the phantom.

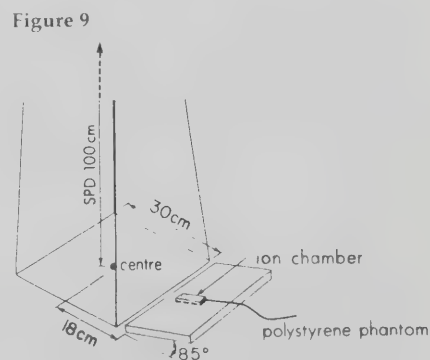
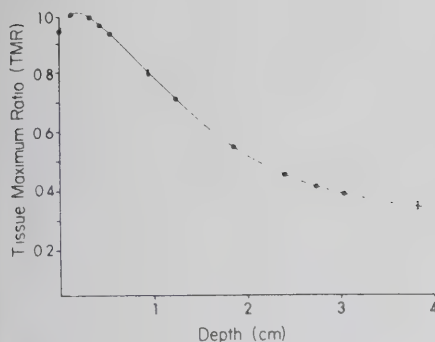


Diagram of the experimental arrangement to determine the build-up curve outside the field.

$$^2 \text{ Angle of tilt} = \tan^{-1} \left( \frac{\text{field width}}{2 \text{ SPD}} \right)$$



Figure 10



Build-up curve obtained 3 cm outside of a 30-cm  $\times$  30-cm field (see Fig. 9).

## Results

Figure 10 illustrates the depth dose curve 3 cm outside a 30-cm  $\times$  30-cm field. The TMR has a peak at a shallow depth (1–2 mm), then falls off rapidly at depths beyond about 2 cm.

## Discussion

The general shape of the curve agrees with the work of one of the authors (10) for 8-MV x-rays. This curve represents the contamination depth-dose due to electrons and scattered photons beyond the field edge. The peak at shallow depth followed by a rapid fall-off in dose is typical of the depth-dose curve for electrons. The relatively slow fall-off at depths beyond 2 cm is due in large part to scattered photons.

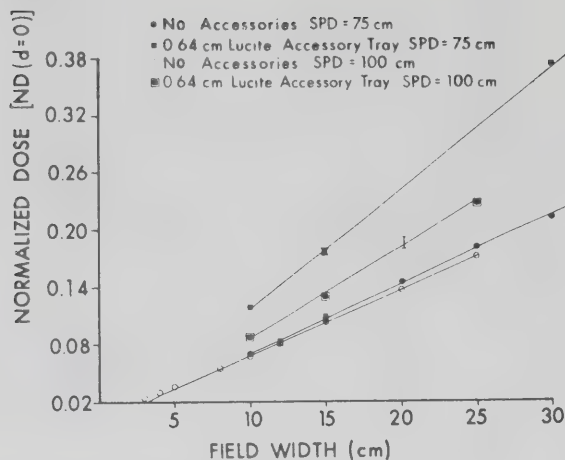
## VI. LINEARITY OF DOSE vs. FIELD WIDTH

### Materials and Methods

The dose as a function of field width was measured for a number of depths with the limited polystyrene phantom of the type illustrated in Figure 2. Since there was unit density material on top of the ion chamber, it could not be assumed that all of the contamination contributing to the dose was due to electrons.

The phantom was placed completely within the field so an increase in detected signal due to increasing field size could only be attributed to beam contamination. To obtain the dose as a function of depth for as many field widths as possible, the phantom lateral dimensions were kept as small as possible (*i.e.*, 10 cm  $\times$  10 cm), which in turn

Figure 11



Linearity of the surface dose with respect to field width under a variety of conditions.

dictated a minimum field size used in the determination of the contamination depth-dose curve of 15 cm  $\times$  15 cm. The maximum square field size attainable for the machine studied was 30 cm  $\times$  30 cm. These field sizes defined the range of the study.

## Results

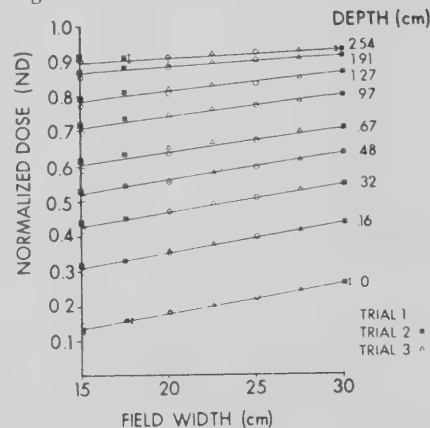
The normalized dose (as defined by Equation 2) for  $d = 0$  is plotted as a function of field width in Figure 11. Under a wide range of conditions there is a linear increase in the surface dose with respect to field width. Note that either decreasing the SPD or placing accessories in the field increases the slope. Since the surface dose for any given field size is proportional to the slope of the line, the slope is also a measure of the electron contamination, but with the advantage that it is not dependent on the field width.

Figure 12 illustrates that for various depths less than  $d_{max}$  there is a linear dependence of dose on field width. Qualitatively, the slope is greater at shallow depths than at deeper depths. As has already been seen for the dose at the surface, the slope of normalized dose *versus* field width is a measure of the magnitude of contamination penetrating to the depth specified. Therefore, there is a greater magnitude of contamination at shallow depths.

## Discussion

A number of authors (3, 5, 6, 8) have

Figure 12



The increase in the normalized dose with respect to field width for various depths within the phantom. The increase can only be attributed to contamination because the phantom (lateral dimensions = 10 cm  $\times$  10 cm) was completely contained within the field boundary.

commented on the dependence of the surface dose on the square root of field area both with and without accessories. Velkley *et al.* (5) normalized the surface dose at each field size to the dose at  $d_{max}$  for the same field size. However, since the dose at  $d_{max}$  increases with field size, such a plot would not unambiguously express the dependence of surface dose on field size. The concept of normalized dose, however, eliminates the ambiguity because the dose is nor-





malized to a quantity that does not change as a function of field size.

The magnitude of contamination has been shown to be proportional to the slope of normalized dose plotted against field width. To obtain a depth-dose profile for the contaminant contribution, the surface slope is set equal to the surface dose. This establishes a conversion between the slope at some depth and the dose due to contamination at the same depth. An assumption is made, as was previously discussed, that the dose measured by a thin-window ion chamber without any build-up is due to contamination electrons.

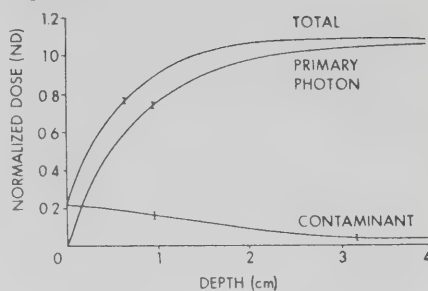
The primary photon contribution is obtained by subtracting the contamination component from the total build-up curve. Figure 13 shows the separate contribution from the contaminant and primary photon components of the total build-up curve for a 20-cm  $\times$  20-cm field. The contaminant contribution curve dominates the exposure dose at depths less than about 1 mm. At depths near  $d_{max}$ , the contamination contribution is less than 5% of the primary photon component.

If the contaminant contribution is renormalized to its own maximum, the depth-dose profile becomes more evident. Figure 14 shows the renormalized contaminant contribution curve. The peak in this depth dose curve occurs at about 1–2 mm. There is a rapid fall-off at depths slightly greater than the  $d_{max}$ . At depths greater than a couple of centimeters, the curve exhibits a slow fall-off with depth. This curve is similar qualitatively to the build-up curve measured outside the field (Fig. 10).

Since the contamination contribution was obtained by attributing the increase in dose to an increase in field size, the primary photon component should be independent of field size. TABLE I confirms this. Thus, the magnitude of contamination depends on the field size but the spectral characteristics of the contamination do not.

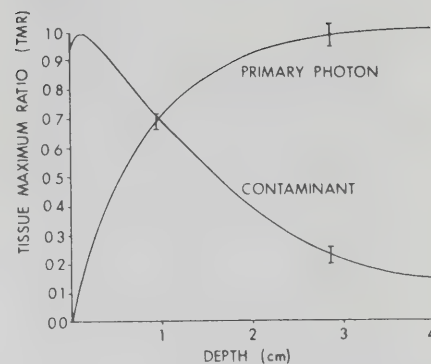
The derived primary photon TMRs in TABLE I are independent of field size. TMR was not, however, designed to be independent of field size for conditions other than an open field and SPD = 100 cm. The primary photon contribution is independent of SPD and the presence of accessories. The primary photon build-up curves for various conditions of SPD and accessory states are shown in TABLE II. The conditions of SPD were tested for 75

Figure 13



The contributions of the contaminant and primary photon components to the total build-up curve for a field size of 20 cm  $\times$  20 cm.

Figure 14



The contaminant and primary photon components in Figure 13 renormalized to their separate maxima.

TABLE I: Primary Photon Tissue Maximum Ratios for Various Field Sizes (No Accessories, Source-Probe Distance = 100 cm)

| No. of Slabs | Depth (cm) | Tissue Maximum Ratio for Field Sizes |                      |                      |                      |                      |
|--------------|------------|--------------------------------------|----------------------|----------------------|----------------------|----------------------|
|              |            | 5 cm $\times$ 5 cm                   | 10 cm $\times$ 10 cm | 15 cm $\times$ 15 cm | 20 cm $\times$ 20 cm | 25 cm $\times$ 25 cm |
| 0            | 0.00       | 0.00                                 | 0.00                 | 0.00                 | 0.00                 | 0.00                 |
| 1            | 0.16       | 0.19                                 | 0.19                 | 0.18                 | 0.19                 | 0.18                 |
| 2            | 0.32       | 0.33                                 | 0.33                 | 0.33                 | 0.33                 | 0.33                 |
| 3            | 0.48       | 0.44                                 | 0.44                 | 0.44                 | 0.44                 | 0.44                 |
| 4            | 0.64       | 0.54                                 | 0.54                 | 0.54                 | 0.54                 | 0.54                 |
| 6            | 0.95       | 0.68                                 | 0.68                 | 0.69                 | 0.69                 | 0.69                 |
| 8            | 1.27       | 0.79                                 | 0.78                 | 0.79                 | 0.79                 | 0.79                 |
| 12           | 1.91       | 0.91                                 | 0.91                 | 0.91                 | 0.91                 | 0.91                 |
| 16           | 2.54       | 0.97                                 | 0.97                 | 0.97                 | 0.97                 | 0.97                 |
| 20           | 3.18       | 1.00                                 | 0.99                 | 0.99                 | 0.99                 | 0.99                 |
| 24           | 3.81       | 1.00                                 | 1.00                 | 1.00                 | 1.00                 | 1.00                 |

TABLE II: Primary Photon Tissue Maximum Ratios under Various Conditions (Field Size = 30 cm  $\times$  30 cm)

| No. of Slabs | Depth (cm) | Tissue Maximum Ratios     |                            |                            |                              |                             |
|--------------|------------|---------------------------|----------------------------|----------------------------|------------------------------|-----------------------------|
|              |            | SPD = 75 cm<br>No Access. | SPD = 100 cm<br>No Access. | SPD = 140 cm<br>No Access. | SPD = 100 cm<br>0.64-cm LTA* | SPI = 100 cm<br>3.2-cm LTA* |
| 0            | 0.00       | 0.00                      | 0.00                       | 0.00                       | 0.00                         | 0.00                        |
| 1            | 0.16       | 0.19                      | 0.19                       | 0.18                       | 0.19                         | 0.18                        |
| 2            | 0.32       | 0.34                      | 0.33                       | 0.32                       | 0.33                         | 0.33                        |
| 3            | 0.48       | 0.45                      | 0.44                       | 0.43                       | 0.45                         | 0.45                        |
| 4            | 0.64       | 0.54                      | 0.54                       | 0.53                       | 0.56                         | 0.55                        |
| 6            | 0.95       | 0.68                      | 0.68                       | 0.67                       | 0.70                         | 0.69                        |
| 8            | 1.27       | 0.78                      | 0.78                       | 0.77                       | 0.80                         | 0.79                        |
| 12           | 1.91       | 0.90                      | 0.90                       | 0.90                       | 0.91                         | 0.91                        |
| 16           | 2.54       | 0.97                      | 0.96                       | 0.96                       | 0.97                         | 0.98                        |
| 20           | 3.18       | 0.99                      | 0.99                       | 0.99                       | 1.00                         | 1.00                        |
| 24           | 3.81       | 1.00                      | 1.00                       | 1.00                       | 1.00                         | 1.00                        |

\* LTA = Lucite tray accessory

cm, 100 cm, and 140 cm, whereas the electron contamination curve was derived for SPD = 100 cm. The independence of the primary photon build-up curve for these wide-ranging conditions illustrates that contamination accounts for the difference in depth-dose curves encountered. By defini-

tion, the primary photon contribution to the total build-up dose is due to that portion of the beam that does not interact before reaching the phantom. Changes in the primary photon build-up could only be due to changes in the phantom size, density, or configuration.





## CONCLUSIONS

The contamination depth-dose curve (Fig. 14) and the build-up curve outside the field boundary (Fig. 10) have similar shapes. The surface dose has been established as being due to contaminant electrons. The contaminant electrons evident at the surface must penetrate to some depth beneath the phantom. The peaks and rapid fall-off at shallow depths illustrated in Figures 10 and 14 are characteristic of electrons. The slow fall-off at depths greater than 2 cm is probably due to scattered photon contamination. Thus, the contamination radiation appears to be a combination of an electron contribution primarily at shallow depths and photons contributing primarily at greater depths.

Figures 10 and 14 differ in shape due to a difference between the relative amount of contamination electrons and photons present inside and outside the field boundary. Figure 8 demonstrated a Gaussian lateral distribution of the surface dose. Consequently for a 30-cm  $\times$  30-cm field there were about 45% fewer electrons present at 18 cm from the central axis than were present at the central axis.

Although the contaminant electrons are produced by the fixed components in the beam defining head, the size of the collimator opening dictates the relative amount of electron contamination emerging from the beam defining head. Low energy electrons are scattered by air through wide angles. The product of mass angular scattering power, density, and the electron path length for low energy electrons in air is of the same order of magnitude as the central axis angle.<sup>3</sup> Therefore, the angle of an electron when emerging through the collimators is not critical in determining whether it will arrive at the detector. The greater the collimator opening, the greater the flux of contamination electrons arriving at the detector. It has been shown empirically that the magnitude of electron contamination reaching the detector at the central axis is directly proportional to field width for square fields.

The contamination attributable to photons was derived from the increase in the dose as a function of field width.

<sup>3</sup> For example Rossi (13) states that a 3-MeV electron in air has a mass angular scattering power of 0.602 radians<sup>2</sup>·cm<sup>2</sup>/g which, after passage through 100 cm of air, corresponds to a mean scattering angle of 16.0°.

Therefore, the amount of material with which the primary photons could have interacted to produce scattered photons must be dependent on field size. The surface area of the collimator faces and the amount of air in the field both increase with field size. The contamination dose due to photons and the surface area of the collimator faces are both approximately proportional to field width, so it is likely the contamination photons are photons scattered by interaction of the primary photon beam with the collimators.

The shift in  $d_{max}$ , especially when accessories are present in the beam, can be attributed to a greater magnitude of electron contamination. Since the depth-dose profile for the scattered photons is likely to be similar to the primary photon profile, they are unlikely to contribute significantly to the shift in  $d_{max}$ . The peak in the contamination curve due to electrons occurs at very shallow depths, so increasing the magnitude of electron contamination results in a  $d_{max}$  shift towards shallower depths. This also explains why the shift is accompanied by an increased surface dose. These findings agree with Biggs and Ling (4) who observed that a shift in  $d_{max}$  did not occur when electrons were swept from the beam.

**Acknowledgment:** This research was sponsored in part by the Alberta Heritage Foundation for Medical Research, the Provincial Cancer Hospitals Board (Alberta), the Alberta Division of the Canadian Cancer Society, and the Physics Department, University of Alberta.

Physics Department  
Cross Cancer Institute  
University of Alberta  
Edmonton, Alberta  
Canada T6G, 1Z2

## References

1. Gray L. Relative surface doses from super-voltage radiation. *Radiology* 1973; 109: 437-442.
2. Jackson W. Surface effects of high-energy X rays at oblique incidence. *Br J Radiol* 1971; 44:109-115.
3. Padikal TN, Deye JA. Electron contamination of a high-energy X-ray beam. *Phys Med Biol* 1978; 23:1086-1092.
4. Biggs PJ, Ling CC. Electrons as the cause of the observed  $d_{max}$  shift with field size in high energy photon beams. *Med Phys* 1979; 6:291-295.
5. Velkley DE, Manson DJ, Purdy JA, Oliver GD Jr. Build-up region of megavoltage photon radiation sources. *Med Phys* 1975; 2:14-19.
6. Wu A. Effects of an acrylic resin tray on relative surface doses for 10 MV x-ray beams. *Int J Radiat Oncol Biol Phys* 1980; 6:1257-1260.
7. Dawson DJ. Percentage depth doses for high energy x-rays. *Phys Med Biol* 1976; 21:226-235.
8. Nilsson B, Brahme A. Absorbed dose from secondary electrons in high energy photon beams. *Phys Med Biol* 1979; 24:901-912.
9. Gagnon WF, Grant W III. Surface dose from megavoltage therapy machines. *Radiology* 1975; 117:705-708.
10. Scrimger J, Kolitsi Z. Scattered radiation from beam modifiers used with megavoltage therapy units. *Radiology* 1979; 130: 233-236.
11. Bagne F. A method for calculating megavoltage x-ray dose and dose parameters. *Med Phys* 1980; 7:664-671.
12. Almond PR. Dosimetry considerations of electron beams. In: Kramer S, Suntharalingam N, Zininger GF, eds. High-energy photons and electrons. New York: J. Wiley and Sons, 1976:129-168.
13. Rossi B. Radiation dosimetry: electrons with initial energies between 1 and 50 MeV. ICRU Report 24, 1972: p 13.











**B30425**